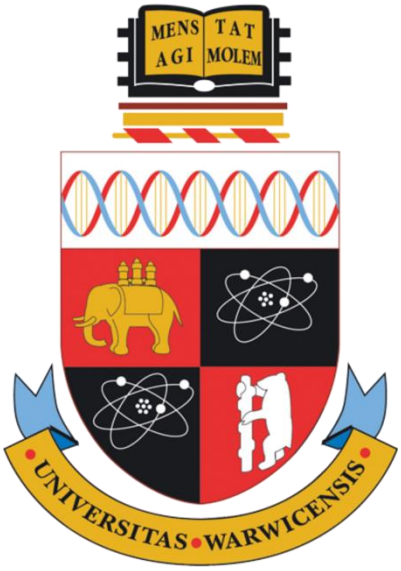

Safety of Automotive Lithium-ion Battery Cells under Abusive Conditions

EngD Innovation Report

Ahmed Abaza
BSc, MSc

A thesis submitted in partial fulfilment of the requirements for the degree of Doctor of Engineering

WMG, University of Warwick
September 2017

Abstract

The research carried out in this report focuses on the topic of safety of Li-ion battery cells, specifically for automotive applications. Electric vehicle battery safety is a challenge that must be tackled, especially with the rapid electrification of vehicles. Cell abuse testing simulates their failure process under different scenarios. This helps develop a deeper understanding of the failure process, its root cause and associated mechanisms, hence enabling the improvement of their safety. This research has experimentally investigated four abusive conditions; mechanical penetration, external short circuit, cell swelling as a result of overcharge and overcharge in an adiabatic environment. A number of potential industrial applications based on the research findings are also discussed.

During nail penetration testing the effect of nail material and diameter were investigated. Firstly, cells were fully penetrated using 10 mm diameter nails with three different materials; copper, steel and plastic. Secondly, cells were penetrated using 10 and 3 mm diameter copper nails. It was found that there was a clear distinction between the outcome of the conducting and non-conducting nails. However, the outcome of using electrically conductive nails suffered from poor reproducibility. Post-mortem examination showed that at the point of penetration the nail dragged the copper current collector in the direction of penetration along with the separator. The hole in the positive electrode looked less circular and the aluminium current collector was not dragged as deep as the copper one.

During external short circuit testing the effect of the short resistance and the short duration was investigated. Firstly, cells were short-circuited using a range of resistance values. Secondly, a programmable power supply to control the shorting duration was used. It was found that the degree of damage experienced by a cell during a short is not only defined by the short resistance, but also its duration. The cells were cycleable after the short circuit event and their capacity and resistance increase depended on the short circuit current magnitude and the short duration. Opening the cells after testing and studying their components using SEM showed no change in the surface morphology of the electrodes.

During the third set of experiments, purpose-built equipment was designed and built for in-situ volume measurement. The change in cell volume during cycling, overcharge and 10 cycles after the overcharge event was monitored and measured in-situ. The effect of the degree of overcharge and the magnitude of the charging current were studied. After the overcharge event the cycling behaviour of the cells was investigated. Electrochemical Impedance Spectroscopy (EIS) and Direct Current Internal Resistance (DCIR) were used to track the change in resistance. An Equivalent Circuit Model (ECM) was built to investigate the individual components contributing to the cell's impedance. The overcharge-induced capacity fade was analysed using incremental capacity analysis (ICA). The reversibility of cell volume after swelling was also investigated. Results show that cell swelling and the extent of damage depended on the degree of overcharge and the C-rate. Cell swelling was partially reversible and the cells were cycleable after the overcharge event.

Finally, cells were overcharged in ambient and adiabatic conditions. This was carried out to study the effect of heat dissipation on the outcome of an overcharge event. Results highlighted the critical role of heat dissipation from the cell in determining the outcome of the test. The same overcharge regime under different conditions resulted in very different outcomes. Cells overcharged in ambient conditions swelled significantly, but did not vent nor catch fire, whereas, all cells overcharged under adiabatic conditions either ruptured or caught fire. The magnitude of the overcharge current in adiabatic conditions determined the failure mode. Cells overcharged using 0.13 C current ruptured after swelling significantly, but did not catch fire. Cells overcharged with 0.33 and 1.3 C currents were completely combusted.

Acknowledgements

I am grateful to my wonderful parents; Dr Essam El-Din and Dr Heba, and my beloved siblings; Alaa, Mohamed and Abdelrahman for their endless unconditional love and support.

I would like to thank my supervisors; Dr Hin Kwan Wong, Dr Chris Lyness and Dr Rohit Bhagat, and my colleagues, especially Ronny Genieser for their guidance and help through this project.

I would also like to offer special thanks to Jaguar Land Rover (JLR), the Engineering and Physical Sciences Research Council (EPSRC) and WMG, University of Warwick for funding and supporting this project.

Last but not least, I would like to thank everyone who has helped me in any way, without which this would not have been possible.

Declaration

I confirm that the work presented in this report is my own unless otherwise stated. This work has not been previously submitted for any other degree.

Ahmed Abaza

30th September 2017

Contents

List of Figures

List of Tables

Acronyms and Abbreviations

Abbreviation	Description
ARC	Accelerating rate calorimetry
BMS	Battery management system
BTU	British thermal unit
C_2H_4	Ethene
C_2H_6	Ethane
CC	Constant current
CH_4	Methane
CID	Current interrupt device
CO	Carbon monoxide
CO_2	Carbon dioxide
CT	Computed Tomography
CPE	Constant phase element
Cu	Copper

DCIR	Direct current internal resistance
DEMS	Differential electrochemical mass spectroscopy
DMC	Dimethyl carbonate
EC	Equivalent circuit
EDX	Energy-dispersive X-ray
EIS	Electrochemical impedance spectroscopy
EngD	Engineering Doctorate
EUCAR	European Council for Automotive R&D
EV	Electric vehicle
EXSC	External short circuit
FMA	Failure mode analysis
FMMEA	Failure mode, mechanism and effects analysis
H_2	Hydrogen gas
ICA	Incremental capacity analysis
JLR	Jaguar Land Rover
LAM	Loss of active material
LCO	Lithium cobalt oxide ($LiCoO_2$)
LFP	Lithium iron phosphate ($LiFePO_4$)
Li-ion	Lithium-ion
LLI	Loss of lithium inventory
LMO	Lithium manganese oxide ($LiMn_2O_4$)
NMC	Lithium nickel manganese cobalt oxide ($LiNiMnCoO_2$)
NPD	Neutron power diffraction
ORI	Ohmic resistance increase
PTC	Positive temperature coefficient
SAE	Society of Automotive Engineers
SEI	Solid electrolyte interface
SEM	Scanning electron microscopy
SNR	Signal-to-noise ratio
SOC	State of charge
SOH	State of health
SOS	State of safety
SPEIS	Staircase potential electrochemical impedance
THT	Thermal Hazard Technology
XRD	X-ray diffraction

Units

Parameter	Symbol	Unit
Area	A	Square metres (m^2)
Capacity	Q	Ampere-hours (Ah)
C-rate	C	1C/hour
Length	L	Metre (m)
Resistance	R	Ohms (Ω)
Resistivity	ρ	Ohm-metre (Ωm)
State of charge	SOC	%
Temperature	T	Degree Celsius (°C)
Voltage	V	Volts (V)

Chapter 1 – Introduction

This chapter provides an introduction for this innovation report. It highlights the research focus, approach taken, aim and objectives. It also outlines the structures of the EngD portfolio and innovation report. Finally, it lists the innovations and contributions of the work carried out.

1.1 EngD Research Focus and Approach

The focus of this Engineering Doctorate (EngD) was to carry out studies on the topic of Li-ion battery cell safety, especially for their use in electric vehicles in abusive conditions. The topic was mainly approached experimentally, through testing. All testing was carried out at the Energy Innovation Centre at WMG, University of Warwick.

1.2 Aim and Objectives

The aim and objectives of this project were formulated in cooperation with the project partner and sponsor JLR. JLR have an ambitious electrification plan. JLR's decision to invest in this project came after the realisation of the importance of the safety of Li-ions batteries to be used in their vehicles. They would need to understand and assess the behaviour of cells under certain abnormal and abusive conditions to help with a number of applications, such as cell selection and making sure that these cells meet the required safety standard in a number of overseas markets, such as, China.

Aim

The overall aim of the EngD was to develop a deeper understanding of the behaviour of Li-ion battery cells under a number of abuse scenarios.

Objectives

The following objectives were achieved in order to meet the project's aim:

1) Investigating the failure mechanism during nail penetration testing
2) Investigating the cell behaviour during and after an external short circuit event
3) In-situ monitoring and quantifying the change in cell volume during overcharge and study its behaviour after an overcharge event

4) Studying the overcharge behaviour of cells in an adiabatic environment and compare it to overcharge in ambient conditions.

1.3 Structure of the EngD Portfolio

As Figure 1-1 demonstrates, the three main components of the EngD portfolio are; the submissions, the innovation report and the personal profile.

During the course of the EngD five submissions were completed.

Submission 1: Literature Review – sets the scene for the use of Li-ion cells in electric vehicles and highlights the importance of their safety. It also presents the main safety challenges and explores the gaps where improvements are most needed.

Submission 2: Experimental Study of Internal and External Short Circuits – experimentally investigates two short circuit scenarios. Firstly, internal short circuits caused by penetration with nails of different properties. Secondly, external short circuits caused by shorting the cell tabs using a circuit with a range of resistance values. Finally, it discusses the correlation between both tests.

Submission 3: International Industrial Placement Report – presents the placement at the Global Battery Competence Team at AVL.

Submission 4: In-situ Measurement of Cell Volume Change during Overcharge and Post-overcharge Cycling Behaviour – investigates the behaviour of cells during and after an overcharge event in terms of cell volume change and its reversibility, and change in cell impedance and capacity. It also presents the purpose-built equipment used in measuring the cell volume.

Submission 5: Effect of Short Resistance and Short Duration during an External Short Circuit – Investigates the behaviour of cells under different external short circuit resistance and duration conditions. It also studies the cycling behaviour of the short-circuited cells and presents the results of post-mortem analysis of the cells.

The *Innovation Report* is the most important piece of work in the portfolio. Its structure and description are presented in the following section (Section 1.4).

The *Personal Profile* of the author is also included within the EngD portfolio. It summarises how the author has developed in terms of the competences required for

the EngD. Evidence of each of the competences is provided through competences acquired and developed during the embedded Innovation and Entrepreneurship MSc, the international industrial placement and other activities carried out during the course of the EngD, such as presenting at conferences and supervision of undergraduate students.

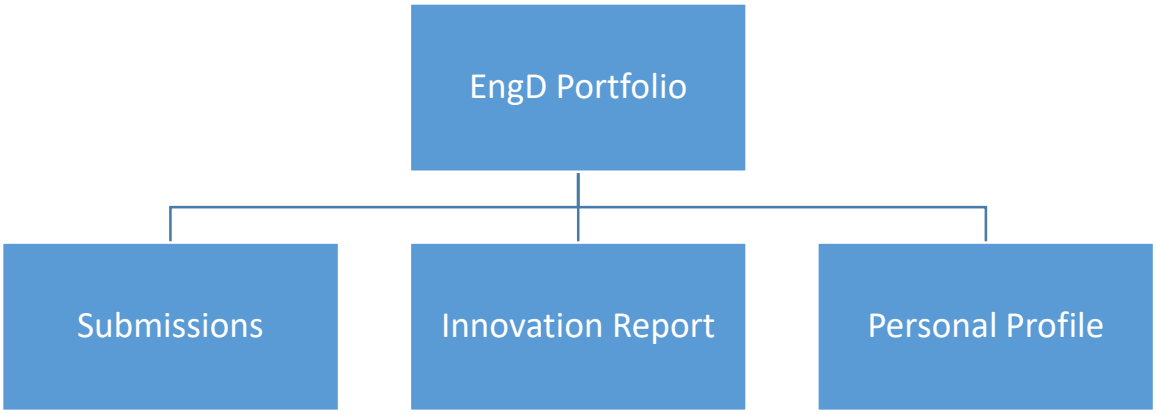

Figure 1-1: Components of the EngD portfolio

1.4 Structure of this EngD Innovation Report

The purpose of this report is to present the main findings of the research carried out as part of the Engineering Doctorate at WMG, University of Warwick.

Chapter 1 – outlines the EngD Programme and its components. It presents the focus of the EngD and the research approach taken, the aim and objectives are listed, the structure of the portfolio and innovation report are then outlined. Finally, it presents a summary of innovations and findings, the value of research, contributions and limitations.

Chapter 2 – introduces the main topics related to the research and provides the background information required for the following chapters. It starts with presenting the relationship between the wider concept of sustainability and the role of Li-ion batteries in low carbon mobility. Battery safety and failure topics are discussed after that, starting from hazard levels, stages of failure, possible outcomes, abuse testing, and the role of cell components in failure to the mechanism of performance degradation. Finally the business context of battery safety is discussed.

Chapter 3 – presents the findings of the nail penetration testing. It starts with the significance of the nail penetration test and provides a summary of the main nail penetration test standards for automotive applications. The experimental methodology is then presented. Finally, the effect of changing the nail material and diameter on the behaviour of cells during the nail penetration test are discussed.

Chapter 4 – presents the findings of the external short circuit testing. The significance of external short circuit testing and a summary of the main external short circuit automotive test standards are presented. The design of the rig used in testing is described and the experimental methodology is outlined. Finally the effect of short resistance and short duration on the cell during and after an external short is discussed.

Chapter 5 – presents how the cell volume changes during and after an overcharge event. First, the context of cell overcharge is presented, followed by background information, including, automotive overcharge test standards, mechanism of failure of overcharge and volume increase. The design of the test equipment and set-up are presented. Finally, the effect of the degree of overcharge and the magnitude of the charging current during and after the overcharge event are discussed.

Chapter 6 – presents the results of overcharging cells with different C-rates in two conditions; adiabatic and ambient.

Chapter 7 – lists a number of industrial applications and explores how the research output can be used in industrial applications.

Finally *Chapter 8* – draws the final conclusions of the innovation report.

1.5 Summary of Innovations and Contributions by Chapter

The research carried out during the course of the Engineering Doctorate produced a number of contributions to knowledge and innovation in the application of knowledge. The following is a list of them and their location within the Innovation Report:

1) Understanding the effect of changing the nail properties on the outcome of nail penetration test (Chapter 3)
2) Understanding the effect of short resistance and short duration during an external short circuit test (Chapter 4)

3) Designing and building a rig for external short circuit tests (Chapter 4)
4) In-situ monitoring the volume change of pouch cells during overcharge (Chapter 5)
5) Designing and building an apparatus for the in-situ volume measurement of pouch cells (Chapter 5)
6) Highlighting the significant role of heat dissipation during overcharge (Chapter 6)
7) Developing test procedures (Chapters 4, 5, and 6)
8) Developing a model to estimate the shorting resistance during a nail penetration event (done by JLR based on the findings of chapters 3 and 4).

1.6 List of Publications

Jaguar Land Rover internal report: Modelling Nail Penetration of Battery Cells through Correlation with External Short-circuit Experiments

Hin Kwan Wong, Ahmed Abaza, Maria Martin Blanco, Julia Weaving (Internal JLR report, December, 2015)

Conference presentation: The Effect of Contact Resistance during Nail Penetration of Commercial Automotive Lithium-ion Cells

Ahmed Abaza[1], Chris Lyness[2], Julia Weaving[3], Maria Blanco-Martin[2], Andy Moore[1], Richard Dashwood[1], Rohit Bhagat[1]

WMG, University of Warwick[1], Jaguar Land Rover[2], Tata Motors European Technical Centre[3] (UK Energy Storage Conference 2015)

Journal paper: Experimental Study of Internal and External Short Circuits of Commercial Automotive Pouch Lithium-ion Cells (Journal of Energy Storage)

Ahmed Abaza[1], Stefania Ferrari[1], Hin Kwan Wong[2], Chris Lyness[2], Andy Moore[1], Julia Weaving[3], Maria Blanco-Martin[2], Richard Dashwood[4], Rohit Bhagat[1]

University of Warwick[1], Jaguar Land Rover[2], Tata Motors European Technical Centre[3], Coventry University[4]

Journal paper: In-situ Cell Volume Measurement during Overcharge (in progress)

Chapter 2 – Background

2.1 Sustainability, Low Carbon Mobility and Li-ion Batteries

The world's energy consumption has been steadily increasing and is expected to continue growing [1]. The 2016 International Energy Outlook predicts that compared to the 549 quadrillion BTU of energy used worldwide in 2012, 629 quadrillion BTU will be used in 2020 and 815 quadrillion BTU in 2040 – an increase of 48% from 2012 to 2040 [2]. Unfortunately, currently the unsustainable, polluting fossils fuels, such as coal, oil and natural gas provide most of the world's energy [3]. It is projected that fossil fuels will account for 78% of the world's total energy consumption in 2040 [2].

In terms of end-use sector, the transportation sector accounted for 25% of the total energy consumption in 2012. Transportation energy use is expected to increase by 1.4% per year until 2040 [2]. The transportation system has been reliant on conventional internal combustion engine (ICE) vehicles. They have been in use for more than a century. Although they proved to be convenient and reliable, they come with their downsides. ICE vehicles inefficiently use fossil fuels, as its current maximum efficiency is between 25% and 30% and its maximum theoretical efficiency is 40% [4]. ICEs also produce harmful emissions, climate change is caused by the greenhouse gases in these emissions [5]. Moreover, these emissions increase air pollution and reduce local air quality, especially in urban areas, causing health problems [6]. Studies suggest that outdoor air pollution is contributing to about 40,000 early deaths a year in the UK [7]. The dependence on oil also has political and economic implications. The reliance on foreign oil, especially from unstable areas represents a risk to national security. Moreover, its price is vulnerable to geopolitical tensions, which causes price volatility and economic instability. All these factors dictate the decarbonisation of our energy and transportation systems and looking for sustainable clean energy sources.

The need for low carbon mobility transportation led to the development of a number of technologies, such as electric vehicles (EVs) and fuel cell vehicles (FCVs). Electric vehicles can be hybrid electric vehicles (HEVs) or battery electric vehicles (BEVs). Hybrid vehicles have both ICE and electric motors, hence they can run on both electricity and fuel, and are capable of having a fully electric driving range. They are considered the transition stage from conventional to the fully electric BEVs, which only

use electric motors for traction and purely run on electrical power stored in batteries on board.

Worldwide electrified vehicles has been rapidly growing. Data show that during the five years from 2010 to 2015 there has been an increase in the numbers by 1.26 million, as shown in Figure 2-1. Although both the battery electric vehicles (BEVs) and plug-in hybrid electric vehicles (PHEV) increased, the uptake of BEVs is faster [8]. Future EV figures are even expected to increase at a higher rate. This is because the wide spread of EVs is crucial to meet the climate change targets. The Electric Vehicles Initiative (EVI) of the Clean Energy Ministerial is encouraging to target 20 million EV by 2020 [9]. The Paris Declaration on Electro-Mobility and Climate Change and Call to Action target is 100 million electric cars and 400 million electric two- and three-wheelers by 2030 [10]. As shown in Figure 2-2, there are different scenarios for the path of EVs until 2030. The IEA ambitious scenario to limit the average global temperature increase to 2 degrees (2DS), requires the increase of the number of EVs to 140 million by 2030. In case of a 4 degrees (4DS) scenario, more than 25 million EVs are required by 2030. Although the difference in EV numbers between both scenarios is significant, a substantial increase of the number EVs is required from the current 1.26 million vehicles [8]. It is predicted that hybrid and electric vehicles will account for at least 50% of the total light duty vehicle sales worldwide by 2050 [11]. This shows the extent by which the EV market is expected to grow.

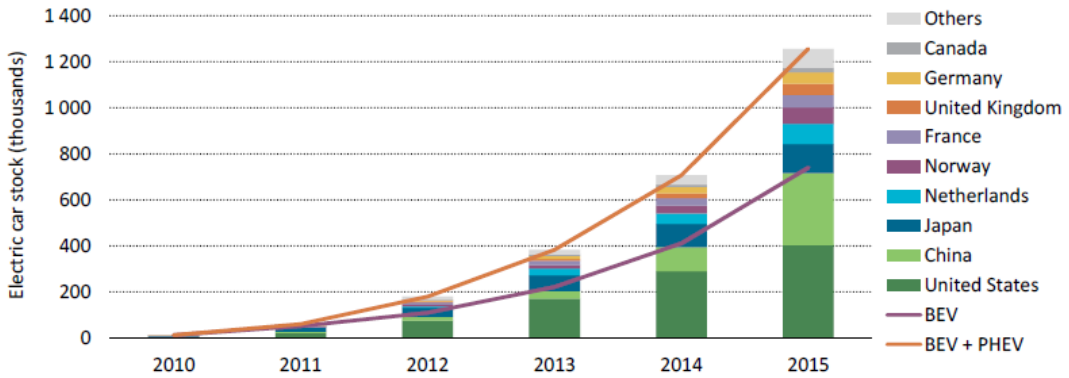

Figure 2-1: Cumulative number of electric vehicles until 2015 [8]

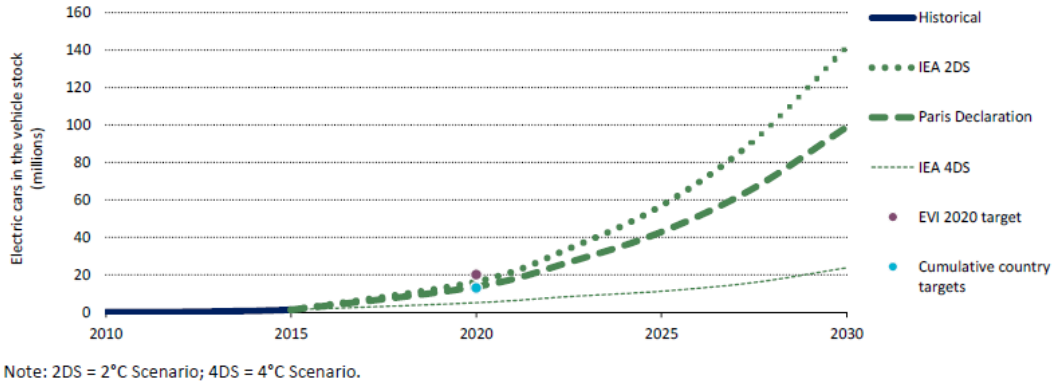

Figure 2-2: Scenarios for EV future trends until 2030 [8]

Large-format Li-ion batteries are currently the main battery technology used for hybrid and electric vehicles primarily because of their high energy and power densities [12], [13]. Despite their unique properties, batteries are still the main barrier for EV uptake on a larger scale. The initial cost and the range of EVs compared to ICE vehicles are some of the main factors that are affecting the spread of EVs [14], both are attributed to the battery. The high initial cost of EVs is mainly attributed to the price of the Li-ion battery. Although, advances in technology and mass production are leading to performance improvements and cost reduction. This will lead to the EVs being more affordable and appealing. According to the US Department of Energy (DOE), as shown in Figure 2-3 battery cost dropped from $1000/kWh in 2008 to $268/kWh in 2015, which is a 73% reduction in 7 years. The DOE's target is to reach a cost of $125/kWh by 2022 [15]. Some original equipment manufacturers (OEMs) like General Motors (GM) are more ambitious and are targeting a cost of $100/kWh and Tesla aims to even go below $100/kWh. In terms of performance, according the DOE the energy density of batteries increased from 60 to 295 Wh/L, which is equivalent to 400%, in 7 years, from 2008 to 2016 [8]. It should be noted that, in comparison to ICE vehicles, the current relatively high initial cost of EVs can be offset by the significantly lower running cost over the life time of the vehicle [16].

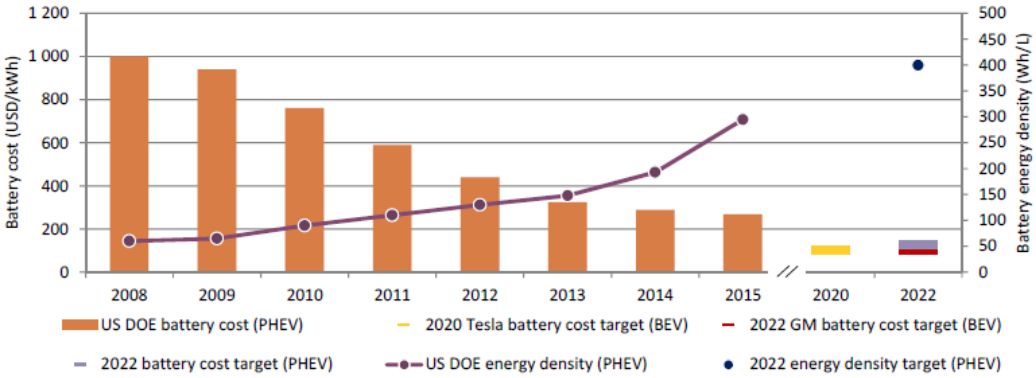

Figure 2-3: Automotive Li-ion battery cost and energy density trends [8]

Domestically, EVs will help the UK meet its greenhouse gas emission targets, as the UK is legally bound to cut its greenhouse gas emissions by 80% of the 1990 baseline by 2050 by the 2008 Climate Change Act [17]. In 2013, 25% of the total UK CO_2 emissions were caused by domestic transport [18]. Studies show that the most promising technology to shift to ultra-low emission vehicles is BEVs [19], as they are more energy efficient than vehicles using petrol or diesel and they produce less harmful emissions. It should be noted though that to harvest the best outcome from electric vehicles, they should be powered by sustainable, clean electricity coming from renewable energy sources, rather than the electricity generated in conventional power stations, hence a complete decarbonisation of our energy system is required [20]. However, it should be highlighted that with the UK's current electricity gird mix, electric vehicles are still more efficient and less polluting than ICE vehicles [21].

2.2 Battery Safety Failure and Hazard Levels

There are three key factors that determine the use of Li-ion batteries in electric vehicles. As discussed in Section 2.1, the first two are cost and performance. The third and most crucial factor is safety, it can hinder the uptake of electric vehicles [22], due to concerns regarding their violent failure [23]. Li-ion batteries have been safely used in other applications, such as electronics and stationary applications. Considering a number of more than 1 billion cells used, Li-ion cells have caused relatively very few incidents where personal injury or property damage were caused [24]. However, the automotive battery size and working environment are different. During normal operation automotive batteries are subjected to more demanding conditions such as mechanical shock and vibration [25]. Moreover, there is a possibility of them being

subjected to extreme abusive conditions in the case of accidents, such as crush or penetration by a foreign object. These safety challenges must be overcome to allow for safer and more abuse tolerant automotive batteries [26]. In addition, requirements such as having higher energy for longer range, and the possibility for fast recharge of the battery come with their extra safety challenges.

Failures presenting safety risks can happen as a result of abuse or spontaneous internal failures (field failures). Abuse includes operation outside the design parameters or beyond useful life. Field failures are usually caused by manufacturing defects and have a failure rate between 1 in 10 million and 1 in 40 million cells [27]. Abuse failures happening during assembly, transportation, operation or maintenance have a much higher frequency of occurrence. Risk is defined as the probability of an event happening multiplied by the severity of its outcome. To enhance Li-ion battery safety both should be reduced. At cell level the probability of cell failure should be reduced. Moreover, in the case of a single cell failure cell to cell heat propagation should be minimised to avoid adjacent cells from going into thermal runaway, hence preventing cascading failure of the entire module or battery pack.

The European Council for Automotive R&D (EUCAR) has defined the severity hazards levels that are used to describe and characterise the response of battery cells to abuse tests. Table 2-1 presents the EUCAR hazard levels, their description and classification criteria and effect.

Table 2-1: EUCAR Hazard levels, description and classification criteria and effect [28]

Hazard Level	Description	Classification Criteria & Effect
0	No effect	No effect. No loss of functionality.
1	Passive protection activated	No defect; no leakage; no venting, fire, or flame; no rupture; no explosion; no exothermic reaction or thermal runaway. Cell reversibly damaged. Repair of protection device needed.
2	Defect/Damage	No leakage; no venting, fire, or flame; no rupture; no explosion; no exothermic reaction or thermal runaway. Cell irreversibly damaged. Repair needed.

3	Leakage Δmass < 50%	No venting, fire, or flame; no rupture; no explosion. Weight loss <50% of electrolyte weight (electrolyte = solvent + salt).
4	Venting Δmass ≥ 50%	No fire or flame; no rupture; no explosion. Weight loss ≥50% of electrolyte weight (electrolyte = solvent + salt).
5	Fire or Flame	No rupture; no explosion (i.e., no flying parts).
6	Rupture	No explosion, but flying parts of the active mass.
7	Explosion	Explosion (i.e., disintegration of the cell).

2.3 Stages of Failure and Possible Outcomes

Heat generation inside battery cells is a common response to abusive conditions. If the rate of heat generation within the cell is higher than the rate of heat dissipation from the cell, heat builds up and the cell temperature rises [29]. If the temperature reaches a certain value (onset temperature), internal exothermic reactions are triggered and self-heating starts. The continuation of heat build-up can lead to thermal runaway, causing cell venting, fire or explosion [30]. Figure 2-4 shows how different abuse events can lead to thermal runaway.

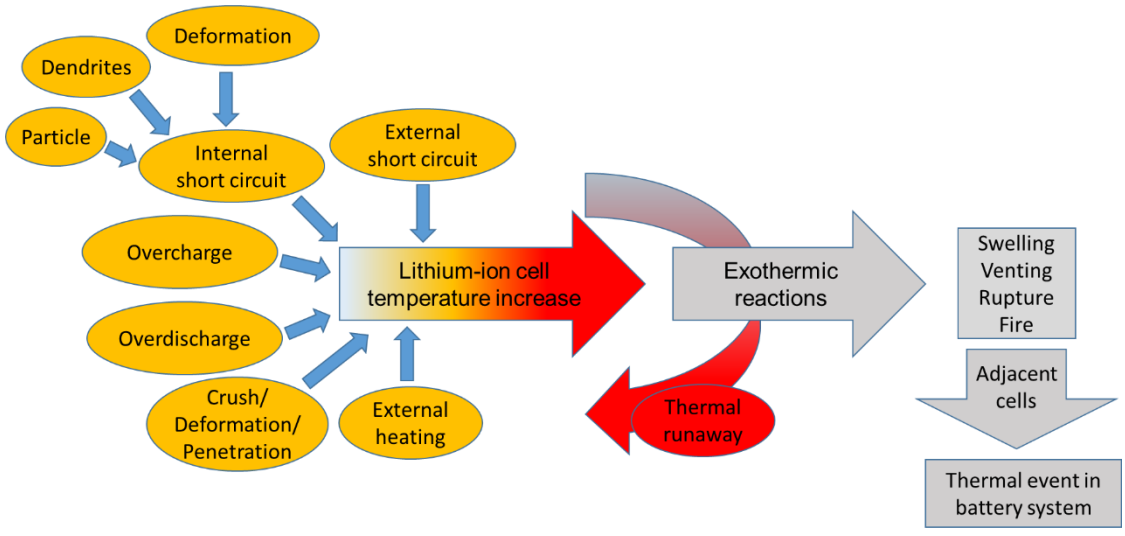

Figure 2-4: Abuse events that can lead to Li-ion battery thermal runaway [25]

Accelerating Rate Calorimetry (ARC) and thermal ramp tests are used to characterise heat and gas generation during abusive conditions. Figure 2-5 shows the three major

temperature stages of the thermal runaway process during a thermal ramp test of a fully charged cell [31]. The first stage involves raising the cell temperature until it reaches the on-set temperature that is marked by a self-heating rate of 0.2 °C/min. This self-heating is attributed to reactions between the anode and the electrolyte. The exposure of the anode to the electrolyte is a result of solid electrolyte interface (SEI) break down because of the elevated temperature [32]. If the heat generated is not dissipated, the cell temperature will continue to rise and will enter the second stage. During this stage the rate of heat generation accelerates, releasing more heat. The source of this heat generation increase is the further breakdown of the SEI and the start of chemical reactions between the electrolyte and the cathode. The further increase in the heat generation rate drives the cell into the final stage, which is defined by a self-heating rate of 10 °C/min or greater. This high self-heating rate is a result of high-rate cathodic and anodic reactions. At this point it is highly unlikely that any intervention would stop the thermal runaway and fire, explosion and disassembly of the cell may follow [27].

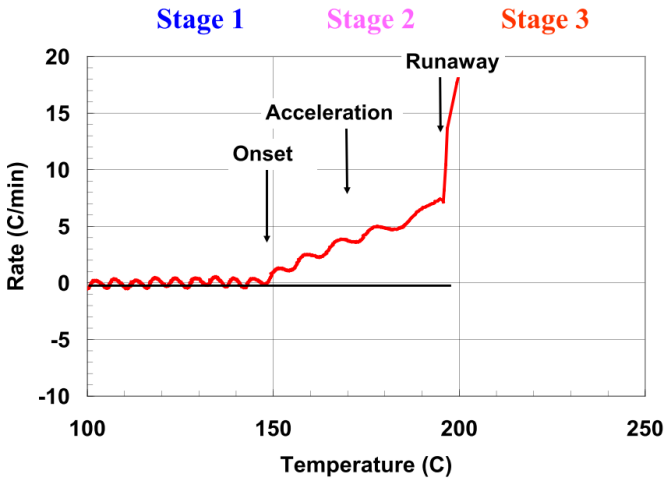

Figure 2-5: Stages of cell heating leading to thermal runaway during a forced thermal ramp test of a Li-ion cell [31]

The thermal runaway behaviour of a cell is a function of the cell properties (materials, design and size). The cathode chemistry plays an important role, the more oxygen is released by the cathode at high temperature the higher the reaction rates. Figure 2-6 shows the self-heating rate measured by ARC for different cathode materials. It can be seen that Lithium iron phosphate ($LiFePO_4$) is the most thermally stable, since it has the highest self-heating onset temperature and lowest self-heating rate. On the

other hand because of its relatively low onset temperature and high self-heating rate Lithium manganese oxide ($LiCoO_2$) is the least thermally stable. It should be noted though that the cathode materials with higher onset temperatures do not necessary make the cell safer. This is for two reasons; first, the decomposition of the anode is generally the lower temperature trigger that initiates thermal runaway after internal heating generated by an internal short circuit, and second, higher cathode decomposition temperature the threshold energy (not the power) required to induce a thermal runaway, but cannot eliminate it [33].

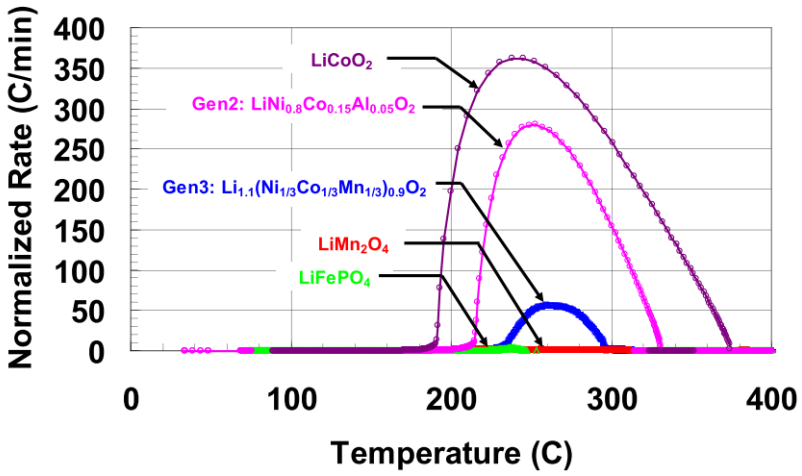

Figure 2-6: Self-heating rate of full 18650 cells with different cathode materials measured using ARC [11]

In terms of consequences failures can be classified into; graceful failure, having minor consequences or catastrophic failure, having catastrophic consequences. It should be noted that safety should be approached at a system/battery pack level, as cell safety does not directly translate into battery safety. Failures can be graceful at cell level, but can start catastrophic failure in system level [34]. Table 2-2 summaries the three scenarios of failure as a result of an abuse event. This event can be mechanical, electrical or thermal. To improve the safety of Li-ion batteries heat and gas generation must be controlled, at least at pack level.

Table 2-2: Possible scenarios of an abuse event outcome [11]

Scenario Description	Progression of Failure			Outcome Description
	Onset	Acceleration	Runaway	
Graceful failure at cell level	Abuse event causes cell temperature to rise	Exothermic reactions onset temperature is reached	Heat dissipation rate > heat generation rate. No thermal runaway on cell level	The preferred outcome
Graceful failure at module/pack level	Abuse event causes cell temperature to rise	Exothermic reactions onset temperature reached	Heat dissipation rate < heat generation. Cell enters thermal runaway. Propagation to other cells is stopped.	Acceptable outcome
Catastrophic failure at module/pack level	Abuse event causes cell temperature to rise	Exothermic reactions onset temperature is reached	Heat dissipation rate < heat generation. Cell enters thermal runaway. Failure propagates to other cells, consuming whole module/pack.	Unacceptable outcome

2.4 Abuse Testing and Failure Analysis

Standards are adopted by organisations, companies or governments that have interest in a particular technology or service. Battery standards aim to test them for certain characteristics such as performance, reliability and safety. A number of safety standards worldwide specify battery tests at cell, module and pack levels that must be passed in order for a cell to be approved for use in a specific application, typically for a cell to pass the test should not result in fire or explosion. These tests include mechanical, electrical and thermal abuse tests [11], [35]. Abuse refers to using the cell outside the conditions specified by the manufacturer. A description of the relevant

standards of the abuse tests carried out in this research is presented in the corresponding Chapter.

The main testing bodies/standards are as follows:

1) SAE J2464 “EV & HEV Rechargeable Energy Storage System (RESS) Safety and Abuse Testing Procedure” [36]
2) SAE J2929 “Electric and Hybrid Vehicle Propulsion Battery System Safety Standard – Lithium-based Rechargeable Cells” [37]
3) IEC 62660-2:2010 “Secondary Li-ion cells for the propulsion of electric road vehicles – Part 2: Reliability and abuse testing” [38]
4) United States Advanced Battery Consortium (USABC) “FreedomCAR Electrical Energy Storage System Abuse Test Manual for Electric and Hybrid Electric Vehicle Applications [26]
5) ISO 12405-3:2014 “Electrically propelled road vehicles – Test specification for Li-ion traction battery packs and systems – Part 3: Safety performance requirements” [39]
6) UL 2580 “Standard for Safety – Batteries for Use in Electric Vehicles” [40]
7) AIS-048 “Battery Operated Vehicles – Safety Requirements of Traction Batteries” [41]
8) UN38.3 Lithium Metal and Li-ion Batteries “Transport of Dangerous Goods – Manual of Tests and Criteria” [42]
9) GB/T 31485-2015 National Standard of the People’s Republic of China “Safety Requirements and Test Methods for Traction Battery of Electric Vehicle” [43]

Tests carried out to pass standards typically rely on pass/fail criteria and usually information from these test are not used in other applications. Although these abuse tests simulate the failure process under different scenarios and hence can also be used to develop a deeper understanding of the root cause of failure and its associated mechanisms through analysis such as, Failure Modes, Mechanisms and Effects Analysis (FMMEA) [44], [45] and fault tree analysis [34]. The hazard severity level observed during these tests can also be used as an input to a risk assessment and management approach [11]. Safety standards can be used for selection, design, testing, evaluation, use, packaging, storage, transportation, and disposal of batteries.

2.5 Role of Main Cell Components in Safety

A battery works by storing energy in the form of chemical energy and converting it into electrical energy when needed. Under normal operation it is desired to convert the stored energy electrochemically, which means from chemical to electrical energy with minimum heat generation and negligible gas production. As shown in Figure 2-7 the main four functional components of a Li-ion cell are the cathode, anode, separator and electrolyte. During normal operation the cell undergoes charge and discharge cycles. The charge and discharge of the cell works with an intercalation mechanism which involves the intercalation/insertion of lithium ions into the crystalline structure of the hosting electrode. During discharge lithium ions are de-intercalated from the anode, travel across the electrolyte towards the cathode and are intercalated into its structure. At the same time electrons travel around the external circuit from the anode to the cathode generating electricity across the cell tabs. During charging the whole process is reversed, electrical energy is introduced to the cell across the tabs and the direction of ion movement is reversed storing energy in the cell. Figure 2-7 shows the principle of operation of Li-ion cells.

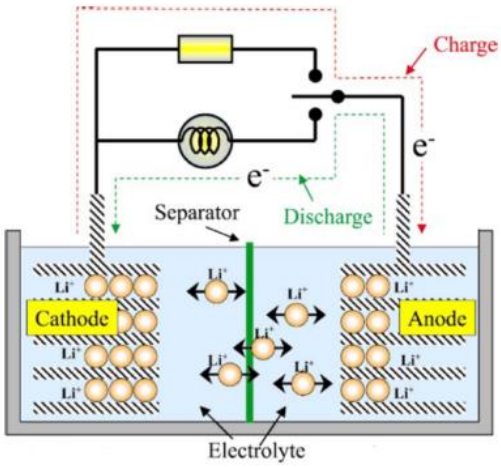

Figure 2-7: Components and principle of operation of Li-ion cells [46]

When it comes to the safety of Li-ion cells, thermal stability is the most important factor. Thermal stability is highly dependent on cell components since both fuel (anode as well as flammable electrolyte) and oxidiser (cathode) are packed together in a sealed container. This combination has high explosion potential. Under normal operation it is desired to convert the stored energy electrochemically which means from chemical to

electrical energy with minimum heat generation and negligible gas production. However, if the oxidizer and the fuel are allowed to react chemically, the stored energy will be mainly converted into heat and gas instead. Once these exothermic chemical reactions start it is almost impossible to stop them and will likely proceed to completion, due to the intimate contact between the oxidiser and fuel. This uncontrolled behaviour becomes a thermal runaway, which once starts there is no ability to stop it [27]. The amount of heat released in the case of thermal runaway due to the exothermic reactions depends on the material of the anode, cathode, electrolyte and separator. Hence each component contributes to the failure process. Material selection also affects the cell performance. It is desired to have a safe high performing cell, but unfortunately, the best performing cells are usually the less safe ones. Regarding cell components the main issues affecting cell safety are:

1) The oxidative capacity of the cathode
2) The reactivity of the anode and the stability of its SEI layer
3) Separator strength and stability.
4) Electrolyte flammability and its reactivity with electrode materials.

Cathode role in cell safety

The choice of cathode material is crucial since it has a strong influence on the safety, performance and life of the battery. Table 2-3 is a summary of the most common cathode chemistries currently in use. Calorimetry is used to assess the thermal stability by measuring the reactivity of cell components. Plotting the self-heating rate versus the cell temperature gives an indication about the thermal stability of the material. Self-heating at lower temperatures is a sign of low thermal stability and hence if the material is used may result in less safe cell.

Figure 2-6 is a plot of the self-heating rate versus temperature of 18650 cells with different common cathode chemistries. The key points to notice on this plot are the onset temperature, the maximum heating rate and temperature width of the thermal runaway. Improving the cathode thermal stability results in a higher thermal runaway temperature and reduced peak heating rate and therefore more thermally stable cells. It can be seen that LCO has the least thermal stability and LFP is the most stable based on their onset temperatures and maximum heating rates. But it should also be noticed that LFP has a lower nominal voltage as shown in Table 2-3, i.e. the more

thermally stable the cells the lower performance they have. LCO ($LiCoO_2$) has good performance as shown in Table 2-3, but has poor thermal stability compared to other cathodes as Figure 2-6 shows. At elevated temperatures it decomposes exothermically producing oxygen that reacts with the organic solvents of the electrolyte. The choice or cathode material is a compromise between capacity and safety, cathode materials which deliver good capacity have poor thermal stability.

The thermal stability of a cathode chemistry depends on the amount of oxygen it produces when decomposed at elevated temperatures. There is a correlation between the amount of oxygen produced from cathode decomposition and the onset temperature and the peak heating rate. This explains why cathode chemistries like LFP are very stable as they don't produce oxygen gas even when fully decomposed. When it comes to safety events cathodes with higher oxygen content act as strong oxidisers and anodes act as fuel. Since they are packed closely together in the cell containment, if thermal runaway is triggered, there is no way to interrupt the reaction since both the fuel and oxidizer are in such intimate contact and it will proceed to completion. Thermal runaway in chemistries like LFP with no oxygen content is dominated by reactions between the anode and the electrolyte resulting from the breakdown of the SEI layer on the anode.

Another safety issue of the cathode is its contact with the electrolyte. This contact can result in increased cathode surface impedance due to the formation of reactive products or dissolution of the transition metal active species from the cathode. This can decrease the thermal stability of the cathode and produce a significant amount of heat that might lead to a thermal runaway.

Table 2-3: Summary of the most common commercial cathode chemistries [11]

Material	Specific Capacity mAh/g	Midpoint V vs. Li at C/20	Comments
$LiCoO_2$	155	3.9	Poor thermal stability. Co is expensive and has toxicity issues

$LiNi_{1-x-y}Mn_xCo_yO_2$ (NMC)	140-180	~3.8	Capacity depends on upper voltage cut-off, safer and less expensive than $LiCoO_2$
$LiNi_{0.8}Co_{0.15}Al_{x0.05}O_2$ (NCA)	200	3.73	High capacity, about as safe as $LiCoO_2$
$LiMn_2O_4$ (Spinel)	100-120	4.05	Poor high temperature stability (but improving with R&D), safer and less expensive than $LiCoO_2$
$LiFePO_4$ (LFP)	160	3.45	Synthesis in inert gas leads to process cost, very safe, low volumetric energy
$Li[Li_{1/9}Ni_{1/3}Mn_{5/9}]O_2$	275	3.8	High specific capacity, R&D scale, low rate capability

Anode role in cell safety

Currently anodes used are carbon based. They can be natural or synthetic graphite with varying surface areas and different morphologies. It is desired to have a high performing anode with low irreversible loss on formation cycling, and good stability when exposed to high temperatures. During the initial charging process reductive decomposition of the electrolyte happens on the anode surface forming a film called Solid Electrolyte Interface (SEI) layer. Although the formation of the SEI layer results in irreversible capacity loss, it protects the anode and prevents further reaction between the anode and the electrolyte. The most common failure mode of carbon anodes is the dissolution of the SEI layer at elevated temperatures exposing the anode surface to the electrolyte. The reactions between the anode and the electrolyte are exothermic that may cause rapid heating and lead to thermal runaway. Another failure mode is the plating of lithium metal forming dendrites on the anode. These dendrites may puncture the separator causing an internal short circuit that heats up the cell and can lead to a thermal runaway [47].

Separator role in cell safety

Although separators are electrochemically inactive components in a Li-ion cell, they have a critical role in determining the abuse tolerance of the cell and its performance [48], [49]. The separator is a porous sheet that prevents contact between the cathode and the anode to avoid internal short circuits but allows the transfer of ions across it during operation. To fulfil these functions a separator should have poor electronic conductivity but good ionic conductivity respectively. Cell safety is very sensitive to the integrity and stability of the separator under mechanical stress and elevated temperatures. Cell safety can be significantly improved by making the separator with higher mechanical stress to be puncture resistant, and by having high thermal stability to avoid melting at elevated temperatures and hence avoid short circuit in both cases [50].

The three most common types of separators are polymeric membranes, nonwoven mats, and ceramic enhanced membranes. Polymeric membranes have relatively low cost and small thickness. A thin separator provides higher energy and power densities as it facilitates the movement of ions. However, separators must have mechanical properties to withstand the stretching during cell assembly, cyclic deformation, and resist penetration due to dendritic growth on the electrodes or from foreign particles introduced in the battery manufacturing process [50]. The design of safe separators is a challenge since it is a trade-off between mechanical robustness and transport properties.

A short circuit due to separator failure may lead to a thermal event with catastrophic consequences. Hence it is important to make sure that the separator design is safe and incorporates some safety features to avoid short circuits. For electric and hybrid vehicle applications using large Li-ion cells the application of micro layers of ceramic coating on the separator could reduce the risk of thermal runaway during an internal short circuit. There are also shutdown separator designs which stop current flow after a certain temperature acting as a thermal fuse to prevent further heating and reaching thermal runaway.

Figure 2-8 shows the ideal separator shutdown function for a Li-ion cell during an overcharge test. The cell is overcharged until its surface temperature reaches 135 °C. At this point the separator shuts down as it is designed and the cell becomes resistive.

The current then drops to zero and the voltage increases to the maximum set limit. The heating stops and the cell begins to cool down safely. The separator should also retain its mechanical integrity after shutdown, otherwise the electrodes could come into contact leading to a thermal runaway. Due to thermal inertia it is possible that the temperature rise continues even after separator shutdown, this might lead to separator meltdown and subsequent thermal runaway. Therefore, to ensure cell separator safety the difference between the shutdown and meltdown temperatures should be maximised [30]. However, the use of separator shutdown in large Li-ion cells for electric vehicles is controversial. Incomplete separator shutdown, where only part of the separator pores close and the rest stay open can lead to an increase in the current density resulting in additional localised heating and potentially could accelerate cell failure [51].

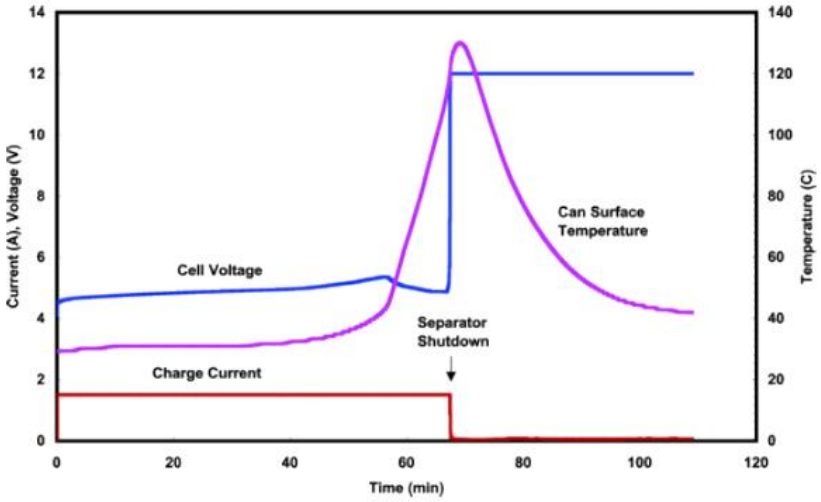

Figure 2-8: Ideal separator shutdown function of a Li-ion cell during an overcharge test [51]

Electrolyte role in cell safety

Li-ion cells use lithium-containing salts dissolved in a mixture of organic solvents instead of aqueous electrolytes. These organic electrolytes have good conductivity that enables the design of high-power cells. On the downside their high volatility and flammability cause serious safety issues. Under normal conditions these electrolytes are stable because of the SEI layer which limits the reactions with the anode. However, under abnormal conditions of voltage and temperature this kind of electrolytes can react with the active materials of the electrodes producing heat and gas. Additives are

added to reduce the flammability of the electrolytes and modify the reactivity of the anode [47].

The choice of the electrolyte mix in terms of electrolytic species, solvent ratios, salts and additives affects both the performance and safety of the cell. The performance is affected through the conductivity, operating temperature range, and voltage stability range. The thermal stability and abuse tolerance of the cell affect the safety. The performance should be optimised with maximum safety, but unfortunately some electrolytes with high performance cannot be used due to safety considerations because of their toxicity and reactivity. During an abuse event the choice of electrolyte has an effect on the thermal runaway reactions and hence the peak heating rate. Figure 2-9 shows the effect of different electrolytes on the peak heat generation rate of a nickel-cobalt-aluminium cell. It can be see that the EC:PC:DMC(1:1:3)/1.2M significantly reduces peak heating rate.

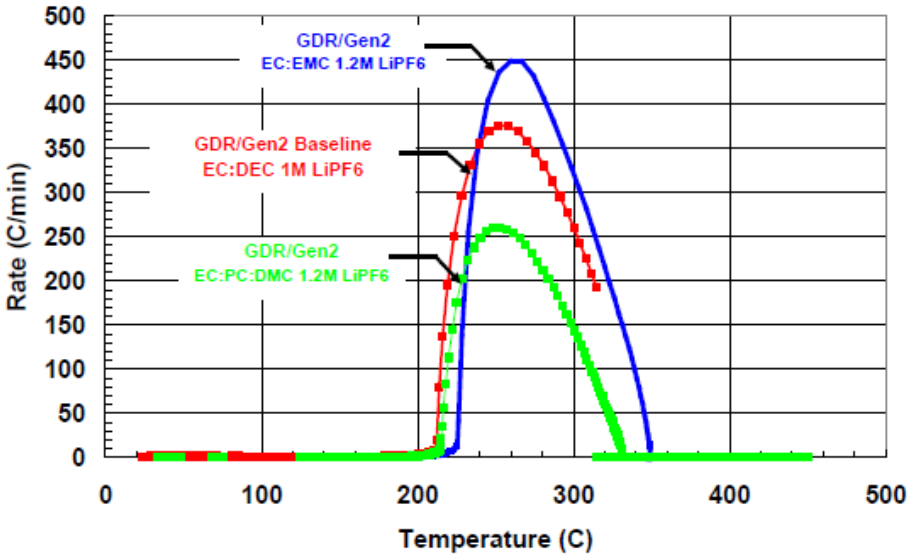

Figure 2-9: ARC profiles of 18650 Cells with different electrolyte species [11]

During an event the energy released by electrolyte reactions depends on the cell chemistry and state of charge (SOC). As discussed in the cathode section the most energetic reactions result from the oxidation of the electrolyte by the oxygen produced from the decomposition of the cathode. Figure 2-10 shows the ARC profiles of anodes and cathodes compared to full cells. It can be seen that the full cell has the highest heating rate.

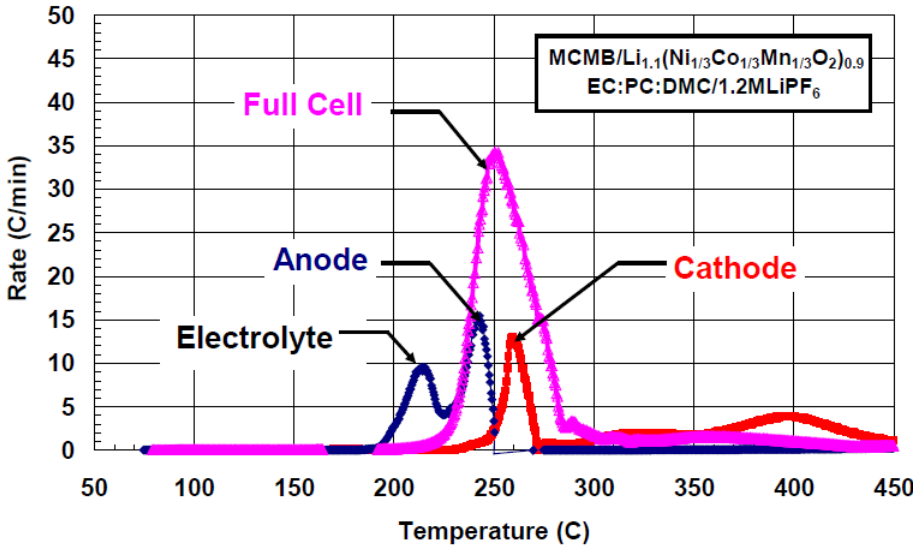

Figure 2-10: ARC profiles of anode and cathode in electrolytes compared to full cell response [11]

Molar calculations show that the amount of oxygen produced from cathode decomposition is not sufficient for the complete combustion of electrolyte and only a small percentage (5 to 15%) of the electrolyte is oxidised. Figure 2-11 shows the amount of energy released from decomposition reactions and compares it to the amount of electrical energy stored. The largest source of oxygen for electrolyte combustion comes from external air when the cell containment is compromised. The flammability of vented electrolytes is a big safety issue since events involving burning electrolyte have the most serious consequences as they result in cascading failure of the other cells in the battery pack and burning other battery components.

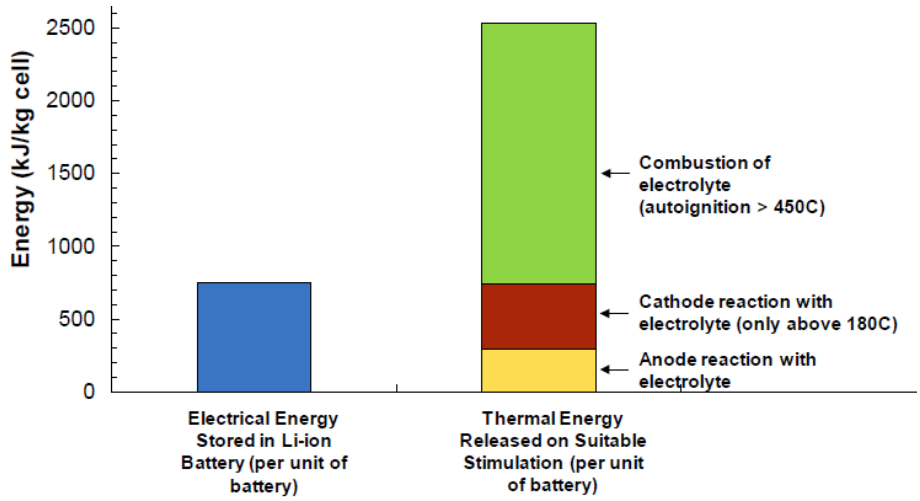

Figure 2-11: Comparison between the amount energy released from decomposition reactions and the amount of stored electrical energy [11]

2.6 Capacity Fade Mechanisms

The chemical side reactions taking place at the electrode during normal cycling can cause significant changes in the active materials of the cell. This results in the decrease in the capabilities of the cell known as ageing [52]. During an abuse event, such as overcharge or external short circuit, more side reactions happen which can accelerate or cause extra cell degradation [53]. In terms of cell capacity, there are three main mechanisms that result in capacity fade/loss: loss of active material (LAM), loss of lithium inventory (LLI) and Ohmic resistance increase (ORI) [54], [55].

LAM on the cathode side happens as a result of the dissolution of its active material [56] and the decomposition of its structure [57]–[59], as given by Equation 5-1 for the decomposition of LMO cathode. Cathode ORI can happen as a result of its structural changes caused by over-delithiation. On the anode side, LAM is not expected to happen at normal temperatures as the anode is protected by the SEI. At high temperatures as the SEI starts to break down, LAM happens as a result of the reaction between the over-lithiated carbon anode and electrolyte [60]. Solvent molecules also tend to co-intercalate into the crystalline structure of the anode causing its expansion/exfoliation and degradation [61]. The loss of lithium to the SEI layer is the most common form of LLI, it is also the fundamental source of capacity fade [62]. Dendrite growth was detected under some conditions during charge [63]. The overcharge of the negative electrode might cause accelerated deposition of lithium on its surface causing LLI [64]. Moreover, the increase in the anode's SEI layer thickness as result of the reaction between the deposited lithium and the electrolyte increases the ORI.

2.7 Battery Safety in a Business Context

In a business context, the safety of Li-ion batteries is crucial at all stages; their development, their introduction into markets for specific use and during their operation. Failing to improve safety can hinder the uptake of Li-ion batteries. It can also prevent certain batteries or products from being introduced into a market. Moreover, safety related events during its lifetime can have significant damaging effects on companies and whole industries. Therefore, battery safety issues justify intensive investigation along their value chain.

As discussed in Sections 2.1 and 2.2, the three most important parameters that would make Li-ion batteries more competitive are: cost, performance and safety. Industry optimises for performance and cost, but safety is a threshold criterion. Unfortunately, some market trends suggest that battery safety may restrain the search for an acceptable compromise between performance and cost of Li-ion batteries [65]. Li-ion cells can only be used in a specific market after passing certain safety legislations. Therefore, manufacturers and any business that uses cells in their products needs to ensure that their cells pass tests as those described in Section 2.4.

Incidents involving Li-ion batteries have very significant cost of failure in terms of both liability and cost of replacement. Battery failures force companies to withdraw their products, usually leading to loss of market share [30]. Moreover, the reputation of the company gets tarnished and their share price is affected. Accidents involving electric vehicle failures that result in fire usually receive significant negative press coverage and have damaging financial implications for the automotive companies. It can also affect the public perception and slow down the uptake of electric vehicles. In May 2012, in China, an electric vehicle manufactured by BYD was involved in a fatal accident. Just after the initial news, even before the root cause of the fire was discovered, BYD's shares hit a 7-month low [66]. In the aviation industry, on 16 January 2013, all Boeing 787 Dreamliners worldwide were grounded as a result of two separate Li-ion battery incidents [67]. Battery failures like this cause significant damage to a number of companies, in this case, it tarnished the reputation of Boeing and implicated big financial losses on the airlines, Boeing and its suppliers [68]. In the electronics market, a recent example is Samsung Galaxy Note 7, in which an internal short circuit due to separator damage caused the positive and negative electrodes to meet within the jellyroll, causing it to catch fire [69]. There have been a number of incidents and recalls involving Li-ion batteries, Table 2-4 lists some of them.

Table 2-4: Summary of some of the main incidents and recalls involving Li-ion batteries

Date	Place	Application Type	Incident Description
20 March, 1991 to 22 May, 2017	USA	Battery-powered devices	160 air/airport incidents involving lithium batteries carried as cargo or baggage have been recorded.

			Events involved smoke, fire, extreme heat and explosion [70]
February 2014	Toronto, Canada	EV – Tesla Model S	Fire started when the vehicle was parked in garage and not plugged in [71]
1 October, 2013	Kent, Washington, USA	EV – Tesla Model S	Fire in the battery pack caused by direct impact of a large metallic object [72]
March 2013	A123 Systems plant, Livona, Michigan, USA	EV battery packs	Manufacturer (A123) recalled battery modules and packs that contain prismatic cells that may have a defect that affects their performance [73]
20 March, 2013	Mitsubishi Motors dealership, Yokohama	PHEV – Outlander	Battery pack overheated and some of its components melted [74]
18 March, 2013	Mitsubishi Motors Mizushima battery pack assembly plant	EV – Mitsubishi i-MiEV	Li-ion battery caught fire while connected to test equipment [74]
16 January, 2013	Takamatsu Airport, Shikoku Island	Aircraft – Boeing 87-8	Error message indicating battery malfunction and odd smell detected in cockpit and cabin [75]
7 January, 2013	Logan International Airport, Boston, USA	Aircraft – Boeing 787 Dreamliner	Battery overheated starting smoky fire [76]
July 2012	Worldwide	Electronics – Nikon cameras	Recall of rechargeable batteries sold with two camera models that may short-circuit and melt. Nikon has received complaints

			regarding the batteries overheating [77]
May, 2012	Shenzhen, China	EV – BYD E6	Electric arcs caused by short-circuit of high voltage distribution with the car body after an accident started a fire [66]
18 July, 2011	Shanghai, China	EV – bus	Fired caused by overheating of LFP batteries [46]
June 2011	USA	EV – Chevrolet Volt	Vehicle catching fire 3 weeks after crash test [78]
April, 2011	Hangzhou, China	EV – Zotye M300	Short circuit in defective battery pack due to insulation damage between battery cells and walls of the aluminium container [79]

2.8 Battery Cell Tested in this Experimental Work

The cells used in this study were 15 Ah commercial automotive pouch Li-ion cells. The cathode material is a LMO-NMC mix and the anode material is graphite. It generally exhibits better safety property than NMC and higher energy density than LMO [80]. All testing was done with the cell fully charged (100% SOC). Table 2-5 summaries the specifications of the cells used. The name of the manufacturer is not revealed.

Table 2-5: Specifications summary of cell used in the experimental work

Cell Property	Description
Type	Pouch
Capacity (Ah)	15
Chemistry	LMO-NMC
Design	Stacked
Internal Resistance at 100% SOC (mΩ)	6 ± 1
Voltage Operating Range (v)	4.2 – 2.7

Chapter 3 – Nail Penetration Test

3.1 Chapter Highlights

- Nail material affects the outcome of nail penetration test
- Nail diameter affects the outcome of nail penetration test
- Nail penetration test suffers from low repeatability

3.2 Chapter Abstract

In order to develop a deeper understanding of the behaviour of commercial automotive Li-ion pouch cells during nail penetration test, two parameters of the nail properties were experimentally investigated. Firstly, cells were fully penetrated using 10 mm diameter nails with three different materials; copper, steel and plastic. Secondly, copper nails with two nail diameters; 10 and 3 mm were used. There was a clear distinction between the outcome of the conducting and non-conducting nails, although the outcome using conducting nails suffered from poor reproducibility. The poor reproducibility could be attributed to the variation in the contact resistance between the nail and the cell layers.

3.3 Chapter Introduction

3.3.1 Nail Penetration and Its Significance

In a vehicle environment, nail penetration is an important and widely used mechanical abuse test that attempts to simulate the piercing of the pack by a foreign object during a crash [81], [82]. An example is Tesla Model S battery pack catching fire after impact with a metallic object on the road [65]. Penetration induced thermal runaway propagation within a module was also experimentally investigated [83].The nail body can connect the cell electrodes via a low resistance path causing an internal short circuit. This can result in a high current and subsequent high Ohmic heating rates. This heating can initiate exothermic reactions leading to thermal runaway causing fire, gassing and explosion [84], [85]. Therefore, short circuits in Li-ion cells often result in serious safety failure which can have serious consequences.

Nail penetration testing is also widely used to simulate an internal short circuit [86] due to causes that are hard to replicate. Internal short circuits occur when impurities,

lithium dendrite growth or manufacturing defects puncture the separator providing a low resistance path between electrodes. The high capacity cells are at a higher risk of thermal runaway from internal short circuits [87]. Even though nail penetration may not be completely representative for internal short circuits occurring during the course of normal use (field failures) [24], it is still used to study them. Nail penetration causes a relatively large shorting as the nail brings multiple electrode layers together into electrical contact, whereas typical field failures usually result from smaller internal short circuits caused by localised small defects or lithium dendrites [88]. It was also noted that during nail penetration, the nail provides a thermal pathway for heat dissipation from the cell, reducing the probability of thermal runaway [87], [89]. Moreover, nail penetration tests have generally low reproducibility since it is almost impossible to control the type of short and the localised interaction between the nail and the cell layers, even though parameter such as speed and angle of penetration have been controlled for [81], [86].

3.3.2 Nail Penetration Test Standards

Nail penetration is a mechanical abuse test that causes physical damage to the cell by puncturing it. The nail penetrates the cell layers and usually puts the electrodes in contact causing an internal short circuit. There are a number of parameters that can be controlled during the nail penetration test, such as the nail properties, speed of penetration and location of penetration. Table 3-1 summaries the main nail penetration test standards for the automotive industry.

Table 3-1: Summary of the most common nail penetration test standards for automotive applications

Test Standard	Test Description			
	Cell Level		Module and Pack Level	
	Nail Properties	Test Conditions	Nail Properties	Test Conditions
SAE J2464 “EV & HEV Rechargeable Energy Storage System (RESS) Safety and Abuse	3 mm D	Nail speed ≥ 8 cm/s	20 mm D	Nail speed ≥ 8 cm/s

Testing Procedure" [36]				
FreedomCAR EESS Abuse Test Manual (SAND2005 – 3123) [26]	3 mm D	Nail speed = 8 cm/s	20 mm D	Nail speed = 8 cm/s
India AIS-048 "Battery Operated Vehicles – Safety Requirements of Traction Batteries" [11]	3 mm D	Nail speed = 8 cm/s	20 mm D	Nail speed = 8 cm/s
GB/T 31485-2015 National Standard of the People's Republic of China "Safety Requirements and Test Methods for Traction Battery of Electric Vehicle" [43]	- High-temperature-resistant steel. - 5≤D≤8 - conical angle of spike tip 45° ~ 60°	Nail speed = 25 ± 5 mm/s	- High-temperature-resistant steel. - 6≤D≤10 - conical angle of spike tip 45° ~ 60°	Nail speed = 25 ± 5 mm/s

3.3.3 Mechanism of Failure of Nail Penetration

In the case of nail penetration (shown in Figure 3-1), when the nail penetrates a battery cell, it internally connects the anode and cathode current collectors. The circuit formed between the current collectors and the nail carry the majority of the electric current [85]. Note that lithium ion battery cells usually have multiple stacked or spirally wound layers, and that Figure 3-1 only shows one such layer. The connection cause a current loop to form between the nail and the electrodes. It is assumed that when the nail fully penetrates the cell each layer is shorted independently by the nail.

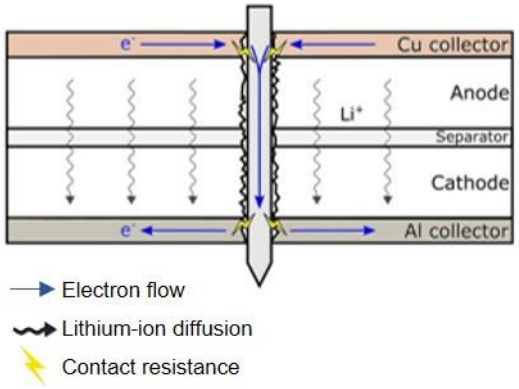

Figure 3-1: Schematic diagram showing electron flow, Li-ion diffusion and contact resistance during nail penetration

The discharge process of the cell takes place as follows; electrons and Li-ions are produced by delithiation reactions at the anode active material. Electrons then travel to the anode copper current collector where they converge towards the short circuit contact spot created by the nail. The electrons are then conducted along the nail to the cathode aluminium current collector. The Li-ions on the other hand are transported from the anode to the cathode through the electrolyte and separator. The lithiation reaction takes place at the cathode active material when the electrons transported by the nail meet the Li-ions transported through the separator. Heat is generated in both the nail and the cell primarily by large current flowing through them, i.e. Ohmic heating [90] [91]. The initial heating stage after penetration is crucial since it determines whether exothermic reactions that might lead to thermal runaway are triggered or not [92]. The Ohmic heating power (P) during this process is mathematically expressed as:

$$P = I^2 R_s \qquad \text{Equation 3-1}$$

Where I is the shorting current and R_s is the shorting resistance.

The initial shorting current is influenced by the shorting resistance, contributed primarily by the contact resistance of the electrical interface between the nail and the current collectors of the cell, as well as the resistance of the nail. After an initial surge of high current, lithium ions are depleted in the cathode active material; the ionic conductivity through the electrolyte and separator limits the replenishment of lithium ions and in turn limits the shorting current and the Ohmic heating [85], [93].

The shorting resistance (R_s) is determined by the nail resistance (R_{nail}) and how well the contact between the nail and the current collectors known as the contact resistance

(R_{ct}). Therefore, it is expected that both the nail properties and the contact resistance affect the outcome of the nail penetration test. The shorting resistance can be mathematically expressed as:

$$R_s = R_{nail} + R_{ct} \qquad \textit{Equation 3-2}$$

The electrical resistance of the nail is defined by its resistivity (ρ), length (L), and cross-sectional area (A), mathematically expressed as:

$$R_{nail} = \frac{\rho L}{A} \qquad \textit{Equation 3-3}$$

Zhao et al [86] describe the contact resistance as extra series resistance to the electron flow between the nail and the electrodes as shown in Figure 3-1.

Modelling work shows that for the same penetration test the cell can respond differently because of the difference in shorting resistances [86]. It is expected that the nail properties would affect the nail resistance and hence the shorting resistance, but this might not be the case as the contact resistance is not the same every time, because of the randomness of the geometrical deformation and the interaction between the nail and the cell layers when they were punctured.

3.4 Experimental Hypothesis

Changing the nail properties, such as material and diameter would affect its electrical and thermal properties. The shorting resistance can determine the outcome of the internal short circuit (nail penetration), since it defines the amount of Ohmic heating. Changing the properties of the nail changes its electrical resistance. Since the initial stage of heating during nail penetration is Ohmic, it is expected that changing the nail material and diameter will have an effect on the outcome of the nail penetration test (Section 3.3.3). The tests are designed to investigate the effect of changing the nail material and diameter on the outcome of nail penetration.

3.5 Experimental Design and Methodology

3.5.1 Cell Pre-conditioning and Check

Before testing, all cells were preconditioned through full charge-discharge cycles to record their capacity, nominal voltage and internal resistance. Using a MACCOR

cycler for preconditioning the cells inside a thermal chamber, the cells were cycled twice between the voltage limits of 4.2 V and 2.7 V with a 0.5 C-rate current at 25 °C. This pre-conditioning profile was based on manufacturer's recommendations and testing experience. Figure 3-2 shows the cycling profile and Table 3-2 shows the programme used. The cell capacity was determined after the second charge step, shown as step number 7 in Table 3-2. Based on the capacity check of 10 cells, the average capacity was 14.27 Ah and the standard deviation was 0.33 Ah, which is equivalent to ± 2.25%.

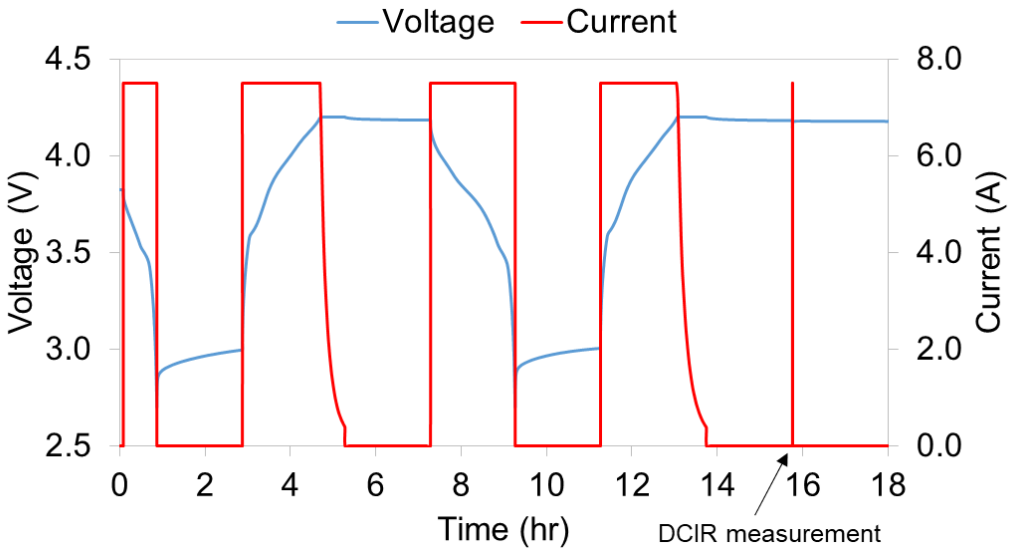

Figure 3-2: Cell preconditioning cycles profile before testing

Table 3-2: Programme of cell preconditioning before testing

Step No.	Step Description	Condition
1	Constant current discharge	0.5 C to 2.7 V
2	Rest	2 hr
3	Constant current charge	0.5 C to 4.2 V
4	Rest	2 hr
5	Constant current discharge	0.5 C to 2.7 V
6	Rest	2 hr
7	Constant current charge	0.5 C to 4.2 V
8	Rest	2 hr
9	Internal resistance measurement	Subroutine shown in Table 3-3
10	End	

The internal resistance was measured using the direct current internal resistance (DCIR) measurement method as a subroutine at the end of the cycling profile shown in Figure 3-3. This method involves sending a constant current pulse following a period of rest (no current) and followed by a period of rest for a specific time. The DCIR is the difference between the average of the cell voltage before and after the pulse and rest and the final voltage reading with the current applied divided by the pulse current as expressed by Equation 3-4 [94] and shown in Figure 3-3 on the pulse profile. Table 3-3 shows the programme for the pulse and the measurement at each step.

$$DCIR = \frac{(\frac{(V_1 + V_3)}{2} - V_2)}{I_2}$$ *Equation 3-4*

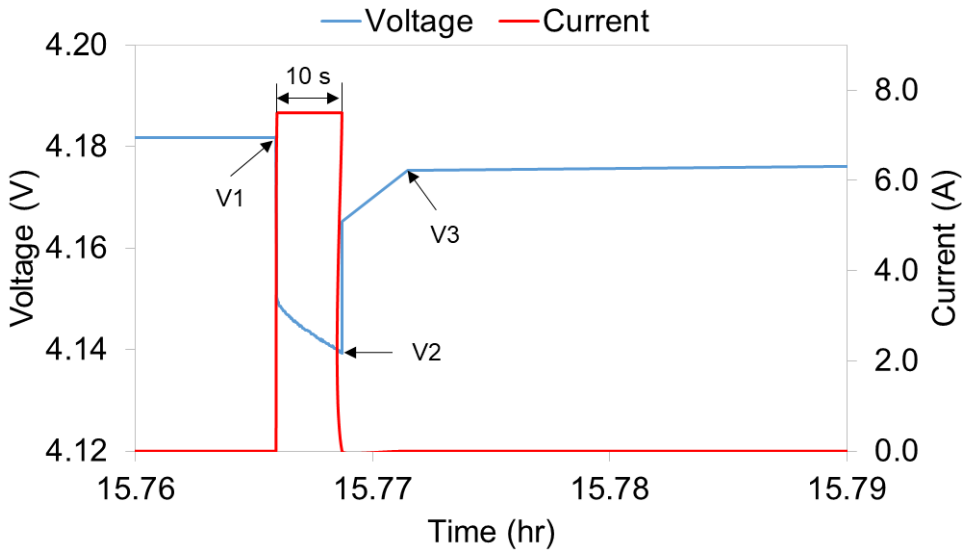

Figure 3-3: Pulse profile for internal resistance measurement – part of the cycling profile in Figure 3-2

Table 3-3: Programme steps of the DCIR measurement pulse – subroutine of cycling programme in Table 3-2

Step No.	Step Description	Condition	Measurement
1	Discharge	0 C for 0.05 s	V1 at the end of the step (no current)
2	Constant current discharge	0.5 C for 10 s	V2 at the end of the step

3	Discharge	0 C for 0.05 s	V3 at the end of the step (no current)
4	End		

3.5.2 Test Set-up and Experimental Procedure

All tests were carried out in a purpose-built battery abuse testing chamber. During penetration test a nail was driven through a fully charged cell at room temperature. A calibrated hydraulic ram was used to drive the nail at a speed of 10 cms^{-1}, perpendicular to the cell layers. The cell was fully pierced to make sure all layers were penetrated. The nail was left inside the cell until the end of the test. During the test, the cell was put inside a thermal box to minimise heat dissipation. Three different materials were used to make nails: copper, steel and plastic, with their diameters being either 3 or 10 mm and all being 50 mm in length (Figure 3-4). A number of each nail were manufactured, in order to use a new nail for each test. The cell voltage, cell surface temperature and nail temperature were measured by thermocouples and recorded using a MACCOR Battery Tester. As failures can have an incubation period of several hours, measurements continued until the cell surface and nail temperatures return to ambient temperature and/or cell voltage drops to approximately zero. Table 3-4 summaries the penetration test specifications/conditions. Figure 3-5 shows the test set-up.

Table 3-4: Summary of penetration test specifications/conditions

Nail Properties	Diameter (mm)	3 and 10
	Length (mm)	50
	Head angle (degrees)	60
	Tip diameter (mm)	0.5
	Material	Copper, steel and plastic
Test Conditions	Temperature (°C)	16 ± 3
	Ram/nail speed (cm/s)	10

Figure 3-4: A sample of nails used in nail penetration test (not to scale)

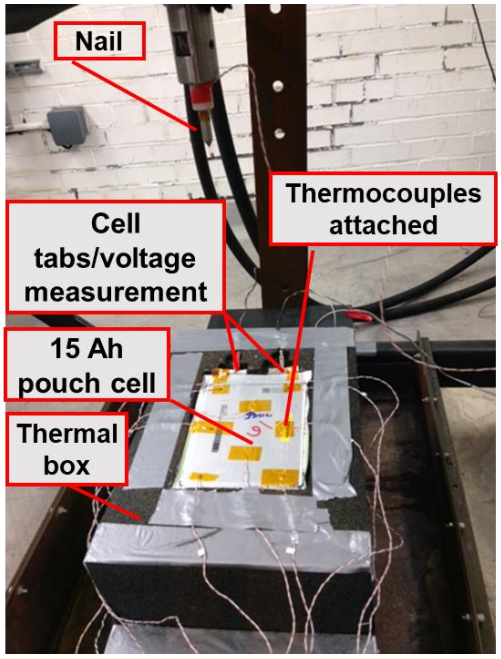

Figure 3-5: Nail penetration test set up (before putting the thermal box top part)

3.6 Results and Discussion

3.6.1 Effect of Changing Nail Material

This section presents and discusses the cell electrical and thermal data, as a result of being penetrated by 10 mm nails made of three different materials; copper, steel and plastic.

3.6.1.1 Electrical response – voltage profile

The cell voltage profile is an indication of the degree of shorting during the nail penetration process. A high voltage drop rate is an indication of a hard short, i.e. high

shorting current as a result of low shorting resistance. During a nail penetration test this low shorting resistance is achieved by low nail resistance and good contact between the nail and the cell layers as explained by Equation 3-2 in section 3.3.3, whereas if the voltage drop rate is low, it is an indication of a soft short as a result of high shorting resistance, i.e. high nail resistance and/or poor contact between the nail and the cell layers.

Figure 3-6a shows the cell voltage profiles during a number of nail penetration tests using a 10 mm copper nail. Starting from a fully charged state at around 4.2 V, all the cells were eventually discharged and reached zero volts except for one cell that showed very low rate voltage drop even after 800 minutes.

Figure 3-6b shows the cell voltage profiles when using steel nails. Compared to the copper nail, steel nail was less likely to cause the cell to completely discharge. The lower electrical conductivity of steel compared to copper may be a factor, in addition to other potential factors such as, a difference in nail surface roughness and the formation of resistive materials caused by chemical reactions between the nail material and the electrolyte. This suggests that the final result is determined by the total shorting resistance, which includes the random component of contact resistance and the effective electrical resistance due to nail material differences. As a result of the randomness of contact resistance, the same test can result in significantly different outcomes.

As shown in Figure 3-6c, the cell voltage profiles for the non-conducting nail indicate that there was almost no shorting. After 16 hours the cell voltage consistently remained around 4 V. Therefore, it can be concluded that in this case the nail acts as the main current path during nail penetration and there is no shorting as a result of direct contact between the cell electrodes. This validates the hypothesis presented in Section 3.4 that the nail during nail penetration is the main current path and it acts like the shunt resistance during the external short circuit test. Hence, their outcome can be correlated as discussed in Section 7.5.

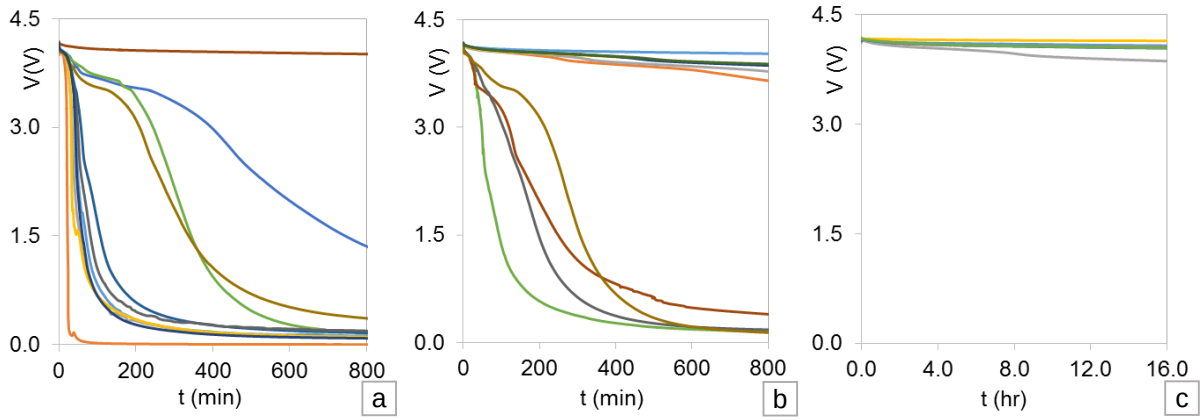

Figure 3-6: Cell voltage profiles of several repeats of 10 mm nail penetration test using a) copper b) steel c) plastic

Plotting the voltage profiles for copper, steel and non-conducting nails on one plot as in Figure 3-7, shows that the data for nails with different materials (copper, steel, and plastic) can be divided into two groups, conducting and non-conducting. Although the conducting group can be divided further into two subsets according to the nail material (copper and steel), there is still a degree of overlap between their results and that is believed to be caused by the random contact resistance between the nail and cell layers. The copper nail was more likely to short the cell. Therefore it can be concluded that in order to predict the behaviour of the cell under nail penetration, the knowledge of both the nail conductivity and contact resistance is required.

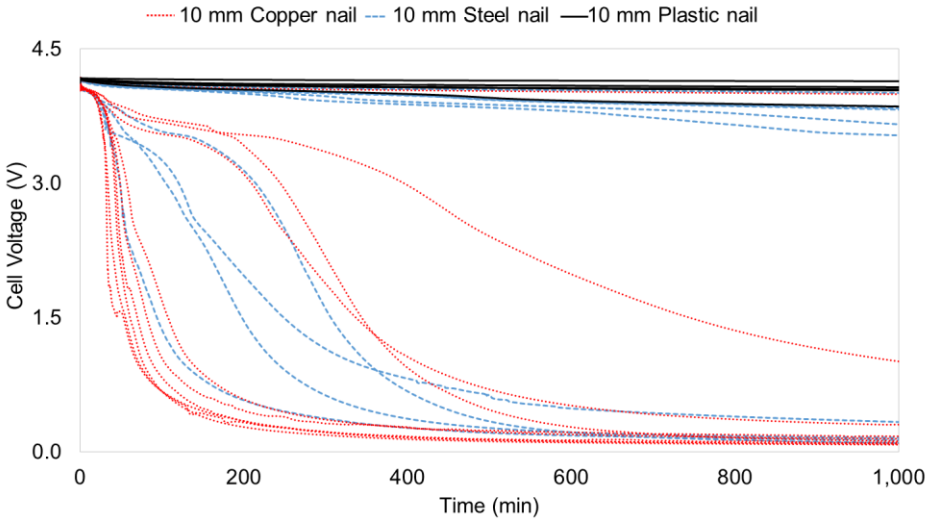

Figure 3-7: Combined plot of cell voltage profiles during nail penetration using copper, steel and plastic nails

3.6.1.2 Thermal response

The temperature rise is determined by the rate of heat dissipation and the thermal properties of the cell, mainly the specific heat capacity and thermal conductivity [95]. In these tests, the main heat sink was the thermal mass of the nail since the cell was thermally insulated by a thermal box to minimise heat loss from its surface as shown in Figure 3-5.

The thermal response goes hand in hand with the electrical response. A higher voltage drop rate translates to a higher temperature rise rate, as the cell's electrical energy is converted to heat energy mainly by Ohmic heating as explained in Section 4.4.2. Figure 3-8 shows the voltage and temperature profiles of a cell during a nail penetration test. The highest voltage drop rate happens initially when the nail penetrates the cell, it also corresponds to the highest rate of temperature rise. As the cell energy decreases the voltage drops further and the temperature follows.

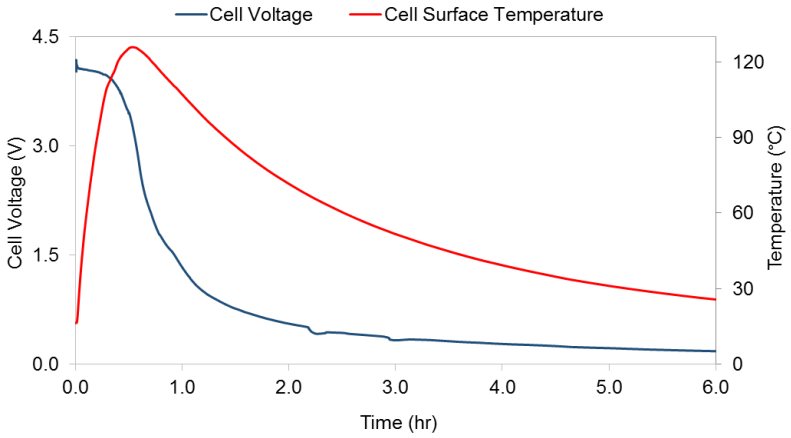

Figure 3-8: Relationship between voltage and temperature during nail penetration test

Figure 3-9a, b and c show the cell surface temperature measured close to the point of penetration for copper, steel and plastic nails respectively. Cells penetrated with copper nail experienced the highest temperature rise, followed by those penetrated by steel nail. Cells penetrated by the non-conducting nail shows relatively low temperature rise, as there was minimum shorting as pointed out in Section 3.6.1.1.

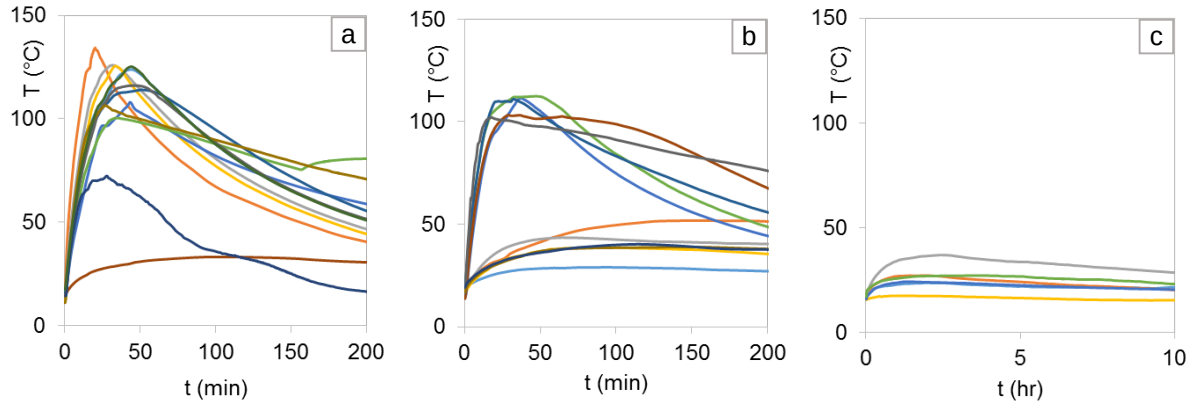

Figure 3-9: Cell surface temperature profiles of several repeats of 10 mm nail penetration test using a) copper b) steel c) plastic

The temperature profile of a cell undergoing thermal runaway caused by any abuse condition can be broken down into stages (Section 2.3). For a short circuit the first and most critical stage is from the beginning of the short circuit to the point of initiation of exothermic reactions. This stage is crucial since it can determine whether the cell will go into thermal runaway or not. Before the initiation of exothermic reactions most of the heat generation is Ohmic in nature, with a heating power of (I^2R_s), where I is the shorting current and R_s is the shorting resistance as defined in Equation 3-1.

Figure 3-10 shows the rate of cell surface temperature change (°C/min) as a function of cell temperature, from the point of penetration until the maximum temperature reached. The temperature rate profile can be divided into two stages according to the heating mechanism. The first stage is Ohmic heating and the second stage is self-heating by exothermic reactions. At 18 °C, once the cell is penetrated, its voltage dropped from 4.2 to 4.0 V. This voltage drop corresponds to highest temperature rate of around 27 °C/min. As the short continues, the cell runs out of energy and the heating rate decreases. When the cell temperature goes beyond 120 °C, there is another peak in the heating rate. It is believed that this point marks the start of exothermic reactions between the anode and electrolyte as a result of SEI breakdown due to elevated temperatures. The voltage and temperature behaviours do not show signs of separator shutdown or shorting, this suggests that the melting temperature of the separator was not reached.

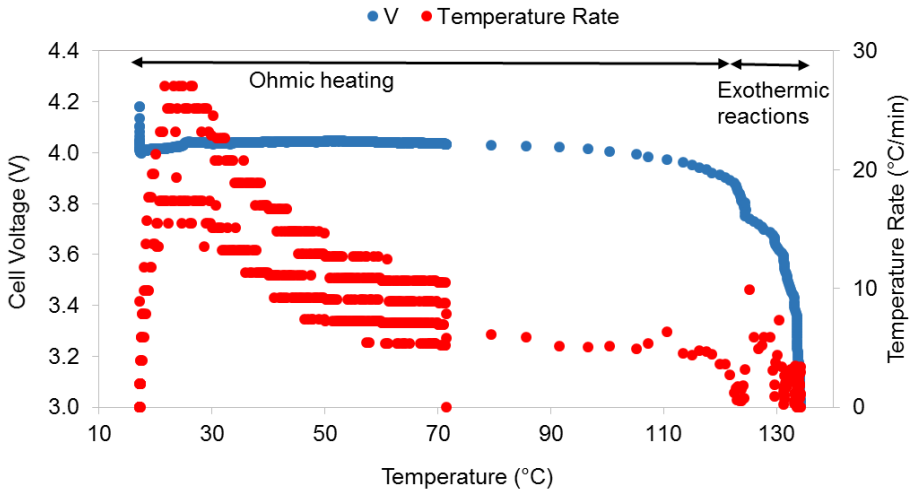

Figure 3-10: Cell voltage and cell temperature rate as a function of cell temperature during nail penetration test

As pointed out in Section 2.3, a cell self-heating of a rate of 0.2 °C/min marks the initiation of exothermic reactions and a heating rate of 10 °C/min or greater marks the start of a cell going into thermal runaway. As shown in Figure 3-10, the maximum self-heating rate reached was around 7 °C/min. This suggests that the heat build-up was not enough to drive the cell into the thermal runaway stage.

3.6.2 Effect of Changing Nail Diameter

This section presents and discusses the cell electrical and thermal data, as a result of being penetrated by copper nails of 3 and 10 mm diameter.

3.6.2.1 Electrical response – voltage profile

As pointed out by equation 3, the resistance of a nail is inversely proportional to its cross-sectional area. A lower current would flow in a 3 mm nail than a 10 mm one as the 3 mm nail has about 11 times higher resistance than the 10 mm nail. This is expected to result in a higher rate of cell voltage drop during nail penetration of the larger nail. Figure 3-11 shows the voltage profiles of cells penetrated by 10 and 3 mm diameter nails. Although the 10 mm diameter nail had a higher probability of having a higher rate of voltage drop, there is still a degree of overlap. This is believed to be due to the random contact resistance.

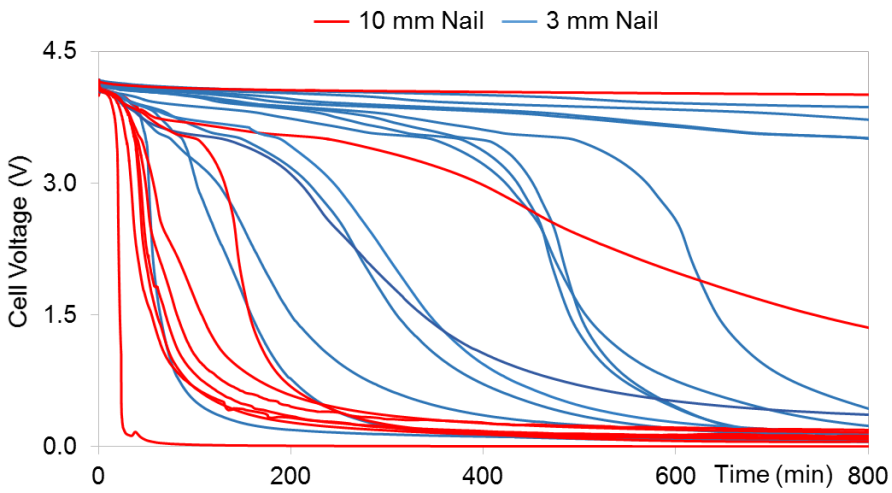

Figure 3-11: Cell voltage profiles of several repeats of nail penetration using 10 and 3 mm copper nails

3.6.2.2 Thermal response – temperature profile

The heat generation is directly affected by the degree of shorting, as is the voltage. Therefore the temperature profiles of those cell penetrated by 3 mm copper nail follows their voltage profiles. Figure 3-12 shows that generally the temperature rise caused by a 3 mm nail is less that a 10 mm nail.

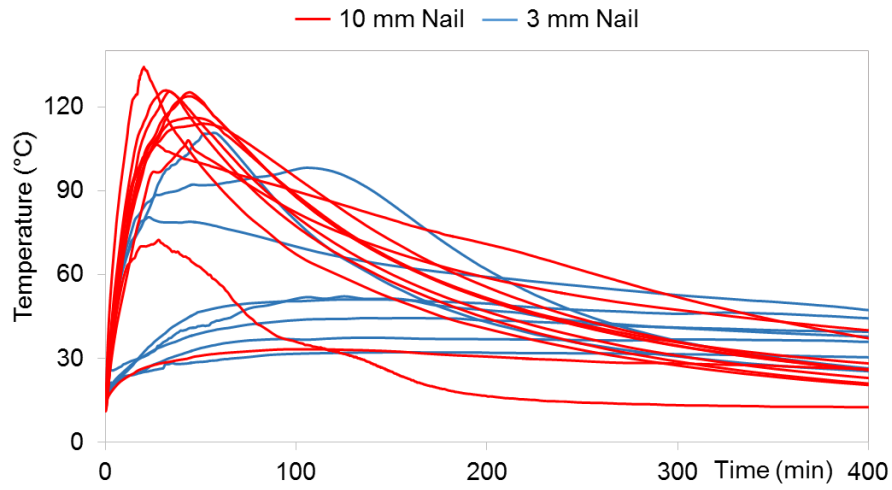

Figure 3-12: Cell surface temperature close to the point of penetration, during penetration test using 10 and 3 mm copper nails

3.6.3 Temperature Distribution and Heating Regime

3.6.3.1 Cell surface temperature distribution

The cell surface temperature was measured at 10 different locations; 8 thermocouples were attached to the body of the cell and a thermocouple was attached to each of the two tabs. A thermocouple was also attached to the nail. Figure 3-13 shows the locations of the temperature measurement points. The point of penetration is marked with a black circle.

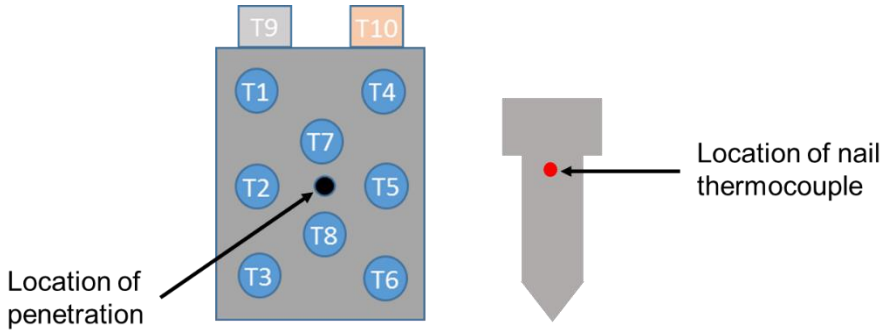

Figure 3-13: Temperature measurement locations on the pouch cell (top view) and nail (side view) during a nail penetration test

Figure 3-14 shows the maximum cell surface temperature reached at each point for all cells penetrated by the 10 mm copper nail. The data show symmetry along the cell, T1 was similar to T4, T2 to T5, and T3 to T6. The highest temperatures recorded were those closest to the point of penetration as this was the main source of heat generation. It can also be attributed to the higher heat dissipation rate points closer to the cell edge have [92].

Taking the point of penetration as a reference point there were two gradients; one in the direction of the tabs and another in the direction away from the tabs. The temperature gradient was steeper away from the tabs, as T2-T1 < T2 - T3 and T5 – T4 < T5 - T6 as Figure 3-15 shows. This is believed to be due to heating caused by current flow through the tabs.

It is also worth mentioning that the temperature of the positive (cathode) tab, made of aluminium, was consistently higher (4.25 °C) than that of the negative (anode) tab, made of copper. This can be attributed to the higher electrical resistivity of aluminium compared to copper, leading to a higher Ohmic heating rate at the aluminium current collector of the positive electrode. It should be noted that heat loss from the cell

through the tabs was minimised by using crocodile clips instead of brass blocks to connect the cell to the cycler for voltage measurement. These findings can be used for the thermal management system as discussed in the industrial applications in Chapter 7.

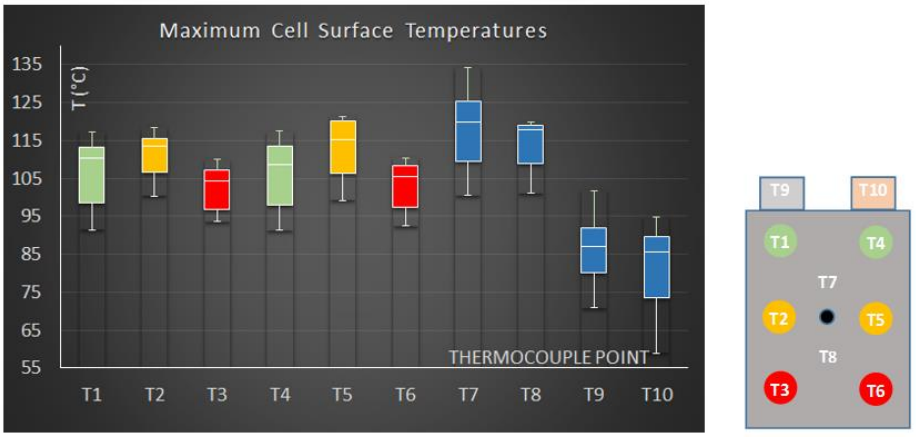

Figure 3-14: Maximum cell surface temperatures and temperature distribution during nail penetration test

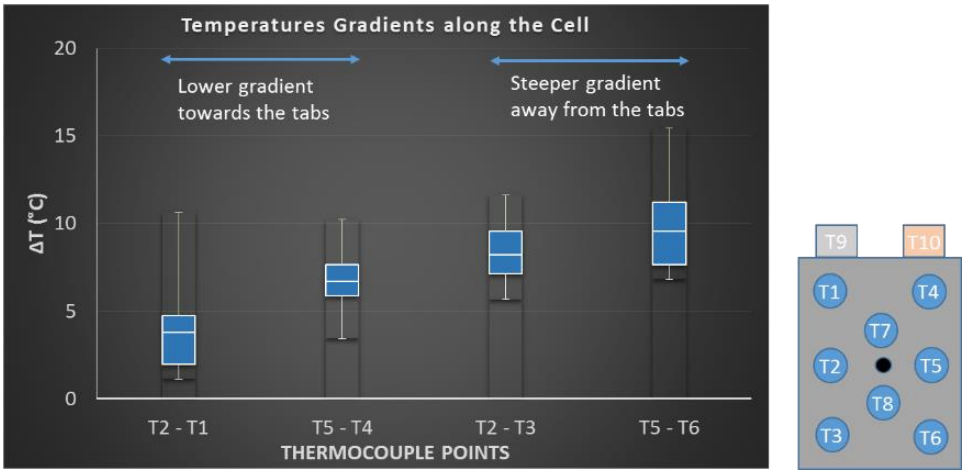

Figure 3-15: Temperature gradients towards and away from the cell tabs with respect to the point of penetration

3.6.3.2 Heating mode

During nail penetration the equivalent circuit diagram of the internal short can be represented by two resistances connected in series; the cell internal resistance and the shorting resistance as shown in Figure 3-16. The cell current response is defined by the shorting resistance - the lower the shorting resistance the higher the current and vice versa. In terms of thermal response, current flowing through both resistances generates heat and therefore during nail penetration heat is generated from both the

cell and the nail. If more heat is generated by the nail than by the cell, it results in a hot spot at the point of penetration, i.e. localised heating [90]. However, if the difference in heat generation is not significant, this results in more uniform heating, i.e. global heating [86].

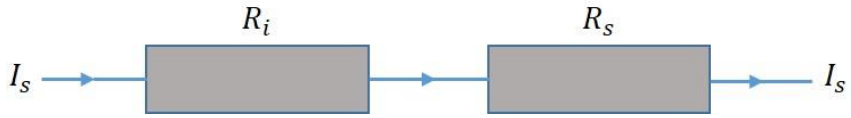

Figure 3-16: Schematic diagram for the shorting current flowing through the internal resistance of the cell and the shorting resistance

According to Ohm's law the shorting current (I_s) is defined as:

$$I_s = \frac{V_c}{R_t} \qquad \text{Equation 3-5}$$

Where V_c is the cell voltage and the total resistance R_t is the sum of the shorting resistance R_s and the internal resistance of the cell R_i.

Treating the power generation from the cell P_c as Ohmic, it can be calculated as:

$$P_c = I_s^2 R_i \qquad \text{Equation 3-6}$$

Power generation by the short caused by the nail is calculated as:

$$P_s = I_s^2 R_s \qquad \text{Equation 3-7}$$

Figure 3-17 shows the calculated maximum heating power generation by the cell and the nail as a function of the shorting resistance. The heating mode is defined by the ratio between R_s and R_i. As shown in Figure 3-17 when $R_s < R_i$ heat generation is dominated by the cell and heating mode is global. When $R_s > R_i$ more heat is generated by the short and the heating is localised. This agrees with the modelling findings by Zhao et al. [86]. However, it should be noted that this is a rough estimation as the resistance of the cell can significantly change during the internal short circuit [93]. As the shorting resistance is increased further, the difference in heating contribution between the cell and the nail decreases. This leads to lower temperature difference between the penetration point and the rest of the cell, resulting in more uniform temperature profile across the cell. A high shorting resistance also reduces the heating from both as the shorting current is reduced.

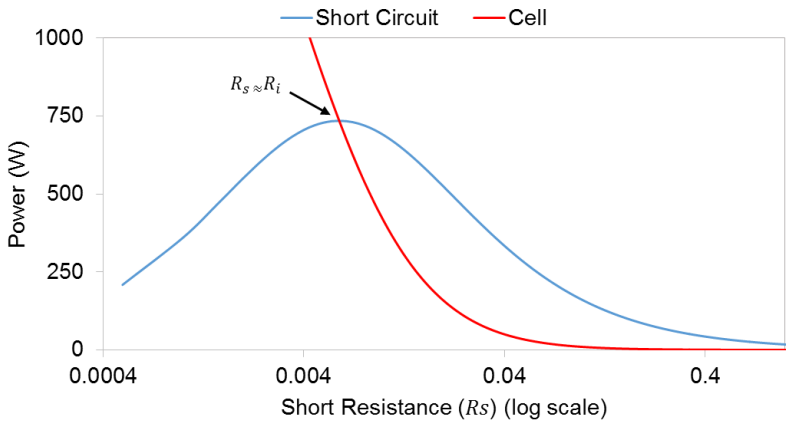

Figure 3-17: Calculated maximum heat generation rate by the short circuit and cell as a function of shorting resistance

Figure 3-18a and b show the cell voltage, nail temperature and cell surface temperature close to the point of penetration of two nail penetration tests under identical configuration that resulted in very different outcomes. Plotting the nail and surface temperatures on the same plot shows the difference in cell temperature at the point of penetration and the rest of the cell. A bigger difference between them indicates more localised the heating, i.e. less uniform cell temperature. Figure 3-18a is an example for a test that resulted in a relatively large temperature difference between the nail temperature and the cell surface temperature, a maximum of 105 °C (231 °C – 126 °C). Nail penetrated large-format cells reached a higher temperature without ignition or explosion in a previous study [96]. Figure 3-18b shows the same test resulting in a much smaller temperature difference, a maximum of only 10 °C (43 °C – 33 °C). Note that the maximum nail temperature is always higher than the maximum cell surface temperature measured to the point of penetration. This is believed to be due to the relatively high thermal conductivity of the metal nail compared to the cell material and the nail's proximity to the point of penetration [97].

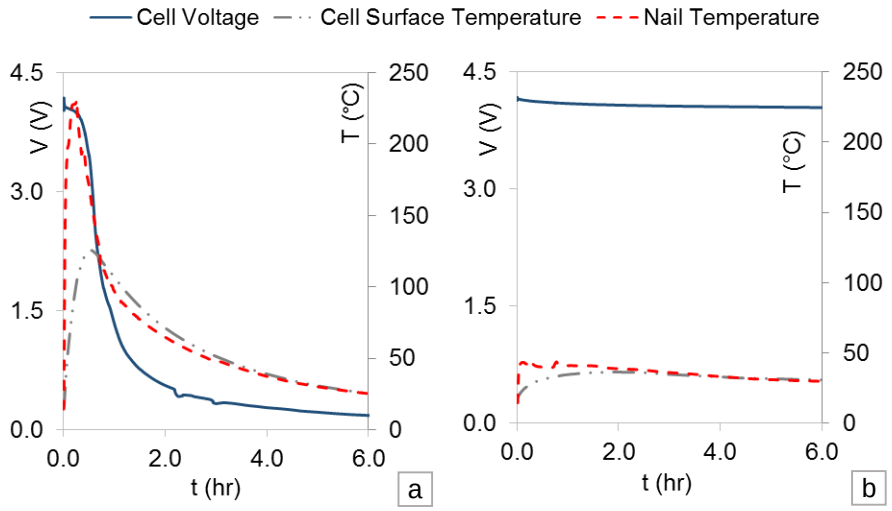

Figure 3-18: Cell voltage, nail and surface temperatures for a nail penetration test a) resulting in a relatively hard short circuit and more localised heating b) resulting in a relatively soft short circuit and less localised heating

Adding the voltage profile to the plot clearly shows the coupling between the electrical and thermal behaviours of the cell during the short. A higher rate of voltage drop, i.e. hard short, results in a higher temperature rise and more localised heating. The nail temperature naturally gives a more accurate indication of the cell internal temperature at the short-circuit location. Comparing the nail temperature to the cell surface temperature for different degrees of shorting highlights the effect of the shorting resistance on the thermal behaviour. When the rate of voltage drop is high (hard short), the difference between the nail and surface temperatures is significant. However, when the rate of voltage drop is low (soft short) the difference between the nail and surface temperatures is small. Having both scenarios as outcomes of the same test shows how variable the nail penetration test outcome is.

3.6.4 Post-mortem Examination

Tearing down (deconstructing) the cell after the test can provide useful information to further understand the nail penetration process. A teardown was performed on one of the cells penetrated by the 10 mm steel nail. A glovebox filled with argon was used and the cell voltage prior to the teardown was 0 V. Figure 3-19a shows a photograph of the negative electrode. It can be seen that at the point of penetration the nail dragged the copper current collector in the direction of penetration. The surface of the

electrode was covered with light grey patches. Examining the separator confirms that the light grey patches on both electrodes come from the separator.

The positive electrode as shown in Figure 3-19b has similar pattern of light grey patches. The hole in the electrode looked less circular and the aluminium was not dragged as deep as in the case of the copper current collector. The difference can be attributed to the difference in mechanical properties between the two metals as well as the presence of a separator layer between the nail and copper current collector, the separator was clearly dragged by the nail as shown in Figure 3-19c.

Figure 3-19: Photographs of cell components from the teardown analysis of a nail penetrated cell a) negative electrode b) positive electrode c) separator

3.7 Chapter Conclusion

There are a number of parameters that can affect the outcome of nail penetration test resulting in very different outcomes. Some of these parameters are possible to control such as the nail properties, state of charge, penetration speed, penetration angle, and the location of penetration. Others are not possible to control such as the shorting resistance and current. A number of literature argues that this test is not useful for safety assessment due to several reasons: 1) A poor reproducibility [98]. 2) Inability to control the type of internal short (e.g. between active materials or foils) [98]. 3) it may not be representative of an internal short circuit event (e.g. single layer short vs. full nail penetration; having nail as heat sink vs. none) [33], [87].

Results show that changing the nail material and diameter affect the outcome of the nail penetration test, but also shows the highly variable outcome of nail penetration.

Thermal data show that the cell temperature distribution and temperature gradients are similar for most nail penetration tests.

Tearing down the cell after nail penetration gives the opportunity to visualise how the nail interacts with the cell layers during the penetration process. The observations from the teardown suggest that when the nail penetrated the cell the copper current collector and the separator material in the vicinity are wrapped and dragged into the aluminium current collector. Further analysis is needed to characterise the light grey material.

3.8 Recommendations for Future Work

In this study the nail penetration test was only done on one cell technology. A more comprehensive study can include cells with different formats, capacities and chemistries. Moreover, the effect of other parameters such as, nail head angle, nail surface roughness, speed and angle of penetration can be explored.

Nail penetration of dummy cells can be done in order to investigate how the nail mechanically interacts with the cell bilayers. Computed tomography (CT) scan, using synchrotron facilities, during the nail penetration test can also provide valuable information.

Chapter 4 – External Short Circuit Test

4.1 Chapter Highlights

- A purpose-built external short circuit rig was designed and built
- 15 Ah commercial automotive pouch cells were exposed to a number of external short circuit scenarios
- The effects of short resistance and short duration were investigated
- The evolution of capacity and internal resistance during cycling after the external short circuit was monitored
- Post-mortem analysis was performed on abused cells

4.2 Chapter Abstract

External short circuit is the most common type of abuse of Li-ion cells. In order to develop a deeper understanding of the behaviour of commercial automotive Li-ion pouch cells under different external short circuit conditions. Two short circuit parameters were experimentally investigated – the short resistance and the short duration. The first set of experiments involved externally short circuiting the cell tabs using an external circuit with a range of resistance values. The second set of experiments involved using a programmable power supply to control the time during which the cells were short-circuited. Although the cell swelled significantly in the case of a hard short, the cell did not rupture and no thermal runaway happened. The cells were cycleable after the short circuit event and their degradation depended on the short circuit conditions. It was found that the degree of damage experienced by a cell during a short is not only defined by the short resistance, but also its duration. The cells were opened after testing and their electrodes were studied using Scanning Electron Microscopy (SEM). No change in the surface morphology of the electrodes was observed when investigated by SEM.

4.3 Chapter Introduction

4.3.1 External Short Circuit and its Significance

An external short occurs when the terminals of the cell are connected via a conducting path [99]. A short circuit condition can cause high current flow, rapidly converting the stored chemical energy mainly to heat. This can trigger exothermic reactions leading to thermal runaway causing gassing, fire or explosion. Although short-circuiting a single-cell battery can have serious consequences, the short circuit of a cell in a multi-cell battery as in the case of automotive applications can have catastrophic consequences on a large scale. Short-circuiting a cell may cause it to catch fire and explode affecting other cells in the battery pack. If the heat is not contained, propagation of failure from cell to cell can consume the whole pack. An example is a Chevy Volt catching fire in June 2011. In the accident investigation, the battery fire was traced back to coolant fluid leakage following a side-impact crash. The coolant was electrically conductive, causing an external short circuit between the terminals of the battery. In this case the heat generated from the short circuit was enough to heat the cell into thermal runaway [100].

A short circuit can be classified as “hard” short circuit, where the short resistance is relatively low causing high current flow, whereas a “soft” short has a relatively high resistance. The shorting resistance may significantly vary in magnitude depending on the distance between the fault location and the battery terminals, hence the resulting shorting current and the heating rate can also vary significantly. Any conductive pathway between the terminals, even a high resistance one, will have damaging effects. For example, moisture surrounding the terminals of the battery can cause short-circuiting of the cell through corrosion reactions, this can result in a slow discharge of the battery causing unwanted heating [44].

An external short circuit event has the highest probability of occurrence amongst other abuse scenarios. It can happen during manufacturing, assembly, transportation, servicing or operation. The safety of personnel involved in rescue operations in case of an accident is also a concern [25]. In 2012, due to the fear of the implications of short circuits causing fire in the cargo departments of planes, the US postal service put a ban on the international shipping of Li-ion batteries [101].

Large format Li-ion batteries have relatively very low impedance, consequently during an electrical short significant damage can be caused if either the duration or the current magnitude was not limited/controlled. Currently the general industry practice is to discard any cells that have been subjected to any kind of short circuit [102]. However, short-circuiting the cell can be stopped before reaching a critical stage. In this case the cell could be reused after this event, if it is proved to be safe and if its performance is not severely degraded.

Since the most two important parameters that determine the outcome of an external short circuit event is the short resistance and the duration of the short, this study is aims to experimentally investigate the response of commercial automotive Li-ion cells to a range of external short resistances and the effect of the short duration on the cell behaviour.

The ultimate aim of this work is to help better understand electrical fault diagnostics, develop more representative and useful testing procedures, help improve the battery pack design and make Li-ion cells safer and more abuse tolerant to external short circuits for the use in the automotive industry.

4.3.2 Aim and Objectives

The aim of this study is to develop a deeper understanding of the behaviour of Li-ion cells during and after different external short circuit event scenarios.

The objectives to meet this aim are:

1) Investigate the effect of short resistance
2) Investigate the impact of the short duration
3) Study the effect of storage and monitor the cycling behaviour after an EXSC event

4.4 Background

4.4.1 External Short Circuit Test Standards

The external short circuit test is an electrical abuse tests in which the tabs of the cell are connected through a path with a very low electrical resistance, comparable in orders of magnitude to the internal resistance of the cell, resulting in current flow that is much higher than the manufacturer's rated maximum discharge rate the cell can support. A shorting resistance with a relatively small value compared to the internal resistance results in a "hard short", whereas a "soft short" is caused by a shorting resistance relatively higher than the cell's internal resistance [35]. EXSC test is one of the most widely applied electrical abuse tests [103]. For the purpose of this report the most common standards for external short circuit tests for Li-ion battery cells are summarised in Table 4-1.

Table 4-1: Summary of the most common external short test standards for automotive applications

Test Standards	Test Description
SAE J2464 "EV & HEV Rechargeable Energy Storage System (RESS) Safety and Abuse Testing Procedure" [36]	Two short circuit tests: a hard short (≤ 5 mΩ) and moderate short at a resistance comparable to the test article resistance at 25 °C ± 5 °C
FreedomCAR EESS Abuse Test Manual (SAND2005 – 3123) [26]	Apply a 'hard short' of ≤5 mΩ in less than one second; hold for 10 minutes at 20 C
SAE J2929 "Electric and Hybrid Vehicle Propulsion Battery System Safety Standard – Lithium-based Rechargeable Cells" [37]	UN Test Manual, Test T.5; or the pack hard short circuit condition defined in SAE J2464. With flammable gas monitoring
IEC 62660-2:2010 "Secondary Li-ion Cells for the Propulsion of Electric Road Vehicles – Part 2: Reliability and Abuse Testing" [38]	≤5 m ohm for 10 min. at 20 C. The sample rate for voltage and current recording shall be ≤ 10 ms
ISO 12405-3:2014 "Electrically Propelled Road Vehicles – Test Specification for Li-ion Traction Battery Packs and Systems	Use an appropriately sized conductor of ≤100 mΩ to apply a 'hard short' in less than one second for 10 minutes

– Part 3: Safety Performance Requirements” [104]	
UL 2580 “Standard for Safety – Batteries for Use in Electric Vehicles” [40]	Total circuit resistance less than or equal to 20 mΩ. Testing is repeated at a load that draws a maximum current no less than 15% below the operation of the short circuit protection
Korea MVSS 18-3 "Driving Battery Safety Test" [11]	Resistance = 50mΩ for 1 hour or when current does not flow for 5 minutes. SOC 80%
India AIS-048 "Battery Operated Vehicles – Safety Requirements of Traction Batteries" [11]	Resistance less than or equal to 5 mΩ for 10 minutes.
GB/T 31485-2015 National Standard of the People’s Republic of China “Safety Requirements and Test Methods for Traction Battery of Electric Vehicle” [43]	Resistance less that 5 mΩ for 10 min. Observe for one hour.

4.4.2 Mechanism of Failure of External Short Circuit

The current flow path during an external short circuit is similar to that of a normal discharge. As shown in Figure 4-1, lithium ions and electrons are liberated at the anode. Lithium ions travel across the electrolyte towards the cathode where they are intercalated into its structure, while electrons travel from the anode to the cathode through the external circuit resulting in an electrical current. The shorting current is determined by the total resistance of the current path. This resistance includes the resistance of the external circuit elements, the wiring, the connections, the tabs and the internal resistance of the cell. The current is limited by the ionic movement of Li-ions in the electrolyte in the case of high currents.

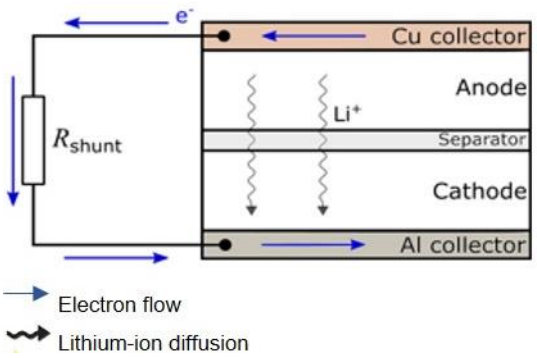

Figure 4-1: Schematic diagram showing electron flow, Li-ion movement and shorting resistance during an external short circuit test

4.5 Experimental Design and Methodology

4.5.1 External Short Circuit Rig and Test Set-up

The external short circuit test was conducted by connecting the tabs of the cell through an external low-resistance circuit as shown in Figure 4-2. The external circuit is composed of a shunt resistor, high power high gauge copper cables and a remotely-controlled contactor that controls the opening or closing of the circuit. During the experiment, the cell voltage, the voltage drop across the shunt resistor (to calculate the current), and the cell surface temperatures reading from the thermocouples were recorded.

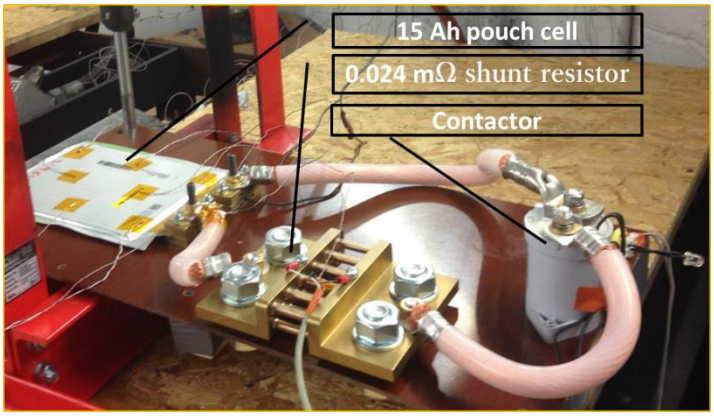

Figure 4-2: Rig and experimental set up for external short circuit test

4.5.2 Experimental Procedure

The experimental procedure followed was as shown in Figure 4-3. The following sections describe each of its stages.

Figure 4-3: Sequence of experimental procedure stages

4.5.2.1 Pre-testing cell performance check

These tests were conducted on the cells before the external short circuit test regime to ensure that their capacity and internal resistance values were sound.

Capacity and internal resistance check

The procedure in Section 3.5.1 was followed to check the capacity and internal resistance of cells.

Galvanostatic electrochemical impedance spectroscopy (GEIS)

GEIS is a common non-destructive technique used to study the transfer behaviour of systems in a number of applications. For Li-ion cells the electrochemical impedance can be measured at different conditions providing key electrochemical parameters of a sealed battery [105], [106]. The impedance is determined as a function of a voltage response in response to a current input. A range of input frequencies can be used, giving the advantage to separate the individual components contributing to the impedance, such as series resistance, charge transfer resistance and double layer capacitance, which can be used to evaluate the performance of a battery [107], [108]. In this research the galvanostatic impedance measurements were performed in the frequency scan range of 10 mHz to 10 KHz before testing using Bio-logic VMP3 cycler and EC-lab V11.02 software. The value of the excitation current signal was set to 800 mA and the temperature of the thermal chamber was set to 25 °C. The sampling rate was set to 6 points per decade. Section (A) of the appendix shows a screenshot of the EIS software settings.

4.5.2.2 The external short circuit event

The EXSC tests were composed of two sets of experiments to investigate two parameters; the short resistance value and the short duration. For the first set, different shunt resistors were used to investigate the effect of the resistance on the behaviour of the cell during short-circuit. The combined resistances of the whole external circuit, including the circuit elements, the cable connections and contact resistances were measured using a micro-ohmmeter to be 0.562, 0.788, 24.0, 236, 501 and 821 mΩ.

During the second set the lowest value of short resistance (0.562 mΩ) was used to short-circuit cells for different durations (20, 10, 5, 1, and 0.5 s). The second set was composed of three groups. Cells in Group 1 were only short-circuited for different durations. In Group 2, after the EXSC test, cells of the short durations 5, 1, and 0.5 s were cycled for 155 cycles within 2-3 hours after the EXSC. In Group 3, cells were shorted (for 5, 1, and 0.5 s), then stored for an extended period (31 days, equivalent to the time taken to complete 155 cycles) before being cycled for 155 cycles. The aim of Groups 2 and 3 was to compare the effect of storing sort-circuited cells to immediately cycling them after an EXSC. Each test was repeated 3 times. The shorting time was controlled by remotely operating the contactor using a programmable power supply (ROHDE & SCHWARZ HMP4040). Table 4-2 summarises the experiments.

Table 4-2: Summary of EXSC experiments

Test Set	Group No.	Parameter Investigated	Parameter Values	Test Stage(s)
A	0	Short resistance value	0.562, 0.788, 24.0, 236, 501 and 821 mΩ	EXSC only
B	1	Short duration	20, 10, 5, 1 and 0.5 s, using 0.562 mΩ	EXSC only
	2	Short duration	5, 1 and 0.5 s, using 0.562 mΩ	EXSC → cycling
	3	Short duration	5, 1 and 0.5 s, using 0.562 mΩ	EXSC → storage → cycling

4.5.2.3 Cycling and storage after external short circuit

Full charge-discharge cycles were conducted on the cells to investigate their EXSC cycling behaviour. Cells were cycled between 4.2 and 2.7 V for 155 cycles using Maccor cycler. Non-abused cells were also cycled as control. The cycling method affects the cell performance, reliability and lifetime [109]–[111], hence the same cycling profile as presented in Section 4.5.2.1 was followed for all cells. The internal resistance of the cells was measured every 5 cycles using the DCIR measurement method outlined in Section 4.5.2.1. Figure 4-4 shows the cycling regime of the charge/discharge cycles after the overcharge event. A screenshot of the cycling programme is shown in Section (B) of the appendix.

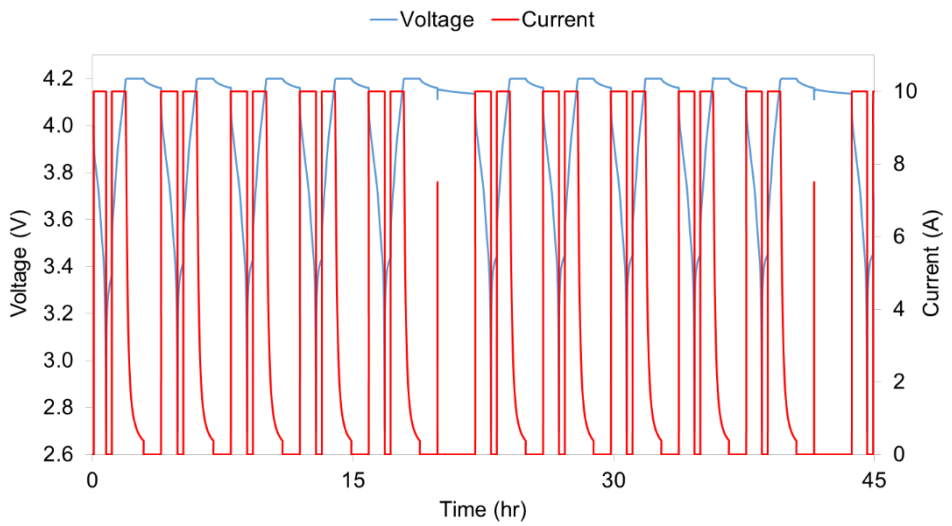

Figure 4-4: Post external short circuit cycling regime

4.5.2.4 Electrochemical impedance spectroscopy

EIS measurements were done on all cells after all testing stages (EXSC, storage and cycling) to investigate the change in their impedance as a result of the previous testing stage. The same EIS settings as in Section 4.5.2.1 were used.

4.5.2.5 Post-mortem analysis

After testing post-mortem analysis was performed on a number of cells to investigate any changes in their internal components. Three cells were used; cells shorted for 20 and 0.5 s and a non-abused cell used as a reference. The cells were opened in an argon filled glovebox in an abuse chamber. The oxygen and water vapour concentration inside the glovebox were below 0.1 ppm. The cell components (mainly electrodes and separator) were visually inspected. Samples of the cathode and anode

were cut and washed with DMC (di-methyl carbonate) as preparation for SEM. SEM images were obtained using a Carl Zeiss Sigma Field Emission Scanning Electron Microscope (FE-SEM). The acceleration voltage was 5 kV and the lens working distance was approximately 2 mm.

4.6 Results and Discussion

4.6.1 Effect of Short Circuit Resistance

This section presents and discusses the electrical and thermal response of Li-ion cells to an EXSC for a wide range of external resistances, ranging from 0.562 mΩ to 821 mΩ.

4.6.1.1 Electrical response

As pointed out in Section 4.5.1 of the Methodology, besides measuring the cell voltage, the voltage drop across the shunt connected in series with the cells was also measured. The knowledge of the shunt resistance value allows the current profile to be obtained during the EXSC.

Figure 4-5 shows the voltage profiles during an EXSC test for a range of short resistances. The data sets can be divided into three groups according to their voltage response. The first group includes the cases with very small short resistances (0.562 and 0.788 mΩ) in this group the voltage drops dramatically once the short circuit starts, reaching almost zero volts. The majority of the cells' stored electrochemical energy was released as heat and the cells were almost fully discharged within tens of seconds. The behaviour of this group can be classified as hard short circuit. The second group consists of short circuits with intermediate resistance values (24.0 mΩ). For this group, once the short starts, the voltage drops, but the voltage profile can be broken down into two clear stages with different rates of voltage drop (dV/dt). During the first stage the rate of voltage drop is high until it reaches a voltage value of 3.6 V, where the magnitude of the gradient decreases and the cell discharges at a steady rate. The third group is where the voltage does not drop significantly and it follows the profile of a normal load discharge process.

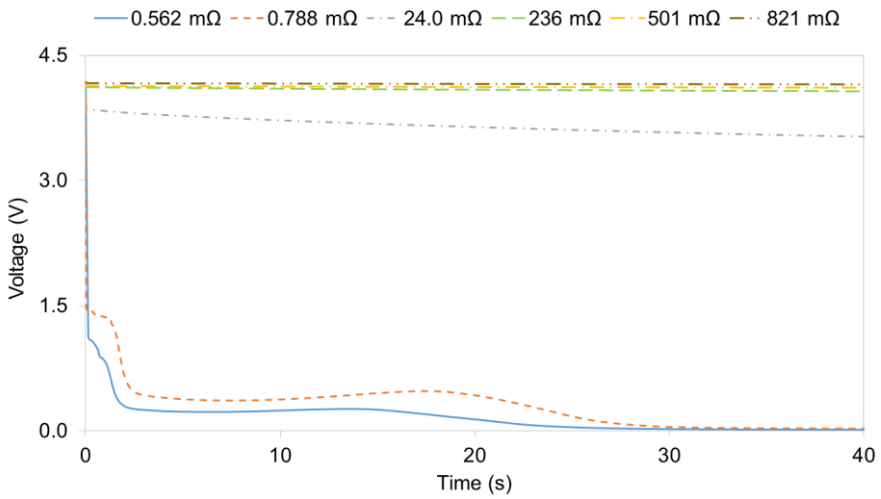

Figure 4-5: Cell voltage profiles during an external short circuit test for a range of short resistances

The corresponding current response in Figure 4-6 clearly shows that the cell current response vary significantly for different shorting resistances and matches the voltage response. The current values are shown on a log scale. The larger the shorting resistance the lower the current and the voltage profile follows that of a normal discharge. For the smallest shorting resistance (0.562 mΩ), the current profile can be broken down into three stages from the start of the short until the cell almost fully discharges. The first stage is when the short starts and there is a current surge peaking at 1840 A (123 C), the cell cannot maintain this high current due to the depletion of lithium ions at the proximity where the active material and current collector meet. The replenishment of lithium ions, constrained by ionic transport, drives the second stage, when the current drops until it reaches about 500 A (33 C). The final stage comes when the cell is nearly depleted; a less severe current drop rate that continues until the voltage drops to zero. The secondary current peak observed in the figure is thought to be due to an increase in ionic transport rates due to the increase in cell temperature. It can be noticed that as the shorting resistance increases, the peak current decreases and the duration of the second stage increases.

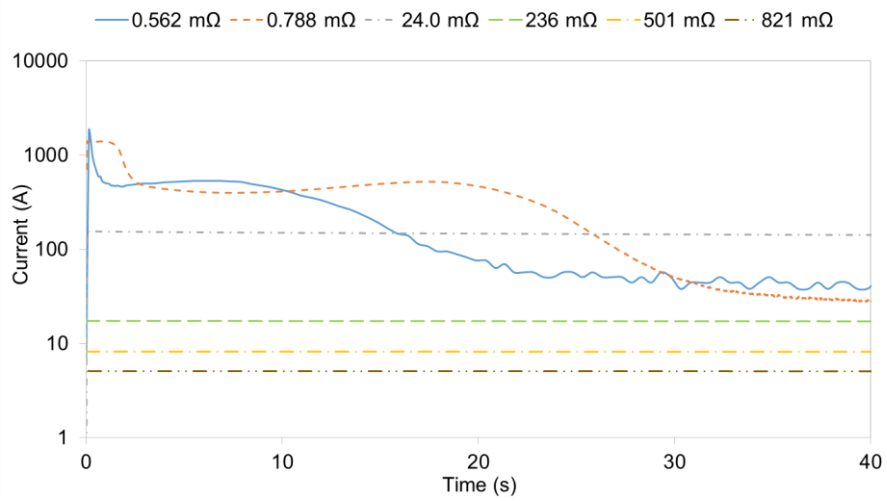

Figure 4-6: Current profiles during an external short circuit test for a range of short resistances

4.6.1.2 Thermal response

The thermal response of the cell varied significantly according to the short resistance used. Figure 4-7 shows the temperature profiles for different resistances that represent the three short circuit scenarios. For the hard short scenario (0.562 mΩ), once the short circuit started the cell surface temperature peaked at 113 °C in just a few seconds. It is worth mentioning that the cell swelled significantly due to the build-up of gases. This means that the actual cell temperature may be underestimated, as swelling affects the surface temperature measurement. However, the cell did not rupture and no thermal runaway happened. Swelling of prismatic cells during external short-circuit has been observed by others [112]. For the soft short-circuiting case, both the rate of temperature rise and the peak value of temperature were less, it took more than 500 seconds for the cell surface temperature to peak at 68 °C. For the third scenario, where the cell behaviour resembled normal discharge, there was no significant temperature rise and the surface temperature stayed almost constant until the cell was fully discharged.

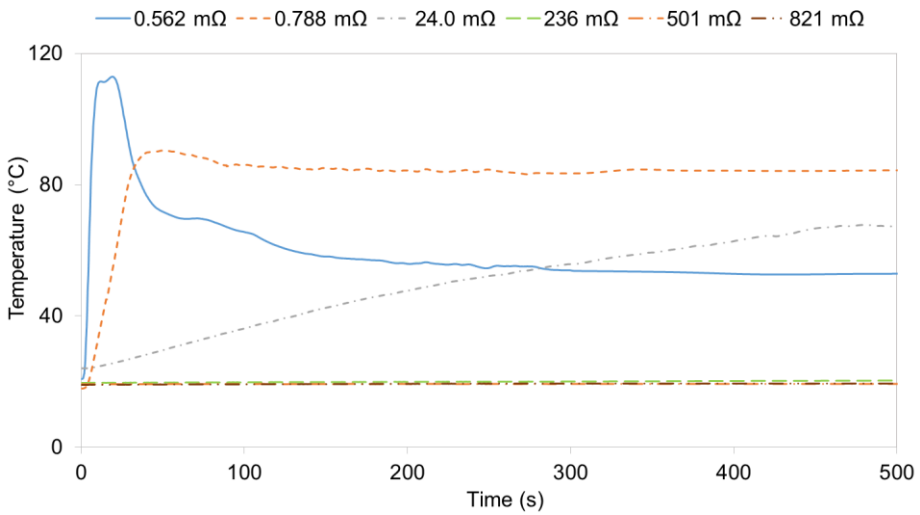

Figure 4-7: Cell surface temperature profiles during an external short circuit test for a range of short resistances

It is clear that the lower the shorting resistance, the higher the rate of temperature rise (dT/dt) and the higher the peak temperature value. This is because the shorting resistance determines the magnitude of current which is responsible for the heating, especially at the initial stage of the short circuit. Figure 4-8 and Figure 4-9 combine the voltage, current and temperature profiles for a hard short-circuit and a soft short-circuit respectively; the close correlation between the cell's electrical and thermal behaviours can be seen.

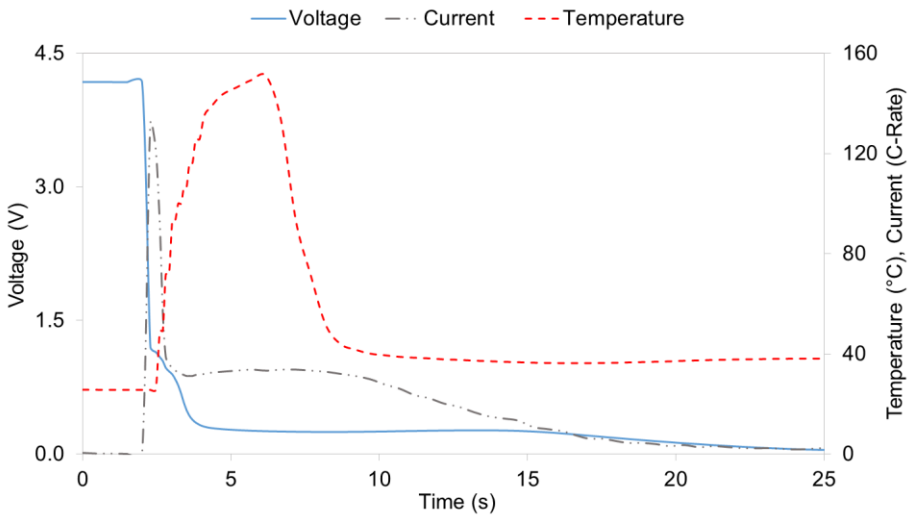

Figure 4-8: Voltage, current and temperature profiles of a hard short circuit during an external short circuit test

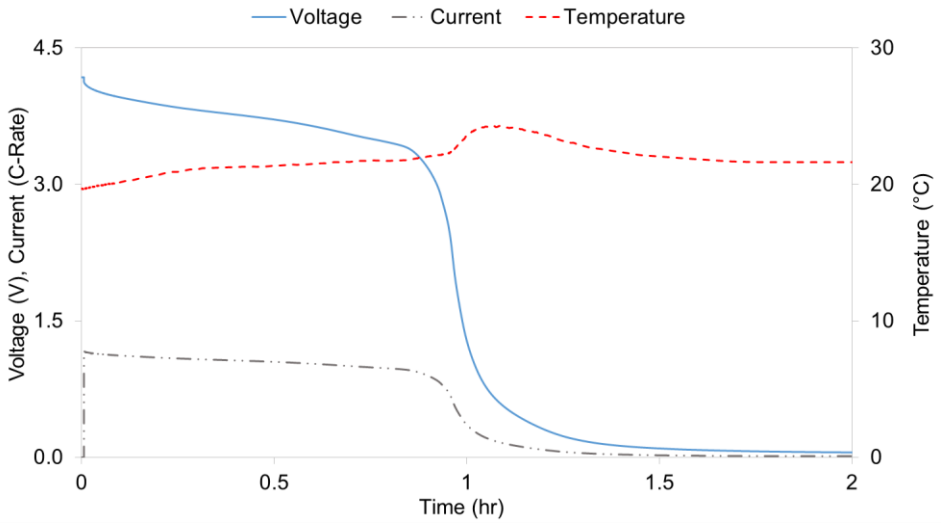

Figure 4-9: Voltage, current and temperature profiles of a soft short circuit during an external short circuit test

The following section investigates the effect of the short duration for the hard short circuit scenario (0.562 mΩ).

4.6.2 Effect of Short Circuit Duration

This section presents and discusses the electrical and thermal response of Li-ion cells exposed to a hard EXSC (0.562 mΩ short resistance) for a range of short durations, ranging from 0.5 s to 20 s. It can be noted from Figure 4-10 that the duration of the short determines the following:

- The degree of voltage drop, i.e. the time the cell spends in the (undervoltage state)
- The duration the cell spends under high currents (overcurrent state)
- The maximum cell temperature reached

The following sections present and discuss the data related to these abusive conditions.

4.6.2.1 Electrical response

Figure 4-10 shows the current and voltage profiles of cells under a hard short circuit for different durations; 20 s, 10s, 5 s, 1s and 0.5 s. Since the short resistance is identical, all cells experience the same initial voltage drop and current surge. However, cells exposed to longer duration of short circuit experience high currents for longer periods. Moreover, they suffer deeper under voltage for longer periods. Even short-

circuiting the cell for 0.5 s drives the voltage down to 1.575 V, which is less than the normal operation lower voltage limit (2.7 V). This combination suggests that cells short-circuited for longer periods would suffer more damage. It should be noted that the dissolution of the anode's copper current collector happens when the cell is deeply discharged to a voltage at which the anode potential increases to above ~3.1 V vs. Li/Li^+ [113]. Studies show that copper dissolution should be avoided, because it plates on the anode surface and could lead to degraded cell performance [114].

After the contactor was open the voltage of all cells starts to recover as Figure 4-11 shows. However, cells that experienced longer short circuit periods recovered to a lower open circuit voltage value. This can be attributed to the amount of energy lost during the short and/or the damage caused by the short. Figure 4-12 shows the cell initial voltage, voltage immediately after the short and 120 s after the start of the short. It confirms that as the shot time increases the voltage drop is more and the voltage recovery is less.

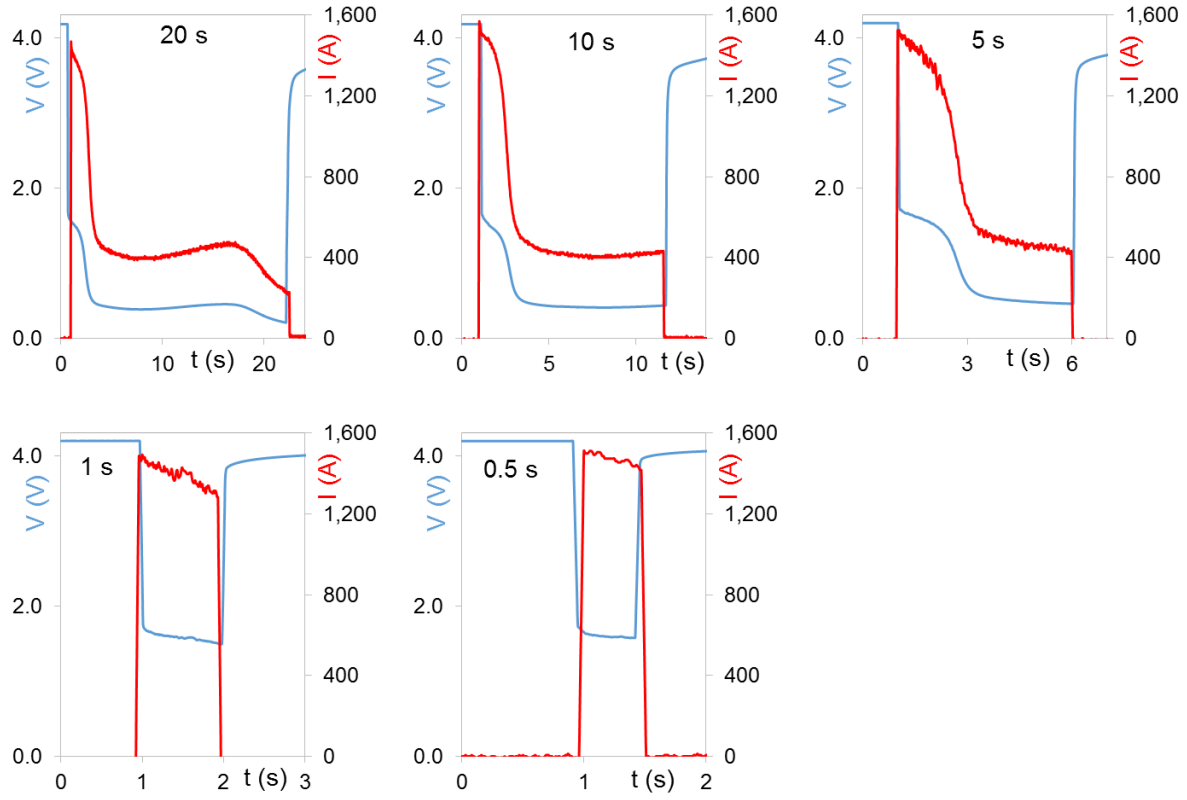

Figure 4-10: Voltage and current profiles during a hard external short circuit test for a range of short circuit times (20 s, 10 s, 5 s, 1 s and 0.5 s)

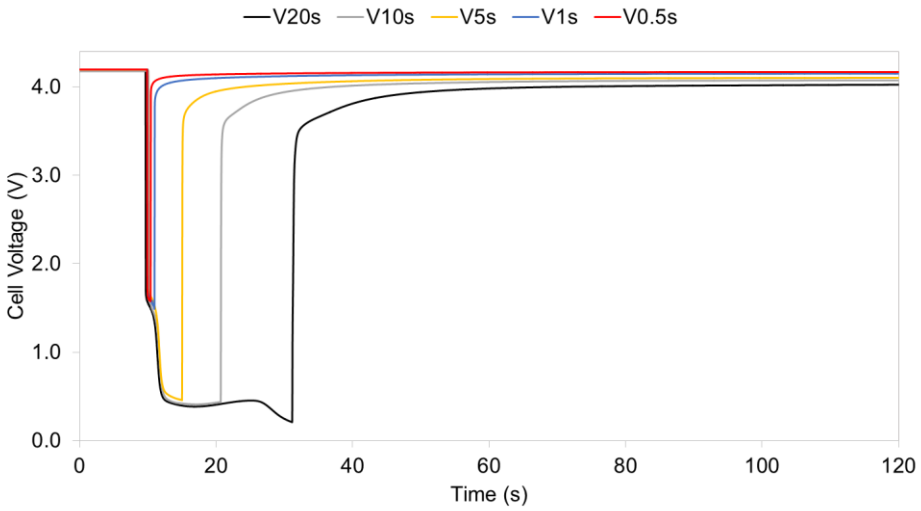

Figure 4-11: Cell voltage profiles during and after an external short circuit event showing voltage recovery

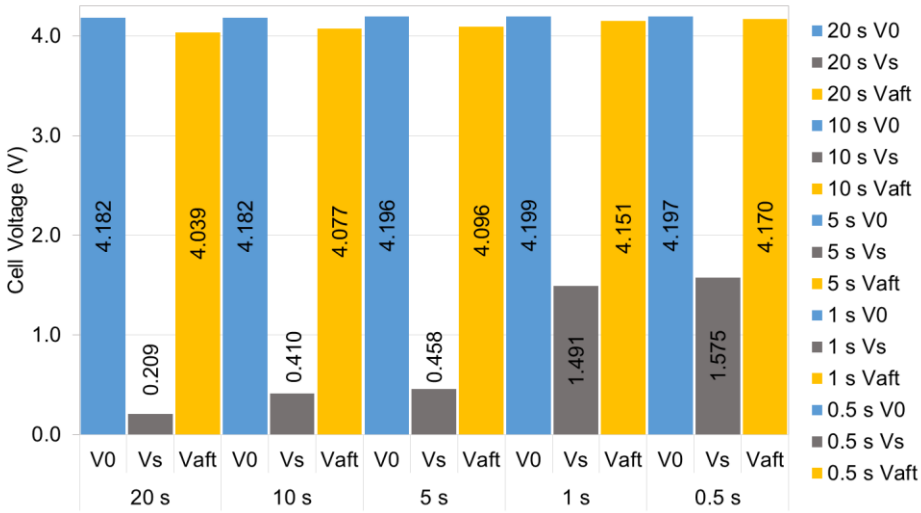

Figure 4-12: Cell initial voltage, voltage immediately after the short ends and 120 s after the start of the short

4.6.2.2 Thermal response

The thermal response of the cells varied according to the short duration. Longer short duration mean longer periods of current flow, resulting in more heat generation and higher temperature rise. Figure 4-13 shows the cell current profiles and their corresponding temperature profiles during the short circuit for all the short durations (20 s, 10 s, 5 s, 1 s and 0.5 s). The cell surface temperature of the cells shorted for 20 s peaked at 78.9 °C with a temperature increase of 52.9 °C, while that of the cells

shorted for 0.5 s peaked at 29.3 °C, with a temperature increase of 4.2 °C. Figure 4-14 shows the maximum temperature increase for the different short durations, longer short duration resulted in higher temperature rise. The current and temperature profiles in Figure 4-13 show that as the current stops the heating stops, this suggests that Ohmic heating was the main source of temperature rise and no exothermic reaction were triggered.

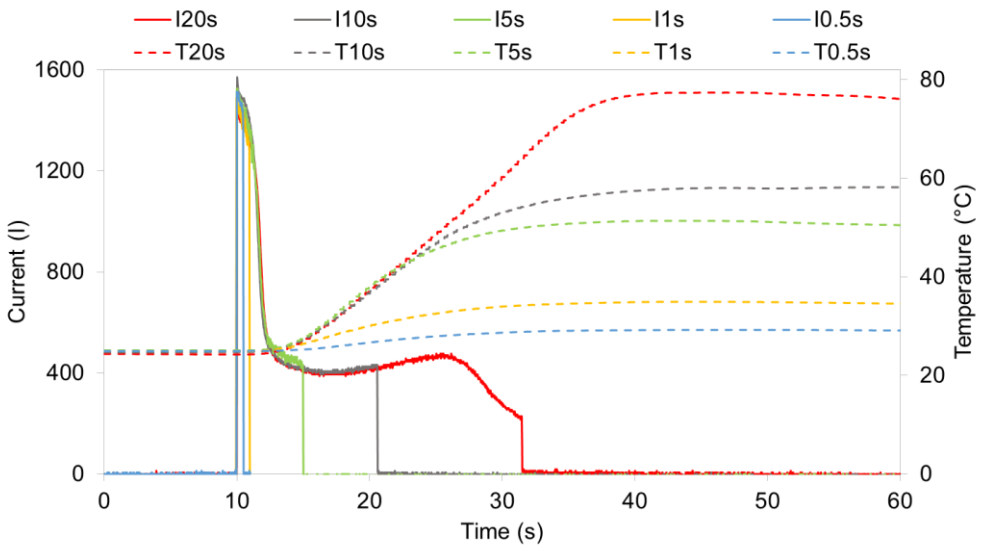

Figure 4-13: Cell current profiles and their corresponding temperature profiles during a hard external short circuit test for a range of short circuit durations (20 s, 10 s, 5 s, 1 s and 0.5 s)

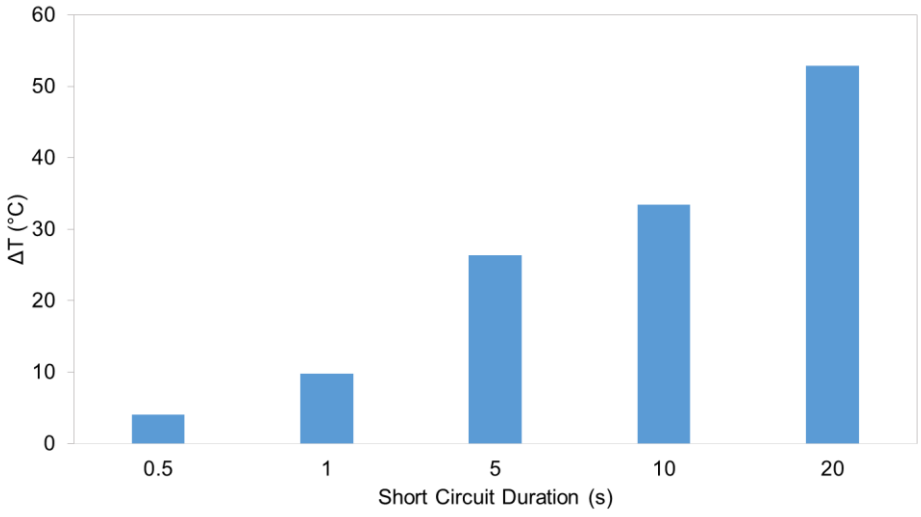

Figure 4-14: Maximum temperature increase for different short durations

Nine thermocouples were used to monitor the cell surface temperature of the cell at different locations. Figure 4-15 shows the increase in temperature (°C) at different

locations of the surface temperature of cells shorted for 20 s. The temperature distribution showed the following:

- The closer to the tabs the higher the temperature rise
- The centre of the cell experienced higher temperature increase. Points closer to the cell boundary experience lower temperature rise, this can be attributed to better heat dissipation by convection.
- The positive terminal (aluminium) heats to a higher temperature than the negative (copper) one. This can be attributed to the higher electrical resistivity of aluminium compared to the copper, since the current flowing through both of them is the same. Moreover, the thermal conductivity of aluminium is lower than copper.

+		-
52.0	53.1	50.7
49.3	50.2	49.3
46.1	49.8	46.0

Figure 4-15: Cell surface temperature distribution of cells shorted for 20 s

4.6.3 Cycling Behaviour after External Short Circuit

This section presents and discusses the impact of the short circuit duration on the evolution of capacity and internal resistance of cells during cycling after the EXSC event. Two groups of cells were studied; cells cycled hours after the EXSC and cells stored for an extended period before cycling. The change in thermal behaviour during cycling was also investigated.

4.6.3.1 Cells cycled immediately after EXSC

Figure 4-16 shows the evolution of the normalised discharge capacity as a function of cycle number after EXSC events of different durations (5 s, 1 s, 0.5 s). A control cell which has not been abused was included as a reference. The capacity of all cells was normalised to the initial capacity obtained during the pre-conditioning step in section 4.5.2.1 of the experimental procedure. The variation in the initial capacity of all cells

was less than ± 2.5% as presented in Section 3.5.1. This group of cells was cycled within 2-3 hours after being the EXSC. After 155 full charge-discharge cycles the capacity of the control cells dropped by 0.85% of its initial capacity. Cells that experience a 0.5 s short showed a capacity drop of 2.1% after 155 cycles. Cells short-circuited for 1 s had a higher capacity fade of 3.2%. The highest capacity fade was suffered by cells short-circuited for 5 s as their capacity dropped by 4.9%. This shows that the damage caused to a cell increases as the short duration increases and abuse speeds up the capacity fade mechanisms.

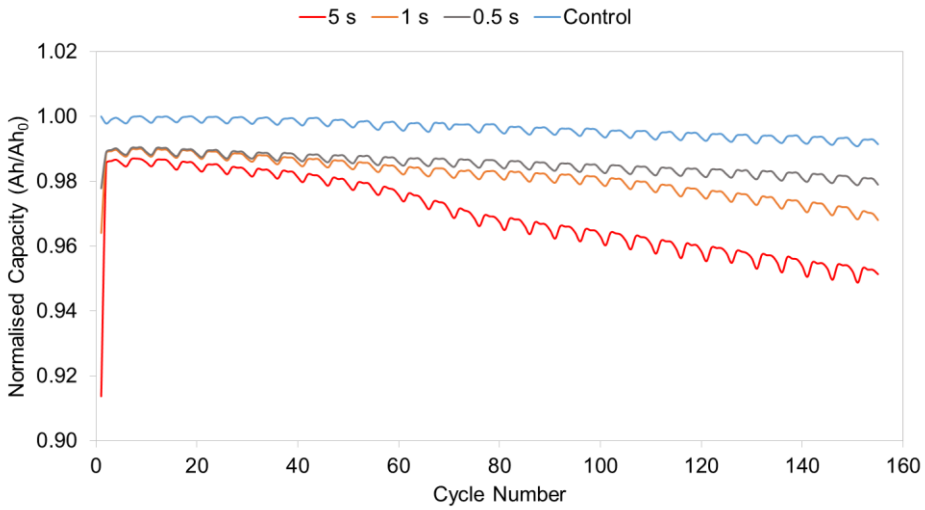

Figure 4-16: Evolution of normalised discharge capacity with cycle number after external short circuit events of different durations

The internal resistance trends shown in Figure 4-17 followed the cell capacity trends in Figure 4-16. Cells short-circuited for longer periods experienced higher internal resistance increase. A possible explanation can be the time spent in an under-voltage/overdischarged state, as this can result in the oxidation of the copper current collector causing copper dissolution into the electrolyte [115]. As the cell is cycled the dissolved copper can block the electrode pores reducing the cells' performance [99]. Copper dissolution is one of the factors the contribute to cell aging and its capacity fade [116].

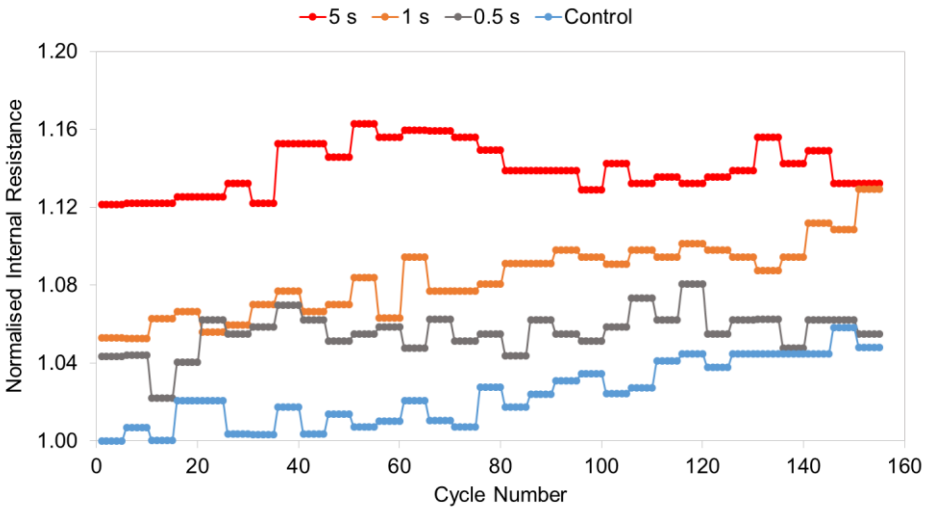

Figure 4-17: Evolution of normalised DCIR resistance measurements with cycle number after external short circuit events of different durations

4.6.3.2 Cells stored between EXSC and cycling

A group of cells were stored for 35 days (time taken for 155 cycles) before being cycled. This was done to investigate if it was better to cycle cells after an EXSC event or store them in order to minimise the damage. Figure 4-18 shows the evolution of the normalised discharge capacity after the same EXSC event (5 s) for two groups; cells cycled immediately after the EXSC and cells stored before cycling. Cells cycled immediately after (2-3 hours) the EXSC event showed a capacity fade of 4.9% after the 155 cycles, whereas, the capacity of cells stored before being cycled faded by 6.5%. It can be also be noted that the fade in capacity of the stored cells after storage/before cycling was 4.2%, compared to a fade of only 1.4% immediately after the EXSC. This shows that storing the cells caused more capacity fade and suggests that cycling the cells after an EXSC event can be better to minimise their damage.

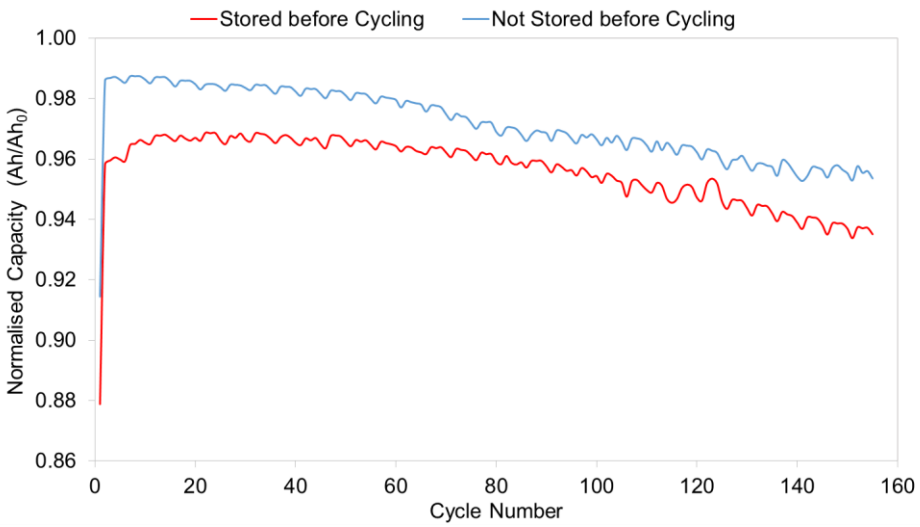

Figure 4-18: Evolution of normalised discharge capacity with cycle number after external short circuit for two groups: cells cycled immediately after the EXSC and cells stored before cycling

The evolution of the internal resistance trends shown in Figure 4-19 followed the cell capacity trends in Figure 4-18. Short-circuited cells stored before cycling experienced higher internal resistance increase. However, it should be highlighted that the stored then cycled cells were assessed 70 days after the external short circuit, whereas cells cycled without storage were assessed 35 days after the external short circuit. Further investigation to exclude the effect of time might be needed. This can involve cycling the cells then storing them before assessment.

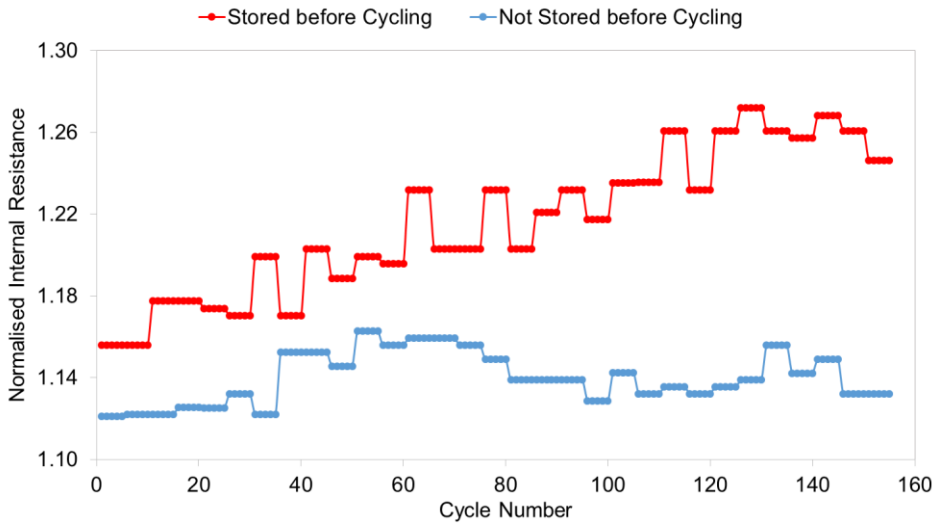

Figure 4-19: Evolution of normalised DCIR resistance measurements for two groups: cells cycled immediately after the EXSC and cells stored before cycling

4.6.3.3 Thermal behaviour during cycling after EXSC

During cycling heat is generated by current flow through the cell. The main mechanism of heat generation is Ohmic, expressed by Equation 4-1. This means that any increase in the current of the cell's resistance causes more heating and subsequent temperature rise.

$$P_{Ohmic} = I^2R \qquad \textit{Equation 4-1}$$

Where *I* is the current and *R* is the cell resistance.

Figure 4-20 shows the surface temperature and voltage profiles of the control cell and a short-circuited cell (5 s) during cycling. As the cell voltage changes the cell temperature changes. The cells were cycled using a constant current as described in Section 4.5.2.3 of the experimental procedure. Hence, the change in heat generation is caused by the change in the internal resistance of the cell as it changes with its SOC. For the control cell, the temperature change was between 24.5 °C at 4.2 V to 25.6 °C at 2.7 V, with a temperature window of 1.1 °C, whereas for the short-circuited cell, the temperature change was between around 26.4 °C at 4.2 V to 28.5 °C at 2.7 V, with a window of 2.1 °C. It can be noticed that the lower and upper temperature limits of the short-circuited cell is higher. Moreover, its temperature window widened. This can be attributed to the increase in internal resistance caused by the EXSC as backed by the resistance measurements.

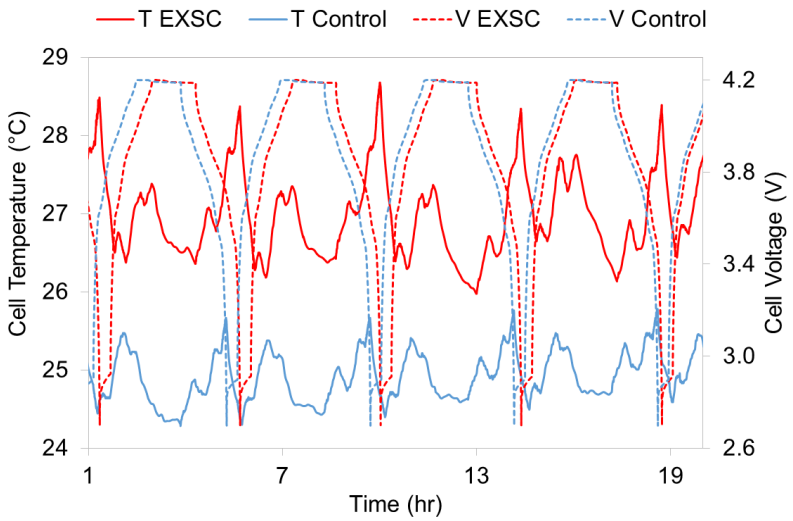

Figure 4-20: Surface temperature and voltage profiles of the control cell and short-circuited cell during cycling

The increase in temperature values is determined by the increase in internal resistance caused by the EXSC. Therefore, cells that were short-circuited for longer period experienced higher charge and discharge temperatures increase during cycling, as shown in Figure 4-21 and Figure 4-22 respectively. However, it can be noticed that cells shorted for 5 s and 1 s experienced a reduction in the maximum charge and discharge temperatures with cycling. A possible explanation for this could be that the reduced capacity of the damaged cells mean reduced charge throughput and therefore reduced heat generation.

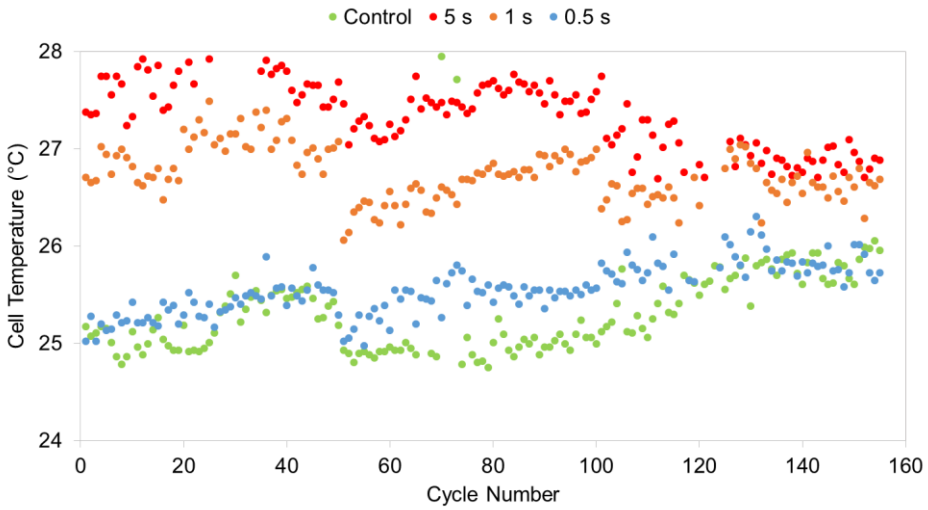

Figure 4-21: Evolution of the maximum charge temperature with cycling of cells short-circuited for different durations

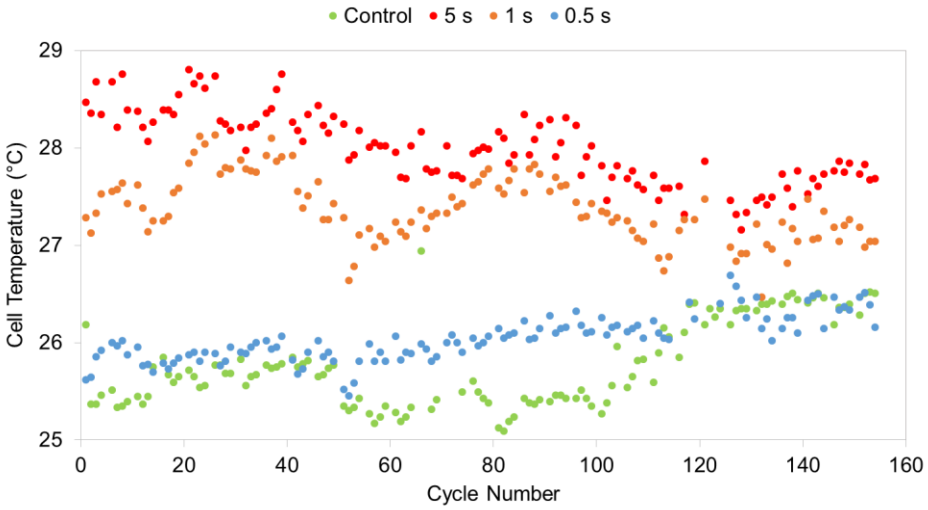

Figure 4-22: Evolution of the maximum discharge temperature with cycling of cells short-circuited for different durations

4.6.4 Evolution of Cell Impedance using Electrochemical Impedance Spectroscopy

This section discusses the evolution of the cell impedance after the EXSC event and after subsequent cycling. The two short-circuited cell groups are also compared; cells cycled hours after the EXSC and cells stored for an extended period before cycling.

EIS measurements were performed on cells at different stages. Based on these EIS measurements Nyquist plots were plotted to investigate the change in the components contributing to the cell's internal impedance. Figure 4-23 shows the Nyquist plot for the average EIS measurement for all cells. The standard deviation for the real Re(Z) and imaginary Im(Z) components was 0.108 and 0.142 mΩ respectively. As annotated on the figure, the high frequency range (KHz) represents the inductive behaviour attributed to the porous structure of the cell electrodes [117], the point of intersection between the curve and the x-axis (real component) is estimated to be the cell's series resistance (R_{Ω}). The charge transfer resistance (R_{ct}) is represented by the semi-circle at the medium frequency region (Hz). The diffusion effect of lithium ions can be described by the slope of the line in the low frequency region (mHz) [118]–[120].Since the inductance depends on the porosity of the electrodes, it should remain constant as long as the electrodes were not mechanically damaged [121]. Therefore, the inductive tail can be excluded from the EIS analysis [117].

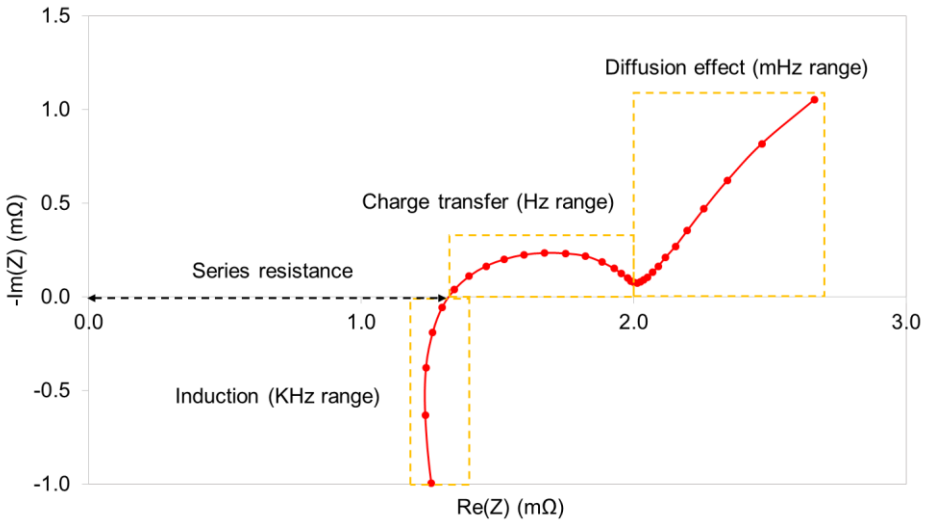

Figure 4-23: Pre-EXSC average Nyquist Plot showing the components contributing to the cell's impedance

4.6.4.1 EIS after EXSC

Figure 4-24 shows the EIS measurements before and after the EXSC event of the different durations. The Nyquist plots of all cells moved to the right, the semi-circle at the medium frequency range increases in size and was more depressed and the line at the low frequency range increased in length and its angle with the vertical axis increased. These changes suggest increases in the series resistance, charge transfer resistance and the diffusion resistance respectively. Figure 4-25 combines the Nyquist plots for all short durations, it shows that longer EXSC durations increased the cell impedance.

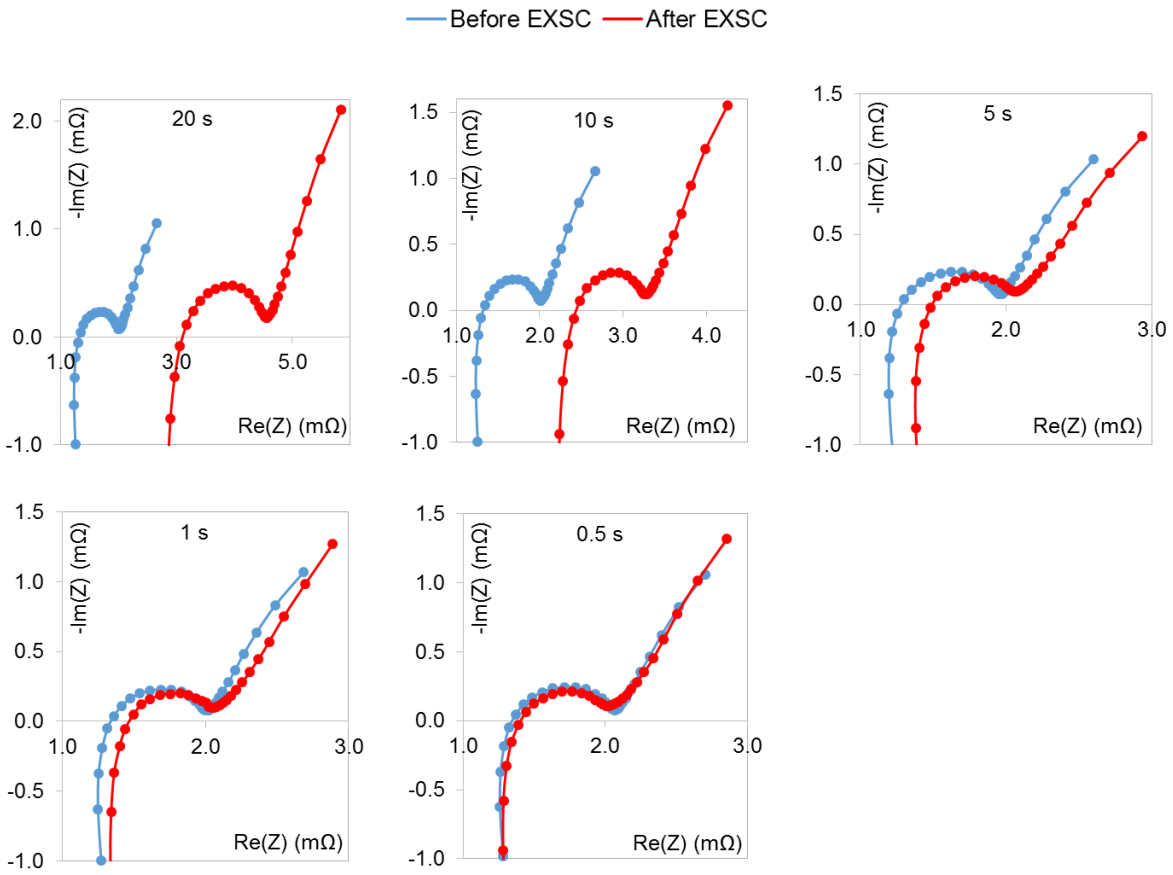

Figure 4-24: Cell EIS measurements before and after external short circuit events of different durations

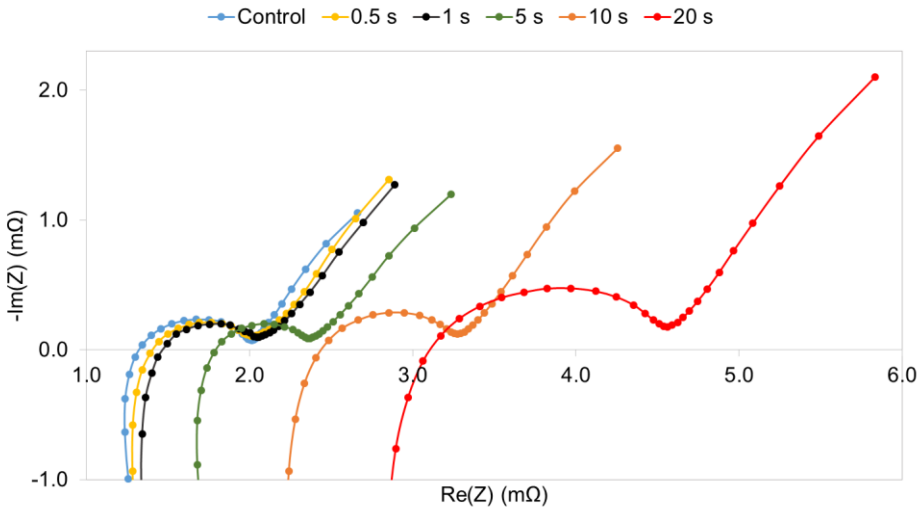

Figure 4-25: EIS measurements after the EXSC of all cells short-circuited for different durations

4.6.4.2 EIS after cycling

Cycling the cells after the EXSC event further increased the impedance of all cells as shown in Figure 4-26. Figure 4-27 combines all the Nyquist plots for all short durations after cycling, it shows that longer EXSC durations increased the cell impedance more during cycling.

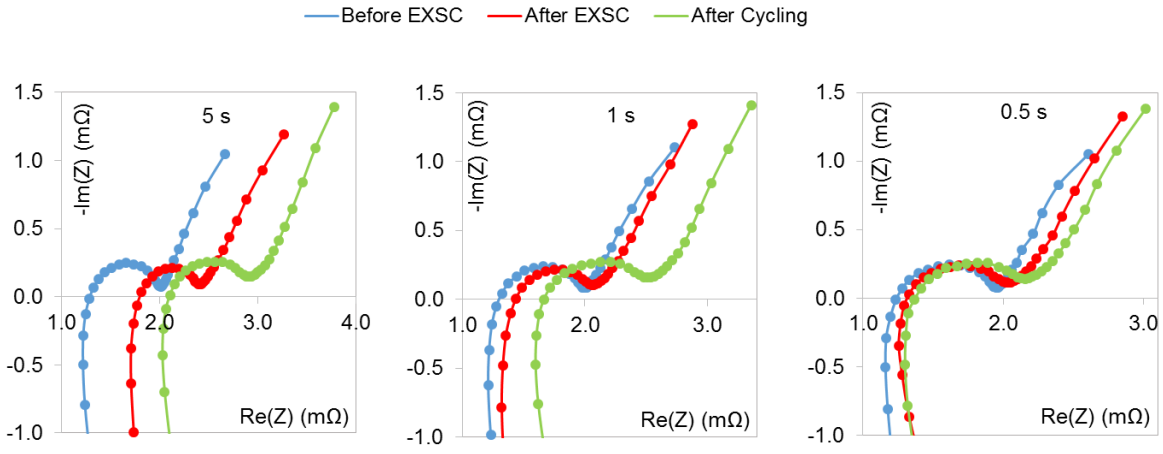

Figure 4-26: EIS measurements of cells short-circuited for different durations; before EXSC, after EXSC and after cycling

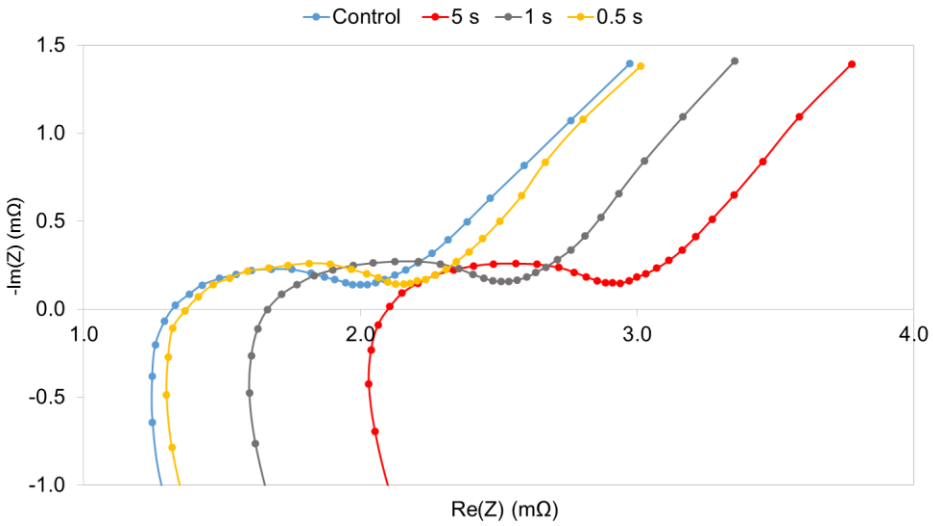

Figure 4-27: EIS measurements after cycling of all cells short-circuited for different durations

Figure 4-28 shows the Nyquist plots for cells stored and not stored before cycling. The data agrees with the capacity trend presented in section 4.6.3.2. Storing the cell after the EXSC event increases their impedance. Moreover, when cycled their impedance increased more than the cells that were not stored.

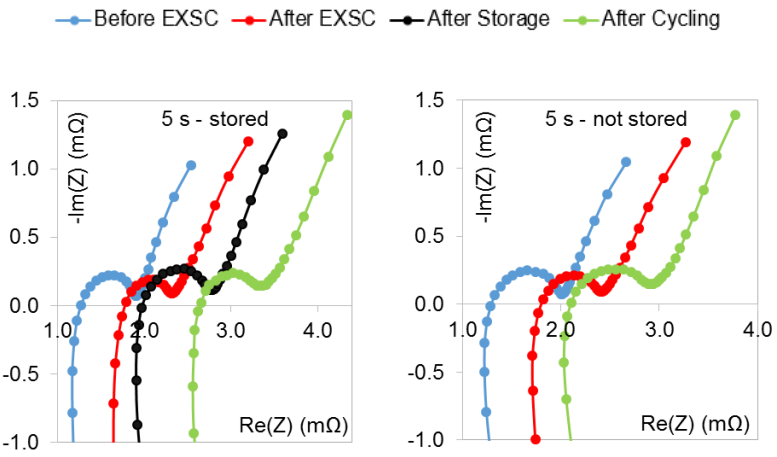

Figure 4-28: EIS measurements of cell stored and cells not stored before cycling

4.6.5 Post Mortem Analysis and SEM

Post-mortem examination was carried out to assess the type and extent of damage caused to the cell components as a result of the external short circuit. A teardown was performed on hard short-circuited cells and a control cell to be used as a

reference. First, the cell components were inspected visually, then samples of the electrodes and separator were studied using SEM.

When the cell case was removed the colour of the separator was not uniform. There were spots on it as shown in Figure 4-29a. When pulling the separator layer attached to the negative electrode, there was a pattern on both the separator and the electrode as Figure 4-29b shows. Swelling due to gas formation might be what caused this pattern. Close inspection of the positive current collector showed red stains on its surface Figure 4-29d. This can be attributed to copper dissolution as a result of the cell's rapid overdischarge [99]. There was also a pattern of a light grey colour on the positive current collector, which is believed to be ceramic coating material from the separator, as the separator appeared to be covered with a grey powder as shown in Figure 4-29c.

SEM was used to further investigate the cell electrodes for damage. Figure 4-30a shows the SEI images of anodes of two cells short-circuited for 20 s and 0.5 s. Figure 4-30b shows the cathodes of both cells. The anode and cathode of a non-abused cell is included as a reference. No change in surface morphology of both electrodes was observed.

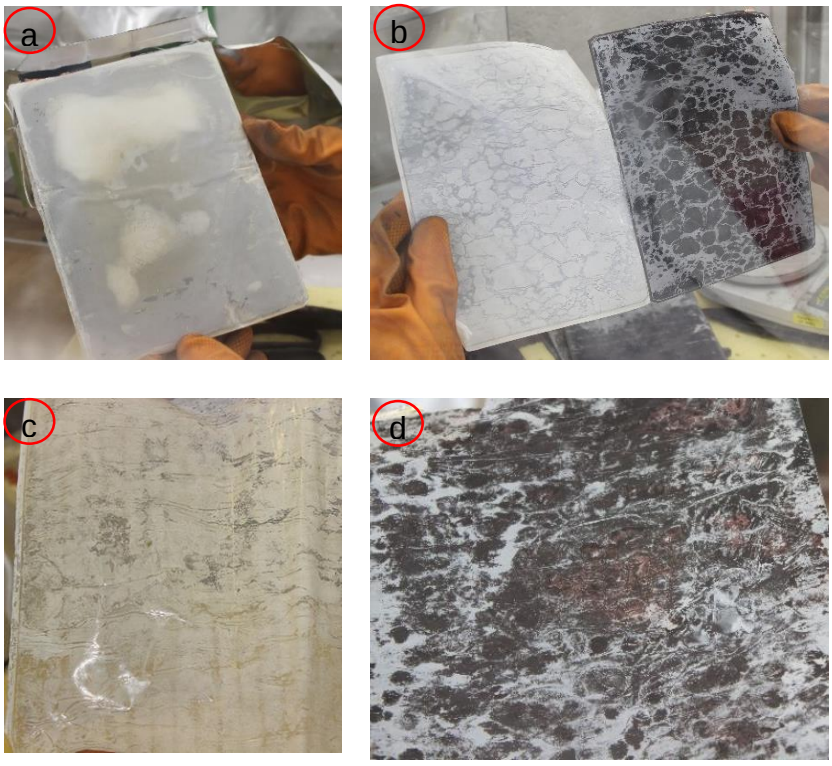

Figure 4-29: Photographic images of cell teardown after EXSC (a) whole stack with casing removed (b) separator and anode separated apart (c) separator pattern (d) cathode

a) Anodes

b) Cathodes

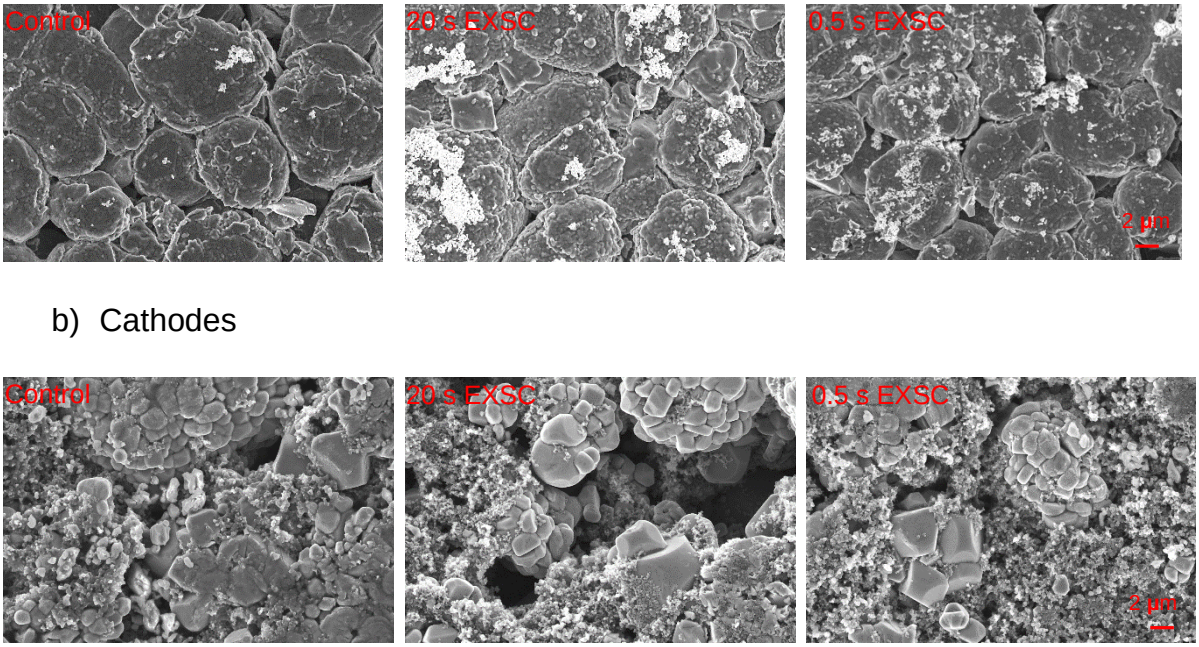

Figure 4-30: SEM images of control and abused (a) anode (b) cathodes

4.7 Chapter Conclusion

Externally short-circuiting commercial automotive Li-ion pouch cells showed that their behaviour during an external short circuit event depends on both the short current and short duration. After the external short circuit event cells were successfully cycled. However, they suffered more capacity fade and resistance increase than non-abused cells. The degree of damage was proportional to the duration of the short circuit. Cells short-circuited for longer durations suffered more capacity fade and resistance increase. Storing the cells after the external short circuit event increased their impedance. Moreover, when cycled they suffered more capacity fade than cells cycled immediately after the short circuit.

4.8 Recommendations for Future Work

This short circuit study was limited to one cell technology. A more comprehensive study can include cells with different formats, capacities and chemistries. It would also be useful to quantify the volume increase under the different short circuit conditions

and analyse the gas composition that causes the swelling. Tearing down the short-circuited cells and using techniques other than SEM, such as energy dispersive X-ray (EDX) to perform the post-mortem analysis on the cell components can provide useful information.

It should also be noted that in a battery pack environment cells are constrained, therefore a more representative test would be short circuiting the cells under compression.

Chapter 5 – In-Situ Volume Measurement during Overcharge

5.1 Chapter Highlights

- A purpose-built in-situ volume measurement apparatus was designed and built
- Overcharge to different degrees of overcharge
- Overcharge using different C-rates
- In-situ volume measurement during and after an overcharge event
- Impedance representation using equivalent circuit model
- Post overcharge long-term cycling
- Electrical and thermal behaviour during post-overcharge cycling

5.2 Chapter Abstract

This work investigates the behaviour of large format commercial automotive pouch Li-ion cells during and after an overcharge event. The change in cell volume during cycling, overcharge and 10 cycles after the overcharge event was monitored and measured in-situ using Archimedes' principle. Cells were then cycled for 155 cycles to study the impact of the degree of overcharge and the C-rate on the cell performance. Electrochemical Impedance Spectroscopy (EIS) measurements were made and an Equivalent Circuit Model (ECM) was built to investigate the individual components contributing to the cell's impedance. The overcharge-induced capacity fade and internal resistance increase are analysed using incremental capacity analysis (ICA) and DCIR measurement respectively. The reversibility of cell volume after swelling was also investigated. Results show that cell swelling and the extent of damage done reflected by the cell's impedance and capacity after an overcharge event depends on the degree of overcharge and the C-rate. Cell swelling was partially reversible and the cells were cycleable after the overcharge event, suggesting that they could be reused. Although their temperature during cycling is higher compared to non-abused cells, due to the increase in their internal resistance.

5.3 Chapter Introduction

5.3.1 Battery Safety and Overcharge

Overcharge occurs when the current is forced into the cell beyond its nominal cut-off voltage/upper voltage limit [90]. Overcharge can be caused by a faulty charger which fails to detect the end of charge of the battery [29], [84], [122] or an inappropriate BMS design or malfunction. Severe cell imbalance/mismatch within series or parallel connected strings can also result in individual cells being overcharged [123]–[126]. In a series string of cells, if one cell has higher SOC than the others, it will fully charge before them. If the charger is designed to charge series strings rather than individual cells, as the string becomes fully charged this cell will be overcharged. A cell in an overcharged state is less thermally stable than cells under normal charge conditions. This might create a safety event such as, gassing, fire or explosion. Venting might lead to the emission of harmful gases that can be toxic and/or flammable [25]. Cells that gas without venting in a restricted volume in a battery pack, can swell and impose mechanical stress on the surrounding cells and battery components such as cooling plates and other parts [102].

Overcharge can be the most severe abuse test since additional energy is added to the cell. The rate at which this energy is added (C-rate) to the cell is crucial to determining the outcome of the overcharge event [112], [127]. Other factors such as cell materials, construction and design also have a significant effect. Cells with the same chemistry but different capacity and energy density can behave differently [128].

Thermal stability is the main challenge in terms of safety. When it comes to the thermal stability of the cell during overcharge, both electrodes and the electrolyte contribute significantly. For the negative electrode (anode) the amount of energy it releases depends on its lithiation state and its reactivity with the electrolyte. It is believed that a cell going into thermal runaway during overcharge is initiated by the reaction of the over-lithiated anode and electrolyte as a result of SEI breakdown. A thermal runaway during overcharge can also happen as a result of the violent reaction between the lithium deposited on the anode surface and the electrolyte [129].

For the positive electrode the energy released depends on its chemistry as the chemistry determines the amount of oxygen produced during decomposition. Studies

on different cathode chemistries such as Li_xCoO_2, Li_xNiO_2, and $Li_xMn_2O_4$ found that, during decomposition, the amount of oxygen released by the cathode into the electrolyte increases as x increases [130]. This oxygen fuels the oxidation of the electrolyte [84]. Therefore a highly reduced cathode could lead to a violent explosion as the amount of oxygen produced is significant. Most efforts to improve Li-ion battery reaction to overcharge are directed towards finding safer cathode materials or enhancing the thermal stability of the current cathode materials by coating their surface with additives [131], [132]. Efforts to improve cell safety also include adding overcharge protection additives to the electrolyte, given its important role in heat generation [133]–[135].

Although overcharge of a single-cell battery can have serious consequences, the overcharge of a cell in a multi-cell battery as in the case of automotive applications can have catastrophic consequences on a big scale. Overcharging a cell may cause it to catch fire and explode affecting other cells in the battery pack, if the heat is not contained or somehow quickly dissipated, propagation of failure from cell to cell can consume the whole pack, potentially releasing a large amount of energy in fire or explosion.

Overcharging the cell can be stopped before it reaches a critical stage, i.e. thermal runaway. In this case the cell could be reused after this event, if it is proved to be safe and if its performance is not severely degraded. The side reactions during overcharge leads to internal resistance increase and capacity degradation.

This work experimentally investigates the in-situ behaviour of large format commercial automotive pouch cells during and after an overcharge event (different degrees of overcharge and C-rates) to develop a deeper understanding of the failure mechanism and root cause(s). This work is the first, as far as the author knows, to report in-situ volume change during overcharge. The ultimate aim of this work is to help develop more representative and useful testing procedures, help improve the battery pack design and make Li-ion cells safer and more abuse tolerant for the use in the automotive industry.

5.3.2 Aim and Objectives

The aim of this study is to develop a deeper understanding of the Li-ion cell behaviour during and after an overcharge event.

The objectives to meet this aim are:

1) Quantify the volume change and determine its source(s)
2) Assess the reversibility of volume increase after an overcharge event
3) Investigate the capacity degradation behaviour of the Lithium ion cell after an overcharge event
4) Characterise the overcharged cells after an overcharge event and after post-overcharge cycling

5.4 Background

5.4.1 Abuse Test Standards

There are a number of overcharge abuse test standards that cells are required to pass in order to be used in automotive applications. The most common test standards that specify overcharge tests are summarised in Table 5-1.

Table 5-1: Summary of the most common overcharge test standards for automotive applications

Test Standards	Test Description
SAE J2464 “EV & HEV Rechargeable Energy Storage System (RESS) Safety and Abuse Testing Procedure” [36]	Cells are charged at two rates: 1) 1 C-rate constant current. 2) The maximum use current to 200% SOC
FreedomCAR EESS Abuse Test Manual (SAND2005 – 3123) [26]	Cell are charged with a 32 A constant current of 32 A until it reaches 200% SOC, for 4 hours, or until it fails
SAE J2929 “Electric and Hybrid Vehicle Propulsion Battery System Safety Standard – Lithium-based Rechargeable Cells” [37]	Simulate single point failure of the charge control of the battery system when the battery system charge device is no longer being controlled
IEC 62660-2:2010 “Secondary Li-ion Cells for the Propulsion of Electric Road	Charge until the cell voltage reaches two times the maximum voltage, or up to 200 % SOC

Vehicles – Part 2: Reliability and Abuse Testing" [38]	
ISO 12405-3:2014 "Electrically Propelled Road Vehicles – Test Specification for Li-ion Traction Battery Packs and Systems – Part 3: Safety Performance Requirements" [104]	Charging until 200% SOC or until failure using a 32 A current (recommended, but can be modified)
UL 2580 "Standard for Safety – Batteries for Use in Electric Vehicles" [40]	Imbalanced charging test – one module at 50% SOC, other modules at 0% SOC. The charging process is carried out according to manufacturer's recommendations
GB/T 31485-2015 National Standard of the People's Republic of China "Safety Requirements and Test Methods for Traction Battery of Electric Vehicle" [43]	Charging using a current of 1 C-rate until the cell voltage reaches 1.5 time the manufacturer's end-of-charge voltage or for one hour
Korea MVSS 18-3 "Driving Battery Safety Test" [11]	Charging to 1.5 times the nominal voltage or until 150% SOC using a 32 A current
India AIS-048 "Battery Operated Vehicles – Safety Requirements of Traction Batteries" [11]	Charging using a current of 0.1 C until 200% SOC or for 10 hours

5.4.2 Mechanism of Failure during Overcharge

When a cell is being overcharged, its cathode becomes over-delthiated while its anode becomes over-lithiated, this results in a series of side reactions [127], [130].These lead to irreversible structural changes of the cathode and the decomposition of its active materials as exemplified by Equation 5-1 for LMO cathode material. The resistance of the cathode also increases. Significant amount of heat can be produced due to Ohmic heating and due to the oxidation of the electrolyte by the oxygen produced from the decomposition of the cathode, gases are also produced. On the anode side the over-lithiation causes solid metallic lithium to be deposited on its surface as given by

Equation 5-2. This deposited lithium can exothermally react with the electrolyte. The heat generated can initiate the self-heating of the cell which might make it reach the point of no return – thermal runaway. The deposition of lithium might also form dendrites that can puncture the separator causing an internal short circuit [128]. The cell might also be equipped with a shutdown separator, which shuts down as a result of the increase in temperature and stops current flow [136]. It should be noted that the mechanism of failure of the cell depends on a number of factors such as the chemistry of the electrodes, the cathode-to anode ratio and the thermal dissipation efficiency of the cell [137]. Figure 5-1 summarises the probable stages of failure that can lead to thermal runaway during overcharge.

$$MnO_2 \rightarrow \frac{1}{2} Mn_2O_3 + \frac{1}{4} O_2(gas)$$

Equation 5-1: Decomposition reaction of LMO cathode during overcharge [138]

$$Li^+ + e^- \rightarrow Li\ (solid)$$

Equation 5-2: Primary side reaction producing lithium metal during overcharge [53]

Stage 1	• Cathode over-delithiation and anode over-lithiation (lithium deposited on its surface) • Cathode resistance increases and oxygen is produced due to its decomposition • Cell voltage and temperature increase
Stage 2	• Cell impedance increases as a result of cathode resistance increase • Cell temperature rises further as a result of increased ohmic heating and heat of electrolyte decomposition
Stage 3	• The cell temperature rises faster as a result of the exothermic reactions between the delithiated cathode and the electrolyte • Gases are produced
Stage 4	• If the cell is equiped with a shutdown separator that manages to shut down before the point of no return, the charging current is stopped and the cell cools down. • If the cell is not equipped with a shutdown separator or the separator fails to shut down before the point of no return, the temperature will sharply rise leading to the violent reaction between the over-lithiated anode and electrolyte. This will probably cause thermal runaway and cell rupture and or fire.

Figure 5-1: Stages leading to thermal runaway during the overcharge of a Li-ion cell

5.4.3 Effect of Cathode Chemistry on the Overcharge Response

The active materials of the cell especially its cathode chemistry define its cost, performance and most importantly its safety. The choice of the cathode chemistry largely determines the thermal stability [138], tolerance to abuse [139] and the thermal response of Li-ion cells during overcharge [27]. There are a wide range of cathode chemistries such as Lithium Cobalt Oxide ($LiCoO_2$ or LCO), Lithium Manganese Oxide ($LiMn_2O_4$ or LMO), Lithium Nickel Manganese Cobalt Oxide ($LiNiMnCoO_2$ or NMC) and Lithium Iron Phosphate ($LiFePO_4$ or LFP). Cathodes can also be a mix/blend of two chemistries to improve their characteristics. This report is going to focus on LMO and NMC chemistries, since the cell used in testing has an LMO-NMC cathode. Moreover, the LMO-NMC blend is used in many electric vehicles, such as Chevrolet Volt, Nissan Leaf and BMW i3.

LMO has a three-dimensional spinel structure that improves the ion flow. This results in the advantages of LMO of having low resistance and improved current handling capacities (high power). Moreover, spinel structures have a relatively high thermal stability and enhanced safety [140]. LMO is more tolerant to electrical and thermal abuse than other chemistries such as LCO and LNO as shown in Figure 2-6. When heated at 1 °C/min, the reduction (oxygen loss) began at 200 °C for the LNO, 240 °C for the LCO and 385 °C for the LMO [53]. On the downside, LMO has limited cycle and calendar life [141].

NMC is one of the most successful cathode chemistries used in Li-ion cells. Its strength lies in combining nickel and manganese. Nickel has high specific energy, but poor stability, since Ni^{+4} is generated during charge and when reduced forms a resistive NiO film at the cathode surface leading to capacity fade [142]. Manganese has low internal resistance due to its spinel structure, but has low specific energy, hence combining them can strengthen their characteristics. LMO and NMC are blended to bring the best characteristics of both chemistries. The cathode material is LMO-NMC mix, it exhibits better safety property than NMC and higher energy density and prolonged life than LMO [80].

5.4.4 Cell Volume Increase and Its Mechanisms

During normal operation of Li-ion cells chemical reactions continuously occur. The products of these reactions can be solids, liquid, gases or a combination of these. This can result in either a change of volume in unconstrained cells or the exertion of force when the expansion is restricted [143]. During abnormal/abusive conditions the volume increase can be more significant. Cell swelling during overcharge was reported by a number of studies [112] [25]. Understanding how the volume of the cell changes is important for the safety and design of Li-ion cells and batteries. A number of mechanisms could account for this volume increase. This section presents these mechanisms.

5.4.4.1 Electrode expansion

The expansion and contraction of the electrodes happens during normal charge and discharge due to lithium ion movement between them (intercalation and de-intercalation) [144]. All intercalation compounds expand when lithium is inserted in them. This expansion is reversible as long as the lattice mismatch does not exceed a specific percentage of strain [62]. Studies show that the change in anode volume is higher than that of the cathode [145]. Hence the anode experiences higher stress levels than the cathode [146].

During normal cycling it is desirable to minimise the expansion and contraction of the electrode materials to minimise the increase in resistance, which can have a negative effect on the cycle life of the cell [137], [147]–[149]. Moreover, reducing electrode expansion reduces the stress difference generated at the inner/outer electrode (especially in wound cells). This can enhance the cell's performance and safety [150].

During overcharge both the cathode and the anode contribute to the volume increase. As the delithiation of the cathode continues, an anisotropic volume change occurs due to phase transition [130]. At high states of overcharge the anode thickness increases as a result of lithium metal plating and the deposition of decomposed electrolyte on its surface [151]. Gas generation during overcharge can also crack the SEI and hence increase its thickness [152]. Although it was reported that the contribution of the anode to the volume increase is much higher than the cathode's. A study of NMO cathode-carbon anode showed that the thickness of the cathode was increased by 1.65% when

the cell was overcharged from 100% to 180% SOC, while the thickness of the anode was increased by 21.95% [153].

5.4.4.2 Gas generation

The most significant component of volume increase during overcharge is gas generation. It has been reported that a number of gases mainly carbon dioxide (CO_2), carbon monoxide (CO), methane (CH_4), ethane (C_2H_6), ethylene (C_2H_4) and hydrogen (H_2) were produced during the overcharge process. Each stage of the overcharge process as presented in Section 5.4.2 is responsible for the production of specific gases. CO_2 and CO are generated by the oxidation of the electrolyte by the oxygen produced as a result of the decomposition of the over-delithiated cathode. H_2 is mainly produced as a result of the reduction of the electrolyte by the over-lithiated anode. The reactions at the anode also produce relatively small amounts of CH_4, C_2H_4, C_2H_6, CO and CO_2. Although usually CO_2 and H_2 are the main gases produced, it was reported that the composition of the gas generated was largely dependent on the cell temperature as a result of the ratio between heat generation and heat dissipation [129].

Cell design affects the failure mode as a result of gas generation. Cells with hard casing such as cylindrical cells usually do not experience significant increase in their volume, and their internal pressure increases as a result of gas generation. Pressure build-up can cause cell to explode or vent if they are designed to do so when their internal pressure reaches a specific level. Cell designs with softer casing such as prismatic and pouch cells usually swell as a result of gas generation. In a battery pack this increase in volume can induce mechanical stresses on the surrounding battery pack components. Pouch cells are also usually designed to vent in the case of pressure build-up. Although cell venting might be classified as a safe event on a cell level, venting of flammable gases triggered in a battery pack coinciding with an electric spark can ignite the gases and lead to a fire [34]

5.4.5 Methods of Cell Volume Measurement

There are a number of methods that can be used to measure/detect the changes in cell volume. The first method is by measuring the external dimensions of the cell. Measurement of the external dimensions of the aluminium can of prismatic cells to monitor the change in volume during overcharged was done by a number of studies.

This can give an indication of when electrolyte decomposition and gas generation happen. However, this method does not offer a precise measurement of the cell volume.

The second method is to use a gas syringe. During overcharge gas evolution is the largest component of volume increase. The volume of gas evolved can be measured by collecting it with a gas syringe [154]. In this method gas is withdrawn from the cell to measure its volume. This means that the volume cannot be measured in-situ on preserved cells under operation. Moreover, the gas volume might be changed during the measurement process.

The operation of other methods, such as, water drainage or loads cell is based on the Archimedes' principle. During the water drainage method the cell is submerged into a beaker filled with deionised water. The weight change of the beaker for different cell SOCs is monitored by a high precision balance [153]. The load cell method involves hanging the cell from a load cell while being fully submerged in silicone oil. The change in cell volume can be detected by the load cell. This method proved to be simple and robust [155]. In both methods the change in cell volume is calculated according to the Archimedes' Principle (explained in Section 5.5.1.1).

5.4.6 Business Context of Cell Swelling

In a business context minimising the swelling of pouch Li-ion pouch cells is crucial for their successful application. Excessive cell swelling can cost a company huge amounts of money and affect its reputation. An example for battery recalls due to excessive swelling is Samsung Galaxy S4. Users complained of swelling to the point that their phones did not lie flat. Samsung declared that they were aware of the issue and offered a trade-in programme on their batteries [156].

5.5 Experimental Design and Methodology

5.5.1 Equipment and Materials Used and Test Set-up

5.5.1.1 Theory

An apparatus was built to monitor and measure the change in volume of the pouch cells as a function of time in-situ during the overcharge regime. It relies on the

Archimedes' principle for its operation. The weight of the cell submerged in silicone oil was measured to a very high accuracy using a load cell. The change in the volume of the cell was calculated as follows; the relationship between the buoyant force on a submerged object and its volume is given by the Archimedes' Principle. The buoyant force (F_b) is equal to the weight of the fluid displace by the submerged object:

$$F_b = \rho g V \qquad \textit{Equation 5-3}$$

Where ρ is the density of the fluid, g is the gravitational acceleration and V is the volume of the submerged object.

Figure 5-2 shows the forces acting on the submerged cell. The weight (W) of the cell acting downwards, while the buoyant force (F_b) and the tension (T) in the string are acting upwards. During equilibrium the forces are expressed as:

$$T + F_b = W \qquad \textit{Equation 5-4}$$

As the volume of the cell changes, the buoyant force changes. Since the weight of the cell is constant, for the cell to stay in equilibrium, the tension must change to match the change in the buoyant force. Therefore:

$$\Delta T = -\Delta F_b = -\rho g \Delta V \qquad \textit{Equation 5-5}$$

Since the cell is hanging from the load cell, the change in tension can be accurately measured and the cell volume change can be calculated.

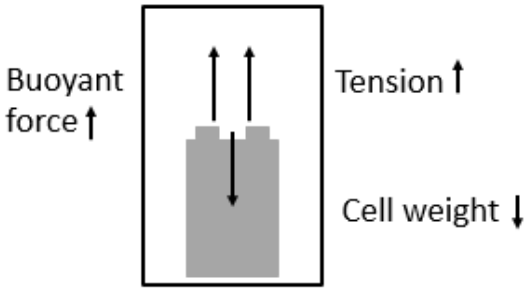

Figure 5-2: Free body diagram of the submerged pouch cell hanging from the load cell

5.5.1.2 Equipment and Set-up

In order to make the ΔF_b measurement required in Equation 5-5, highly sensitive 600 g load cells made by VPG Transducers were used. The data sheet of the load cells is in the Appendix Section (C). The calibration of the load cells was carried out using weights and a high precision scale. The calibration curves of the load cells are shown in Figure 5-3. It can be noticed that the change in their voltage output is linear with the force applied.

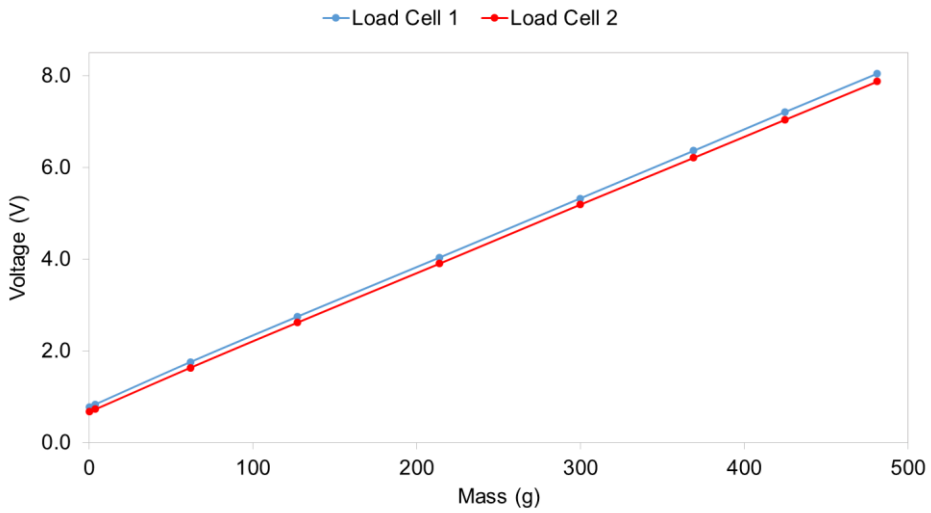

Figure 5-3: Calibration curves of load cells used

Figure 5-4 shows the components and the electrical connections of the set-up. A 12 V power supply was used to power the load cells. Voltage output signal was sent from load cell in response to the changes in the volume of the pouch cell. The signal output from the load cell was amplified using a purpose-built voltage amplifier before being connected to the auxiliary input of the same cycler channels used to cycle the cell, this means that both the cycling data and the load cell data were synchronised. The temperature of the cell surface and the oil were monitored and recorded every 30 seconds using a T-Type thermocouples and a PicoLog TC-08 thermocouple data logger. All data was recorded to a desktop computer.

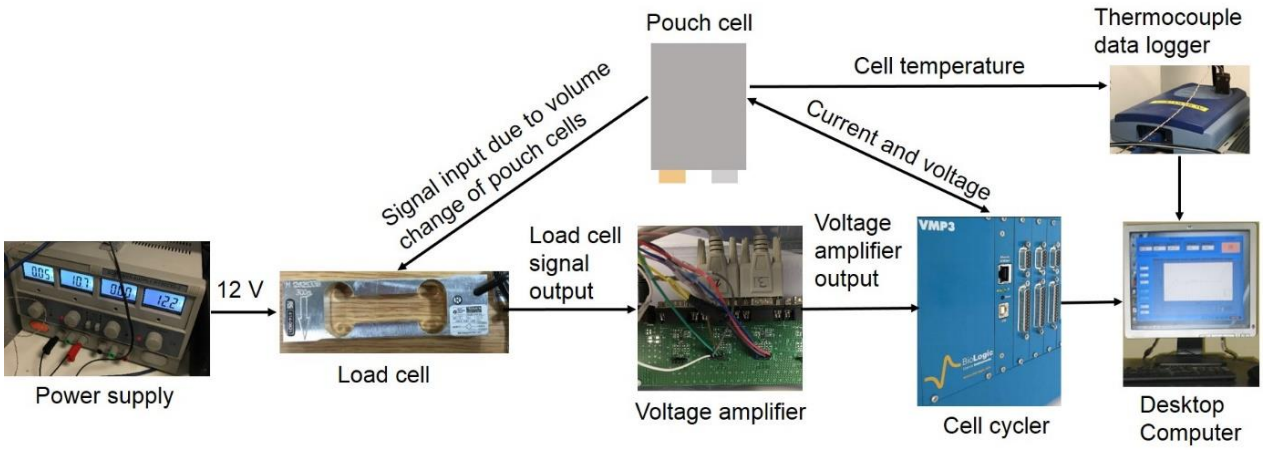

Figure 5-4: Components and electrical connections of the in-situ cell volume measurement set-up

5.5.1.3 Volume Measurement Apparatus and Test Set-up

Figure 5-5 shows a photograph of the apparatus inside a thermal chamber. The apparatus was designed with two channels to run two tests in parallel. Two load cells were fixed to a plastic plate. The plastic plate was supported by a foam base to act as a shock absorber, in order to minimise vibration noise in the load cell reading. Each pouch cell was hung from the load cell using two connection points to ensure its stability. The connection between the load cell and the pouch cell was a polyester thread with a ring on one end and a hook on the other end. As shown in Figure 5-6, two small holes, approximately 3 mm in diameter, were punctured in the top corners of the pouch casing, above the seal of the cell to ensure that the cell stayed intact. A plastic bar with two points of attachment was fixed to the load cell. The hooks were then attached to the pouch cell and the rings to the plastic bar attached load cell. The use of such mechanical attachment allowed for easy changing of cells between tests.

The electrical connections to the cell consisted of current carrying wires and fine voltage sense wires. Two 4 mm sockets, along with the voltage wire were soldered to the cell tabs as shown in Figure 5-6. The purpose of these sockets is to connect current carrying wires between the cell and the Bio-Logic VMP3 electrochemical cycler. The current carrying wires between the cell and the cycler were coiled to allow for the free movement of the cell and minimise any undesired influence on the load cell reading. A thermocouple was attached to the surface of the cell before being immersed in the silicone oil and another one dipped in the oil inside the container. Silicone oil was used due to its properties; electrically insulating, thermally stable and has low vapour

pressure. The data sheet of the silicone oil used can be found in the Appendix Section (D).

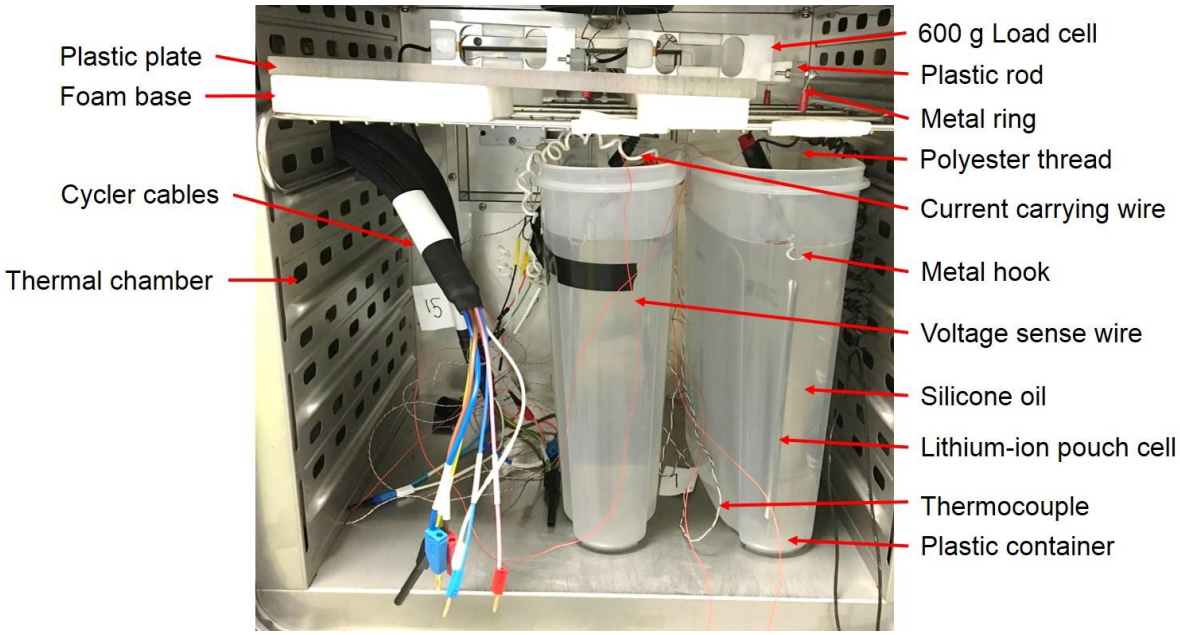

Figure 5-5: A photograph of the in-situ cell volume measurement apparatus and set-up

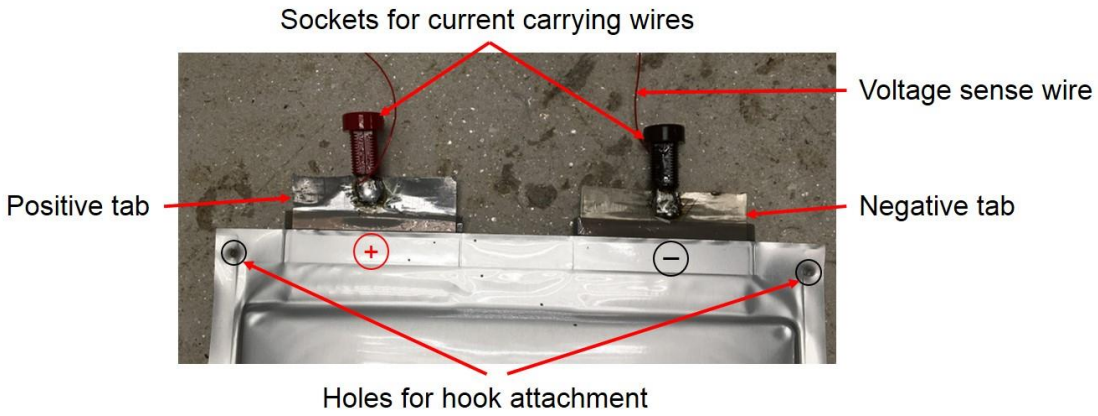

Figure 5-6: Pouch cell electrical connections and mechanical attachment points

5.5.2 Measurement Accuracy

As described in Section 5.5.1.3 the load cells were put on a foam base to minimise vibration noise. Moreover, the whole apparatus was inside a thermal chamber to minimise the effect of air currents on the readings. All tests were also started with a two-hour rest step to allow for the set-up to stabilise. Figure 5-7 shows the base volume change measurement with the cell submerged in the oil, as an indication of the noise level in the volume measurement. The base volume measurement fluctuates between ± 0.5 cm^3. This is equivalent to a noise level of 0.998 cm^3 for an average cell

volume of 173.706 cm^3. The signal-to-noise ratio (SNR) value depends on the magnitude of the measured signal. During charging the cell from 3.8 V to 4.2 V, its volume increased by 0.2% (0.347 cm^3), as shown in Figure 5-11. This is equivalent to a SNR of 0.348 (0.347/0.998). However, it should be noted that the noise fluctuates in both direction. The average noise level is 0.0140 cm^3 as shown in Figure 5-7. Recalculating the SNR using the average noise level gives a SNR of 24.85 (0.347/0.0140). The noise level can be minimised by reducing the level of vibration the load cell is exposed to. For example, putting the set-up in a less vibrating thermal chamber and reducing the air flow in the thermal chamber further.

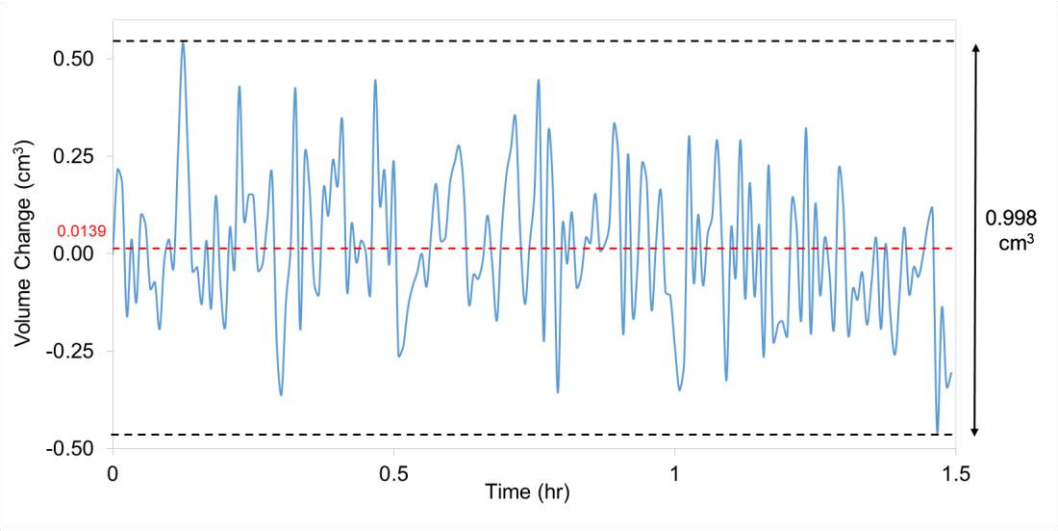

Figure 5-7: Measurement noise level in terms of volume change as a function of time (average noise level shown in red)

5.5.3 Experimental Procedure

The experimental procedure followed was as shown in Figure 5-8. The following sections describe each of its stages.

Figure 5-8: Sequence of experimental procedure stages

5.5.3.1 Pre-testing cell performance check

These tests were conducted on the cells before the overcharge test regime to ensure that their capacity and internal resistance values were sound. The same pre-testing regime as Section 4.5.2.1 was followed.

5.5.3.2 The overcharge regime and volume measurement

During the overcharge test cells were overcharged to different degrees of overcharge/voltage levels. Three different C-rates were also used. Table 5-2 summarises the experiments. The voltage, current, temperature and change in volume of the cell submerged in the silicone oil were monitored and measured using a Bio-logic VMP3 cycler.

Table 5-2: Summary of overcharge experiments

Experiment No.	Charging Current (A)	Terminal Voltage (V)
1	2	4.8
3	2	5.0
5	2	5.2
6	5	5.2
7	10	5.2

The overcharge regime consisted of two pre-overcharge cycles, EIS, overcharge, 10 post-overcharge cycles, then finally EIS. Figure 5-9 summaries the stages of the overcharge regime. Screenshots of the overcharge regime software settings are shown in Section (E) of the Appendix. To study the reversibility of gas generation, the overcharge scenario that produced that highest volume increase was repeated, but as shown in Figure 5-10, the cells were rested after the overcharge event and their volume was monitored. The aim of this was to investigate the effect of both cycling and resting the cell after an overcharge event would have on the reversibility of its volume. The cells after that were moved to the Maccor cycler to perform 150 cycles as explained in Section 4.5.2.3.

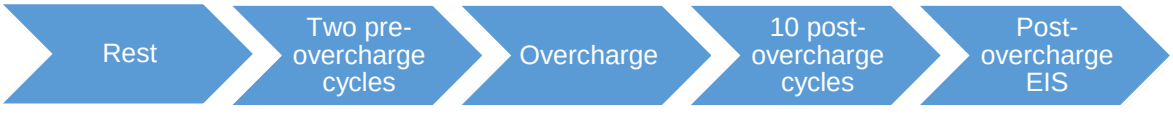

Figure 5-9: Stages of the overcharge regime with post-overcharge cycling

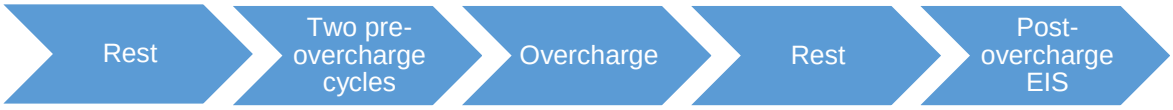

Figure 5-10: Stages of the overcharge regime with no post-overcharge cycling

5.5.3.3 Cycling after overcharge

After the overcharge regime described in section 4.5.2.2, full charge/discharge cycles were conducted on the cells to investigate their post-overcharge behaviour. The cycling regime in section 4.5.2.3 was followed.

5.5.3.4 Electrochemical Impedance Spectroscopy after Cycling

EIS measurements were performed on the cell after the overcharge regime to investigate the change in internal resistance as a result of cycling after the overcharge event. The same EIS settings as in Section 4.5.2.1 were used.

5.6 Results and Discussion

5.6.1 Volume Change during Normal Cycling

As explained in Section 5.4.4.1 during cycling the cell experiences volume change mainly due to the expansion and contraction of its electrodes during charge and discharge. Figure 5-11 shows the change in cell volume and voltage. The reference cell volume was taken at 3.8 V. It can be seen that the cell volume increases by about 0.4% when charged to 4.2 V and decreases by about the same amount when discharged.

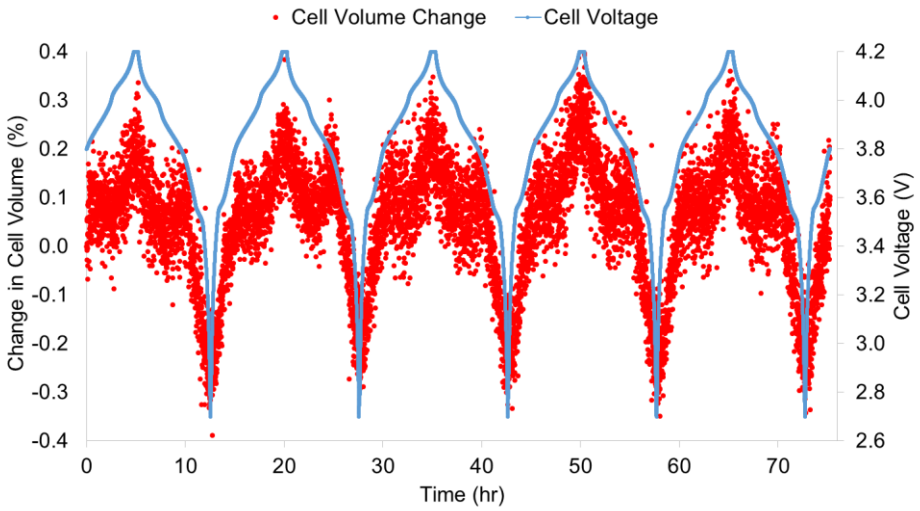

Figure 5-11: Cell volume change and voltage during normal cycling

5.6.2 Effect of Degree of Overcharge

This section presents and discusses the impact of the degree of overcharge on the volume change of the cells, their capacity fade behaviour and change in internal resistance.

5.6.2.1 Volume change and cycling behaviour of cells overcharged to different terminal SOC

Using a current of 2 A, the first group of cells were charged to three different SOCs; 132%, 140% and153%, corresponding to 4.8 V, 5.0 V and 5.2 V respectively. The in-situ change in cell volume as a function of cell voltage and its corresponding cell SOC in the overcharged state are shown in Figure 5-12. During the overcharge process the cell volume increased as its SOC increased. From the gradient of the volume change profile it can be noted that there was a change in gradient around 4.6 V marking the initiation of noticeable gas generation. However, the cell started to swell significantly after 140% SOC at the second change in voltage profile gradient at around 5.0 V. The maximum volume increase during overcharged was 85%. This agrees with previous differential electrochemical mass spectroscopy (DEMS) studies on cells with LMO cathode that showed that evolution started around 4.8 V [157].

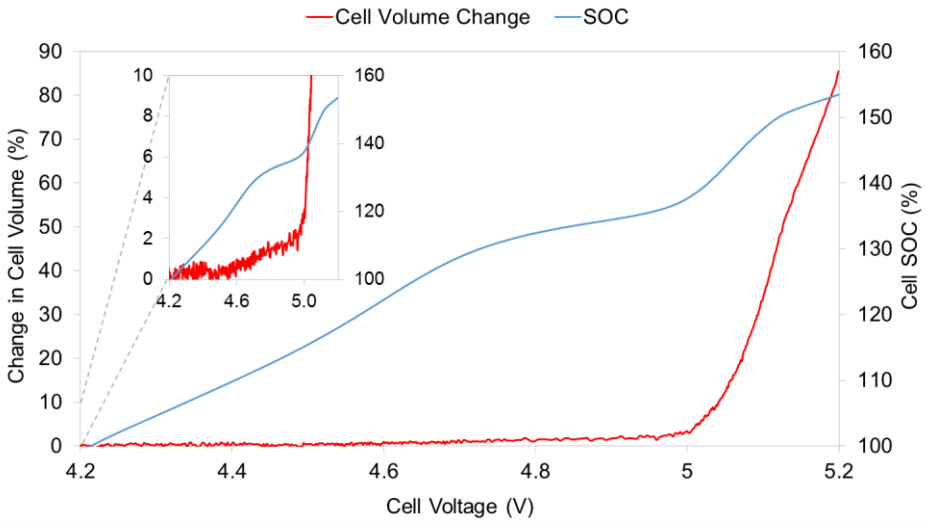

Figure 5-12: Change in cell volume and SOC as a function of cell voltage during overcharge using 2 A current

Figure 5-13 shows the in-situ change in cell volume and the cycling behaviour of all cells before, during and after the overcharge event. While monitoring their volume, all cells were cycled between 2.7 V (0% SOC) and 4.2 V (100% SOC) using a 2 A current before being overcharged, cells were then charged to different degrees of overcharge, then cycled again for 10 full cycles after the overcharge event. Cells charged to 4.8 V showed the least maximum increase in cell volume (4%), followed by those charged to 5.0 V (12%). Cells charged to 5.2 V experienced much more significant volume increase (102%). This can be attributed to gas generation as a result of electrolyte oxidation [80]. It should be noted that the increase in cell volume continued after the current was reversed and the cell was being discharged. The volume reaches a peak then starts to decrease again. The reversibility of volume increase is discussed in more detail in Section 5.6.5.

Figure 5-13 shows that the voltage profiles of all cells overlap before the overcharge event, i.e. they take the same time to complete a full charge-discharge cycle. After the overcharge event the voltage profiles of the cells become out of phase. Cells that experienced a higher degree of overcharge take less time to complete a full charge-discharge cycle. It took the cell charged to 5.2 V 113.9 hours to complete 10 cycles, whereas, it took the cell charged to 4.8 V 149.3 hours to complete the same number of cycles. This can be attributed to the extent of damage done to the cells. Cells charged to a higher degree of overcharge suffer more damage which result in a

reduced capacity. The effect of the degree of overcharge on the cell's capacity and internal resistance is discussed in the following sections. Table 5-3 summaries the findings of charging the cells to different states of overcharge.

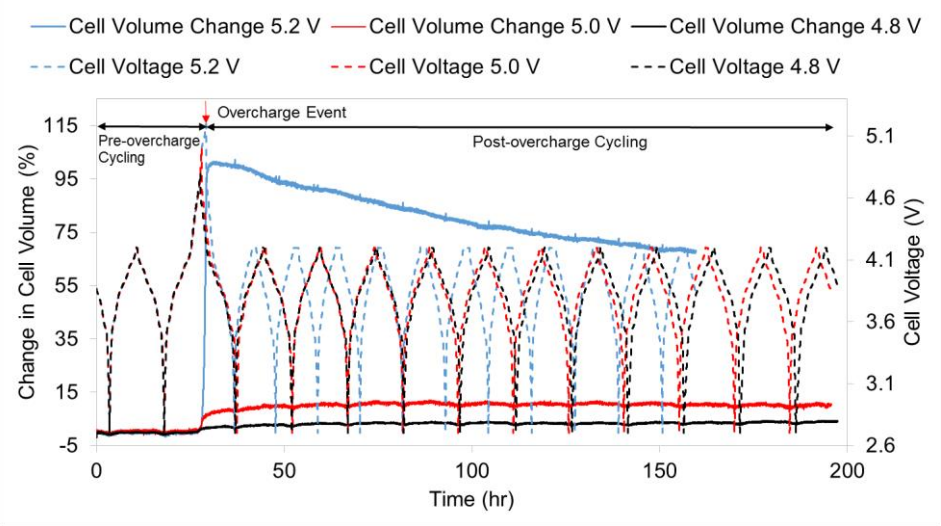

Figure 5-13: In-situ cell volume change and cycling behaviour before and after an overcharge event for different degrees of overcharge

Table 5-3: Summary of findings of cells charged to different degrees of overcharge

Terminal Voltage (V)	Terminal SOC (%)	Maximum Volume Increase (%)	Time to Complete 10 Cycles after the Overcharge Event
4.8	132	4	149.3
5.0	140	12	147.3
5.2	153	102	113.9

5.6.2.2 Capacity degradation behaviour of cells overcharged to different terminal SOC

The normalised charge and discharge capacities of the cells before, during and after the overcharge event are shown in Figure 5-14. The capacity of each cell was normalised to the initial pre-overcharge capacity obtained during cycle 1. The variation in the initial capacity of all cells was less than ± 2.5%, as presented in Section 3.5.1. Cycle 2 is the overcharge event cycle. During the charge part of this overcharge cycle, cells charged to 5.2 V, 5.0 V, and 4.8 V gained 1.535, 1.370 and 1.323 times their initial capacity respectively. During the discharge part of the overcharge cycle only 1.06 times the initial capacity was discharged from the cell charged to 5.2 V, whereas 1.31 and 1.30 times from the cells charged to 5.0 V and 4.8 V respectively. This shows

that although more energy was put into the cells charged to a higher state of charge, less energy was recovered from them. This can be attributed to energy lost as heat and in side chemical reactions producing products, such as gas. The percentage of energy recovered from the cells charged to different SOCs is shown in Table 5-4.

During cycle 3, the first cycle after the overcharge event, the gap between the charge and discharge capacities was reduced. Cells charged to 5.2 V and 5.0 V showed capacity fade. However, their discharge capacities were larger than their charge capacities, this continued for the 10 cycles after the overcharge, although the gap between them was reduced as the cells were cycled. Surprisingly cells charged to 4.8 V did not show any degradation in capacity, their capacity slightly increased on the contrary. The normalised charge and discharge capacities of cycle 3 were 1.017 and 1.106 respectively, after 10 more cycles they dropped to 1.010 and 1.009. It seems that it takes the cell several cycles for the overcharge influence to be reduced. Table 5-4 summarises the findings.

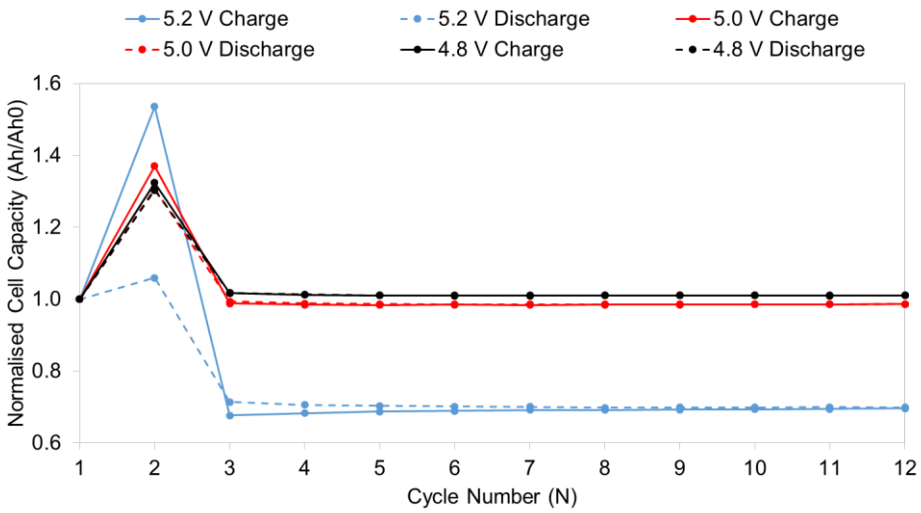

Figure 5-14: Normalised cell charge and discharge capacities before, during and after the overcharge event for cells charged to different degrees of overcharge

Table 5-4: Summary of capacity behaviour of cells charged to different degrees of overcharge

Terminal Voltage (V)	4.8	5.0	5.2
Terminal SOC (%)	132	140	153
Normalised Charge Capacity of Cycle 2 (Overcharge)	1.323	1.370	1.535
Normalised Discharge Capacity of Cycle 2	1.303	1.308	1.059

Energy efficiency of Cycle 2 (%)	98.48	95.47	68.99
Normalised Charge Capacity of Cycle 3 (Post-overcharge)	1.017	0.988	0.676
Normalised Discharge Capacity of Cycle 3	1.016	0.993	0.714
Normalised Charge Capacity of Cycle 12	1.010	0.986	0.696
Normalised Discharge Capacity of Cycle 12	1.009	0.986	0.698

It was shown previously by X-ray Diffraction (XRD) reflection patterns that the structure of the electrodes changes as a result of overcharge. The removal of lithium from the cathode changes its structure. Moreover, further overcharge results in the breakdown of the crystalline structure of the cathode, which is caused by the reaction between the oxidised cathode and the electrolyte [129]. In-situ neutron power diffraction (NPD) measurements show that overcharge causes phase change of carbon anodes [158]. Incremental capacity analysis (ICA) can be used to investigate capacity fade. IC curves can show changes in the electrochemical behaviour of the cell caused by phase transformations of its active materials, they can also be used to give an indication of the aging mechanisms [55], [159]–[161].

The IC curves of the pre-overcharge cycle (Cycle 1 in Figure 5-14) of cells charged to different degrees of overcharge are shown in Figure 5-15. During charge, 3 major peaks denoted as A, C, and D were observed. A minor peak denoted as B was also observed. During discharge, three peaks E, F and G were observed. It can also be noticed that the IC curves for all the tested cells overlap. The peaks represent the IC signature of phase transition of cells with LMO-NMC cathode and carbon anodes [80]. The IC peak A represents the phase transition of C_6 (graphite) to $Li_{(1-x)}C_6$, whereas peaks C and D represent two phase transitions of NMC and LMO [162]. Peaks E, F and G represent the reversed phase transformations during discharge.

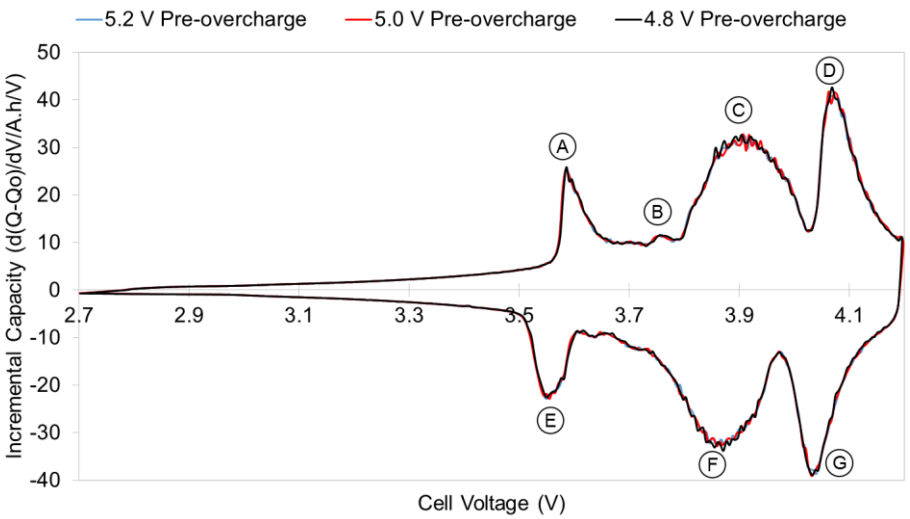

Figure 5-15: IC curves of the pre-overcharge cycle of cells charged to different degrees of overcharge

Figure 5-16 shows the IC curves of the pre-overcharge cycle, overcharge cycle, first cycle after overcharge and tenth cycle after overcharge for the cell charged to 5.2 V, these IC curves are for cycles, 1, 2, 3 and 12 respectively in Figure 5-14. During the charge part of the overcharge cycle the two new peaks; H and I were formed. During the discharge part, two new peaks; J and K were formed. It can be noticed that peaks J and K had smaller size than peaks H and I. This means that peaks H and I represent irreversible phase transformations due to crystal structure changes of NMC and/or LMO.

During the first cycle after the overcharge all the pre-overcharge charge and discharge peaks were reduced and shifted to the left and peak B almost disappeared. It can also be noted that during discharge the IC curve shifted to a lower voltage range. The appearance of new peaks and/or the disappearance of existing ones can be an indication of chemistry change, i.e. existing compounds are broken and/or new ones are formed. The change in the shape of the peaks can be an indication for LLI and LAM. And the shift of the IC curve which indicates a rise in the internal resistance of the cell/higher polarisation and hence reducing the capacity of the cell [159]. Figure 5-17 shows the increase in volume and the incremental capacity as a function of cell voltage. It shows that the new peak H corresponds to the starting point of obvious cell volume increase and peak I corresponds to the swelling of the cell as a result of gas generation.

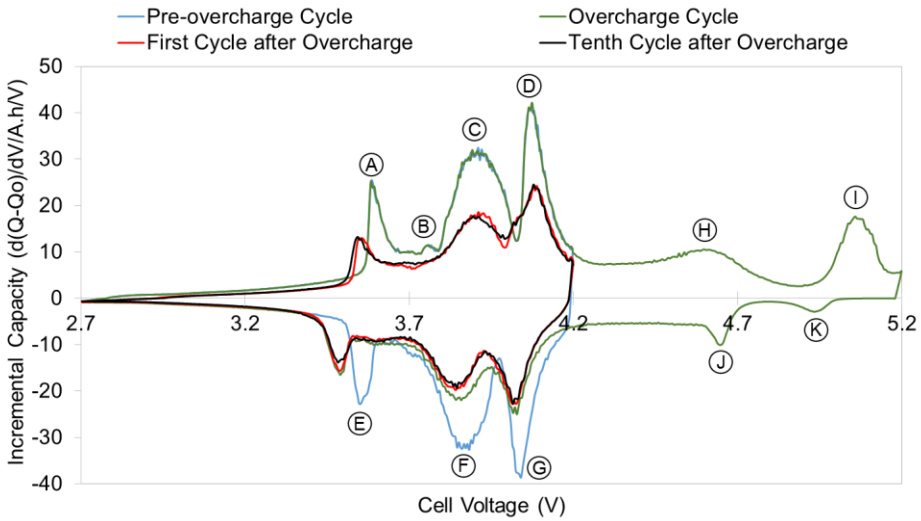

Figure 5-16: IC curves of the pre-overcharge cycle, overcharge cycle, first cycle after overcharge and tenth cycle after overcharge for the cell charged to 5.2 V

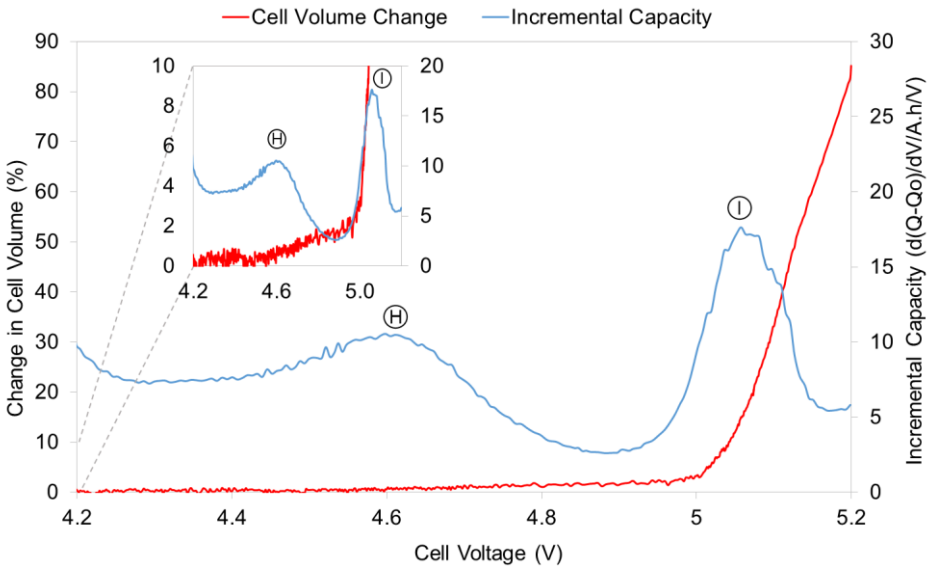

Figure 5-17: Cell volume increase and incremental capacity as a function of cell voltage

The IC curves of all cells before and during the overcharge cycle are shown in Figure 5-18. In terms of new peak formation; all cells developed peak H. Only the cell charged to 5.2 V developed Peak I. However, it can be noticed that the cell charged to 5.0 V started peak I, but was cut short. On the discharge part, only the cell charged to 5.2 V developed Peak K. Although all cells developed peak J, the voltage at which it was formed and shape were different.

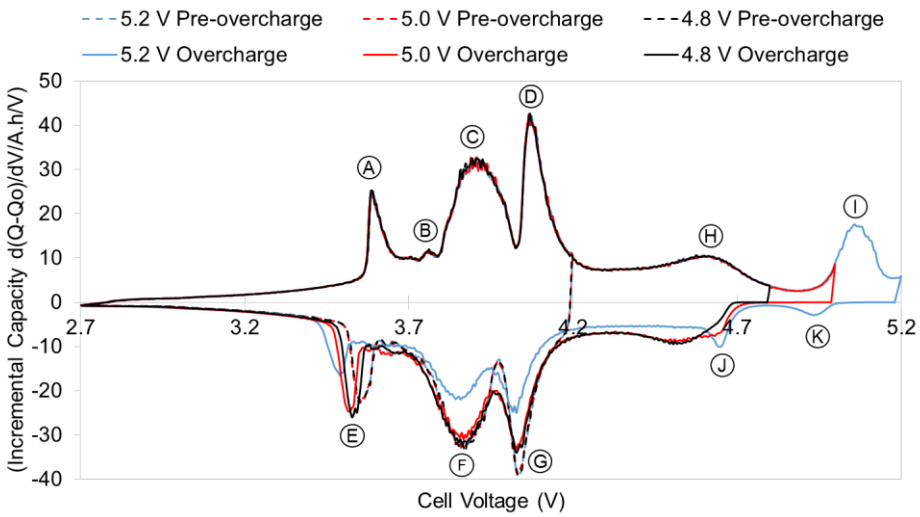

Figure 5-18: IC curves of the overcharge cycle of cells charged to different voltages

The IC curves of the first cycle after the overcharge event of the cells charged to different degrees of overcharge is shown in Figure 5-19. It can be seen that cells charged to higher voltage suffered more damage. The IC curves of all overcharged cells shifted to a lower voltage compared to their pre-overcharge state. However, the cell charged to 5.2 V experienced the highest peak reduction indicating significant capacity loss.

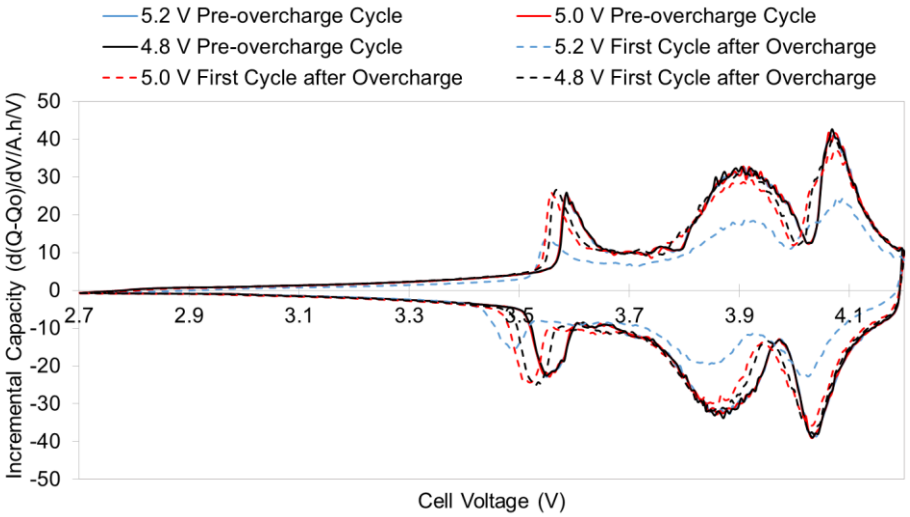

Figure 5-19: IC curves of first cycle after overcharge of cells charged to different voltages

5.6.2.3 Electrochemical impedance spectroscopy of cells overcharged to different terminal SOC

The impedance of the cell can be characterised by two methods as presented in the methodology section. This section presents and discusses the results from the EIS measurements of cells charged to different degrees of overcharge.

5.6.2.3.1 Nyquist plots

EIS measurements were performed on cells overcharged to different voltages before and after the overcharge event, and after cells were cycled for 155 cycles. Based on these EIS measurement Nyquist plots were plotted to investigate the change in the components contributing to the cell's internal impedance. Figure 5-20 shows Nyquist plot for one of the cells before the overcharge event. As annotated on the figure, the high frequency range (KHz) represents the inductive behaviour attributed to the porous structure of the cell electrodes [117], the point of intersection between the curve and the x-axis (real component) represents the cell's series resistance (R_{Ω}). The charge transfer resistance (R_{ct}) is represented by the semi-circle at the medium frequency region (Hz). The diffusion effect of Lithium ions can be described by the slope of the line in the low frequency region (mHz) [118]–[120].Since the inductance depends on the porosity of the electrodes, it should remain constant as long as the electrodes were not mechanically damaged [121]. Therefore, the inductive tail can be excluded from the EIS analysis [117].

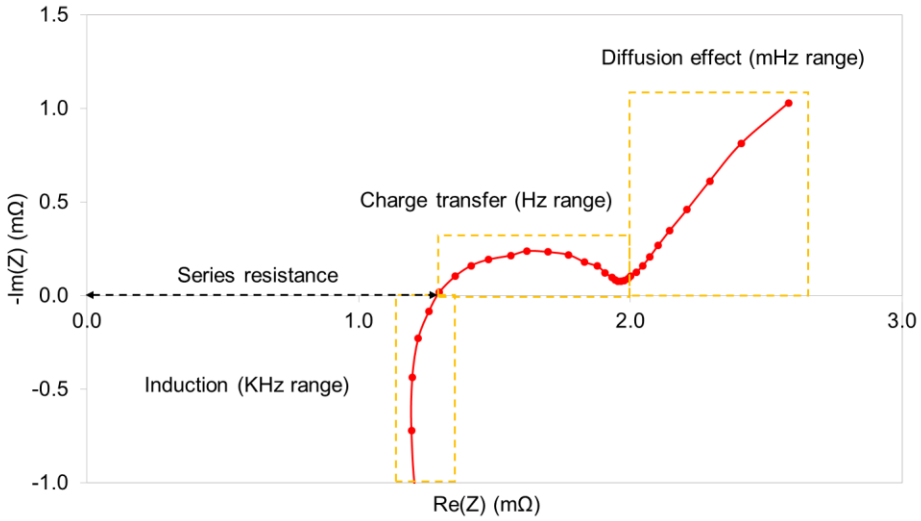

Figure 5-20: Pre-overcharge Nyquist Plot showing the components contributing to the cell's impedance

Figure 5-21 a, b and c show the EIS measurements before and after the overcharge event and after the post-overcharge cycling for cells charged to 4.8 V, 5.0 V and 5.2 V respectively. The EIS profiles of all cells moved to the right, the semi-circle at the medium frequency range increased in size and was more depressed and the line at the low frequency range increased in length and its angle with the vertical axis increased. These changes suggest increases in the series resistance, charge transfer resistance and the diffusion resistance respectively. As Figure 5-22 shows the extent of these changes depended on the extent of overcharge, cells charged to higher voltages experienced more pronounced changes. Cycling the cells after the overcharge event further increase the impedance of all cells as Figure 5-23 shows. Figure 5-24 combines all the previous plots, it shows the EIS data before overcharge, post-overcharge and after post-overcharge cycling for cells charged to different voltages/SOC.

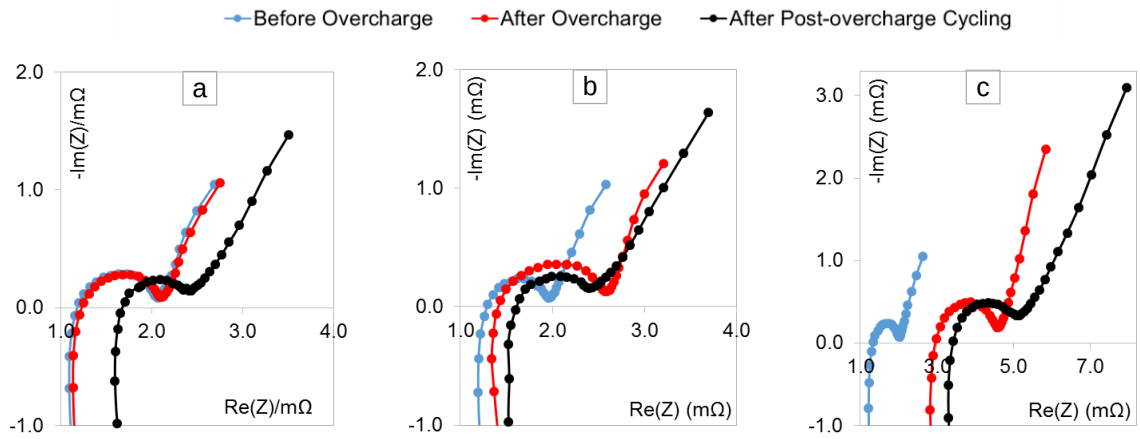

Figure 5-21: EIS measurements before overcharge, after overcharge and after post-overcharge cycling of cell charged to a) 4.8 V b) 5.0 V c) 5.2 V

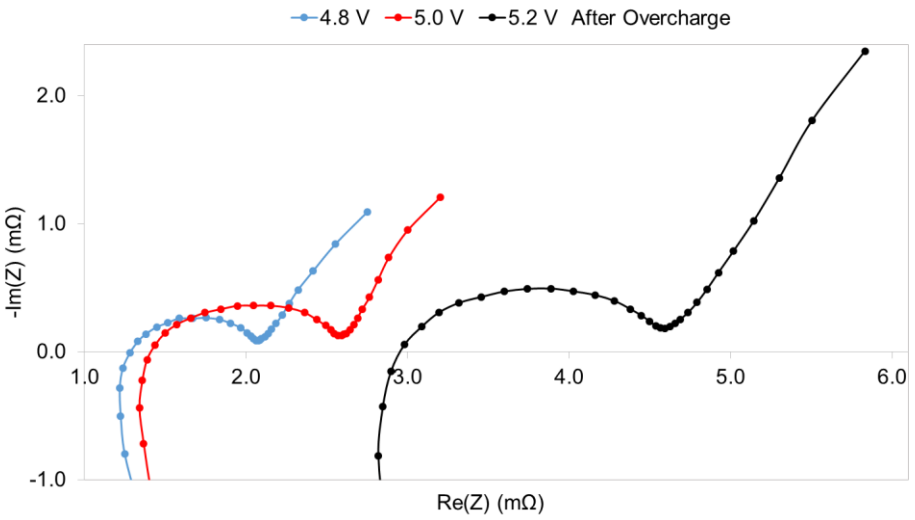

Figure 5-22: EIS measurements of cells charged to different voltages/SOCs after the overcharge event

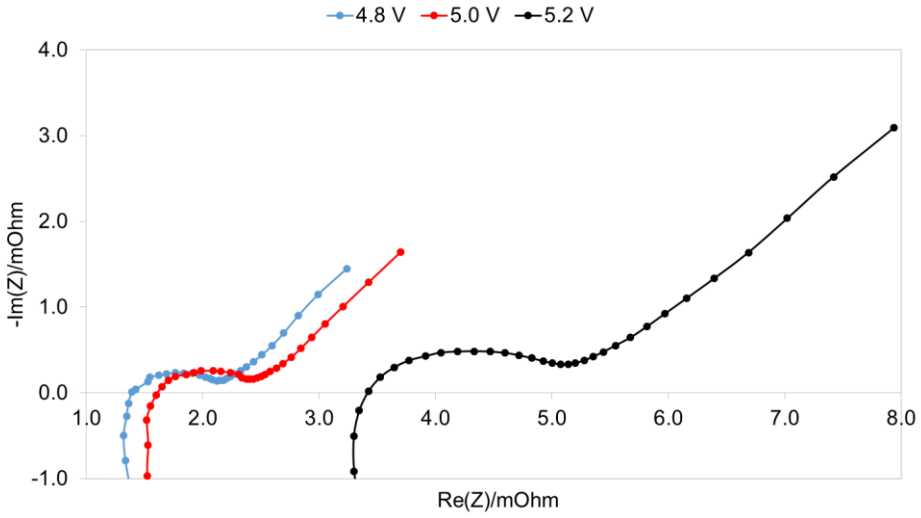

Figure 5-23: EIS measurements of cells charged to different voltages/SOCs after the post-overcharge cycling

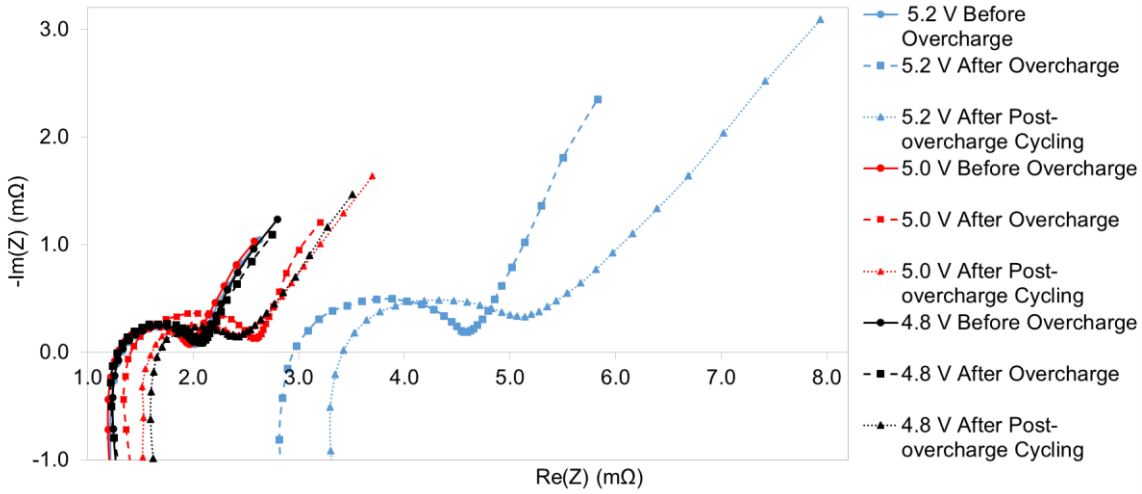

Figure 5-24: EIS data before overcharge, after overcharge and after post-overcharge cycling for cells charged to different voltages/SOC

5.6.2.3.2 Equivalent circuit modelling and impedance components

The excitation of the cell by a low amplitude signal results in an out-of-phase output. This is due to the presence of capacitive and inductive components in the cell. The measured impedance output comprises the resistive and reactive components, which can be represented by an equivalent electric circuit [163], [164]. Equivalent circuit (EC) models are implemented to model the impedance spectrum measured by the EIS. Choosing and implementing the right model can enable the determination of the components contribution to the cells impedance, mainly, the series resistance, charge transfer resistance and diffusion coefficient [165], [166].

Figure 5-25 shows the EC model built to represent the impedance components of the cell. The model is composed of the following components:

- Series resistance (R_s): represents the Ohmic resistance of electrolyte, active materials, separator, current collectors, internal connectors and cell terminals [163]
- Resistance (R_{ct}): represents double layer capacitance and the charge transfer resistance at the electrodes, it can also be used to describe the activation polarisation [121]
- Constant phase element (CPE): placed in parallel with R_{ct} instead of a capacitor to compensate for non-homogeneity in the system, such as, surface roughness or non-uniform porosity. This non-homogeneity causes the semi-circle

representing the charge transfer resistance to be depressed. The CPE can identically act as a capacitor, but when put in parallel with a resistance better represents a real system since a depressed semi-circle (cole-element) is produced [167]

- Warburg element (W_o): represents the diffusion impedance caused by the diffusion of the ions in the active material of the electrodes [168].

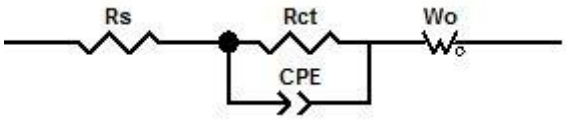

Figure 5-25: Equivalent circuit model of Li-ion cell

Z-View Software was used for modelling and simulation. Figure 5-26 shows the Nyquist plots of the actual EIS measurement data and simulation using the equivalent circuit model. Chi-squared and the weighted sum of squares give an indication of how good the fit is. Chi-squared is the square of the standard deviation between the experimental data and the simulation output. The value of Chi-squared for all the simulations was between 0.000608 and 0.001942. The weighted sum of squares is proportional to the average percentage error between the experimental data and the simulated data, its value was between 0.029773 and 0.095148. Both values show how accurate the equivalent circuit model is. Section (F) of the Appendix includes the simulation fits for all the EIS measurements. The following sections present the different impedance components.

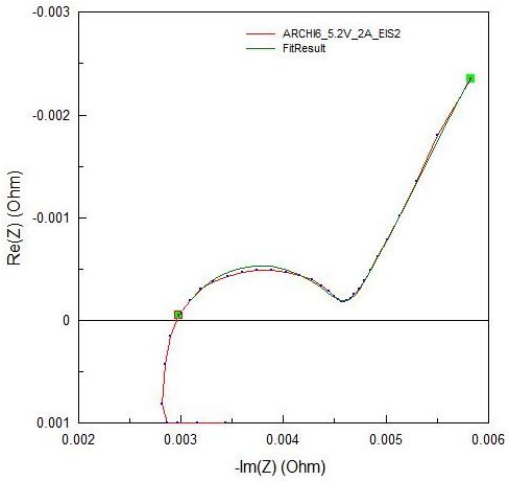

Figure 5-26: Actual and simulated Nyquist plots

Series resistance

The series resistance (R_Ω) of the cell includes the resistance of the active materials, electrolyte, current collectors and terminals [163]. The Nyquist plots in Section 5.6.2.3.1 show that there has been an increase in the series resistance of all cells after the overcharge event and a further increase after the post-overcharge cycling. The increase in series resistance depends on the degree of overcharge as shown in Figure 5-27. The series resistance of the cells charged to 4.8 V increased from 1.29 mΩ to 1.35 mΩ after the overcharge event and to 1.68 mΩ after cycling. Cells charged to 5.0 V experienced series resistance increase from 1.32 mΩ to 1.42 mΩ to 1.69 mΩ. And cells charged to 5.2 V increased from 1.31 mΩ to 2.98 mΩ to 3.51 mΩ. It can be noted the most significant increase in series resistance was experienced by cells charged to 5.2 V. This can be attributed to the increase of the electrolyte resistance as a result of its decomposition. This can be augmented by the gas volume generation presented in Section 5.6.2.1 as cells charged to 5.2 V experienced significantly higher volume increase than those charged to 5.0 V. Another possible source of increase in series resistance is the thickening of the SEI, as a result of the reaction between the deposited lithium on the anode and the electrolyte [53], [169], [170]. Another source for the increase of the cell impedance can result from the deposition of the dissolved metal ions from the cathode on the anode, as it is reported that NMC cathode dissolution starts when the voltage is higher than 4.3 V [56].

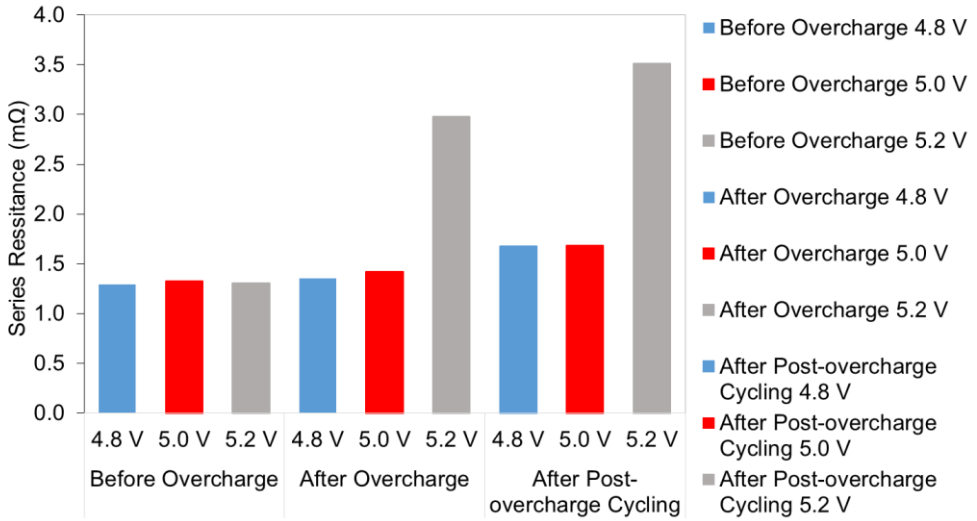

Figure 5-27: Series resistance before and after overcharge and after post-overcharge cycling for cells charged to different voltages

Charge transfer resistance

The charge transfer resistance is caused by the interfacial resistance at the surface of the electrodes [171]. It is represented by the semicircle at the medium frequency range on the Nyquist plot. As Figure 5-28 shows, the charge transfer resistance of all cells overcharged to different voltages increased after the overcharge event. The charge transfer of the cell charged to 4.8 V increased from 0.61 mΩ to 0.80 mΩ and from 0.62 mΩ to 1.12 mΩ for cells charged to 5.0 V. Cells charged to 5.2 V experienced that largest increase in their charge transfer resistance from 0.62 mΩ to 1.44 mΩ.

It is interesting to note that the charge transfer resistance of cells charged to different degrees of overcharged reacted differently to the post-overcharge cycling. After cycling the charge transfer resistance of cells overcharged to 4.8 V and 5.0 V decreased from 0.80 mΩ to 0.61 and from 1.12 mΩ to 0.77 mΩ respectively, whereas the charge transfer resistance of the cell charged to 5.2 V continued to increase to 1.66 mΩ from 1.44 mΩ. The increase in the charge transfer resistance after the overcharge event can be attributed to the growth of a layer (SEI) on the electrode (anode) as a result of its reaction with the electrolyte. This layer can might be reversible in the case of cells charged to 4.8 V and 5.0 V, but was permanent in the case of cells charged to 5.2 V. Another explanation could be that charging the cell to 5.2 V resulted in the reaction between the cathode and the electrolyte causing a film to form on its surface [117], [121]. Two and three electrode impedance studies also showed that increase in cell impedance mostly comes from the interface between the cathode and electrolyte [172]. It was reported that the cathode contributes significantly to the impedance increase [173].

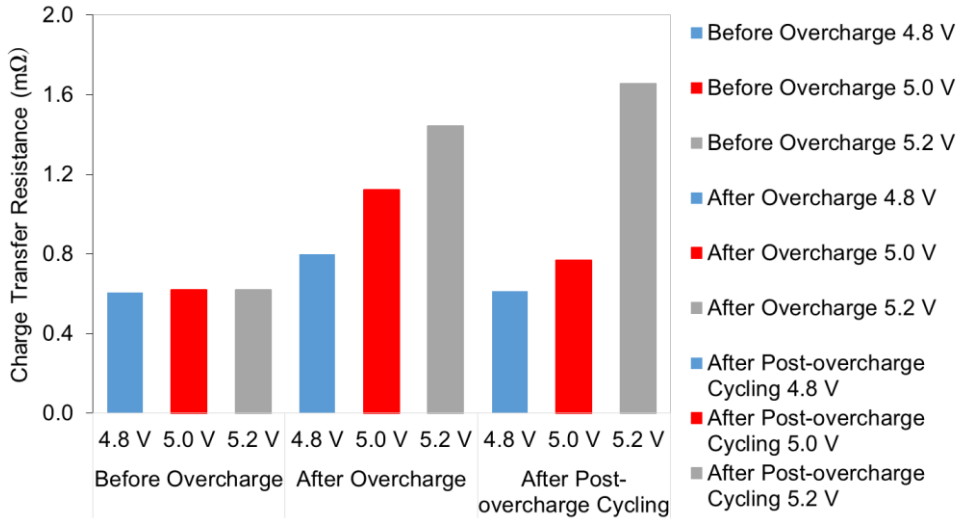

Figure 5-28: Charge transfer resistance before and after overcharge and after post-overcharge cycling for cells charged to different voltages

Diffusion

The solid-state diffusion of the lithium ions in the bulk of the electrode materials is represented by the line at the low frequency part of the Nyquist plot [118]. Figure 5-29 shows that Warburg diffusion resistance increased for all cells after the overcharge event. Surprisingly the diffusion resistance increase much significantly after the cells were cycled. This increase means that there has been an increase in the average length of the diffusion path of Li-ions [168].

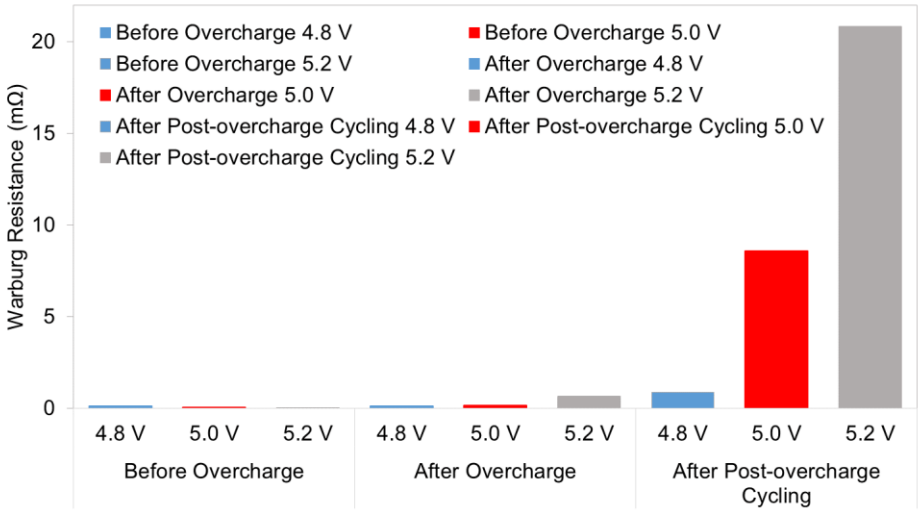

Figure 5-29: Warburg diffusion resistance before and after overcharge and after post-overcharge cycling for cells charged to different voltages

5.6.3 Effect of the Overcharging C-rate

This section presents and discusses the impact of the overcharging C-rate on the volume change of the cells, their capacity fade behaviour and change in internal resistance. Cells were overcharged to the same voltage using different C-rates.

5.6.3.1 Volume change and cycling behaviour of cells overcharged using different C-rates

Figure 5-30, Figure 5-31 and Figure 5-32 show the in-situ change in cell volume and the cycling behaviour of all cell overcharged using 10 A, 5 A and 2 A currents before, during and after the overcharge event. While monitoring their volume, all cells were initially cycled between 2.7 V and 4.2 V before being overcharged, cells were then overcharged to the same voltage, then cycled again for 10 full cycles after the overcharge event.

As Figure 5-30 shows cells overcharged using 10 A experienced the least volume increase (38.3%), followed by cells overcharged using 5 A (51.1%). Cells overcharged using a current of 2 A experienced much more significant volume increase (102%). This can be attributed to the fact that using a lower C-rate adds more charge to the cell as shown in Figure 5-33. Another factor that contributes to this is that cells overcharged using lower C-rate spend longer time in the overcharged state as Figure 5-34 shows. Cells overcharged using 10 A remain above 4.2 V for 1 hr, whereas cells charged using 5 A and 10 A stay for 2.3 hr and 5.6 hr respectively. It should also be noted that the cell volume continued to increase as long as the cell was in the overcharged state, during both the charge and discharge phases as shown in Figure 5-35. Figure 5-36 shows that, at the same voltage, the rate of gas generation during discharge is lower than that during charge. This is because the cell took less time to discharge from 5.2 V to 4.2 V than to charge from 4.2 to 5.2 V as Figure 5-37 shows. Figure 5-37 also shows the fraction of volume increase during charge and discharge and the fraction charge and discharge times.

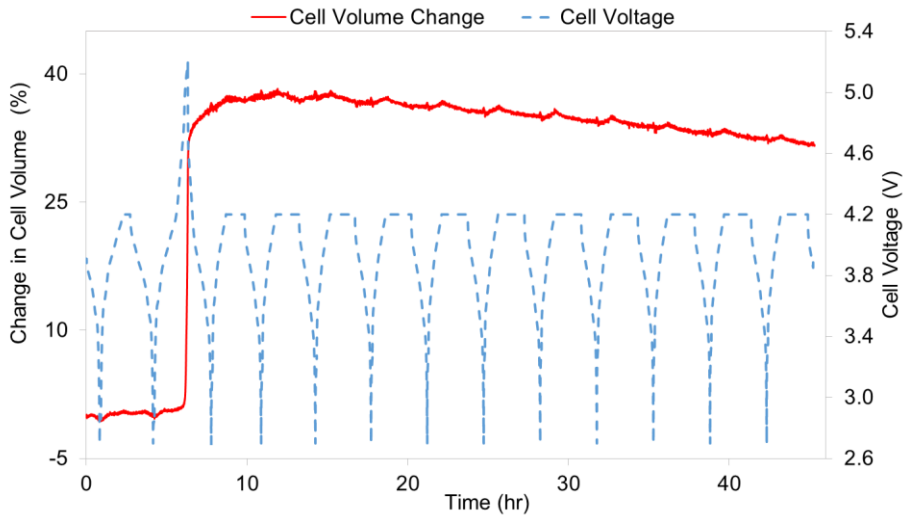

Figure 5-30: Cell volume change and voltage during overcharge using 10 A current

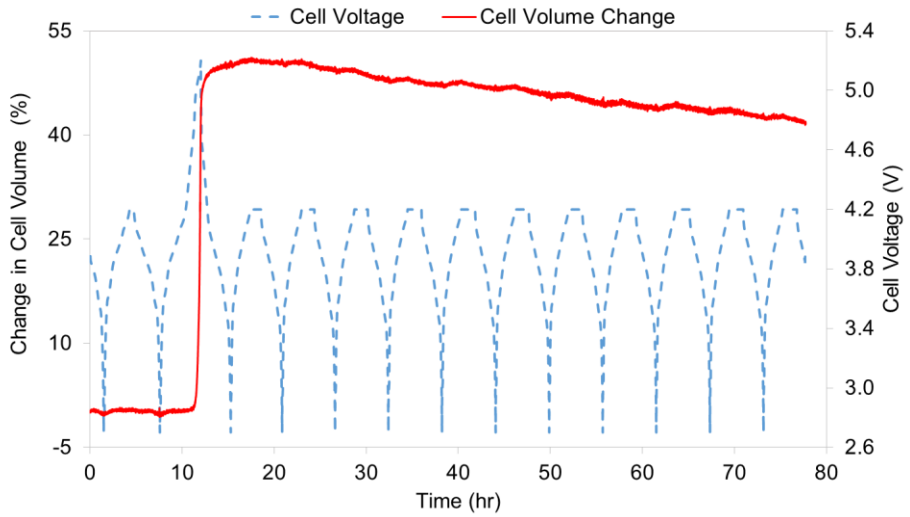

Figure 5-31: Cell volume change and voltage during overcharge using 5 A current

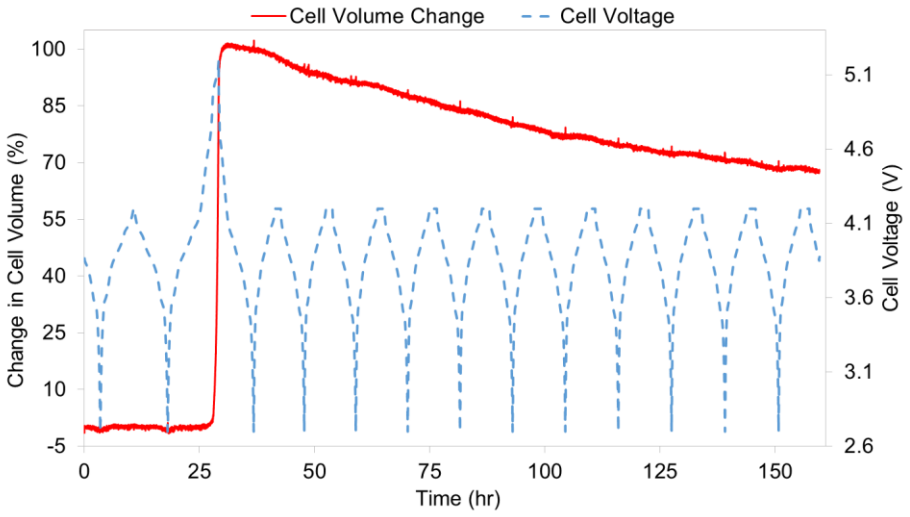

Figure 5-32: Cell volume change and voltage during overcharge using 2 A current

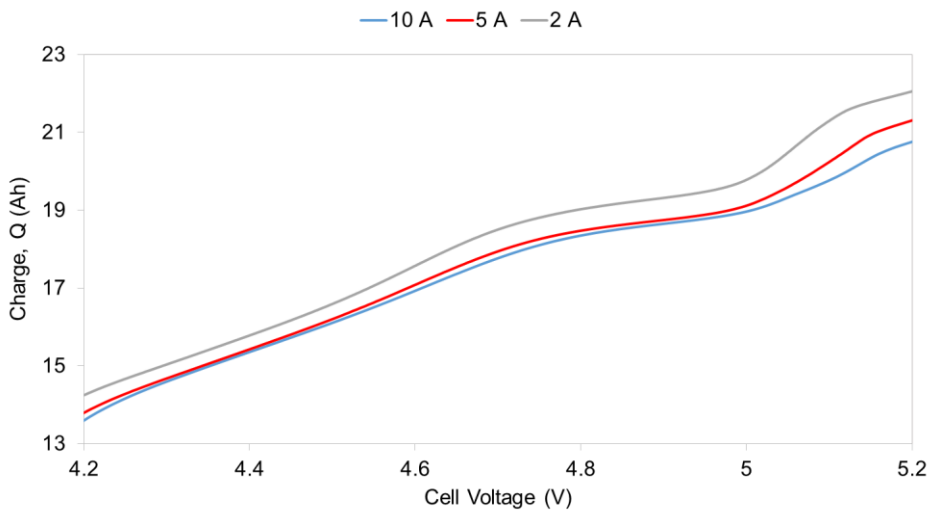

Figure 5-33: Charge as a function of cell voltage during overcharge for the different charging currents

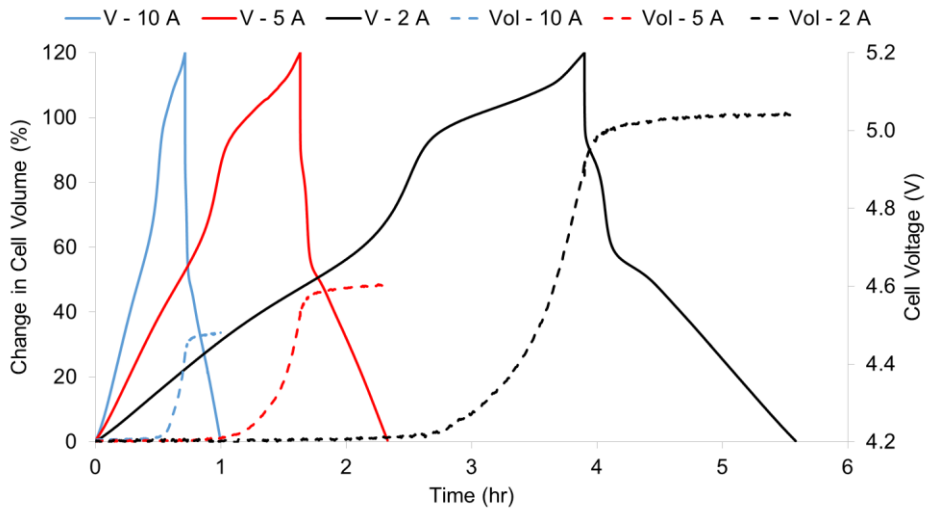

Figure 5-34: Change in cell volume and cell voltage in the overcharged state versus time for different charging currents

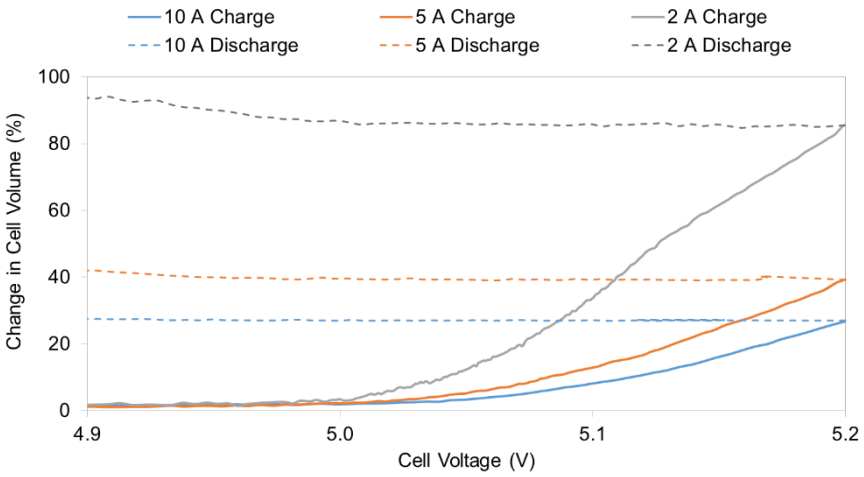

Figure 5-35: Cell volume increase for different charging currents

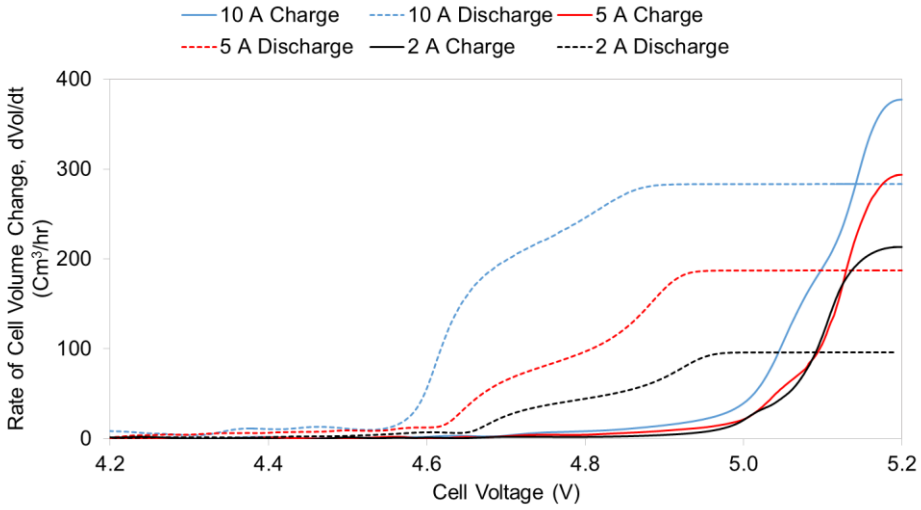

Figure 5-36: Rate of cell volume increase as a function of voltage during charge and discharge in the overcharged state

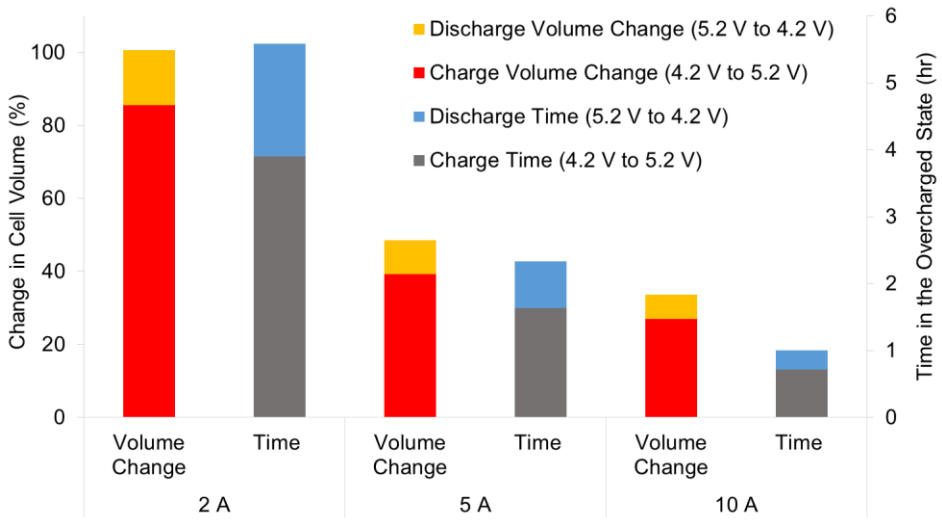

Figure 5-37: Volume increase during charge and discharge in the overcharged state, and charge and discharge times

5.6.3.2 Capacity degradation behaviour of cells overcharged using different C-rates

The same overcharge regime as outlined in Section 5.6.2 was followed other than using different C-rates to charge all cells to a terminal voltage of 5.2 V. Cycle 1 is the pre-overcharge event cycle during which cells were cycled between 2.7 V and 4.7 V using 2 A, 5 A and 10 A. For Cycle 1, Figure 5-38 shows the IC curves during charge and discharge at different C-rates. The shift of the peaks with the C-rate gives an indication of the polarisation resistance [174]. During charge the shift of the IC curve towards higher voltages/higher polarisation potential means that the end-of-charge voltage stops the charging process before the complete removal of lithium from the positive electrode, i.e. under charge (UC). During discharge the shift of the IC curve towards lower voltages means the discharge process is stopped before the complete insertion of lithium in the positive electrode, i.e. under discharge (UD) [175]. Both UC and UD lead to some capacity not being accessible when cycling the cell at higher C-rates [176]. Figure 5-39 shows the IC curves of the overcharge cycle for different C-rates.

Figure 5-40 shows the normalised charge and discharge capacities of the cells cycled using 2 A, 5 A and 10 A. It can be see than lower currents put more charge into the cell during charge. During discharge using lower currents also enables extracting more capacity from the cell.

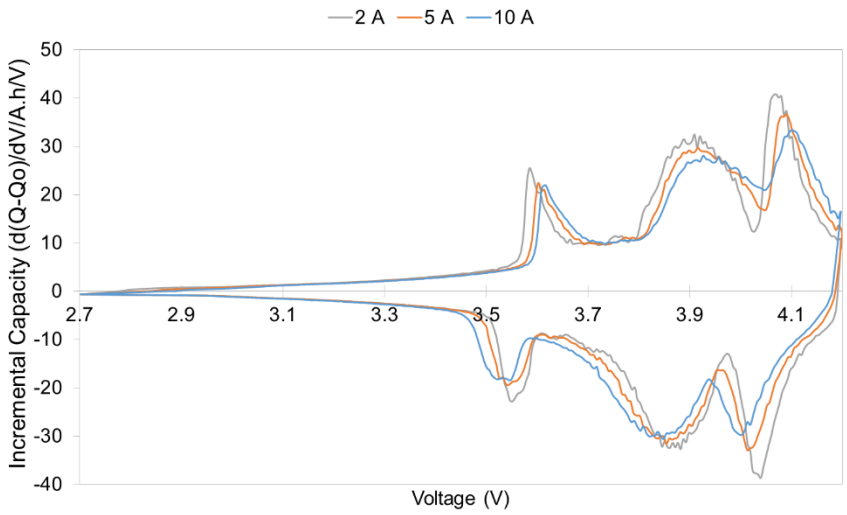

Figure 5-38: IC curves of the pre-overcharge cycle, cells were cycled using different C-rates

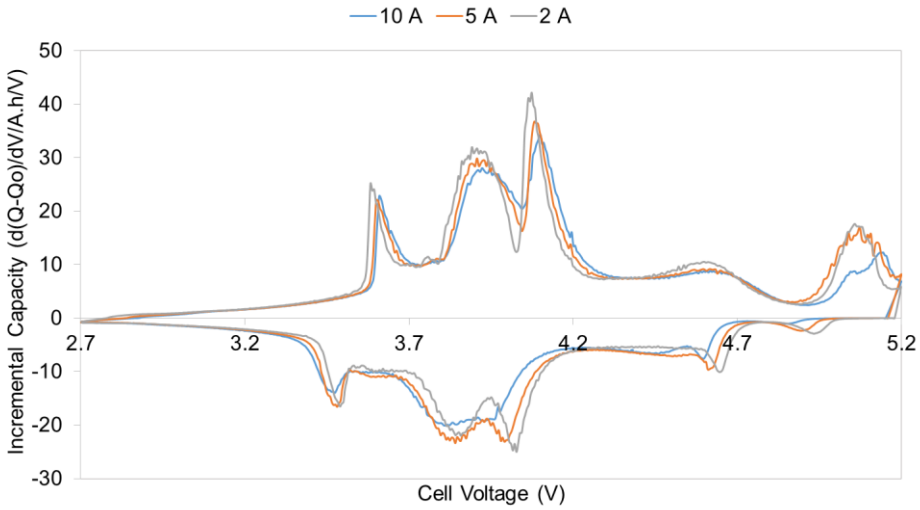

Figure 5-39: IC curves of the overcharge cycle for different C-rates

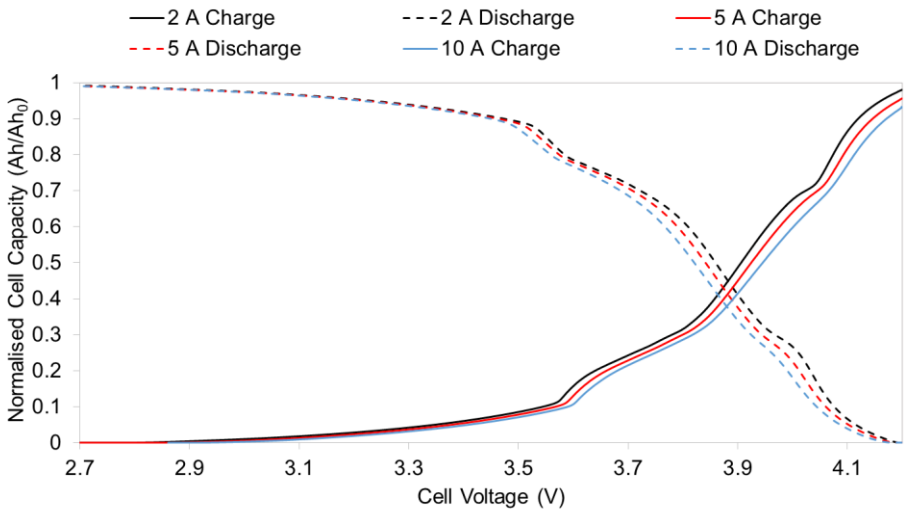

Figure 5-40: Normalised cell charge and discharge capacities for different C-rates

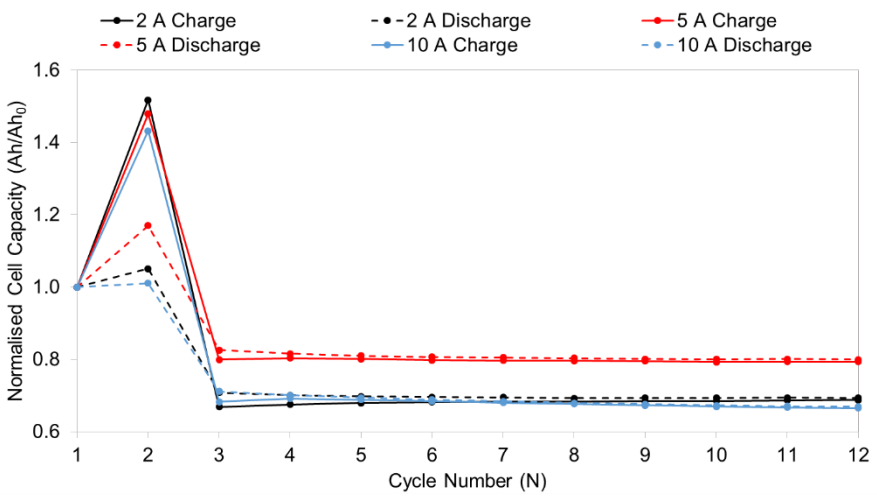

Figure 5-41: Normalised cell charge and discharge capacities before, during and after the overcharge event for cell charged to 5.2 V using different C-rates

The normalised charge and discharge capacities of the cells before, during and after the overcharge event are shown in Figure 5-41. The charge and discharge capacities of each cell were normalised to the pre-testing capacity check cycling regime in section 5.5.3.1 instead of Cycle 1 due to the sensitivity of the charge and discharge capacities to the C-rate used to cycle the cell as shown in Figure 5-40.

Cycle 2 is the overcharge event cycle where cells were charged to 5.2 V using different C-rates. During the charge part of the overcharge cycle cells charged using 2 A, 5 A and 10 A gained 1.518, 1.479 and 1.432 times their initial capacity respectively. During the discharge part of the overcharge cycle only 1.01 times the initial capacity was discharged from the cell charged using 10 A, whereas 1.17 and 1.05 times were recovered from the cells charged using 5 A and 2 A respectively.

This shows that less energy was recovered from cells charged using the highest and the lowest C-rates. Although during charge more energy was put into the cells charged using 2 A in comparison to cells charged using 5 A, less capacity was recovered from them. This can be attributed to energy lost as heat and in side chemical reactions, as using lower C-rates to charge cells to the same voltage puts more charged in them (higher SOC) as shown in Figure 5-33 and Figure 5-40. On the contrary although more energy was put into the cells charged using 5 A in comparison to cell charged using 10 A, the capacity recovered from them was higher. This can be attributed to higher heat energy losses due to higher currents or due to damages done by the relatively higher C-rate. The percentage of energy recovered from the cells overcharged to the same voltage (5.2 V) using different C-rates is shown in Table 5-5.

During cycle 3, the first cycle after the overcharge event, cells charged using 2 A current experienced the highest capacity fade, followed by those charged by 10 A then 5 A. However, the capacity of the cell overcharged by 10 A continued to fall and became less than that of the cell charged using 2 A. The discharge capacity of all cells was larger than their charge capacities. However, the gap between them was reduced as the cells were cycled. It seems that it takes the cell several cycles for the overcharge influence to be reduced. The normalised charge and discharge capacities of cycles 3 and 12 are summarised in Table 5-5.

Table 5-5: Summary of capacity behaviour of cells charged to the same overcharge voltage using different C-rates

Current (A)	2.0	5.0	10.0
Normalised Charge Capacity of Cycle 2 (Overcharge)	1.518	1.479	1.432
Normalised Discharge Capacity of Cycle 2	1.051	1.170	1.011
Energy recovered from the Cycle 2 (%)	69.23	79.13	66.58
Normalised Charge Capacity of Cycle 3 (Post-overcharge)	0.669	0.800	0.682
Normalised Discharge Capacity of Cycle 3	0.708	0.826	0.711
Normalised Charge Capacity of Cycle 12	0.688	0.794	0.665
Normalised Discharge Capacity of Cycle 12	0.693	0.799	0.669

5.6.3.3 Electrochemical impedance spectroscopy of cells overcharged using different C-rates

5.6.3.3.1 Nyquist plots

Figure 5-42a, b and c show the EIS measurements before and after the overcharge event and after the post-overcharge cycling for cells overcharged to 5.2 V, using 2 A, 5 A, and 10 A respectively. The EIS profiles of all cells moved to the right, the semi-circle at the medium frequency range increased in size and became more depressed and the line at the low frequency range increased in length and its angle with the vertical axis increased. These changes suggest increases in the series resistance, charge transfer resistance and the diffusion resistance respectively. Although it should be noted that the line at the low frequency representing the diffusion resistance increased after cycling for cells overcharged with 2 A and 10 A, but decreased after cycling for the cell overcharged with 5 A.

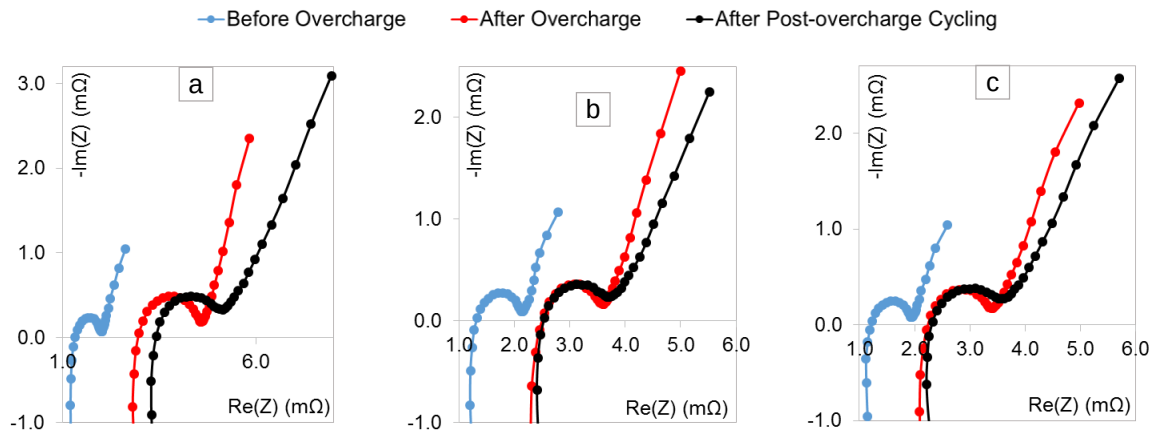

Figure 5-42: EIS measurements before overcharge, after overcharge and after post-overcharge cycling of cell charged to 5.2 V using a) 2 A b) 5 A c) 10 A

As Figure 5-43 shows the extent of change in the cell impedance depended on the overcharging current (C-rate), cells charged using lower currents experienced larger change.

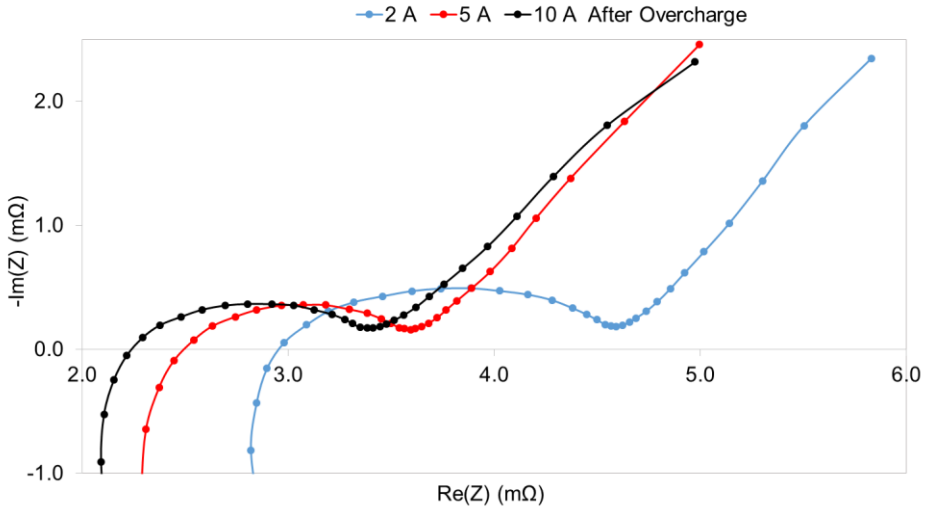

Figure 5-43: EIS measurements of cells overcharged using different C-rates after the overcharge event

Cycling the cells after the overcharge event further increases the impedance of all cells as Figure 5-44 shows. Figure 5-45 combines all the previous plots, it shows the EIS data before overcharge, after overcharge and after post-overcharge cycling for cells charged to different voltages/SOC.

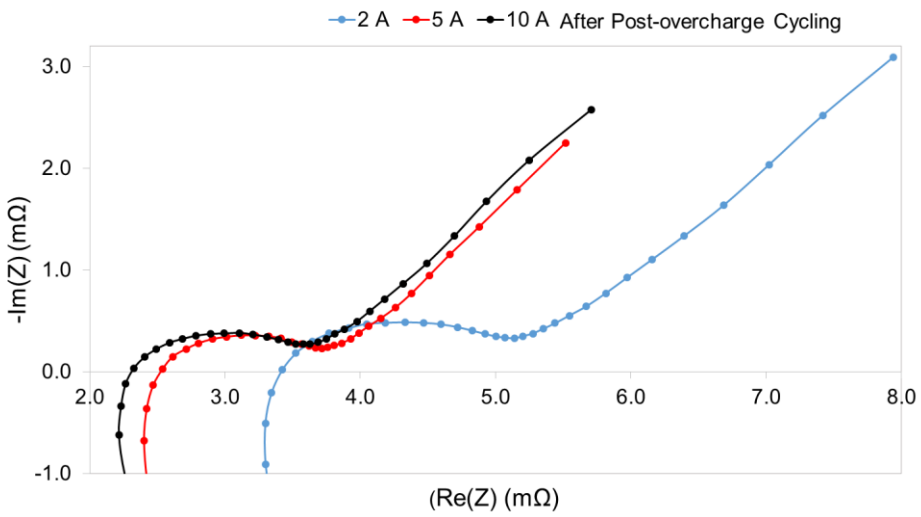

Figure 5-44: EIS measurements of cells overcharged using different C-rates after the post-overcharge cycling

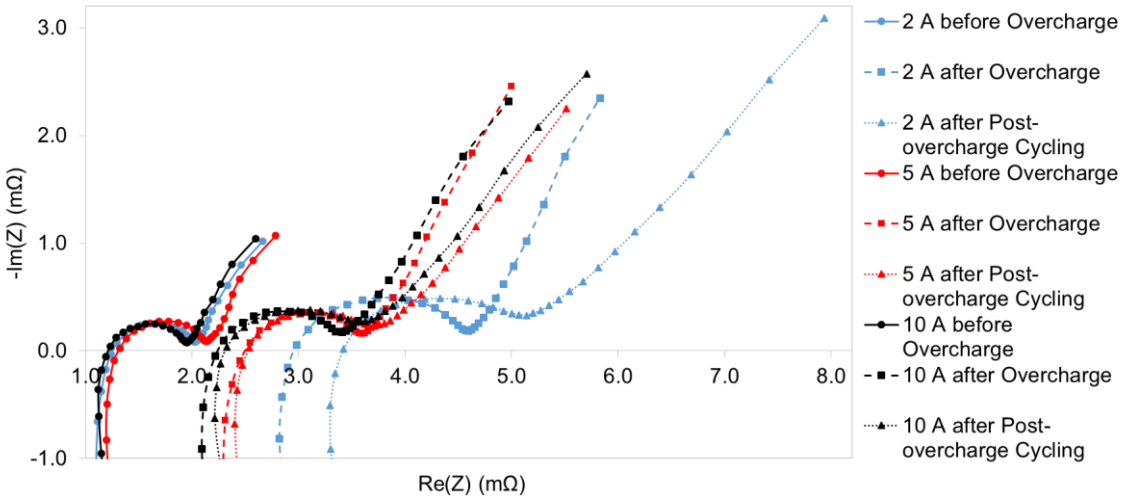

Figure 5-45: EIS data before overcharge, after overcharge and after post-overcharge cycling for cells overcharged using different C-rates

5.6.3.3.2 Equivalent circuit modelling and impedance components

The same equivalent circuit model and analysis as Section 5.6.2.3.2 was followed in this section. Figure 5-46 shows that the increase in series resistance depends on the overcharging C-rate. The series resistance of the cells charged using a 10 A current increased from 1.35 mΩ to 2.26 mΩ after the overcharge event and to 2.30 mΩ after cycling. Cells charged using a 5 A current experienced series resistance increase from 1.37 mΩ to 2.54 mΩ after the overcharge event, but decreased to 2.52 mΩ after cycling. Cells charged using a 2 A current experienced the highest increase in series resistance. It increased from 1.37 mΩ to 2.98 mΩ after overcharge to 3.51 mΩ after

cycling. This can mainly be attributed to the increase of the electrolyte resistance as a result of its decomposition. This can be augmented by the gas volume generation presented in Section 5.6.3.1 as cells overcharged using 2 A experienced higher volume increase than those charged using 5 A and 10 A.

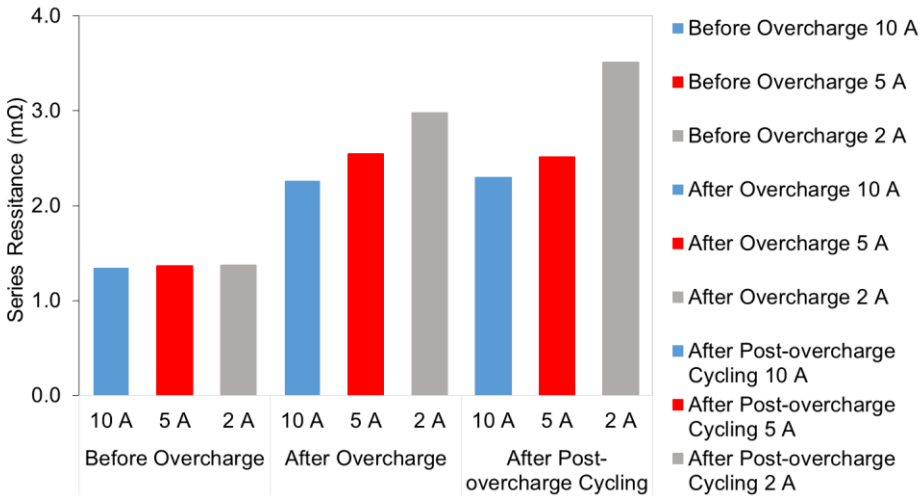

Figure 5-46: Series resistance before and after overcharge and after post-overcharge cycling for cells overcharged using different C-rates

Figure 5-47 shows the charge transfer resistance of all cells overcharged using different C-rates. After the overcharge event the charge transfer of the cell charged using 10 A increased from 0.68 mΩ to 0.92 mΩ and from 0.71 mΩ to 0.84 mΩ for cells charged using 5 A. Cells charged using 2 A experienced that largest increase in their charge transfer resistance from 0.69 mΩ to 1.44 mΩ. The charge transfer resistance of the cells reacted differently to the post-overcharge cycling. After cycling the charge transfer resistance of cells overcharged using 10 A and 2 A currents increased to 1.29 and 1.66 respectively, whereas the charge transfer resistance of cells overcharged using 5 A decreased from 0.84 mΩ to 0.83.

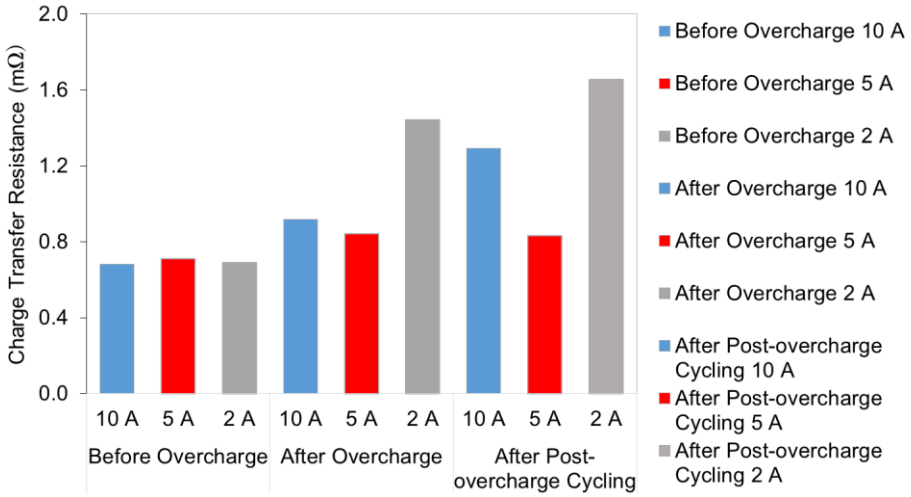

Figure 5-47: Charge transfer resistance before and after overcharge and after post-overcharge cycling for cells overcharged using different C-rates

Figure 5-48 shows that Warburg diffusion resistance increased for all cells after the overcharge event. After cycling the diffusion resistance of all cells increased further, however, cells overcharged using 5 A current experienced a significantly less increase than those overcharged using 2 A and 10 A currents. The post-cycling behaviour of the series, charge transfer and diffusion resistances of the cell overcharged using a 5 A current can be attributed to less damage done as a result of the overcharge compared to 2 A and 10 A. Overcharging the cell using 2 A to puts more charge and hence causes more damage as pointed out in Figure 5-33 in Section 5.6.3.1. Overcharging using 10 A might cause damage due to the relatively high C-rate.

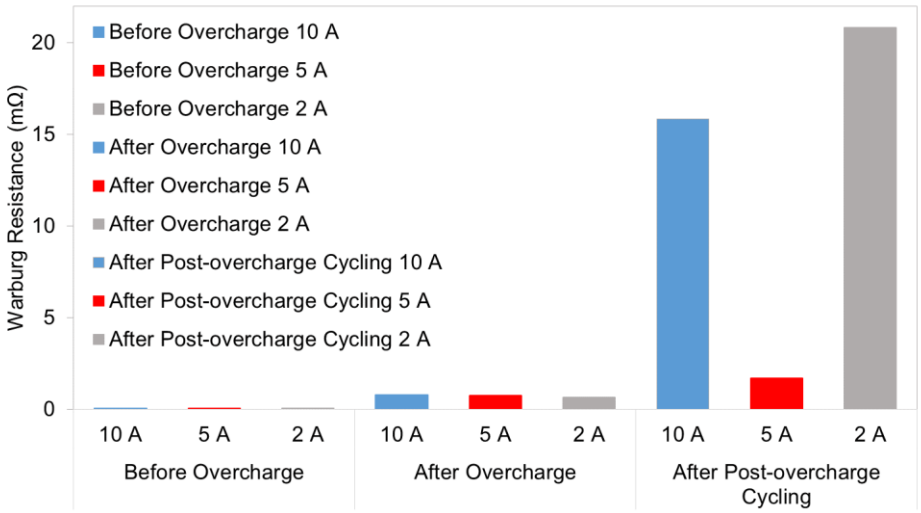

Figure 5-48: Warburg diffusion resistance before and after overcharge and after post-overcharge cycling for cells overcharged using different C-rates

5.6.4 Thermal Behaviour during Overcharge

The two main sources of heat generation in a cell are Ohmic heating and heating due exothermic chemical reactions. Figure 5-49 shows the cell temperature and change in cell volume as a function of voltage during overcharge. There was no noticeable temperature rise until the cell reached 4.6 V. The temperature kept going up as the cell was being overcharged. When the cell voltage reached around 5 V there was a rise in the rate of temperature increase. Note that this also coincides with the start of significant volume increase. It is believed that this rise in temperature is due to the same exothermic reactions that generated the gas. Although there was significant cell swelling and rise in cell resistance as shown in Section 5.6.2.3.2, the temperature peaked at only 33.2 °C. Note that this modest temperature rise is similar to overcharging the cell outside of silicone oil, as presented in section 6.5.1. This suggests that silicone oil had a minimal cooling effect.

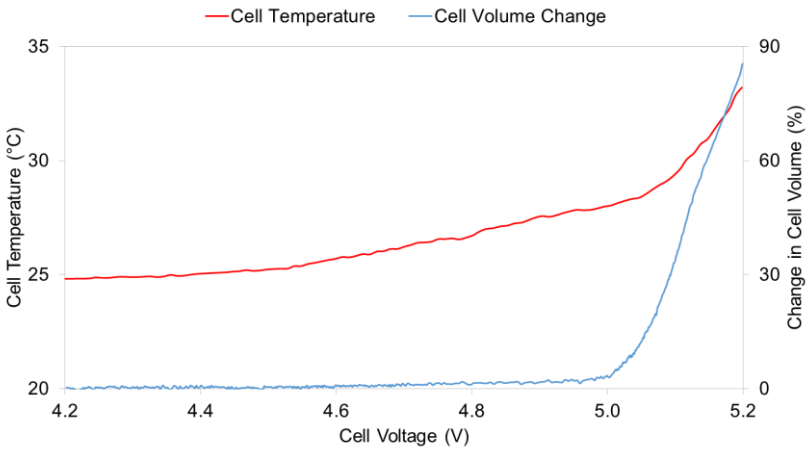

Figure 5-49: Cell temperature and change in cell volume as a function of voltage during overcharge

5.6.5 Reversibility of Cell Volume Increase

The ability of the cells to return to its original volume after an overcharge event was investigated. As Figure 5-50 shows, cells were divided into two groups, the first group were cycled after the overcharge event, whereas the second group of cells were discharged to 3.80 V and left to rest for the same cycling duration taken by the first group. It can be seen that the volume of the cells rested after the overcharge event decreased at a higher rate than those cycled. The reversibility of cell volume was calculated using Equation 5-6.

$$Volume\ reversibility\ (\%) = \frac{Max\ cell\ volume\ - Cell\ volume\ at\ specific\ time}{Max\ cell\ volume}\ x\ 100$$

Equation 5-6

Figure 5-51 shows the reversibility of both groups, at any given point the reversibility of the rested group was higher than the cycled group. After 125 hours from the overcharge event the volume reversibility was 42.5% and 33.7% for the rested and cycled groups respectively. As discussed in Section 5.4.4.2, the largest component of cell volume increase as a result of an overcharge event is gas generation. The reversibility in cell volume can be mainly attributed to the consumption of the gases produced. There have been reports suggesting that some gases can polymerise on the surface of the electrodes, for example ethyne gas could form polyethyne on the anode due to its high reactivity [177].

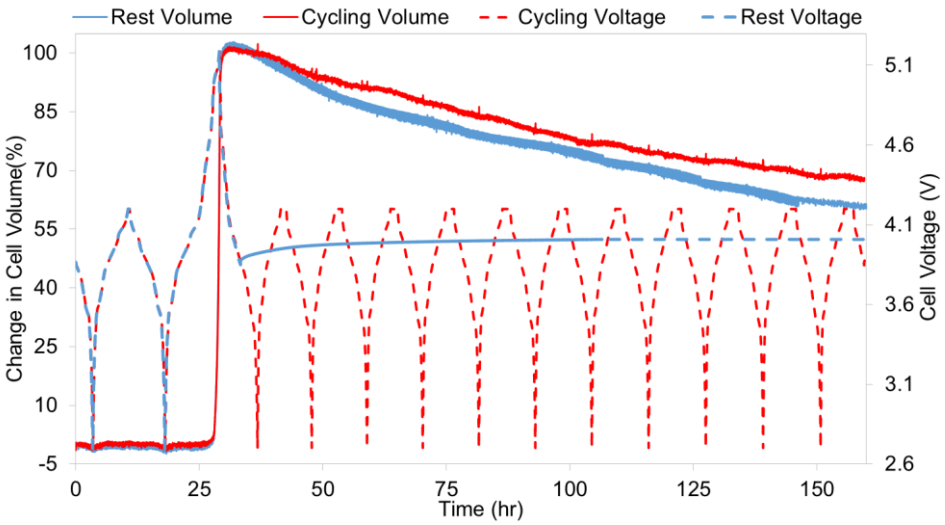

Figure 5-50: Volume change and voltage of cells cycled and cells rested after an overcharge event

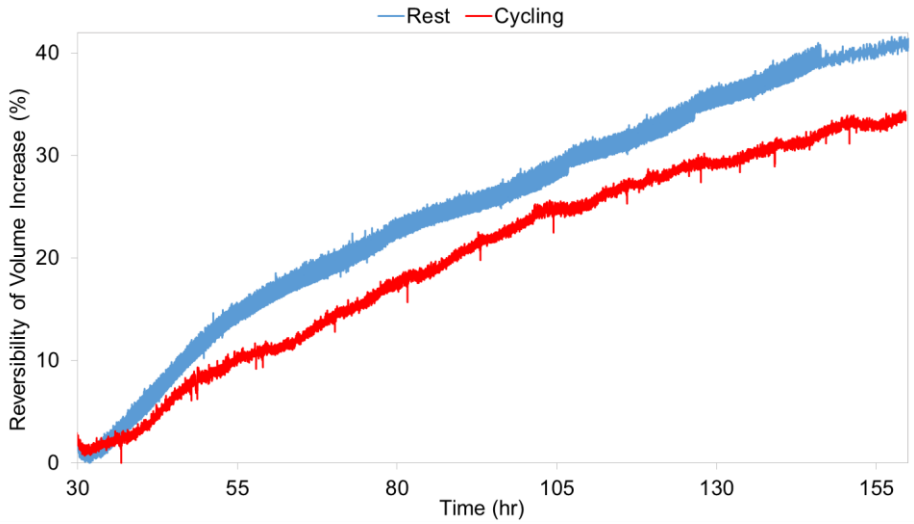

Figure 5-51: Reversibility of expansion of cells cycled and cells rested after the overcharge event

5.6.6 Post-overcharge Cycling Behaviour

This section investigates the cycling behaviour of cells that were overcharged. Generally when Li-ion cells age with cycling, their capacity decreases and their internal resistance increases [55]. Capacity fade can be attributed to LLI, LAM and ORI as described in Section 2.6. The objective of this section is to study the cycling behaviour in terms of capacity and internal resistance of cells that were exposed to an overcharge events as described in section 4.5.2.2. All cells followed the cycling regime presented in Section 4.5.2.3, in which full charge/discharge cycles were conducted to investigate the capacity and impedance. Cells were cycled between 4.2 and 2.7 V for 155 cycles

using Maccor cycler at 25 °C. The internal resistance of the cells was measured every 5 cycles.

5.6.6.1 Effect of the degree of overcharge on capacity fade and resistance increase

Figure 5-52 shows the normalised discharge capacity of cells as a function of the cycle number. After 155 cycles the capacity of the control cell dropped to 0.989 of its original value. Cells overcharged to 4.8 V did not show significant capacity fade for about 80 cycles, but their capacity dropped to 0.962 of its original value after 155 cycles. Cells overcharged to 5.0 V retained 0.911 of their original capacity. Cells overcharged to 5.2 V suffered the biggest capacity fade. They started with 0.614 of their initial capacity. Their capacity recovered up to 0.748 of its original value after 90 cycles before starting to drop again, reaching 0.681 after 155 cycles.

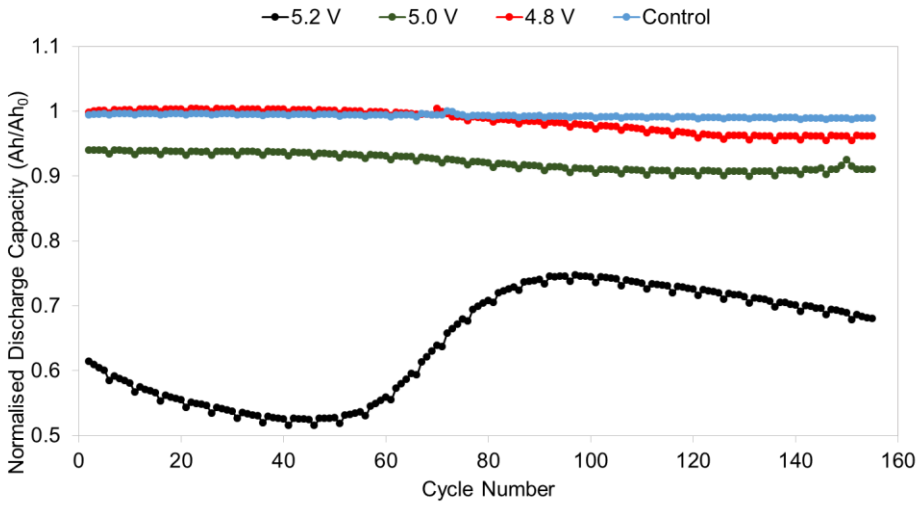

Figure 5-52: Normalised discharge capacity of long term cycling after overcharging to different degrees of overcharge

The internal resistance in Figure 5-53 followed the cell capacity, as the capacity decreases the resistance increases. The behaviour of the cells charged to 5.2 V can be explained by the reversibility of the generated gas. Since these cells suffered the largest swelling, their resistance after the overcharge event was the highest. Part of the increase in internal resistance can be attributed to the separation of the cell electrodes caused by the swelling of the cell [80]. As shown in Figure 5-50 in section 5.6.5 cycling a swollen cell after an overcharge event reduces its volume again, hence,

reducing its resistance and recovering part of its lost capacity. Figure 5-53 also shows that the cells charged to 5.2 V suffered much higher internal resistance increase than those charged to 4.8 V and 5.0 V.

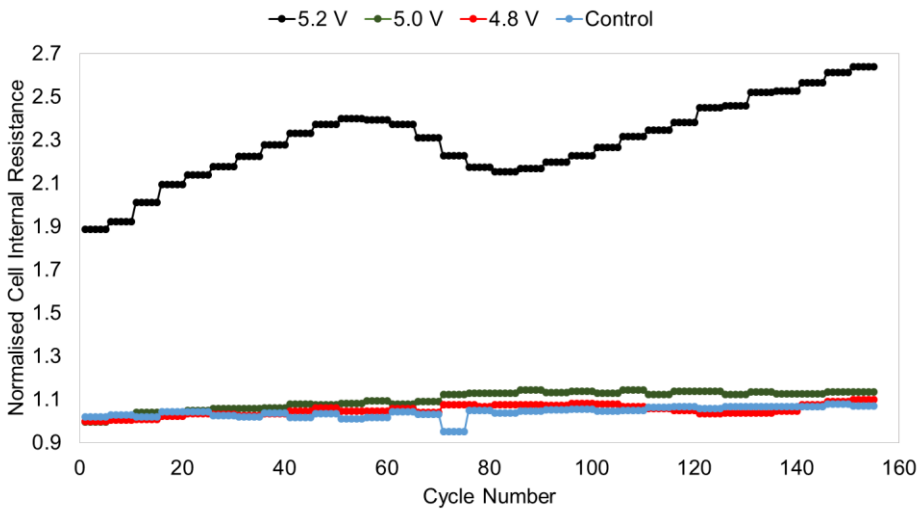

Figure 5-53: Normalised internal resistance of long term cycling after overcharging to different degrees of overcharge

5.6.6.2 Effect of C-rate on capacity fade and resistance increase

All cells in Figure 5-54 were overcharged to 5.2 V, except the control cell. Initially cells overcharged using 2 A showed the highest capacity loss, whereas those overcharged with 5 A showed the least capacity loss. The capacity of all cells recovered with cycling, after 155 cycles cells overcharged with 10 A had the least capacity loss, followed by those overcharged with 5 A then 2 A. Their capacities were 0.828, 0.790 and 0.681 of their original capacity respectively. Figure 5-55 shows the normalised resistance, which correlates with the capacity behaviour – as the resistance increases the capacity decreases and vice versa.

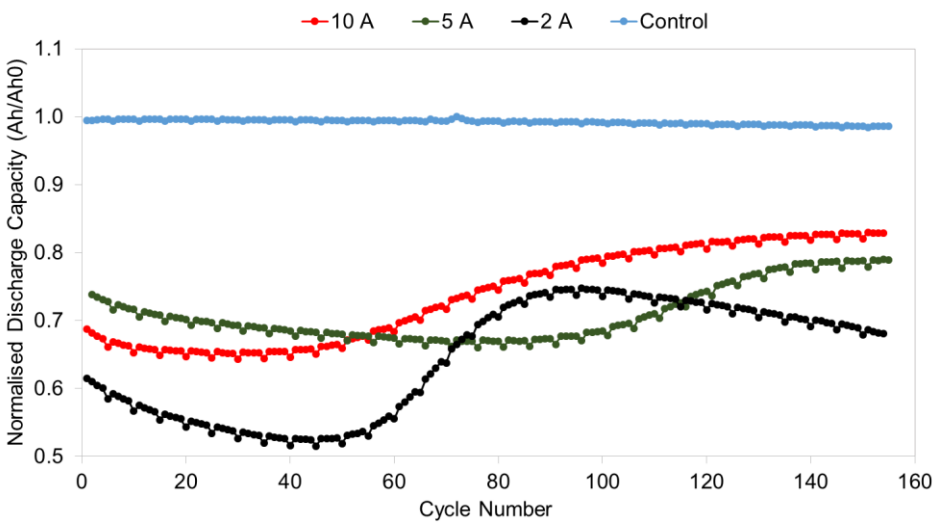

Figure 5-54: Normalised discharge capacity of long term cycling after overcharging using different C-rates

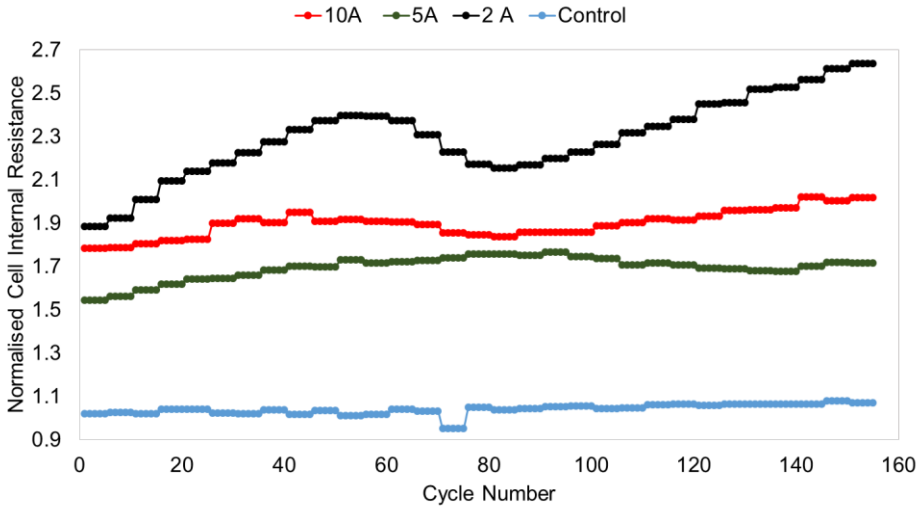

Figure 5-55: Normalised internal resistance of long term cycling after overcharging using different C-rates

5.6.6.3 Thermal behaviour during post-overcharge cycling

During cycling current flows through the cell and heat is generated mainly by Ohmic heating, expressed as:

$$P_{Ohmic} = I^2R \qquad \text{Equation 5-7}$$

Where *I* is the current and *R* is the cell resistance.

Figure 5-56a shows the surface temperature and the voltage of the control cell during the first few cycles. As the cell voltage changes cell surface temperature changes. The cells were cycled using a constant current, hence the change in heat generation is

caused by the change in the internal resistance of the cell, as its internal resistance changes with its SOC [178]. During the first few cycles the temperature change was between around 24.4 ˚C at 4.2 V to 25.6 ˚C at 2.7 V, with a window of 1.2 ˚C.

Figure 5-56b shows the surface temperature and voltage of the control cell after 150 cycles. The temperature change was from 25.1 ˚C at 4.2 V to 26.8 ˚C at 2.7 V, with a window of 1.7 ˚C. It can be noticed that not just both the lower and upper temperatures increased, but also the difference between them increased. This can be attributed to the resistance increase as a result of cycle ageing as augmented by the resistance measurements.

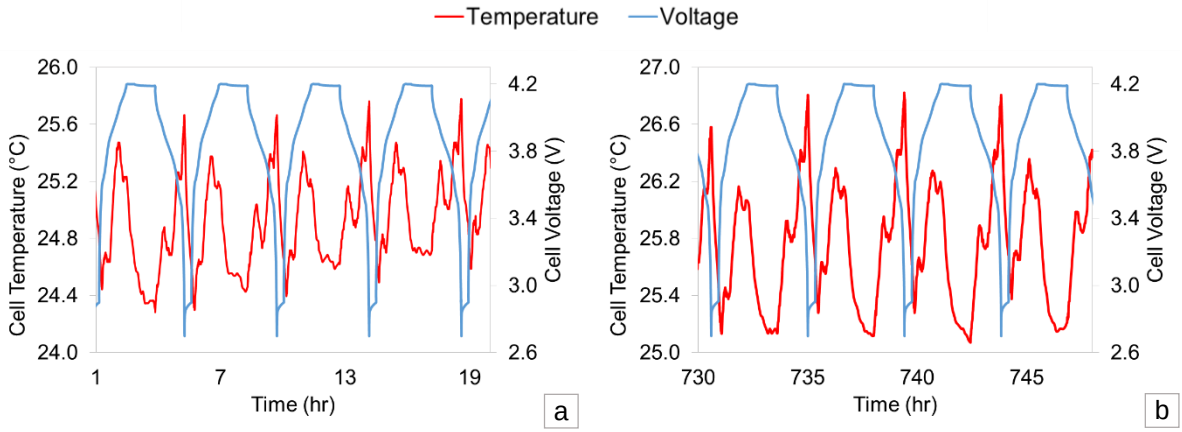

Figure 5-56: Surface temperature and voltage of the control cell during: a) the initial cycles b) after 150 cycles

Figure 5-57a shows the surface temperature and the cell of the cell overcharged to 5.2 V during the first few cycles of the post-overcharge cycling regime. The temperature change was between around 25.0 ˚C at 4.2 V to 27.9 ˚C at 2.7 V, with a window of 2.9 ˚C.

Figure 5-57b shows the temperature change with the voltage of the overcharged cell after 150 cycles. The temperature change was between around 25.3 ˚C at 4.2 V to 31.5 ˚C at 2.7 V, with a window of 6.2 ˚C. The increase is significantly higher than the control cell. Table 5-6 summaries the temperature data.

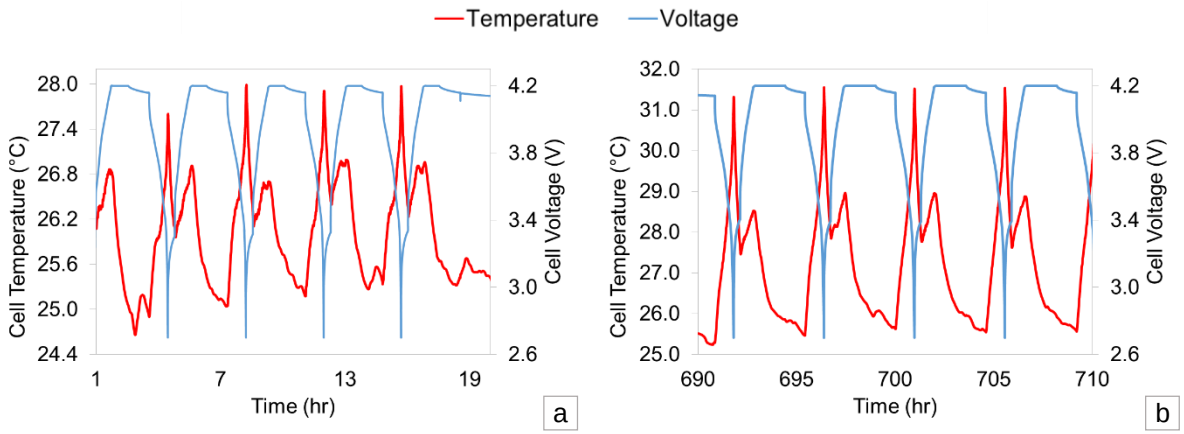

Figure 5-57: Surface temperature and voltage of the cell overcharged to 5.2 V during a) the initial cycles b) after 150 cycles

Table 5-6: Maximum and minimum temperature values during cycling

	Initial Cycles			After 150 Cycles		
	Min. T (°C)	Max. T (°C)	ΔT (°C)	Min. T (°C)	Max. T (°C)	ΔT (°C)
Control Cell	24.4	25.6	1.2	25.1	26.8	1.7
Overcharged	25.0	27.9	2.9	25.3	31.5	6.2

The increase of the minimum and the maximum temperature values mainly depends on the increase in internal resistance. Therefore, cells overcharged to higher degrees of overcharge experience higher temperature increase during cycling as shown in Figure 5-58a and b for the maximum charge temperature and maximum discharge temperature respectively. Cells overcharged to the same voltage (5.2 V) using different C-rates experienced different changes in the temperature values as shown in Figure 5-59a and b for the maximum temperatures during charge and the maximum temperatures during discharge respectively. This agrees with the resistance data presented earlier since lower C-rates caused higher resistance increase (as charging the cell to the same voltage limit using lower currents charges it to a higher degree of overcharge and causes more damage).

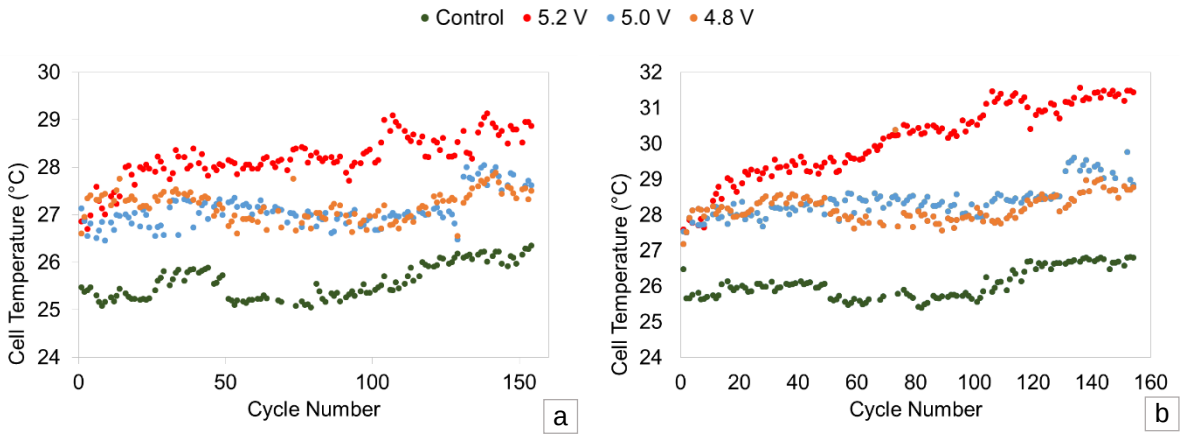

Figure 5-58: Evolution of the maximum a) charge b) discharge temperature with cycling of cells overcharged to different degrees of overcharge

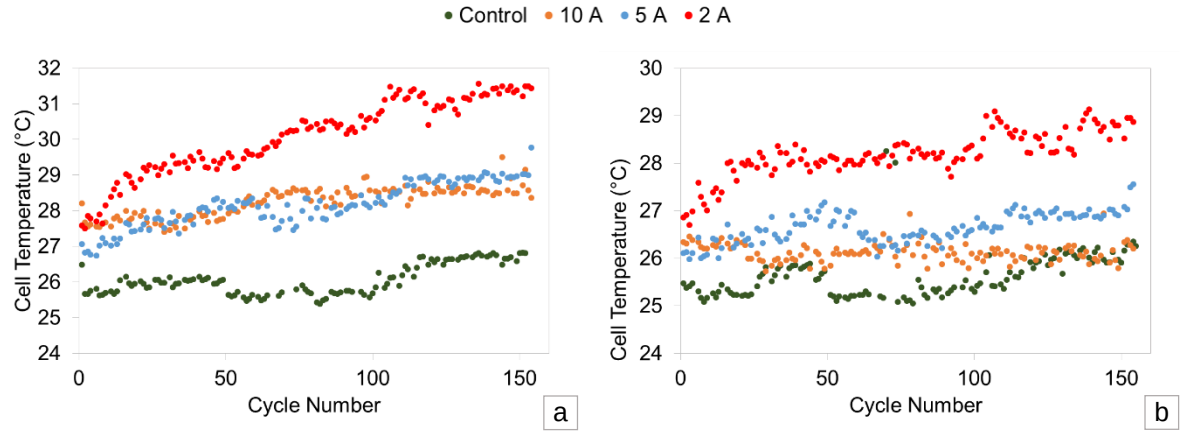

Figure 5-59: Evolution of the maximum a) charge b) discharge temperatures with cycling of cells overcharged with different C-rates

5.7 Chapter Conclusion

This research investigated the effect of an overcharge event on the volume, capacity and internal resistance of a 15 Ah commercial automotive pouch Li-ion cell with NCM-LMO mix cathode. It has been shown that the C-rate and degree of overcharge determine the extent of cell swelling during an overcharge event. Swelling was partially reversible after the cell returned to its normal operating voltage range. Cycling of the cell after the overcharge event showed that the extent of impedance increase and capacity fade depend on the overcharge event. It also showed that cells can be used after an overcharge event depending on the extent of damage. Although their

operating temperature is higher than the non-abused cells as a result of their internal resistance increase.

5.8 Recommendations for Future Work

This study was limited to one cell chemistry and one cell capacity. Investigating other chemistries would provide useful information on the effect of cell chemistry on gas generation during overcharge. Further investigation could also include analysing the gas composition to identify and quantify the gas species generated.

The set-up used in this study proved to be robust for the in-situ volume measurement of pouch cells during overcharge. However, it might be impractical to use for other abuse scenarios such as, external short circuit, due to the need for connections with large cross-sectional area, in order to be able to withstand the high currents. Future work could include the modification of this set-up for other abuse tests and/or find other methods to in-situ measure the volume change of other cell formats such as, prismatic and cylindrical cells.

Chapter 6 – Overcharge in Adiabatic Environment

6.1 Chapter Highlights

- Cells overcharged in adiabatic and non-adiabatic conditions
- Different charging C-rates used in overcharge
- Heat dissipation during overcharge determines the outcome
- Cells failing during overcharge can have different failure modes

6.2 Chapter Abstract

Cells were overcharged in ambient conditions and inside a calorimeter in order to simulate non-adiabatic and adiabatic environments respectively. This was carried out to study the effect of heat dissipation on the outcome of an overcharge event. Results show that the ability of the cell to dissipate the heat generated during overcharge is critical in determining the outcome of the test. The same overcharge regime under different conditions resulted in very different outcomes. Cells overcharged in ambient conditions swelled significantly, but did not vent nor ignite and, whereas, all cells overcharged under adiabatic conditions either ruptured or caught fire. The magnitude of the overcharge current in adiabatic conditions determined the failure mode. Cells overcharged using 0.13 C current ruptured after swelling significantly, but did not catch fire. Cells overcharged with 0.33 and 1.3 C currents were completely combusted.

6.3 Chapter Introduction

6.3.1 Significance of Overcharge in Adiabatic Conditions

Cells in a battery pack can be overcharged for under a number of scenarios as presented in Section 5.3.1. The outcome of an overcharge event is highly dependent on the heat build-up, which is the difference between heat generation and heat dissipation. Conditions in a battery pack can allow for the build-up of heat and subsequent temperature rise. Large battery packs such as those of EVs consist of thousands of cells with small spacing between them [179]. Studies show that in big battery packs, cells with inconsistency in internal resistance can accumulate heat during charging [180]. Hence it is important to investigate the thermal behaviour and

mechanism of failure of cells during overcharge under adiabatic conditions rather than ambient conditions to get a conservative estimation of the possible outcomes.

6.3.2 Aim and Objectives

The aim of this study is to compare the thermal behaviour and mechanism of failure of Li-ion cells during overcharge under adiabatic and non-adiabatic conditions.

The objectives to meet this aim are:

1) Investigate the overcharge behaviour of cells in non-adiabatic conditions
2) Investigate the overcharge of cells in adiabatic conditions
3) Study the effect of the magnitude of the overcharging current

6.4 Methodology

6.4.1 Theory and Equipment Used

An adiabatic environment is one where heat is neither lost nor added to the system. Hence, the cell itself should always be at the same temperature as its surrounding. If the cell temperature rises, the temperature of its surrounding should also rise by the same amount. Shown in Figure 6-1, an extended volume accelerating rate calorimeter (ARC) made by Thermal Hazard Technology (THT) was used for this purpose. In the ARC, the temperature of the cell is continuously monitored and the temperature of its surrounding is changed to match it. This is done by a feedback control loop and a series of thermocouples and electric heaters. However, it should be noted that a perfect adiabatic environment is never obtained. Therefore, the quality of an adiabatic calorimeter relates to its ability to maintain the temperature difference between the sample under test and its environment as close to zero as possible [181].

Figure 6-2 shows a block diagram of the ARC system showing its components and explaining its operation. The electronic support unit (ESU) contains all the electronics for running and controlling the system. During operation the thermocouple signals from the calorimeter vessel are sent to the ESU. The accurate performance of the thermocouples is crucial for the operation of the ARC since they are used for temperature control. There are three thermocouples in the calorimeter vessel; side, base and top. The ESU compares the temperatures from these 3 thermocouples to

the temperature from the thermocouple on the cell. According to this, the heating power is adjusted so that the difference in temperature between the cell thermocouple and vessel thermocouples is almost 0 °C. The efficient operation of this system is the basis of adiabatic operation.

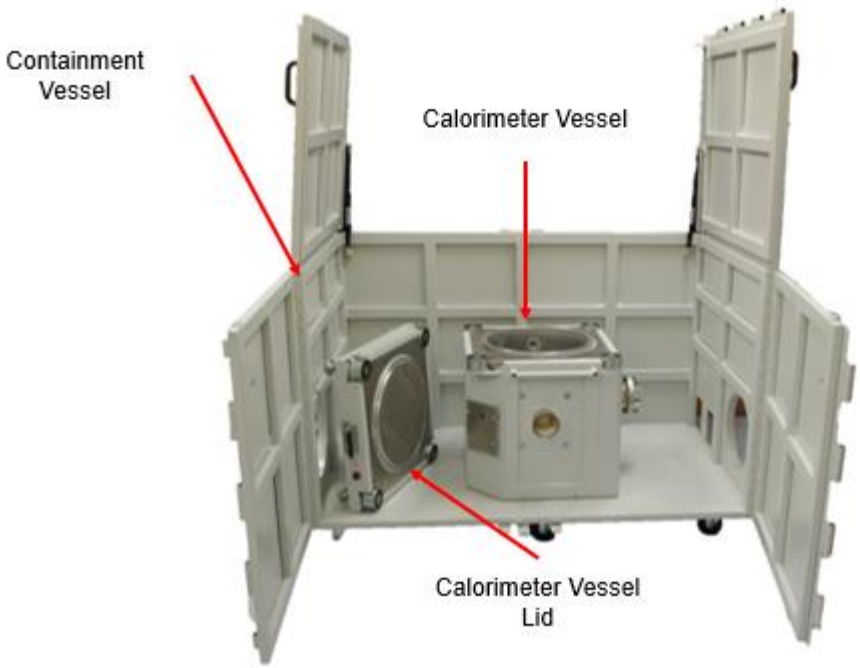

Figure 6-1: Photograph of the extended volume accelerating rate calorimeter used in the adiabatic overcharge test [181]

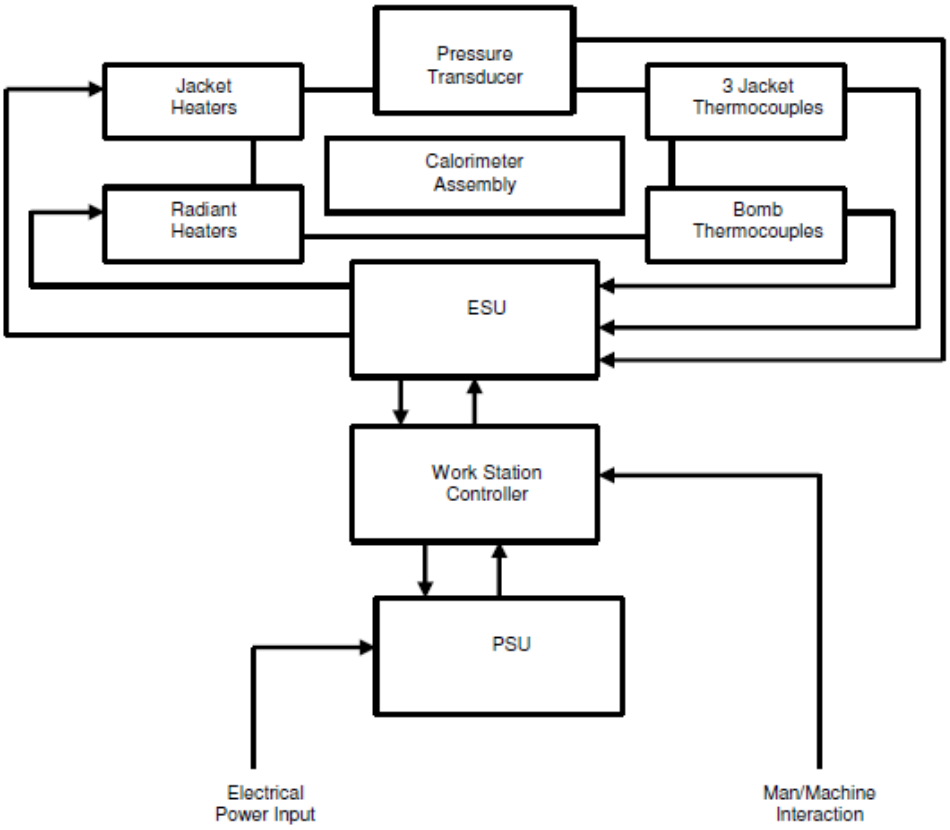

Figure 6-2: A block diagram of the accelerating rate calorimeter system showing its components and operation [181]

6.4.2 Experimental Procedure

The cells were divided into two groups. Group one consisted of cells overcharged in the ARC and group two were overcharged in ambient conditions i.e. non-adiabatic environment. All Cells were preconditioned to a fully charged state using the procedure in Section 4.5.2.1.

In order to overcharge the cells in an adiabatic environment, a Maccor cycler was used in combination with the ARC. Before putting the cell in the calorimeter, the current carrying wires were soldered to the cell tabs to ensure good contact. Inside the calorimeter vessel cells were attached to a metal mounting frame/rig by an aluminium tape. The metal was put above a thermal brick to provide thermal insulation between the bottom of the calorimeter and the cell for accurate temperature monitoring. The ARC thermocouple (N-Type) used to track the cell's temperature was securely attached to the centre of the cell's surface by an aluminium tape. Another two cycler

thermocouples (T-Type) were attached to the centre of the cell, this provided the synchronisation of the temperature data with the voltage and current. The calorimeter vessel is equipped with input ports to connect between the cell and the cycler. The maximum voltage limit of the cycler was 8.0 V. Figure 6-3 shows the set up inside the ARC vessel.

The start temperature at which the overcharge started was set to 20 °C and the wait step time was set to 5 min. The temperature rate sensitivity was 0.02 °C /min. The temperature step was set to 0 °C, so that the calorimeter did not heat the cell and only tracked the cell temperature under adiabatic conditions. The maximum heating capability of the calorimeter used was 15 °C /min. Table 6-1 summarises the main test parameters and their description.

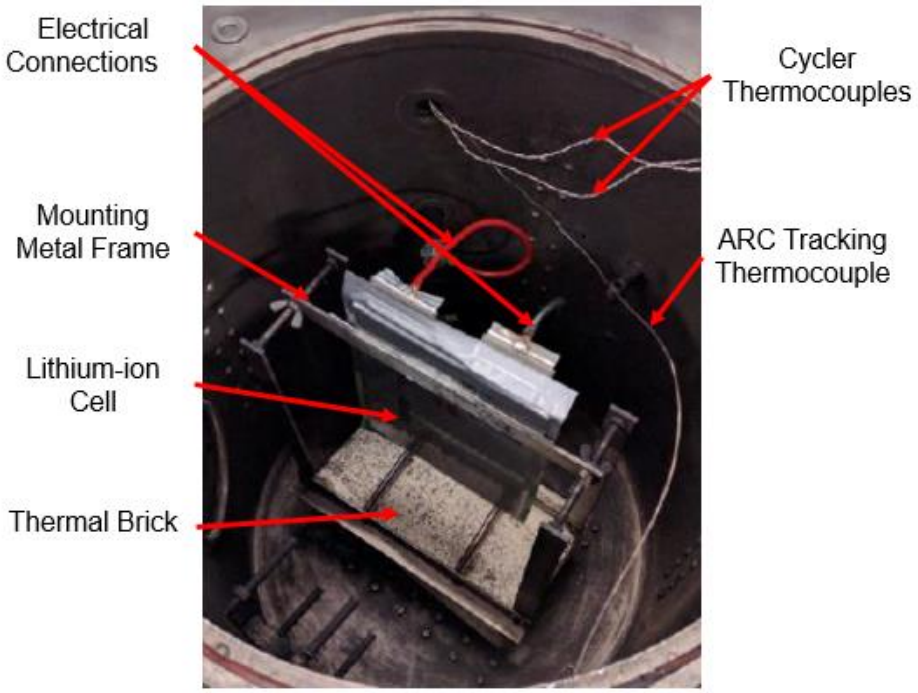

Figure 6-3: Overcharge test set-up inside calorimeter vessel

Table 6-1: Main ARC set-up parameters for overcharge test

Test Parameter	Value	Description
Start Temperature (°C)	20	Temperature at which the cell is stabilised at the start of the test
End Temperature (°C)	305	Temperature at which the test is terminated

Temperature Rate Sensitivity (°C /min)	0.02	Self-heating rate above which self-heating activity is detected
Temperature Step (°C)	0	Temperature by which the cell is raised after failure to detect self-heating
Wait Time (min)	5	Period of time during which calorimeter thermal transients are allowed to settle

For comparison, the second group of cells were overcharged in ambient conditions outside the calorimeter. The test temperature was 20 °C, the same as the starting temperature of the adiabatic overcharge and both groups were overcharged with the same regime. Different C-rates were used to overcharge the cells. Cells in adiabatic environments were overcharged with 0.13 C, 0.33 C and 1.3 C and cell charged in ambient conditions were overcharged with 0.13 C and 1.0 C. The overcharge regime started with a 30-minute rest step followed by a constant current charge until the voltage limit of the cycler was reached (8.0 V), then extended rest period to monitor the behaviour of the cell after the overcharge was terminated. It should be highlighted that the nonmatching C-rates, was due to the limited access to the test facilities. Table 6-2 summaries the overcharge steps and a screenshot of the programme is shown in Section (0 of the Appendix.

Table 6-2: Steps of the overcharge regime

Step No.	Step Description	Condition
1	Rest	30 min
2	Constant current charge	7.9 V
3	Rest	24 hr
4	End	

6.5 Results and Discussion

6.5.1 Overcharge Behaviour in a Non-adiabatic Environment

Figure 6-4 shows the voltage, temperature and current profiles during a 1.0 C and 0.13 C constant current overcharge tests in non-adiabatic conditions. Starting from a 100% SOC at around 4.2 V and an ambient temperature of 20 °C the cells were charged

using a constant current. For the 1.0 C overcharge in Figure 6-4a, as the voltage and cell surface temperature increased with time as the cell was being overcharged. The increase in voltage from 4.2 V to 5.0 V appeared to be steady. Around 5.0 V marked a noticeable change in the rate of voltage increase and the rate of temperature rise. This suggests an increase in the cell resistance as a result of cell swelling, which was also noticed around 5.0 V. This can be attributed to gas generation as a result of overcharge. There are a number of mechanisms that could account for gas generation, such as the decomposition of the electrolyte as outlined in Section 5.4.4, Chapter 5.

Around 5.32 V there was a sudden increase in the cell voltage and temperature, this increase suggests a further increase in the cell resistance. The cell voltage peaked at 5.57 V, then fell slightly before finally sharply rising, in a few minutes, from 5.57 V to 7.9 V, where the overcharge stopped as it was the voltage limit of the cycler. The maximum temperature reached was 70.0 °C. After the current flow stopped there was not further increase in the temperature and cells started to cool down. The cell voltage drops to around 4.7 V after the test.

Although by the end of the test the cells were significantly swollen, they did not vent and there was no fire or explosion in both C-rate cases. This outcome does not agree with the findings of other studies where charging at high C-rates in ambient conditions resulted in cells going into thermal runaway, whereas lower C-rates did not [29] [90]. This shows that the outcome of an overcharge events does not just depend on the C-rate, but also on other factors, such as cell design, dimensions and capacity. The voltage behaviour of cells overcharged using 0.13 C, shown in Figure 6-4b was similar. However, their temperature profile was more spread and they reached a lower maximum temperature (35.0 °C).

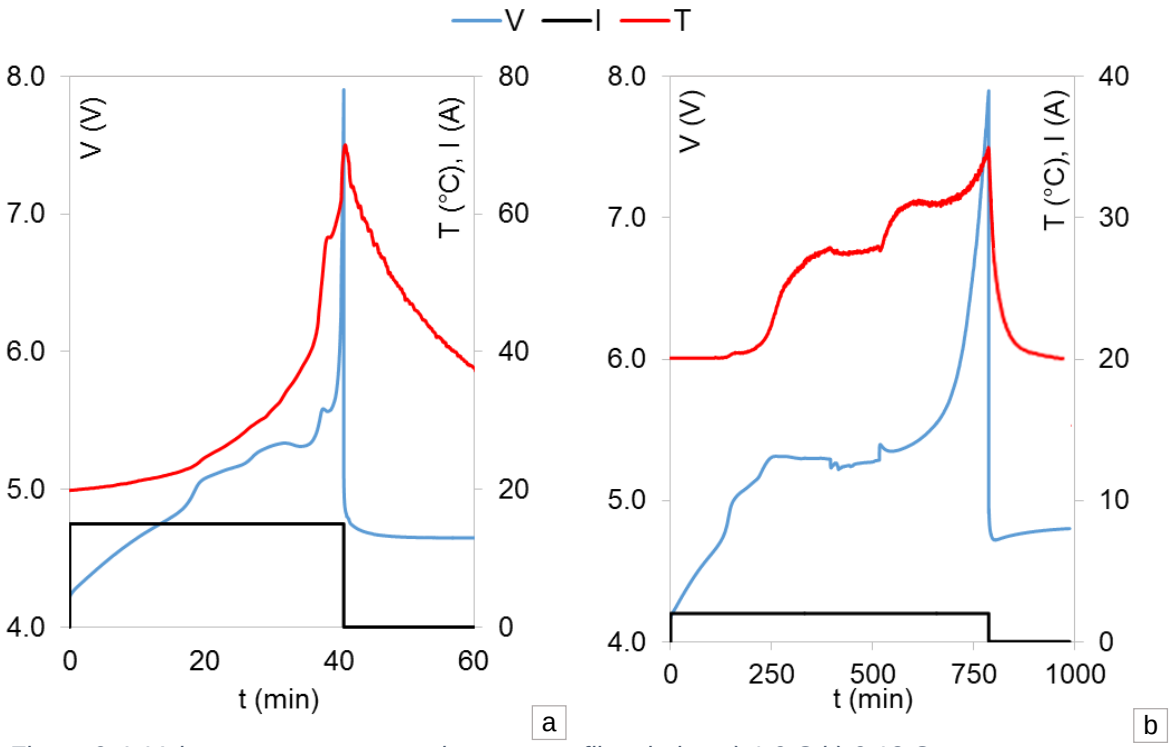

Figure 6-4: Voltage, temperature and current profiles during a) 1.0 C b) 0.13 C constant current overcharge test in non-adiabatic conditions

Figure 6-5 shows the corresponding voltage and cell surface temperature profile as a function of SOC. The SOC was calculated based on coulomb counting, as the current was multiplied by the charging time. The reference capacity for 100% SOC was used for each cell from its preconditioning regime. It should be pointed out though that this calculation assumes 100% coulombic efficiency. At the same SOC the higher C-rate resulted in higher voltage and temperature. This is because higher current cause higher voltage drop *(V=IR)* and more Ohmic heating *(I^2R)*.

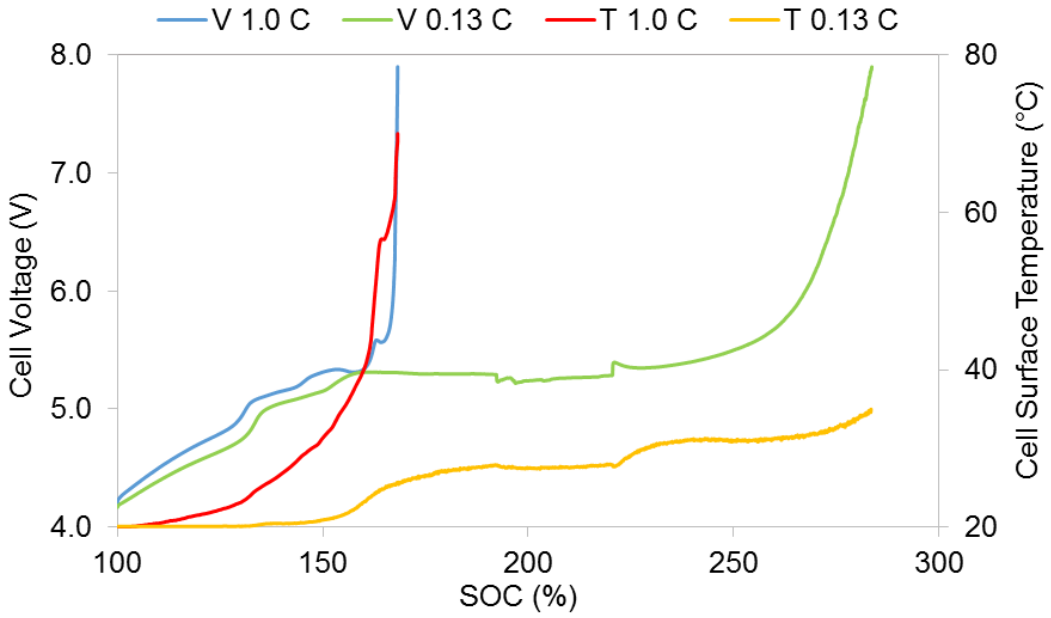

Figure 6-5: Voltage and temperature profiles as a function of SOC during overcharge in non-adiabatic conditions

6.5.2 Overcharge Behaviour in an Adiabatic Environment

Overcharge in the ARC was done to simulate the cell behaviour in low heat dissipation conditions. Figure 6-6 shows the voltage and temperature profiles during 0.13, 0.33 and 1.3 C constant current overcharge test in adiabatic conditions. Starting at 4.2 V and 20 °C, as the cell was being charged the cell voltage and temperature increased steadily. The voltage profile was similar to that of cells charged in ambient conditions, but the temperature rise was steeper, since there was not heat dissipation. Around 5.0 V marked a noticeable change in the rate of voltage increase and the rate of temperature rise. This can be attributed to an increase in Ohmic heating as a result of cell resistance increase [182] [183].

Around 5.32 V there was a sudden increase in the cell voltage and temperature, this increase suggests a further increase in the cell resistance mainly due to the separation of the cell layers as a result of swelling. The cell voltage peaked at 5.57 V, then fell slightly before finally sharply rising, in a few minutes, from 5.57 V to 7.9 V, where the overcharge stopped as it was the voltage limit of the cycler. At this point there was no further Ohmic heating as the current flow was stopped.

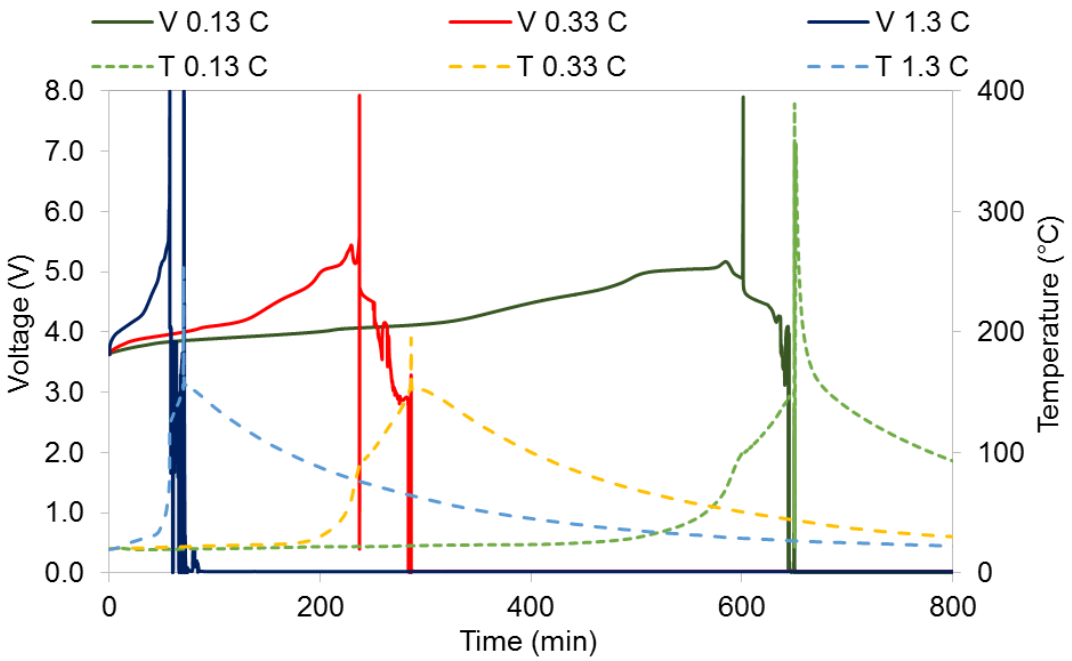

Figure 6-6: Voltage and temperature profiles during 0.13, 0.33 and 1.3 C constant current overcharge test in adiabatic conditions

Figure 6-7 is a magnification to show the cell behaviour after the current was stopped and the incubation period before thermal runaway. Once the overcharged was stopped the cell voltage started to relax and drop down, whereas the temperature continued to rise. This confirms that at this point heating was only caused by exothermic reactions. The cell temperature at this point was around 90 °C, which is higher than the temperature at which the SEI starts to decompose [184]–[188]. After losing its SEI the anode starts to react with the electrolyte releasing heat [84].

Heat build-up caused the temperature to rise further. The shape of the voltage profiles suggests a shorting behaviour, as parts of the separator were compromised due to its melting [182]. This can be confirmed by the temperature data as the temperature exceeded the melting point of most separator materials (around 125 °C for polyethylene and 155 °C for polypropylene) [189], [190]. Separator melting usually triggers a large heat output induced by an internal short [29]. This is a possible failure mechanism for the cells going into thermal runaway. The temperature rises exponentially when thermal runaway happens, the temperature profiles in Figure 6-7 turns into an approximately vertical line when thermal runaway happened. It should be noted that these failures occurred at temperatures well below the thermal runaway

temperatures for cathode materials (NMC and LMO) [191]–[193], backing the suggestion that the failure/melting of the separator, causing an internal short circuit is the cause of the thermal runaway. Table 6-3 summarises the main findings of the different C-rates.

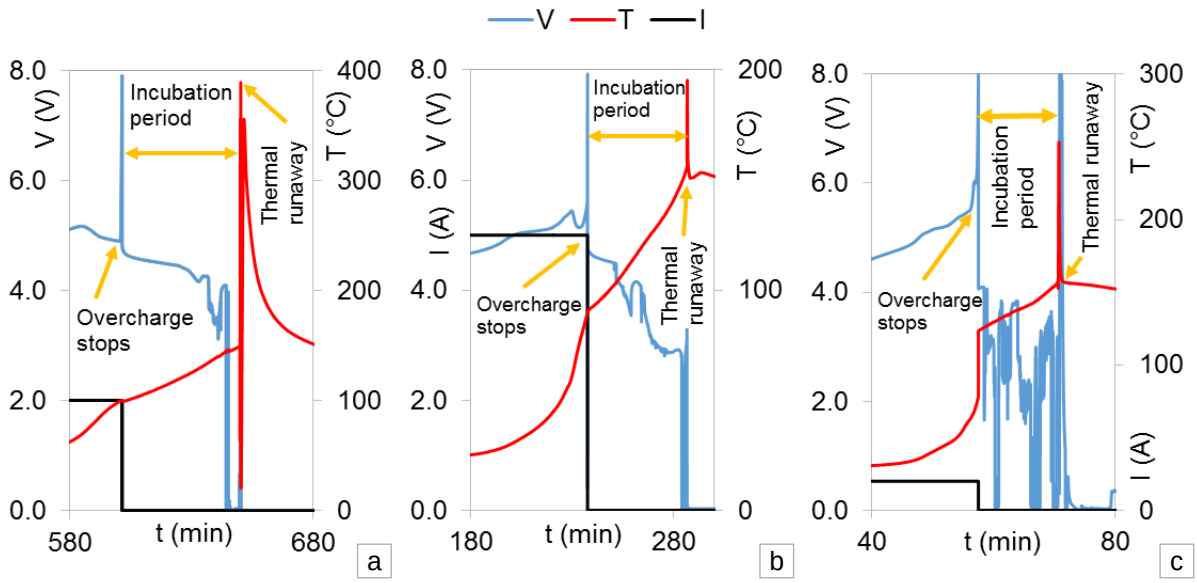

Figure 6-7: Voltage, current and temperature profiles of cells charged in adiabatic environment using different C-rates showing separator shutdown, failure incubation period and thermal runaway a) 0.13 C b) 0.33 C c) 1.3 C

Table 6-3: Summary of the main findings of adiabatic overcharge

C-Rate	Time to Overcharge Stop (min)	Overcharge Stop Temperature (°C)	Failure Incubation Period (min)	Charge added to the cell (Ah)	Failure SOC (%)	Failure Mode
0.13	602	99	48	20.0	233.8	Rupture
0.33	237	91	49	19.8	230.6	Fire
1.3	58	86	14	19.0	227.3	Fire

Figure 6-8 shows the photographs of cells after overcharge in the ARC under adiabatic conditions. Figure 6-8a shows that the cell charged using 0.13 C was significantly swollen and ruptured, however, it did not catch fire. Figure 6-8b shows what happened to cells charged using 0.33 C and 1.3 C. The shape of the cells suggest that they were swollen before they were completely combusted. This shows that the overcharge current magnitude is a crucial factor in determining the outcome of the overcharge test

in adiabatic conditions. This outcome agree with previous studies done on prismatic cells in ambient conditions, where at low currents the cells remained intact, but ruptured at higher currents [112].

Figure 6-8: photographs of cells after overcharge in adiabatic conditions a) 0.13 C b) 0.33 and 1.3 C overcharge currents

6.6 Chapter Conclusion

The outcomes of overcharge tests in ambient conditions (non-adiabatic) and inside a calorimeter (adiabatic) were completely different. Cells overcharged in ambient conditions were swollen, but did not rupture nor ignite. All cells overcharged in adiabatic conditions either ruptured or caught fire depending on the charging C-rate. C-rates as low as 0.13 C and as high as 1.3 C were used. In ambient conditions using lower current resulted in lower rate of voltage and temperature increase. However, more energy was put into the cell before the OC test stopped when a lower C-rate was used. In adiabatic conditions lower C-rate (0.13 C) on resulted in cell rupture, whereas high C-rates (0.3 and 1.3 C) resulted in the catching fire. These results highlight that heat dissipation from the cell during overcharge is critical in determining the outcome of the overcharge test. In adiabatic conditions the magnitude of the overcharge current determines the cell failure mode. Future work would include pressure monitoring in order to detect when cells vent or rupture and studying the failure incubation period.

6.7 Recommendations for Future Work

This study can be made more comprehensive by monitoring the pressure inside the calorimeter in order to detect when the cells vent or rupture. This can be correlated with the temperature and voltage data in order to gain a better understanding of the failure stages. The study can also be extended to other cell formats, chemistries and capacities.

Chapter 7 – Potential Industrial Applications

There are a number of potential industrial applications that could benefit from the findings of this work. The findings have already assisted JLR in making some decisions, such as cell selection and test design. Moreover, the data has been used by JLR's battery modelling and simulation team. The following sections briefly describe some of the potential industrial applications:

7.1 Failure Mode Analysis

Failure modes, mechanisms and effects analysis (FMMEA) is "a systematic methodology to identify potential failure mechanisms and models for all potential failure modes, and to prioritize failure mechanisms" [44]. A systematic approach such as the FMMEA should be used to evaluate the safety performance of Li-ion cells under abusive conditions to ensure that the outcome is safe. Knowledge of all underlying causes and routes that lead to catastrophic failure is important, since a cell can take different routes to failure. An example for this would be from Chapter 6, where just changing the charging C-rate changed the failure mode from the cell just rupturing to catching fire.

The information from these test can be used for FMMEA. There have been a number of studies investigating the reliability and safety of Li-ion batteries based on applying failure mode analysis on testing data [194], [195]. The outcome provides a framework for defining ways Li-ion cells can fail, the mechanisms and stages of the failure process and their possible outcomes. The outcome from the FMMEA can be used in a number of applications as outlined in the following sections such as, cell and pack design, on-board diagnostics and developing models to predict failure [44]. Knowledge of all underlying causes and mechanisms that lead to catastrophic failure can also assist in the design of new safety mechanisms and advanced control techniques that detect and prevent the onset of battery fires and explosions.

7.2 Improvement of Cell Abuse Tolerance

Understanding the stages of failure the cell goes through when subject to a specific type of abuse and the degradation mechanisms can help make the cells more tolerant to abuse conditions [196]. Understanding how a cell fails and the role of each

component plays in the failure process can help reengineer the cell design, add safety mechanisms and/or change its materials.

7.3 Battery Pack Design

An evaluation of all aspects of the battery pack design and its safeguards is necessary to minimise the occurrence of potential unsafe failure modes. As explained in Table 2-2 a graceful failure at cell or module levels can be acceptable, but a failure at pack level is unacceptable. Therefore, it is useful to incorporate the outcome of failure analysis of abuse testing into all accepts of the battery pack design.

Electrical design and operational limits

The results obtained from these tests can be used to redefine the operational and design limits/boundaries, within which the safety hazards and capacity degradation problems can be minimised. It can be used to map and extend the voltage and C-rate ranges for safe operation at higher rates of charge/discharge. Since new cell chemistries and designs are in progress, redefining its operational boundary is important for efficient and safe operation. The specific capacity of the cell almost increases linearly with the voltage from 4.2 V to 4.7 V, as the cell energy is proportional to the voltage multiplied by its capacity, operation at higher voltage leads to an increase in energy density [56]. For example as presented in Chapter 6, investigating the effect of charging the cells to different voltages at different C-rates can help understand the trade-offs between short-term gains and long term implications. Moreover, it provides information about the safety behaviour of cells at higher voltages/states of charge.

Thermal design

The operating temperature is one of the main challenges of Li-ion batteries [197]. The thermal design is key when it comes to the safety, ageing and long-term performance of the battery. When it comes to safety triggering thermal runaway must be avoided. This can be achieved by making sure that exothermic reactions are not triggered by maintaining the temperature of the cell below the onset temperature even during an abnormal scenario [198]. This can be achieved by a thermal management system and cooling system, that is designed to cope with abnormal conditions. This can significantly enhance the safety and abuse tolerance of the battery.

The importance of heat dissipation during an abusive event was highlighted in Chapter 6, where cells overcharged in ambient conditions showed graceful failure, whereas cells overcharged in environment where heat was not dissipated from them suffered thermal runaway. Findings from these tests can be used to size the cooling system and managing the cooling strategy.

The experimental findings show that during the progression of failure, cells do not heat up evenly and that there are hot spots and temperature gradients, as Section 3.6.3.1 and Section 4.6.2.2 shows for the nail penetration and for the external short circuit case respectively. This data can be incorporated into the emergency thermal management strategy.

Mechanical/structural design

The mechanical design is involved with every component of the battery pack, including the enclosure of the individual cells and the whole pack and the supporting structure. Individual cells in the module are usually exposed to some pressure for optimum performance [102] [199]. This pressure should be evenly distributed and be compliant with the changes in cell volume during cycling as shown in Figure 5-11 for changes in cell volume with voltage.

Overcharged cells experience more volume increase/swelling. The swelling of pouch cells can cause mechanical stresses on components around them such as, the cooling plates and neighbouring cells. Swelling has been reported as a common cause of battery pack enclosure damage [200]. The findings from the change in volume as a result of overcharge presented in Chapter 5 is useful for designing the individual pack components and the enclosure, to make sure it withstands the stresses in the case of overcharge. Also knowing the cell shape when overcharged and mapping its pressure as a result of an overcharge event can be useful when designing safety features for an OC event, such as, gas vent/relief valve [201], [202].

Safety mechanisms design

Safety mechanisms can be mechanical such as pressure relief values, gas vents, and mechanical barriers to minimise physical damage, or electrical such as fuses and circuit breakers.

The nail penetration findings presented in Chapter 3 can be used as an input for the design of a protection barrier. The quantification of the current magnitude under different short circuit scenarios as presented in Chapter 4 can be used to assess the need for fuses. For example, would equipping individual cells with fuse improve the safety, or is it sufficient to fuse at module and pack level. The rating of circuit breakers can also be sized based on the current data.

7.4 On-board Fault Diagnostics and Control Techniques

Safety concerns regarding Li-ion batteries have led to the development of specialised systems to monitor and protect them from failure [203]. The BMS employs safety mechanisms and control strategies to mitigate failure. Including fault diagnosis in the BMS is necessary to ensure battery safety. The International Electrotechnical Commission's (IEC) BMS standard requires that it must include fault diagnosis functions. The Chinese standards for BMS specifications also require the BMS to be equipped with fault diagnosis function [204].

Knowing the root causes and mechanisms of failure can assist in the design of control techniques that detect and prevent the onset of battery fires and explosions. Hence, the experimental data can be used to develop algorithms to be implemented for on-board monitoring of the battery pack [205].

Analysis of data such as capacity fade, impedance and OCV characteristics can be used by the BMS to monitor the SOS and SOH of the cell. Algorithms can be developed to help the BMS avoid cell overcharge [80]. Analysis of the EIS components can give an indication of the degradation mechanisms and hence how to reduce them, a more accurate prediction of the cycle life can also be made [117], [121]. The external short circuit data can also be used to develop active diagnostics to detect any short circuits that stops the current quicker than relying on passive fuses.

7.5 Modelling Work

Cell abuse testing data can be used as inputs for battery abuse models. Cell voltage, temperatures, heat generation rates and gas generation can help models predict the response of a system to abnormal abusive conditions. System safety can be enhanced by using physics-based models informed by an FMMEA. The cell level outputs can be used to simulate module and pack response, hence reducing the time and cost needed for abuse testing [44], [65].

The nail penetration test data output was passed onto the modelling team at JLR. Correlation between the external short circuit and nail penetration tests were used to build a model that predicts the short resistance and hence the short current during nail penetration test. Further details about this model cannot be disclosed for confidentiality reasons.

7.6 Development of Test Procedures and Safety Protocols

A key challenge to ensure the safety and reliability of Li-ion batteries is the development of representative and meaningful tests [68]. Changes to the test conditions can lead to significantly different responses [206]. The findings from these tests can be used in the development of more representative test procedures, such as changing the nail properties in the case of the nail penetration test, quantifying the volume increase in the case of overcharge, and testing the cells in environmental conditions more representative of the usage conditions, such as low heat dissipation environments, as carried out in Chapter 6.

The findings can also be used to develop safety protocols. For example, the result of chapter 6 shows that the timing of thermal runaway can be delayed after the abuse event ceases. In the case of overcharge in a low heat dissipation environment, although the current was stopped, the cell temperature continued to rise and thermal runaway took place almost an hour later.

7.7 Design of Test Equipment

The apparatus used for the in-situ gas measurement shown in Figure 5-4 and Figure 5-5 was designed and built in-house with off-the-shelf components. This provides the advantages of modification flexibility, scalability and ease of maintenance and running,

all at a relatively low cost. Hence, different cells sizes can be easily tested. The external short circuit rig was also designed and built in house, it offers the flexibility of testing different cells under different short resistances and short durations.

7.8 Reuse of Abused Cells

Cycling the cells after a number of overcharge and external short circuit scenarios showed that after some abuse conditions the cells did not degrade significantly. In the case of overcharge, if the degree of overcharge is limited the damage was minimal. In the case of the external short circuit, limited short circuit durations and currents did not seem to cause significant damage to the cells. This can open the door for the use of cells exposed to abuse, if it is proved to be safe and if its performance is not severely degraded. Based on the experimental data a test procedure (and a model) can be built to assess the state of health/safety of the abused cells to decide if they fit for reuse. Correlation studies between the cell capacity and impedance can be used to for quick assessment of the SOH of the cell [207]. An increase in the cell's impedance usually translates to loss in its power capabilities. However, if cells fail to meet the requirements of a certain application, such as, in EVs, they can be used in other applications such as stationary energy storage applications [208].

Chapter 8 – Conclusion

This innovation report has highlighted the important role of Li-ion batteries in the electrification of transport. The safety of Li-ion batteries is a significant challenge that must be continually addressed as battery development evolves. A number of abuse tests were carried out on commercial automotive pouch Li-ion cells to investigate their behaviour under a number of abusive conditions; mechanical penetration, external short circuit, cell swelling as a result of overcharge and overcharge in an adiabatic environment.

Results from nail penetration test (Chapter 3) show that changing the nail material and diameter affect the outcome of the nail penetration test. However, it also shows the high variability in the outcome of nail penetration test. This suggests the need for the development of more reliable tests.

Externally short-circuiting (Chapter 4) the cells showed that their behaviour during an external short circuit event depends on both the short current and short duration. After the external short circuit event cells were successfully cycled. However, they suffered more capacity fade and resistance increase than non-abused cells. The degree of damage was proportional to the duration of the short circuit. Cells short-circuited for longer durations suffered more capacity fade and resistance increase.

In-situ monitoring of the cell volume during overcharge (Chapter 5) showed that the degree of overcharge and the magnitude of the charging current determine the extent of cell swelling. Swelling was partially reversible after the cell returned to its normal operating voltage range. Cycling of the cell after the overcharge event showed that the extent of impedance increase and capacity fade depend on the degree of overcharge and the magnitude of the charging current.

Cycling the cells after an external short circuit or overcharge events showed that cells can be reused after an abuse event. However, all abused cells suffered a degree of damage, in terms of impedance increase and capacity fade. Moreover, during operation after abuse their operating temperature is higher than the non-abused cells as a result of their internal resistance increase.

Heat dissipation during an overcharge event is critical in determining the outcome of the test (Chapter 6). Cells overcharged in ambient conditions were swollen, but did not

rupture nor ignite. Whereas, all cells overcharged in adiabatic conditions either ruptured or caught fire depending on the charging C-rate. This also highlights the role of magnitude of the charging current in the failure mechanism.

The experimental findings from these abuse tests carried out have a number of industrial applications, such as failure analysis, battery pack design, on-board diagnostics, developing abuse models and development of test procedures.

References

[1] International Energy Agency, “Key world energy statistics,” *Statistics (Ber).*, p. 80, 2016.

[2] US Energy Information Administration, “International Energy Outlook 2016,” 2016.

[3] British Petroleum, “BP Statistical Review of World Energy,” *BP Stat. Rev. World Energy*, no. June, pp. 1–48, 2016.

[4] US Department of Energy, “Advancing Clean Transportation and Vehicle Systems and Technologies | Internal Combustion Engines,” 2015.

[5] US Environmental Protection Agency, “Sources of Greenhouse Gas Emissions.” [Online]. Available: https://www.epa.gov/ghgemissions/sources-greenhouse-gas-emissions. [Accessed: 03-Apr-2017].

[6] “Cars and air pollution,” *Department for Transport* . [Online]. Available: http://www.dft.gov.uk/vca/fcb/cars-and-air-pollution.asp. [Accessed: 03-Apr-2017].

[7] “UK air pollution ‘linked to 40,000 early deaths a year’ - BBC News,” 2016. [Online]. Available: http://www.bbc.co.uk/news/health-35629034. [Accessed: 16-Apr-2018].

[8] International Energy Agency, “Global EV Outlook 2016 Electric Vehicles Initiative,” *Iea*, p. 51, 2016.

[9] Clean Energy Ministerial, “Electric Vehicles Initiative (EVI) | Clean Energy Ministerial.” [Online]. Available: http://www.cleanenergyministerial.org/Our-Work/Initiatives/Electric-Vehicles/Activities. [Accessed: 03-Apr-2017].

[10] United Nations, “Paris Declaration on Electro-Mobility and Climate Change & Call to Action,” 2015.

[11] D. Doughty and A. Pesaran, “Vehicle Battery Safety Roadmap Guidance,” 2012.

[12] B. Scrosati and J. Garche, “Lithium Batteries: Status, Prospects and Future,” *J. Power Sources*, vol. 195, no. 9, pp. 2419–2430, May 2010.

[13] C. Cluzel and C. Douglas, “Cost and Performance of EV Batteries,” 2012.

[14] B. Schott, A. Püttner, and M. Müller, “The market for battery electric vehicles,” 2015.

[15] U. D. of Energy, “Overview of the DOE Advanced Battery R&D Program,” 2015.

[16] PWC, “State of the Plug-in Electric Vehicle Market,” 2013.

[17] Parliament of the United Kingdom, “Climate Change Act 2008 Carbon Target and Budgeting - The Target for 2050,” 2008.

[18] Committee on Climate Change, “Meeting Carbon Budgets – 2014 Progress Report to Parliament Meeting,” 2014.

[19] C. Cluzel, E. Standen, B. Lane, and J. Anable, “Pathways to high penetration of electric vehicles - Report prepared for Committee on Climate Change,” 2013.

[20] International Renewable Energy Agency, “Roadmap for a Renewable Energy Future,” 2016.

[21] The Houses of Parliament, “Electric Vehicles,” 2010.

[22] Y.-E. Hyung, S.-I. Moon, D.-H. Yum, and S.-K. Yun, “Fabrication and evaluation of 100 Ah cylindrical lithium ion battery for electric vehicle applications,” *J. Power Sources*, vol. 81–82, pp. 842–846, Sep. 1999.

[23] P. I. M. Keyser *et al.*, “Numerical and Experimental Investigation of Internal Short Circuits in a Li-ion Cell,” 2011.

[24] P. Ramadass, W. Fang, and Z. Zhang, “Study of internal short in a Li-ion cell I. Test method development using infra-red imaging technique,” *J. Power Sources*, vol. 248, pp. 769–776, 2014.

[25] F. Larsson and B.-E. Mellander, “Abuse by External Heating, Overcharge and Short Circuiting of Commercial Lithium-Ion Battery Cells,” *J. Electrochem. Soc.*, vol. 161, no. 10, pp. A1611–A1617, Jul. 2014.

[26] D. H. Doughty and C. C. Crafts, “FreedomCAR Electrical Energy Storage System Abuse Test Manual for Electric and Hybrid Electric Vehicle Applications,” 2005.

[27] D. Doughty and E. P. Roth, “A General Discussion of Li Ion Battery Safety,” *Electrochem. Soc. Interface*, vol. 2, no. 21, pp. 37–44, 2012.

[28] Hybrid Commercial Vehicle, “D6200.1 Specification of testing standard for high-voltage components.”

[29] S. Tobishima and J. Yamaki, “A consideration of Lithium Cell Safety,” *J. Power Sources*, vol. 81–82, pp. 882–886, Sep. 1999.

[30] P. G. Balakrishnan, R. Ramesh, and T. Prem Kumar, “Safety mechanisms in lithium-ion batteries,” *J. Power Sources*, vol. 155, no. 2, pp. 401–414, Apr. 2006.

[31] E. P. Roth, “Abuse Response of 18650 Li-Ion Cells with Different Cathodes Using EC:EMC/LiPF6 and EC:PC:DMC/LiPF6 Electrolytes,” in *ECS Transactions*, 2008, vol. 11, no. 19, pp. 19–41.

[32] D. D. MacNeil, “Comparison of the Reactivity of Various Carbon Electrode Materials with Electrolyte at Elevated Temperature,” *J. Electrochem. Soc.*, vol. 146, no. 10, p. 35963602, 1999.

[33] B. Barnett, D. Ofer, S. Sriramulu, and R. Stringfellow, “Lithium-Ion Batteries, Safety,” in *Batteries for Sustainability*, New York, NY: Springer New York, 2013, pp. 285–318.

[34] M. Held and R. Bronnimann, “Safe cell, safe battery? Battery fire investigation using FMEA, FTA and practical experiments,” *Microelectron. Reliab.*, vol. 64, pp. 705–710, 2016.

[35] E. C. Castillo, “18 – Standards for electric vehicle batteries and associated testing procedures,” in *Advances in Battery Technologies for Electric Vehicles*, Elsevier Ltd., 2015, pp. 469–494.

[36] D. H. Doughty, “SAE J2464 ‘EV & HEV Rechargeable Energy Storage System (RESS) Safety and Abuse Testing Procedure,’” 2010.

[37] “J2929: Electric and Hybrid Vehicle Propulsion Battery System Safety Standard - Lithium-based Rechargeable Cells - SAE International.” [Online]. Available: http://standards.sae.org/j2929_201102/. [Accessed: 24-Jul-2015].

[38] International Electrotechnical Commission, “IEC 62660-2:2010 Secondary

lithium-ion cells for the propulsion of electric road vehicles - Part 2: Reliability and abuse testing," 2010. [Online]. Available: https://webstore.iec.ch/publication/7332. [Accessed: 05-Apr-2017].

[39] "ISO 12405-1:2011 - Electrically propelled road vehicles - Test specification for lithium-ion traction battery packs and systems - Part 1: High-power applications." [Online]. Available: http://www.iso.org/iso/catalogue_detail?csnumber=51414. [Accessed: 24-Jul-2015].

[40] UL, "UL 2580 Standard for Safety - Batteries for Use In Electric Vehicles," 2013.

[41] Automotive Industry Standard, "Battery Operated Vehicles - Safety Requirements of Traction Batteries," 2009.

[42] United Nations, "Transport of Dangerous Goods - Manual of Tests and Criteria," New York and Geneva, 2015.

[43] National Standard of the People's Republic of China, "Safety Requirements and Test Methods for Traction Battery of Electric Vehicle GB/T 31485-2015," 2015.

[44] C. Hendricks, N. Williard, S. Mathew, and M. Pecht, "A failure modes, mechanisms, and effects analysis (FMMEA) of lithium-ion batteries," *J. Power Sources*, vol. 297, pp. 113–120, 2015.

[45] P. D. O`Mara, "Failure Modes and Effects Analysis," in *Aircraft System Safety - Assessments for Initial Airworthiness Certification*, 2013, pp. 1–7.

[46] Q. Wang, P. Ping, X. Zhao, G. Chu, J. Sun, and C. Chen, "Thermal runaway caused fire and explosion of lithium ion battery," *J. Power Sources*, vol. 208, pp. 210–224, Jun. 2012.

[47] A. K. Masaki Yoshio, Ralph J. Brodd, *Lithium-Ion Batteries Science and Technology*. New York: Springer, 2009.

[48] E. P. Roth, D. H. Doughty, and D. L. Pile, "Effects of separator breakdown on abuse response of 18650 Li-ion cells," *J. Power Sources*, vol. 174, no. 2, pp. 579–583, Dec. 2007.

[49] S. S. Zhang, "A review on the separators of liquid electrolyte Li-ion batteries," *J. Power Sources*, vol. 164, no. 1, pp. 351–364, Jan. 2007.

[50] A. Sheidaei, X. Xiao, X. Huang, and J. Hitt, “Mechanical behavior of a battery separator in electrolyte solutions,” *J. Power Sources*, vol. 196, no. 20, pp. 8728–8734, Oct. 2011.

[51] C. J. Orendorff, “The Role of Separators in Lithium-Ion Cell Safety,” *Electrochem. Soc. Interface*, vol. 21, no. 2, pp. 61–65, 2004.

[52] M. Broussely, “Battery Requirements for HEVs, PHEVs, and EVs: An Overview,” in *Electric and Hybrid Vehicles*, 1st ed., G. Pistoia, Ed. Elsevier, 2010, pp. 305–345.

[53] P. Arora, “Capacity Fade Mechanisms and Side Reactions in Lithium-Ion Batteries,” *J. Electrochem. Soc.*, vol. 145, no. 10, p. 3647, 1998.

[54] M. Dubarry, C. Truchot, and B. Y. Liaw, “Synthesize battery degradation modes via a diagnostic and prognostic model,” *J. Power Sources*, vol. 219, pp. 204–216, 2012.

[55] X. Han, M. Ouyang, L. Lu, J. Li, Y. Zheng, and Z. Li, “A comparative study of commercial lithium ion battery cycle life in electrical vehicle: Aging mechanism identification,” *J. Power Sources*, vol. 251, pp. 38–54, 2014.

[56] H. Zheng, Q. Sun, G. Liu, X. Song, and V. S. Battaglia, “Correlation between dissolution behavior and electrochemical cycling performance for LiNi 1/3Co 1/3Mn 1/3O 2-based cells,” *J. Power Sources*, vol. 207, pp. 134–140, 2012.

[57] H. J. Bang, H. Joachin, H. Yang, K. Amine, and J. Prakash, “Contribution of the Structural Changes of LiNi0.8Co0.15Al0.05O2 Cathodes on the Exothermic Reactions in Li-Ion Cells,” *J. Electrochem. Soc.*, vol. 153, no. 4, p. A731, 2006.

[58] H. F. Xiang *et al.*, “Thermal stability of LiPF6-based electrolyte and effect of contact with various delithiated cathodes of Li-ion batteries,” *J. Power Sources*, vol. 191, no. 2, pp. 575–581, 2009.

[59] H. Wang, A. Tang, and K. Wang, “Thermal Behavior Investigation of LiNi1/3Co1/3Mn1/3O2-Based Li-ion Battery under Overcharged Test,” *Chinese J. Chem.*, vol. 29, no. 50542004, pp. 27–32, 2011.

[60] Q. Wang, J. Sun, X. Yao, and C. Chen, “Thermal Behavior of Lithiated Graphite with Electrolyte in Lithium-Ion Batteries,” *J. Electrochem. Soc.*, vol. 153, no. 2,

p. A329, 2006.

[61] K. Maher and R. Yazami, “A study of lithium ion batteries cycle aging by thermodynamics techniques,” *J. Power Sources*, vol. 247, pp. 527–533, Feb. 2014.

[62] M. B. Pinson and M. Z. Bazant, “Theory of SEI Formation in Rechargeable Batteries: Capacity Fade, Accelerated Aging and Lifetime Prediction,” *J. Electrochem. Soc.*, vol. 160, no. 2, pp. A243–A250, Dec. 2012.

[63] C. Monroe and J. Newman, “Dendrite Growth in Lithium/Polymer Systems,” *J. Electrochem. Soc.*, vol. 150, no. 10, p. A1377, 2003.

[64] P. Arora, “Mathematical Modeling of the Lithium Deposition Overcharge Reaction in Lithium-Ion Batteries Using Carbon-Based Negative Electrodes,” *J. Electrochem. Soc.*, vol. 146, no. 10, p. 3543, 1999.

[65] S. Abada, G. Marlair, A. Lecocq, M. Petit, V. Sauvant-Moynot, and F. Huet, “Safety Focused Modeling of Lithium-Ion Batteries: A Review,” *J. Power Sources*, vol. 306, pp. 178–192, 2016.

[66] Reuters, “Chinese probe clears electric battery in deadly accident -BYD | Reuters.” [Online]. Available: http://in.reuters.com/article/byd-china-probe-idINL2E8J33CB20120803. [Accessed: 04-Apr-2017].

[67] Reuters, “Boeing Dreamliners grounded worldwide on battery checks | Reuters.” [Online]. Available: http://www.reuters.com/article/us-boeing-dreamliner-idUSBRE90F1N820130117. [Accessed: 04-Apr-2017].

[68] N. Williard, W. He, C. Hendricks, and M. Pecht, “Lessons learned from the 787 dreamliner issue on Lithium-Ion Battery reliability,” *Energies*, vol. 6, no. 9, pp. 4682–4695, 2013.

[69] SAMSUNG, “[Infographic] Galaxy Note7: What We Discovered – Samsung Global Newsroom,” 2017. [Online]. Available: https://news.samsung.com/global/infographic-galaxy-note7-what-we-discovered. [Accessed: 04-Aug-2017].

[70] US Fedral Aviation Administration, “Lithium Batteries & Lithium Battery-Powered Devices Aviation Cargo and Passenger Baggage Events Involving Smoke, Fire,

Extreme Heat or Explosion Involving Lithium Batteries or Unknown Battery Types," 2016.

[71] Financial Post, "Tesla Model S catches fire while sitting in a Toronto garage," 2014. [Online]. Available: http://business.financialpost.com/business-insider/tesla-catches-fire-while-sitting-in-a-toronto-garage/wcm/42d6d1f0-36df-4b6a-879e-90764bc32fc3. [Accessed: 20-Aug-2017].

[72] International Business Times, "Tesla Model S Driver Hits Object On HOV Lane Near Kent, Washington, Car Smokes, Catches Fire; Is Lithium Battery Dangerous?," 2013. [Online]. Available: http://www.ibtimes.com/tesla-model-s-driver-hits-object-hov-lane-near-kent-washington-car-smokes-catches-1414108. [Accessed: 20-Aug-2017].

[73] "A123 Systems To Recall Electric-Car Battery Packs For Fisker, Others." [Online]. Available: http://www.greencarreports.com/news/1074491_a123-systems-to-recall-electric-car-battery-packs-for-fisker-others. [Accessed: 02-Apr-2017].

[74] Green Car Reports, "Mitsubishi Looks Into Separate Japanese Plug-In Battery Fires," 2013. [Online]. Available: http://www.greencarreports.com/news/1083277_mitsubishi-looks-into-separate-japanese-plug-in-battery-fires. [Accessed: 20-Aug-2017].

[75] Reuters, "Japanese airlines ground Dreamliners after emergency landing," 2013. [Online]. Available: http://www.reuters.com/article/us-boeing-ana-idUSBRE90F01820130116. [Accessed: 20-Aug-2017].

[76] National Transportantion Safety Board, "Aircraft Incident Report Auxiliary Power Unit Battery Fire Japan Airlines Boeing 787-8, JA829J Boston, Massachusetts January 7, 2013," p. 110, 2014.

[77] "Nikon recalls more than 200,000 camera batteries due to burn hazard." [Online]. Available: http://www.consumerreports.org/cro/news/2012/07/nikon-recalls-more-than-200-000-camera-batteries-due-to-burn-hazard/index.htm. [Accessed: 02-Apr-2017].

[78] CNN Money, "Volt fire 3 weeks after crash test prompts safety probe," 2011.

[Online]. Available: http://money.cnn.com/2011/11/11/autos/volt_crash_fire/index.htm. [Accessed: 20-Aug-2017].

[79] ChinaAutoWeb, “Battery Pack Defects Blamed for Zotye EV Fire,” 2011. [Online]. Available: http://chinaautoweb.com/2011/06/battery-pack-defects-blamed-for-zotye-ev-fire/. [Accessed: 20-Aug-2017].

[80] M. Ouyang *et al.*, “Overcharge-induced capacity fading analysis for large format lithium-ion batteries with LiyNi1/3Co1/3Mn1/3O2 + LiyMn2O4 composite cathode,” *J. Power Sources*, vol. 279, pp. 626–635, 2015.

[81] M. Rona, Y. Hyung, B. Barnett, and S. Sriramulu, “The Relationship of the Nail Penetration Test to Safety of Li-Ion Cells,” *Dep. Energy Annu. Merit Rev. Meet.*, 2013.

[82] J. Garche and C. K. Dyer, *Encyclopedia of electrochemical power sources*. Academic Press, 2009.

[83] X. Feng *et al.*, “Characterization of penetration induced thermal runaway propagation process within a large format lithium ion battery module,” *J. Power Sources*, vol. 275, pp. 261–273, Feb. 2015.

[84] P. Biensan, B. Simon, and J. P. Peres, “On Safety of Lithium-Ion Cells,” pp. 906–912, 1999.

[85] T. G. Zavalis, M. Behm, and G. Lindbergh, “Investigation of Short-Circuit Scenarios in a Lithium-Ion Battery Cell,” *J. Electrochem. Soc.*, vol. 159, no. 6, p. A848, 2012.

[86] W. Zhao, G. Luo, and C.-Y. Wang, “Modeling Nail Penetration Process in Large-Format Li-Ion Cells,” *J. Electrochem. Soc.*, vol. 162, no. 1, pp. A207–A217, Dec. 2014.

[87] H. Maleki and J. N. Howard, “Internal Short Circuit in Li-Ion Cells,” *J. Power Sources*, vol. 191, no. 2, pp. 568–574, Jun. 2009.

[88] W. Zhao, G. Luo, and C.-Y. Wang, “Modeling Internal Shorting Process in Large-Format Li-Ion Cells,” *J. Electrochem. Soc.*, vol. 162, no. 7, pp. A1352–A1364, 2015.

[89] T. H. Dubaniewicz and J. P. Ducarme, “Are Lithium Ion Cells Intrinsically Safe?,” 2001.

[90] R. Spotnitz and J. Franklin, “Abuse Behavior of High-Power, Lithium-Ion Cells,” *J. Power Sources*, vol. 113, no. 1, pp. 81–100, Jan. 2003.

[91] T. Yamauchi, K. Mizushima, Y. Satoh, and S. Yamada, “Development of a simulator for both property and safety of a lithium secondary battery,” *J. Power Sources*, vol. 136, no. 1, pp. 99–107, 2004.

[92] K.-C. Chiu, C.-H. Lin, S.-F. Yeh, Y.-H. Lin, and K.-C. Chen, “An electrochemical modeling of lithium-ion battery nail penetration,” *J. Power Sources*, vol. 251, pp. 254–263, Apr. 2014.

[93] W. Fang, P. Ramadass, and Z. Zhang, “Study of Internal Short in a Li-Ion Cell-II. Numerical Investigation Using a 3D Electrochemical-Thermal Model,” *J. Power Sources*, vol. 248, pp. 1090–1098, 2014.

[94] Maccor Inc., “Maccor Automated Test System Instruction Manual,” 2012.

[95] H. Maleki, “Thermal Properties of Lithium-Ion Battery and Components,” *J. Electrochem. Soc.*, vol. 146, no. 3, p. 947, 1999.

[96] K. Kitoh and H. Nemoto, “100 Wh Large size Li-ion batteries and safety tests,” pp. 887–890, 1999.

[97] T. D. Hatchard, S. Trussler, and J. R. Dahn, “Building a ‘smart nail’ for penetration tests on Li-ion cells,” *J. Power Sources*, vol. 247, pp. 821–823, Feb. 2014.

[98] C. J. Orendorff, E. P. Roth, and G. Nagasubramanian, “Experimental triggers for internal short circuits in lithium-ion cells,” *J. Power Sources*, vol. 196, no. 15, pp. 6554–6558, Aug. 2011.

[99] A. Arora, N. K. Medora, T. Livernois, and J. Swart, *Safety of Lithium-Ion Batteries for Hybrid Electric Vehicles*. Elsevier B.V, 2010.

[100] National Highway Traffic Safety Administration - US Department of Transportation, “Chevrolet Volt Battery Incident Summary Report,” 2012.

[101] Betanews, “Sorry, you can’t mail your iPhone or iPad overseas ’til next year.”

[Online]. Available: https://betanews.com/2012/05/25/sorry-you-cant-mail-your-iphone-or-ipad-overseas-til-next-year/. [Accessed: 04-Apr-2017].

[102] A123 Systems, “Battery Pack Design , Validation , and Assembly Guide using A123 Systems AMP20M1HD-A Nanophosphate Cells,” pp. 1–71, 2014.

[103] A. Kriston *et al.*, “External short circuit performance of Graphite-LiNi 1/3 Co 1/3 Mn 1/3 O 2 and Graphite-LiNi 0.8 Co 0.15 Al 0.05 O 2 cells at different external resistances,” 2017.

[104] International Organization for Standardization, “ISO 12405-3:2014 - Electrically propelled road vehicles - Test specification for lithium-ion traction battery packs and systems - Part 3: Safety performance requirements,” 2014. [Online]. Available: https://www.iso.org/standard/59224.html. [Accessed: 05-Apr-2017].

[105] V. G. Kumar, N. Munichandraiah, and A. K. Shukla, “Electrode impedance parameters and internal resistance of a sealed LiC/Li-xCoO2 Lithium-ion rechargeable battery,” *J. Appl. Electrochem.*, vol. 27, pp. 43–49, 1997.

[106] F. Huet, “A review of impedance measurements for determination of the state-of-charge or state-of-health of secondary batteries,” *J. Power Sources*, vol. 70, no. 1, pp. 59–69, 1998.

[107] A. Eddahech, O. Briat, and J.-M. Vinassa, “Thermal characterization of a high-power lithium-ion battery: Potentiometric and calorimetric measurement of entropy changes,” *Energy*, vol. 61, pp. 432–439, Nov. 2013.

[108] M. Fleckenstein, S. Fischer, O. Bohlen, and B. Bäker, “Thermal Impedance Spectroscopy - A method for the thermal characterization of high power battery cells,” *J. Power Sources*, vol. 223, pp. 259–267, 2013.

[109] A. A. Hussein and I. Batarseh, “A Review of Charging Algorithms for Nickel and Lithium Battery Chargers,” *IEEE*, vol. 60, no. 3, pp. 830–838, 2011.

[110] N. Omar *et al.*, “Lithium iron phosphate based battery – Assessment of the aging parameters and development of cycle life model,” *Appl. Energy*, vol. 113, pp. 1575–1585, 2014.

[111] M. Abdel Monem *et al.*, “Lithium-ion batteries: Evaluation study of different charging methodologies based on aging process,” *Appl. Energy*, vol. 152, pp.

143–155, 2015.

[112] R. a. Leising, M. J. Palazzo, E. S. Takeuchi, and K. J. Takeuchi, “Abuse Testing of Lithium-Ion Batteries: Characterization of the Overcharge Reaction of LiCoO2/Graphite Cells,” *J. Electrochem. Soc.*, vol. 148, p. A838, 2001.

[113] K. R. Crompton and B. J. Landi, “Near Zero Volt Tolerant Lithium Ion Cells: Benefits for Safe Storage, Shipping, and Medical Implants,” *Meet. Abstr.*, vol. MA2016-02, no. 3, pp. 266–266, Sep. 2016.

[114] M. Zhao *et al.*, “Electrochemical Stability of Copper in Lithium-Ion Battery Electrolytes,” *J. Electrochem. Soc.*, vol. 147, no. 8, p. 2874, 2000.

[115] A. W. Golubkov *et al.*, “Thermal runaway of commercial 18650 Li-ion batteries with LFP and NCA cathodes – impact of state of charge and overcharge,” *RSC Adv.*, vol. 5, no. 70, pp. 57171–57186, 2015.

[116] M. A. Danzer, V. Liebau, and F. Maglia, “Aging of lithium-ion batteries for electric vehicles,” in *Advances in Battery Technologies for Electric Vehicles*, Elsevier Ltd., 2015, pp. 359–387.

[117] J. Li, E. Murphy, J. Winnick, and P. A. Kohl, “The effects of pulse charging on cycling characteristics of commercial lithium-ion batteries,” *J. Power Sources*, vol. 102, no. 1–2, pp. 302–309, 2001.

[118] D. Andre, M. Meiler, K. Steiner, H. Walz, T. Soczka-Guth, and D. U. Sauer, “Characterization of high-power lithium-ion batteries by electrochemical impedance spectroscopy. II: Modelling,” *J. Power Sources*, vol. 196, no. 12, pp. 5349–5356, Jun. 2011.

[119] J. Bisquert, G. Garcia-Belmonte, P. Bueno, E. Longo, and L. O. . Bulhões, “Impedance of constant phase element (CPE)-blocked diffusion in film electrodes,” *J. Electroanal. Chem.*, vol. 452, no. 2, pp. 229–234, 1998.

[120] N. Omar *et al.*, *Aging and degradation of lithium-ion batteries*. Elsevier Ltd., 2015.

[121] J. Li, E. Murphy, J. Winnick, and P. A. Kohl, “Studies on the cycle life of commercial lithium ion batteries during rapid charge-discharge cycling,” *J. Power Sources*, vol. 102, no. 1–2, pp. 294–301, 2001.

[122] Y. Saito, K. Takano, and A. Negishi, “Thermal behaviors of lithium-ion cells during overcharge,” *J. Power Sources*, vol. 97–98, no. January, pp. 693–696, 2001.

[123] X. Gong, R. Xiong, and C. Mi, “Study of the Characteristics of Battery Packs in Electric Vehicles with Parallel-Connected Lithium-Ion Battery Cells,” *Industry Applications, IEEE Transactions on*, vol. PP, no. 99. p. 1, 2014.

[124] T. Bruen, J. Marco, and M. Gama, “Current Variation in Parallelized Energy Storage Systems,” *Vehicle Power and Propulsion Conference (VPPC), 2014 IEEE*. pp. 1–6, 2014.

[125] T. Bruen and J. Marco, “Modelling and experimental evaluation of parallel connected lithium ion cells for an electric vehicle battery system,” *J. Power Sources*, vol. 310, pp. 91–101, Apr. 2016.

[126] M. Dubarry, A. Devie, and B. Y. Liaw, “Cell-balancing currents in parallel strings of a battery system,” *J. Power Sources*, vol. 321, pp. 36–46, Jul. 2016.

[127] R. a. Leising, M. J. Palazzo, E. S. Takeuchi, and K. J. Takeuchi, “A study of the overcharge reaction of lithium-ion batteries,” *J. Power Sources*, vol. 97–98, pp. 681–683, Jul. 2001.

[128] D. Belov and M. H. Yang, “Failure mechanism of Li-ion battery at overcharge conditions,” *J. Solid State Electrochem.*, vol. 12, no. 7–8, pp. 885–894, 2008.

[129] T. Ohsaki *et al.*, “Overcharge reaction of lithium-ion batteries,” *J. Power Sources*, vol. 146, no. 1–2, pp. 97–100, Aug. 2005.

[130] C. H. Doh *et al.*, “Thermal and electrochemical behaviour of C/LixCoO2 cell during safety test,” *J. Power Sources*, vol. 175, no. 2, pp. 881–885, 2008.

[131] J. Cho, T. G. Kim, C. Kim, J. G. Lee, Y. W. Kim, and B. Park, “Comparison of Al2O3- and AlPO4-coated LiCoO2 cathode materials for a Li-ion cell,” *J. Power Sources*, vol. 146, no. 1–2, pp. 58–64, 2005.

[132] J. Cho, “Dependence of AlPO4 coating thickness on overcharge behaviour of LiCoO2 cathode material at 1 and 2 C rates,” *J. Power Sources*, vol. 126, no. 1–2, pp. 186–189, 2004.

[133] G. Chen, K. E. Thomas-Alyea, J. Newman, and T. J. Richardson, “Characterization of an electroactive polymer for overcharge protection in secondary lithium batteries,” *Electrochim. Acta*, vol. 50, no. 24, pp. 4666–4673, 2005.

[134] L. M. Moshuchak, M. Bulinski, W. M. Lamanna, R. L. Wang, and J. R. Dahn, “Direct comparison of 2,5-di-tert-butyl-1,4-dimethoybenzene and 4-tert-butyl-1,2-dimethoxybenzene as redox shuttles in LiFePO4-based Li-ion cells,” *Electrochem. commun.*, vol. 9, no. 7, pp. 1497–1501, 2007.

[135] L. Xiao, X. Ai, Y. Cao, and H. Yang, “Electrochemical behavior of biphenyl as polymerizable additive for overcharge protection of lithium ion batteries,” *Electrochim. Acta*, vol. 49, no. 24, pp. 4189–4196, 2004.

[136] S. Tobishima, K. Takei, Y. Sakurai, and J. Yamaki, “Lithium ion cell safety,” *J. Power Sources*, vol. 90, no. 2, pp. 188–195, Oct. 2000.

[137] C. K. Lin, Y. Ren, K. Amine, Y. Qin, and Z. Chen, “In situ high-energy X-ray diffraction to study overcharge abuse of 18650-size lithium-ion battery,” *J. Power Sources*, vol. 230, pp. 32–37, 2013.

[138] J. Dahn, E. Fuller, M. Obrovac, and U. Vonsachen, “Thermal Stability of LixCoO2, LixNiO2 and ʎ-MnO2 and Consequences for the Safety of Li-ion Cells,” *Solid State Ionics*, vol. 69, no. 3–4, pp. 265–270, 1994.

[139] J. W. Fergus, “Recent developments in cathode materials for lithium ion batteries,” *J. Power Sources*, vol. 195, no. 4, pp. 939–954, Feb. 2010.

[140] P. Peng and F. Jiang, “Thermal safety of lithium-ion batteries with various cathode materials: A numerical study,” *Int. J. Heat Mass Transf.*, vol. 103, pp. 1008–1016, 2016.

[141] N. Nitta, F. Wu, J. T. Lee, and G. Yushin, “Li-ion battery materials: Present and future,” *Mater. Today*, vol. 18, no. 5, pp. 252–264, 2015.

[142] I. Belharouak, W. Lu, D. Vissers, and K. Amine, “Safety characteristics of Li(Ni0.8Co0.15Al0.05)O2 and Li(Ni1/3Co1/3Mn1/3)O2,” *Electrochem. commun.*, vol. 8, no. 2, pp. 329–335, Feb. 2006.

[143] S. Mohan, Y. Kim, J. B. Siegel, N. a. Samad, and a. G. Stefanopoulou, “A

Phenomenological Model of Bulk Force in a Li-Ion Battery Pack and Its Application to State of Charge Estimation," *J. Electrochem. Soc.*, vol. 161, no. 14, pp. A2222–A2231, 2014.

[144] J. B. Siegel, a. G. Stefanopoulou, P. Hagans, Y. Ding, and D. Gorsich, "Expansion of Lithium Ion Pouch Cell Batteries: Observations from Neutron Imaging," *J. Electrochem. Soc.*, vol. 160, no. 8, pp. A1031–A1038, 2013.

[145] B. Rieger, S. Schlueter, S. V. Erhard, J. Schmalz, G. Reinhart, and A. Jossen, "Multi-scale investigation of thickness changes in a commercial pouch type lithium-ion battery," *Adv. Life Course Res.*, vol. 6, pp. 213–221, 2016.

[146] R. Fu, M. Xiao, and S. Y. Choe, "Modeling, validation and analysis of mechanical stress generation and dimension changes of a pouch type high power Li-ion battery," *J. Power Sources*, vol. 224, pp. 211–224, 2013.

[147] T. Iwahori *et al.*, "Development of lithium ion and lithium polymer batteries for electric vehicle and home-use load leveling system application," *Electrochim. Acta*, vol. 45, no. 8–9, pp. 1509–1512, Jan. 2000.

[148] J. Chen, "Recent Progress in Advanced Materials for Lithium Ion Batteries," *Materials (Basel).*, vol. 6, no. 1, pp. 156–183, Jan. 2013.

[149] M.-K. Song, S. Park, F. M. Alamgir, J. Cho, and M. Liu, "Nanostructured electrodes for lithium-ion and lithium-air batteries: the latest developments, challenges, and perspectives," *Mater. Sci. Eng. R Reports*, vol. 72, no. 11, pp. 203–252, Nov. 2011.

[150] Mitsubishi Heavy Industries, "Development of Large High-performance Lithium-ion Batteries for Power Storage and Industrial Use," vol. 49, no. 1, pp. 6–11, 2012.

[151] D. Belov and M. H. Yang, "Investigation of the kinetic mechanism in overcharge process for Li-ion battery," *Solid State Ionics*, vol. 179, no. 27–32, pp. 1816–1821, 2008.

[152] A. Barré, B. Deguilhem, S. Grolleau, M. Gérard, F. Suard, and D. Riu, "A review on lithium-ion battery ageing mechanisms and estimations for automotive applications," *J. Power Sources*, vol. 241, pp. 680–689, Nov. 2013.

[153] Q. Yuan, F. Zhao, W. Wang, Y. Zhao, Z. Liang, and D. Yan, “Overcharge failure investigation of lithium-ion batteries,” *Electrochim. Acta*, vol. 178, no. February, pp. 682–688, 2015.

[154] R. Fong, M. C. Reid, R. S. Mcmillan, and J. R. Dahn, “In Situ Study of Electrolyte Reactions in Secondary Lithium Cells,” *J. Electrochem. Soc.*, vol. 134, no. 3, pp. 516–519, 1987.

[155] C. P. Aiken, J. Xia, D. Y. Wang, D. A. Stevens, S. Trussler, and J. R. Dahn, “An Apparatus for the Study of In Situ Gas Evolution in Li-Ion Pouch Cells,” *J. Electrochem. Soc.* , vol. 161, no. 10, pp. A1548–A1554, 2014.

[156] “Samsung offers S4 owners free replacement on faulty batteries | Technology | The Guardian,” 2014. [Online]. Available: https://www.theguardian.com/technology/2013/oct/17/samsung-s4-faulty-battery-replacement. [Accessed: 30-Mar-2017].

[157] R. Imhof and P. Novak, “Oxidative electrolyte solvent degradation in lithium-ion batteries - An in situ differential electrochemical mass spectrometry investigation,” *J. Electrochem. Soc.*, vol. 146, no. 5, pp. 1702–1706, 1999.

[158] N. Sharma and V. K. Peterson, “Overcharging a lithium-ion battery: Effect on the LixC6 negative electrode determined by in situ neutron diffraction,” *J. Power Sources*, vol. 244, pp. 695–701, 2013.

[159] M. Dubarry, V. Svoboda, R. Hwu, and B. Yann Liaw, “Incremental Capacity Analysis and Close-to-Equilibrium OCV Measurements to Quantify Capacity Fade in Commercial Rechargeable Lithium Batteries,” *Electrochem. Solid-State Lett.*, vol. 9, no. 10, p. A454, 2006.

[160] M. Dubarry, V. Svoboda, R. Hwu, and B. Y. Liaw, “Capacity and power fading mechanism identification from a commercial cell evaluation,” *J. Power Sources*, vol. 165, no. 2, pp. 566–572, 2007.

[161] M. Dubarry *et al.*, “Identifying battery aging mechanisms in large format Li ion cells,” *J. Power Sources*, vol. 196, no. 7, pp. 3420–3425, 2011.

[162] M. Dubarry *et al.*, “Evaluation of commercial lithium-ion cells based on composite positive electrode for plug-in hybrid electric vehicle applications. Part

I: Initial characterizations," *J. Power Sources*, vol. 196, no. 23, pp. 10328–10335, 2011.

[163] S. Rodrigues, N. Munichandraiah, and a. K. Shukla, "AC impedance and state-of-charge analysis of a sealed lithium-ion rechargeable battery," *J. Solid State Electrochem.*, vol. 3, no. 7–8, pp. 397–405, 1999.

[164] W. Waag, S. Käbitz, and D. U. Sauer, "Experimental investigation of the lithium-ion battery impedance characteristic at various conditions and aging states and its influence on the application," *Appl. Energy*, vol. 102, pp. 885–897, 2013.

[165] S. Buller, M. Thele, R. W. De Doncker, and E. Karden, "Impedance-Based Simulation Models of Supercapacitors and Lithium-ion Batteries for Power Electronic Applications," *IEEE Ind. Appl. Mag.*, vol. 11, no. 2, pp. 742–747, 2005.

[166] Q. Zhuang, X. Qiu, and S. Xu, "Diagnosis of Electrochemical Impedance Spectroscopy in Lithium-Ion Batteries," *Lithium Ion Batter. – New Dev.*, pp. 189–226, 2012.

[167] BioLogic, "EC-Lab Data Analysis and Processes," no. December, 2015.

[168] G. Ning, B. Haran, and B. N. Popov, "Capacity fade study of lithium-ion batteries cycled at high discharge rates," *J. Power Sources*, vol. 117, no. 1–2, pp. 160–169, 2003.

[169] W. Lu, C. M. López, N. Liu, J. T. Vaughey, A. Jansen, and D. W. Dees, "Overcharge Effect on Morphology and Structure of Carbon Electrodes for Lithium-Ion Batteries," *J. Electrochem. Soc.*, vol. 159, no. 5, p. A566, 2012.

[170] Y. B. He *et al.*, "Structural and thermal stabilities of layered Li(Ni1/3Co 1/3Mn1/3)O2 materials in 18650 high power batteries," *J. Power Sources*, vol. 196, no. 23, pp. 10322–10327, 2011.

[171] C. Wang, A. J. Appleby, and F. E. Little, "Charge-discharge stability of graphite anodes for lithium-ion batteries," *J. Electroanal. Chem.*, vol. 497, no. 1–2, pp. 33–46, 2001.

[172] G. Nagasubramanian, "Two- and three-electrode impedance studies on 18650 Li-ion cells," *J. Power Sources*, vol. 87, no. 1, pp. 226–229, 2000.

[173] J. Shim and K. A. Striebel, “Characterization of high-power lithium-ion cells during constant current cycling: Part I. Cycle performance and electrochemical diagnostics,” *J. Power Sources*, vol. 122, no. 2, pp. 188–194, 2003.

[174] M. Dubarry and B. Y. Liaw, “Identify capacity fading mechanism in a commercial LiFePO4 cell,” *J. Power Sources*, vol. 194, no. 1, pp. 541–549, 2009.

[175] M. Dubarry, V. Svoboda, R. Hwu, and B. Yann Liaw, “Incremental Capacity Analysis and Close-to-Equilibrium OCV Measurements to Quantify Capacity Fade in Commercial Rechargeable Lithium Batteries,” *Electrochem. Solid-State Lett.*, vol. 9, no. 10, pp. A454–A457, 2006.

[176] M. Dubarry, V. Svoboda, R. Hwu, and B. Y. Liaw, “Capacity loss in rechargeable lithium cells during cycle life testing: The importance of determining state-of-charge,” *J. Power Sources*, vol. 174, no. 2, pp. 1121–1125, 2007.

[177] J. Self, C. P. Aiken, R. Petibon, and J. R. Dahn, “Survey of Gas Expansion in Li-Ion NMC Pouch Cells,” *J. Electrochem. Soc.*, vol. 162, no. 6, pp. A796–A802, 2015.

[178] Y. Inui, Y. Kobayashi, Y. Watanabe, Y. Watase, and Y. Kitamura, “Simulation of temperature distribution in cylindrical and prismatic lithium ion secondary batteries,” *Energy Convers. Manag.*, vol. 48, no. 7, pp. 2103–2109, 2007.

[179] J. Ye, H. Chen, Q. Wang, P. Huang, J. Sun, and S. Lo, “Thermal behavior and failure mechanism of lithium ion cells during overcharge under adiabatic conditions,” *Appl. Energy*, vol. 182, pp. 464–474, 2016.

[180] L. H. Saw, Y. Ye, and A. A. O. Tay, “Electro-thermal analysis and integration issues of lithium ion battery for electric vehicles,” *Appl. Energy*, vol. 131, pp. 97–107, 2014.

[181] Thermal Hazard Technology, “The Accelerating Rate Calorimeter Operations Manual,” 2013.

[182] X. Feng *et al.*, “Thermal runaway features of large format prismatic lithium ion battery using extended volume accelerating rate calorimetry,” *J. Power Sources*, vol. 255, pp. 294–301, Jun. 2014.

[183] H. Ishikawa, O. Mendoza, Y. Sone, and M. Umeda, “Study of thermal

deterioration of lithium-ion secondary cell using an accelerated rate calorimeter (ARC) and AC impedance method," *J. Power Sources*, vol. 198, pp. 236–242, 2012.

[184] M. N. Richard and J. R. Dahn, "Accelerating Rate Calorimetry Study on the Thermal Stability of Lithium Intercalated Graphite in Electrolyte. II. Modeling the Results and Predicting Differential Scanning Calorimeter Curves," *J. Electrochem. Soc.*, vol. 146, no. 6, p. 2078, 1999.

[185] H. Maleki, G. Deng, A. Anani, and J. Howard, "Thermal Stability Studies of Li-Ion Cells and Components," vol. 146, no. 9, pp. 3224–3229, 1999.

[186] Z. Zhang, D. Fouchard, J. R. Rea, and R. Corporation, "Differential scanning calorimetry material studies: implications for the safety of lithium-ion cells," vol. 70, pp. 16–20, 1998.

[187] M. H. Ryou *et al.*, "Effects of lithium salts on thermal stabilities of lithium alkyl carbonates in SEI layer," *Electrochim. Acta*, vol. 83, pp. 259–263, 2012.

[188] Q. Wang, J. Sun, X. Yao, and C. Chen, "Thermal stability of LiPF6/EC + DEC electrolyte with charged electrodes for lithium ion batteries," *Thermochim. Acta*, vol. 437, no. 1–2, pp. 12–16, 2005.

[189] P. Arora and Z. Zhang, "Battery separators," *Chem. Rev.*, vol. 104, no. 10, pp. 4419–4462, 2004.

[190] M. Baginska, B. J. Blaiszik, R. J. Merriman, N. R. Sottos, J. S. Moore, and S. R. White, "Autonomic shutdown of Lithium-ion batteries using thermoresponsive microspheres," *Adv. Energy Mater.*, vol. 2, no. 5, pp. 583–590, 2012.

[191] H. Wang, a Tang, and K. Huang, "Oxygen Evolution in Overcharged LixNi1/3Co1/3Mn1/3O2 Electrode and Its Thermal Analysis Kinetics," *Chinese J. Chem.*, no. 50542004, pp. 1583–1588, 2011.

[192] H.-S. Kim, M. Kong, K. Kim, I.-J. Kim, and H.-B. Gu, "Effect of carbon coating on LiNi 1/3 Mn 1/3 Co 1/3 O2 cathode material for lithium secondary batteries," *J. Power Sources*, vol. 171, pp. 917–921, 2007.

[193] I. Belharouak, Y. K. Sun, J. Liu, and K. Amine, "Li(Ni1/3Co1/3Mn1/3)O2 as a suitable cathode for high power applications," *J. Power Sources*, vol. 123, no. 2,

pp. 247–252, 2003.

[194] R. Li, J. Wu, H. Wang, J. Guo, and G. Li, “Reliability assessment and failure analysis of lithium iron phosphate batteries,” *Inf. Sci. (Ny).*, vol. 259, pp. 359–368, Jun. 2013.

[195] S.-W. Eom, M.-K. Kim, I.-J. Kim, S.-I. Moon, Y.-K. Sun, and H.-S. Kim, “Life prediction and reliability assessment of lithium secondary batteries,” *J. Power Sources*, vol. 174, no. 2, pp. 954–958, Dec. 2007.

[196] M. Development, C. L. Studies, and A. T. Studies, “Fy 2015 Annual Progress Report for Energy Storage R&D -2,” 2015.

[197] A. Väyrynen and J. Salminen, “Lithium ion battery production,” *J. Chem. Thermodyn.*, vol. 46, pp. 80–85, Mar. 2012.

[198] T. M. Bandhauer, S. Garimella, and T. F. Fuller, “A Critical Review of Thermal Issues in Lithium-Ion Batteries,” *J. Electrochem. Soc.*, vol. 158, no. 3, p. R1, 2011.

[199] J. Cannarella and C. B. Arnold, “Stress evolution and capacity fade in constrained lithium-ion pouch cells,” *J. Power Sources*, vol. 245, pp. 745–751, 2014.

[200] K. White and R. T. Long, “Lithium-Ion Batteries Hazard and Use Assessment,” no. July, 2011.

[201] A. Pesaran *et al.*, “NREL Energy Storage Projects : FY2013 Annual Report NREL Energy Storage Projects : FY2013 Annual Report Steve Hartridge,” no. July 2014, 2013.

[202] Ahmad Pesaran *et al.*, “FY2012 Annual Report for NREL Energy Storage Projects,” no. NREL/TP--5400--54491, p. 75, 2011.

[203] B. Kennedy, D. Patterson, and S. Camilleri, “Use of lithium-ion batteries in electric vehicles,” *J. Power Sources*, vol. 90, no. 2, pp. 156–162, Oct. 2000.

[204] L. Lu, X. Han, J. Li, J. Hua, and M. Ouyang, “A review on the key issues for lithium-ion battery management in electric vehicles,” *J. Power Sources*, vol. 226, pp. 272–288, Mar. 2013.

[205] J. Remmlinger, M. Buchholz, M. Meiler, P. Bernreuter, and K. Dietmayer, “State-of-health monitoring of lithium-ion batteries in electric vehicles by on-board internal resistance estimation,” *J. Power Sources*, vol. 196, no. 12, pp. 5357–5363, Jun. 2011.

[206] J. Lamb and C. J. Orendorff, “Evaluation of mechanical abuse techniques in lithium ion batteries,” *J. Power Sources*, vol. 247, pp. 189–196, Feb. 2014.

[207] S. F. Schuster, M. J. Brand, C. Campestrini, M. Gleissenberger, and A. Jossen, “Correlation between capacity and impedance of lithium-ion cells during calendar and cycle life,” *J. Power Sources*, vol. 305, pp. 191–199, 2016.

[208] S. F. Schuster *et al.*, “Nonlinear aging characteristics of lithium-ion cells under different operational conditions,” *J. Energy Storage*, vol. 1, no. 1, pp. 44–53, 2015.

Appendix

A) EIS Software Settings

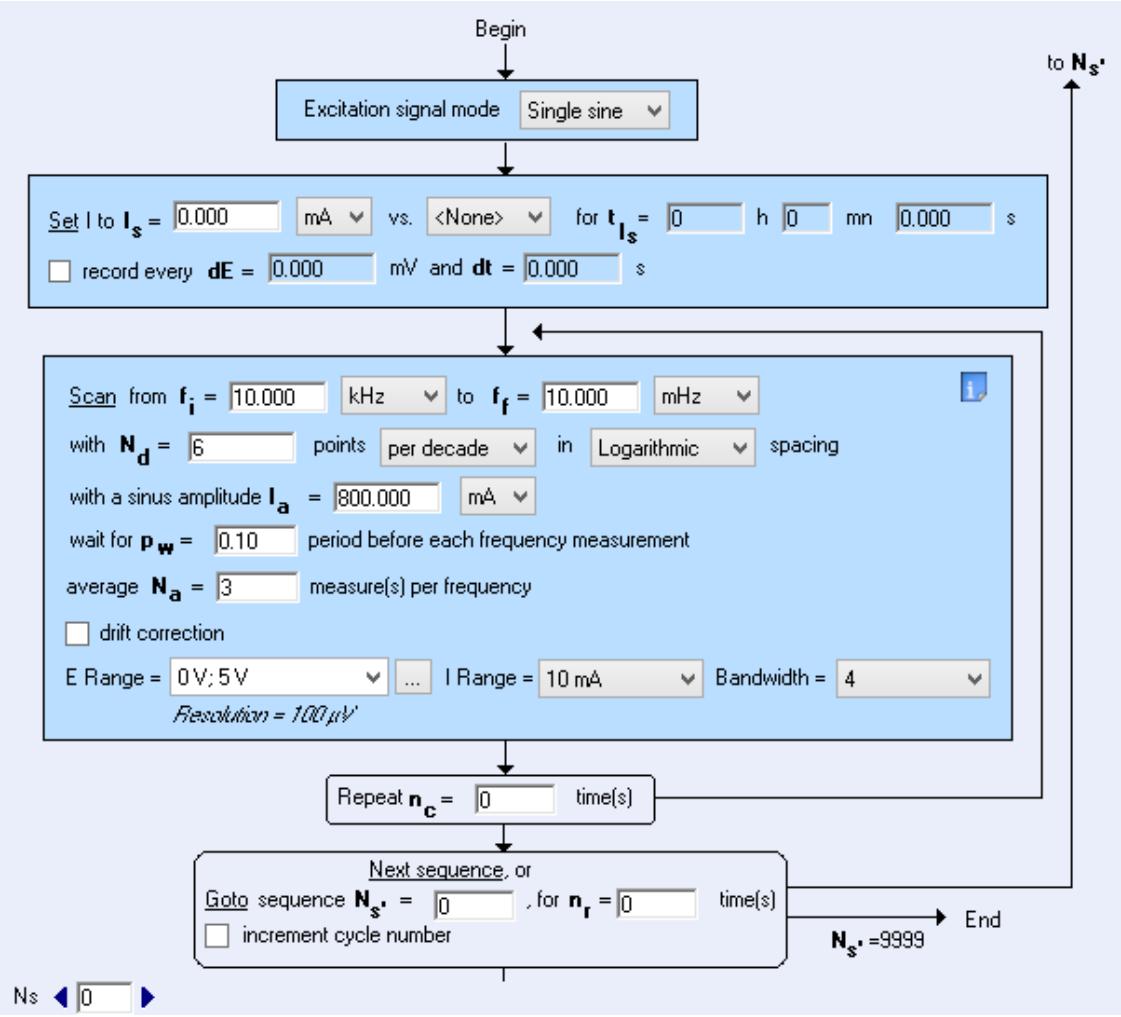

B) Procedure of Post-abuse Cycling Regime

Test Procedure

Test File Name: ARCHI1_5.2V_10A_CYC.014

Test Procedure: [redacted]_CYCAFT_DCIR5CYC.000

Original Test Procedure Description: Sub routine running

Step	Type	Mode	Val	Limit	Val	End Type	Op	Val	Goto	Rpt Type	Val	Options	Step Note
1	Rest					StepTime	=	00:05:00	002	StepTime	00:00:30	ANNN	
2	Do 2												
3	Do 1												
4	AdvCycle												
5	Dischrge	Current	10.0			Voltage	<=	2.7	006	StepTime	00:05:00	ANNN	
										Voltage	0.01		
6	Rest					StepTime	=	00:20:00	007	StepTime	00:05:00	ANNN	
										Voltage	0.01		
7	Charge	Current	10.0	Voltage	4.2	Current	<=	0.375	008	Voltage	0.01	ANNN	
						StepTime	=	04:00:00	013	StepTime	00:05:00		
8	Rest					StepTime	=	01:00:00	009	StepTime	00:05:00	ANNN	
										Voltage	0.01		
9	Loop 1					Loop Cnt	=	5	010				
10	Rest					StepTime	=	00:01:00	011	StepTime	00:00:10	ANNN	
										Voltage	0.01		
11	SubRout		SUB_DCIR_L										
12	Rest					StepTime	=	00:10:00	013	StepTime	00:02:00	ANNN	
										Voltage	0.01		
13	Loop 2					Loop Cnt	=	31	014				
14	End												

C) Load Cell Data Sheet

VPG Transducers
Celtron • Revere • Sensortronics • Tedea-Huntleigh

Model 1004
Tedea-Huntleigh

Aluminum Single-Point Load Cell

FEATURES

- Capacities 0.3–3 kg
- Aluminum construction
- Single-point 200 x 200 mm platform
- IP66 protection
- Total error better than 0.0067% of R.O.
- OIML approved

APPLICATIONS

- Low capacity scales
- Precision scales
- Jewelry scales
- Pharmaceutical scales

DESCRIPTION

Model 1004 is a very low capacity, very high precision single-point load cell designed for direct mounting in low capacity scales and precision balances.

This load cell is suitable for applications including jewelery scales, analytical balances, medical equipment, medical and pharmaceutical research and low-level force measurement.

The Model 1004 offers up to 30000 divisions short-term precision at stable room temperature. A special two-stage humidity resistant protective coating assures long-term reliability.

An overload protection device can be easily included in the application design. A threaded hole is provided in the loading end of the load cell for this purpose.

OUTLINE DIMENSIONS in millimeters

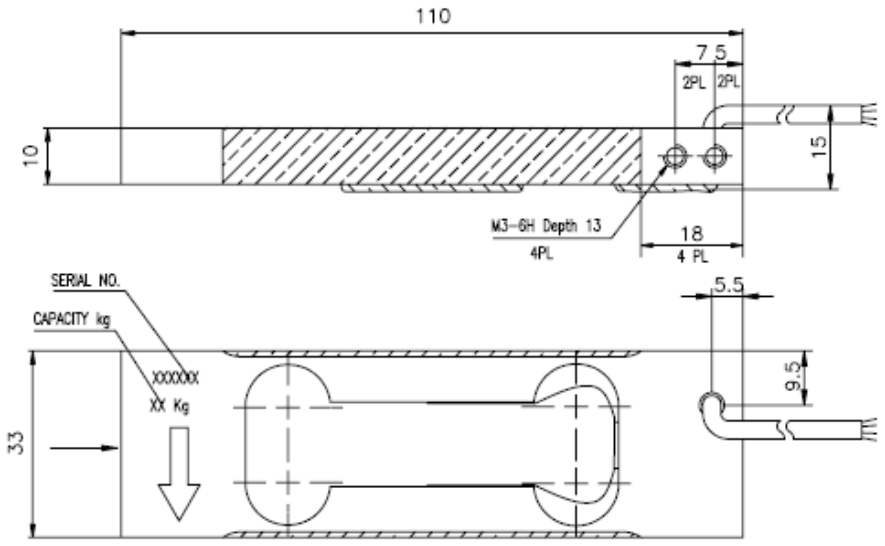

Model 1004
Tedea-Huntleigh

VPG Transducers
Celtron • Revere • Sensortronics • Tedea-Huntleigh

Aluminum Single-Point Load Cell

SPECIFICATIONS					
PARAMETER		VALUE			UNIT
Accuracy class	C3	GW	HW	JW	
Rated capacity—R.C. (E_{max})	0.3, 0.4, 0.6, 1.2, 1.5, 3.0				kg
Rated output—R.O.	0.9				mV/V
Rated output tolerance	0.1				±mV/V
Zero balance	0.04				±mV/V
Zero return, 2 minutes		0.01	0.0055	0.0033	±% of applied load
Zero return, 30 minutes	0.017				±% of applied load
Total error (per OIML R60)	0.02	0.01	0.0067	0.0067	±% of rated load
Temperature effect on zero	0.004	0.004			±% of rated output/°C
Temperature effect on output	0.001	0.002			±% of load/°C
Eccentric loading error		0.0033			±% of rated load/cm
Temperature range, compensated		+5 to +45			°C
Temperature range, safe		–30 to +70			°C
Maximum safe central overload		150			% of R.C.
Ultimate central overload		250			% of R.C.
Excitation, recommended		10			VDC or VAC RMS
Excitation, maximum		15			VDC or VAC RMS
Input impedance		415 ±20			Ω
Output impedance		350±3			Ω
Insulation resistance		>2000			MΩ
Humidity range, safe		<60			%
Cable length		0.4			m
Cable type		4 wire, PVC, spiral shield			
Construction		Aluminum			
Environmental protection		IP66			
Platform size (max)		200 x 200			mm
Recommended torque		2.0			N*m
Humidity Range, Safe		<60			%

All specifications subject to change without notice.

WIRING SCHEMATIC DIAGRAM
(Balanced bridge configuration)

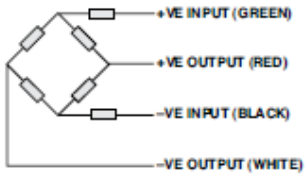

D) Silicone Oil Data Sheet

VWR We Enable Science

VWR PROLABO CHEMICALS

Safety Data Sheet

according to Regulation (EC) No. 1907/2006 (amended by Regulation (EU) No 453/2010)

Revision date: 29.01.2015	*Version: 4.1*	*Print date: 29.01.2015*

SECTION 1: Identification of the substance/mixture and of the company/undertaking

1.1 Product identifier

Trade name/designation:	Silicone oil 47 V 350
Product No.:	83851 (VWR International)
Substance name:	Silicone oil 350 cSt (25°C, Polydimethylsiloxane)
CAS No.:	63148-62-9
INDEX No.:	000-000-00-0
REACH registration No.:	Not yet communicated down the supply chain.
Other means of identification:	

1.2 Relevant identified uses of the substance or mixture and uses advised against

Relevant identified uses:	General chemical reagent

1.3 Details of the supplier of the safety data sheet

Supplier (manufacturer/importer/only representative/downstream user/distributor)

Singapore

VWR Singapore Pte Ltd.

Street	18 Gul Drive
Postal code/city	Singapore 629468
Telephone	+65 6505 0760
Telefax	+65 6264 3780
E-mail (competent person)	SDS@eu.vwr.com

Emergency telephone

Telephone	+65 (0) 6505 0760 (office hours: 8 am-5 pm)

SECTION 2: Hazards identification

2.1 Classification of the substance or mixture

2.1.1 Classification according to Regulation (EC) No. 1272/2008 [CLP]

This substance is classified as not hazardous according to regulation (EC) No. 1272/2008 [CLP].

2.1.2 Classification according to Directive 67/548/EEC or 1999/45/EC

This substance is classified as not hazardous according to 67/548/EEC.

2.2 Label elements

2.2.1 Labelling according to Regulation (EC) No. 1272/2008 [CLP]

According to EC directives or the corresponding national regulations the product does not have to be labelled.

2.2.2 Labelling (67/548/EEC or 1999/45/EC)

According to EC directives or the corresponding national regulations the product does not have to be labelled.

Other hazards

SVHC No

SECTION 3: Composition / information on ingredients

3.1 Substances

Substance name	Silicone oil 350 cSt (25°C, Polydimethylsiloxane)
Molecular formula	—
Molecular weight	no data available
CAS No.	63148-62-9
REACH registration No.	Not yet communicated down the supply chain.
INDEX No.	000-000-00-0

Hazardous ingredients Classification according to Regulation (EC) No. 1272/2008 [CLP]

Substance name	Concentration	Product identifier	Hazard classes and hazard categories
Silicone oil 350 cSt (25°C, Polydimethylsiloxane)	≤100%	CAS No.: 63148-62-9 EC No.: 000-000-0 REACH No.: Not yet communicated down the supply chain.	

Hazardous ingredients Classification according to 67/548/EEC

Substance name	Concentration	Product identifier	Hazard classes and hazard categories
Silicone oil 350 cSt (25°C, Polydimethylsiloxane)	≤100%	CAS No.: 63148-62-9 EC No.: 000-000-0 REACH No.: Not yet communicated down the supply chain.	

SECTION 9: Physical and chemical properties

9.1 Information on basic physical and chemical properties

(a) Appearance	
Physical state:	liquid
Colour:	no data available
(b) Odour:	no data available
(c) Odour threshold:	no data available

Safety relevant basic data

(d) pH:	no data available
(e) Melting point/freezing point:	no data available
(f) Initial boiling point and boiling range:	no data available
(g) Flash point:	<300 °C
(h) Evaporation rate:	no data available
(i) Flammability (solid, gas):	not applicable
(j) Upper/lower flammability or explosive limits	
Lower explosion limit:	no data available
Upper explosion limit:	no data available
(k) Vapour pressure:	no data available
(l) Vapour density:	no data available
(m) Relative density:	0.97 g/cm³ (20 °C)
(n) Solubility(ies)	
at 20 °C:	no data available
Soluble (g/L) in:	no data available
(o) Partition coefficient: n-octanol/water:	no data available
(p) Auto-ignition temperature:	no data available
(q) Decomposition temperature:	no data available
(r) Viscosity	
Kinematic viscosity:	350 cSt (25 °C)
Dynamic viscosity:	no data available
(s) Explosive properties:	not applicable
(t) Oxidising properties:	not applicable

9.2 Other information

Bulk density:	no data available
Refraction index:	no data available
Dissociation constant:	no data available
Surface tension:	no data available
Henry constant:	no data available

E) Bio-Logic VMP3 Overcharge Regime Software Settings

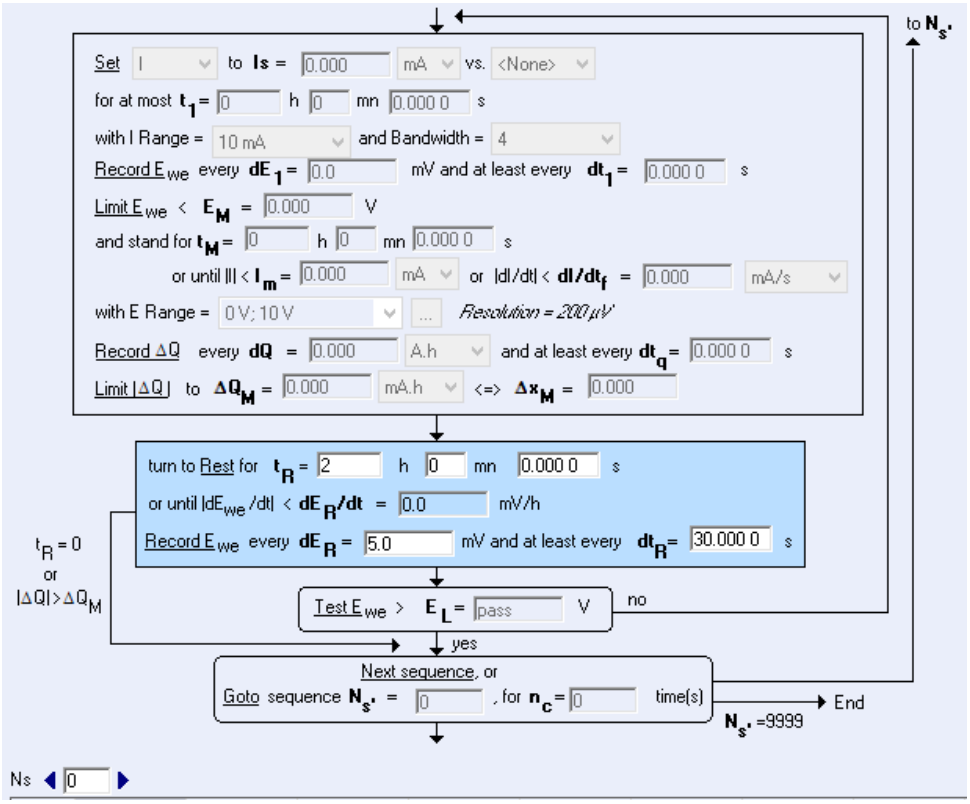

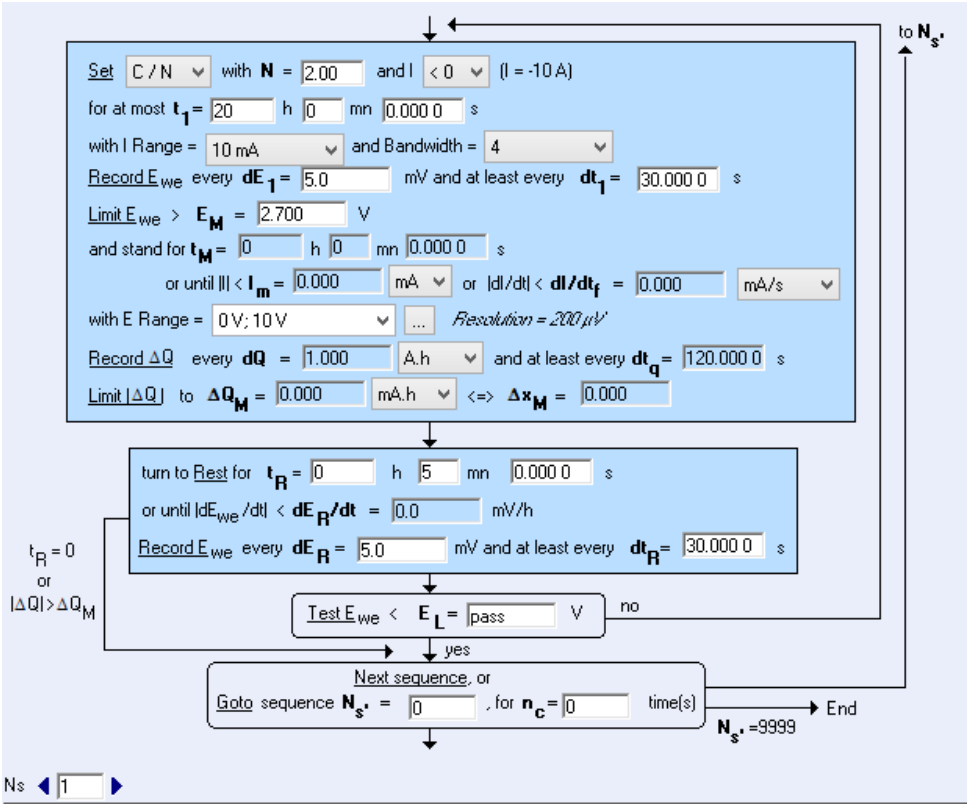

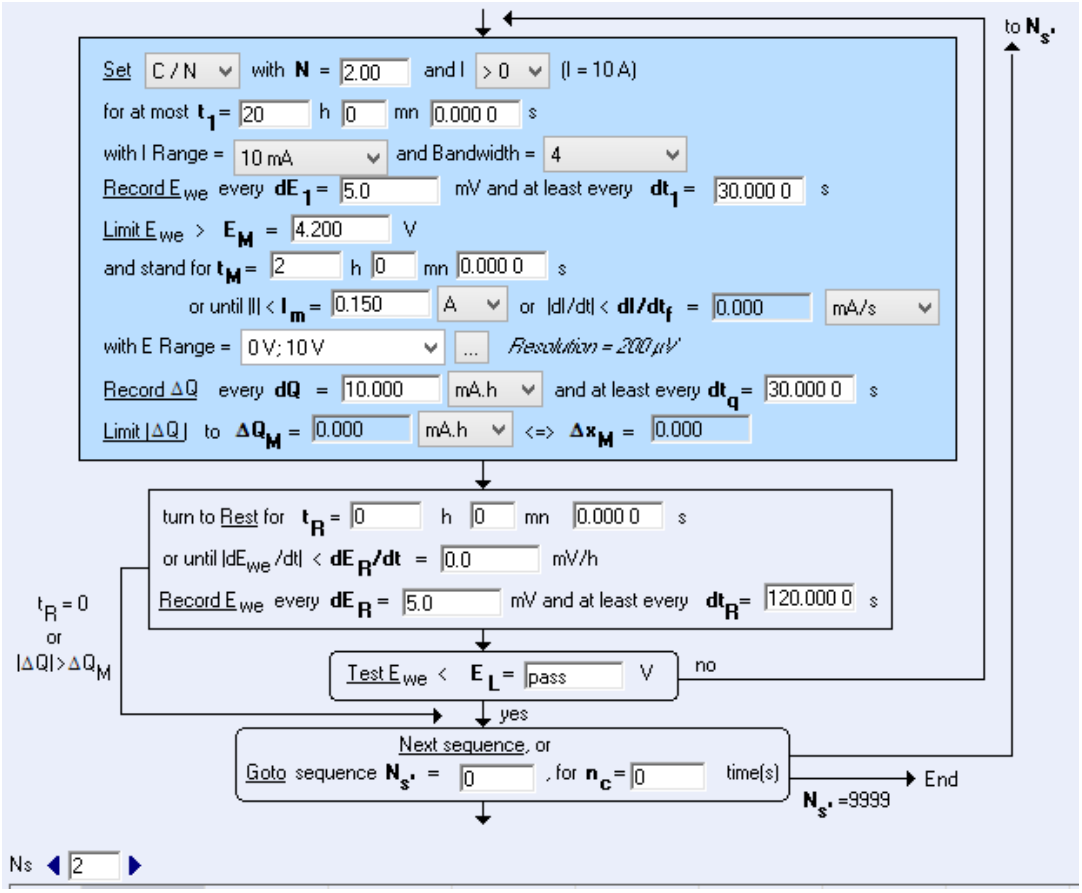
to Ns'
Set C / N with N = 2.00 and I > 0 (I = 10 A)
for at most t1 = 20 h 0 mn 0.000 0 s
with I Range = 10 mA and Bandwidth = 4
Record Ewe every dE1 = 5.0 mV and at least every dt1 = 30.000 0 s
Limit Ewe > EM = 4.200 V
and stand for tM = 2 h 0 mn 0.000 0 s
or until |I| < Im = 0.150 A or |dI/dt| < dI/dtf = 0.000 mA/s
with E Range = 0 V; 10 V ... Resolution = 200 µV
Record ΔQ every dQ = 10.000 mA.h and at least every dtq = 30.000 0 s
Limit |ΔQ| to ΔQM = 0.000 mA.h <=> ΔxM = 0.000
turn to Rest for tR = 0 h 0 mn 0.000 0 s
or until |dEwe /dt| < dER/dt = 0.0 mV/h
Record Ewe every dER = 5.0 mV and at least every dtR = 120.000 0 s
tR = 0 or |ΔQ|>ΔQM
Test Ewe < EL = pass V
no
yes
Next sequence, or
Goto sequence Ns' = 0 , for nc = 0 time(s)
End
Ns' =9999
Ns 2

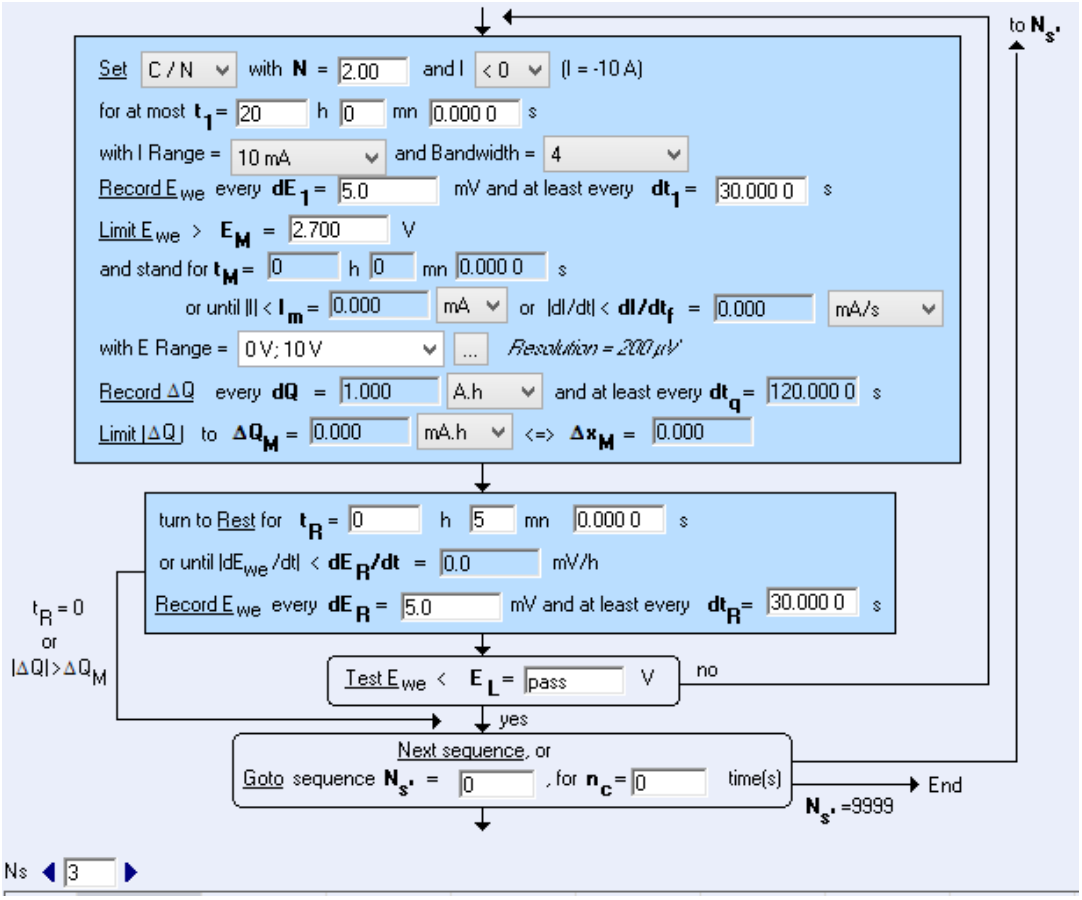
to Ns'
Set C / N with N = 2.00 and I < 0 (I = -10 A)
for at most t1 = 20 h 0 mn 0.000 0 s
with I Range = 10 mA and Bandwidth = 4
Record Ewe every dE1 = 5.0 mV and at least every dt1 = 30.000 0 s
Limit Ewe > EM = 2.700 V
and stand for tM = 0 h 0 mn 0.000 0 s
or until |I| < Im = 0.000 mA or |dI/dt| < dI/dtf = 0.000 mA/s
with E Range = 0 V; 10 V ... Resolution = 200 µV
Record ΔQ every dQ = 1.000 A.h and at least every dtq = 120.000 0 s
Limit |ΔQ| to ΔQM = 0.000 mA.h <=> ΔxM = 0.000
turn to Rest for tR = 0 h 5 mn 0.000 0 s
or until |dEwe /dt| < dER/dt = 0.0 mV/h
Record Ewe every dER = 5.0 mV and at least every dtR = 30.000 0 s
tR = 0 or |ΔQ|>ΔQM
Test Ewe < EL = pass V
no
yes
Next sequence, or
Goto sequence Ns' = 0 , for nc = 0 time(s)
End
Ns' =9999
Ns 3

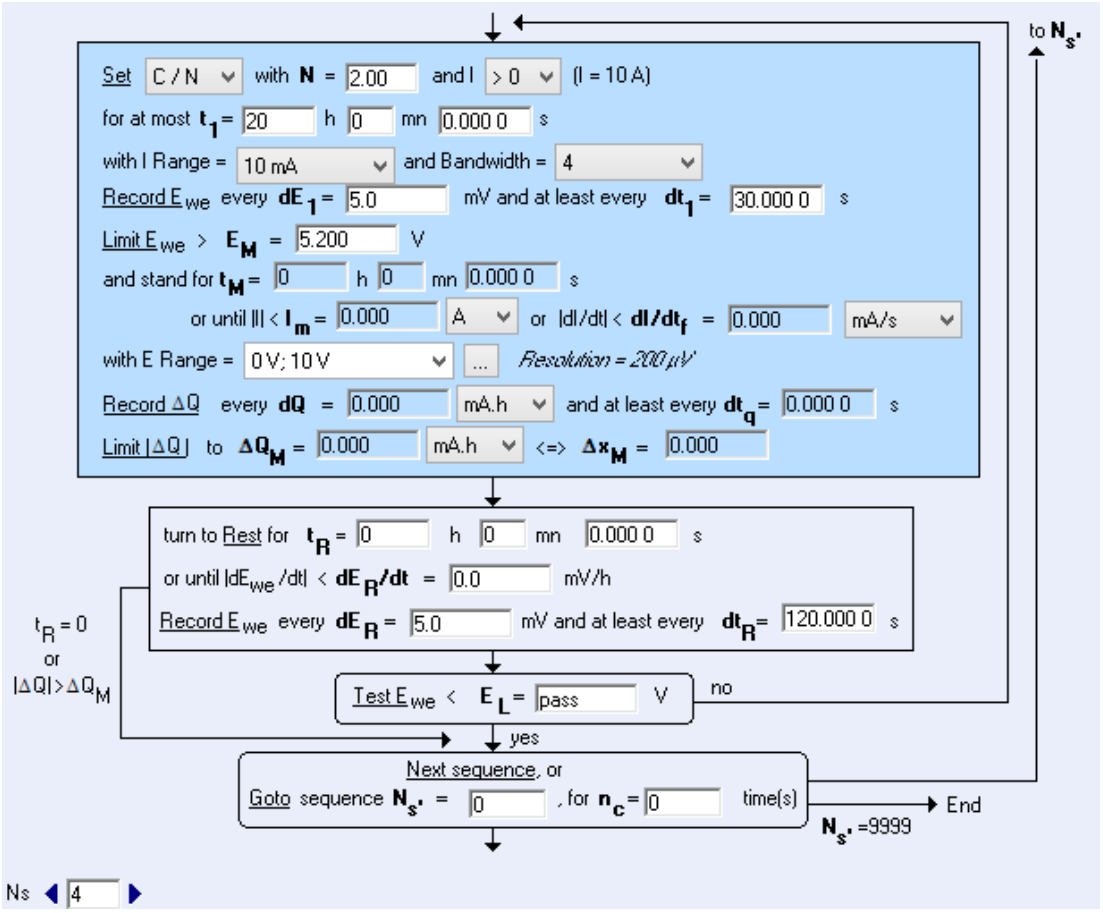
to $N_{s'}$
Set C / N with N = 2.00 and I > 0 (I = 10 A)
for at most t_1 = 20 h 0 mn 0.000 0 s
with I Range = 10 mA and Bandwidth = 4
Record E_{we} every dE_1 = 5.0 mV and at least every dt_1 = 30.000 0 s
Limit E_{we} > E_M = 5.200 V
and stand for t_M = 0 h 0 mn 0.000 0 s
or until |I| < I_m = 0.000 A or |dI/dt| < dI/dt_f = 0.000 mA/s
with E Range = 0 V; 10 V ... Resolution = 200 µV
Record ΔQ every dQ = 0.000 mA.h and at least every dt_q = 0.000 0 s
Limit |ΔQ| to ΔQ_M = 0.000 mA.h <=> Δx_M = 0.000
turn to Rest for t_R = 0 h 0 mn 0.000 0 s
or until $|dE_{we}/dt| < dE_R/dt$ = 0.0 mV/h
Record E_{we} every dE_R = 5.0 mV and at least every dt_R = 120.000 0 s
$t_R = 0$ or $|\Delta Q| > \Delta Q_M$
Test E_{we} < E_L = pass V
no
yes
Next sequence, or
Goto sequence $N_{s'}$ = 0 , for n_c = 0 time(s)
End
$N_{s'}$ =9999
Ns 4

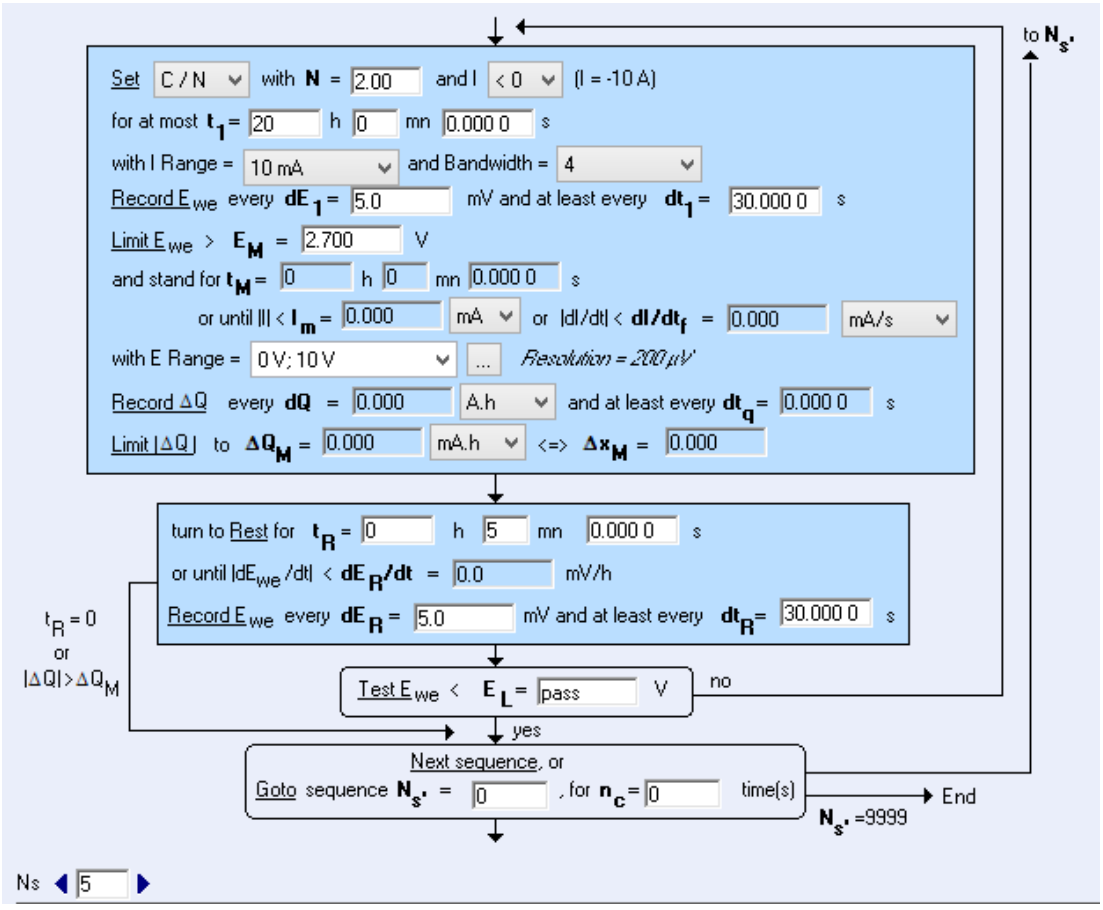
to $N_{s'}$
Set C / N with N = 2.00 and I < 0 (I = -10 A)
for at most t_1 = 20 h 0 mn 0.000 0 s
with I Range = 10 mA and Bandwidth = 4
Record E_{we} every dE_1 = 5.0 mV and at least every dt_1 = 30.000 0 s
Limit E_{we} > E_M = 2.700 V
and stand for t_M = 0 h 0 mn 0.000 0 s
or until |I| < I_m = 0.000 mA or |dI/dt| < dI/dt_f = 0.000 mA/s
with E Range = 0 V; 10 V ... Resolution = 200 µV
Record ΔQ every dQ = 0.000 A.h and at least every dt_q = 0.000 0 s
Limit |ΔQ| to ΔQ_M = 0.000 mA.h <=> Δx_M = 0.000
turn to Rest for t_R = 0 h 5 mn 0.000 0 s
or until $|dE_{we}/dt| < dE_R/dt$ = 0.0 mV/h
Record E_{we} every dE_R = 5.0 mV and at least every dt_R = 30.000 0 s
$t_R = 0$ or $|\Delta Q| > \Delta Q_M$
Test E_{we} < E_L = pass V
no
yes
Next sequence, or
Goto sequence $N_{s'}$ = 0 , for n_c = 0 time(s)
End
$N_{s'}$ =9999
Ns 5

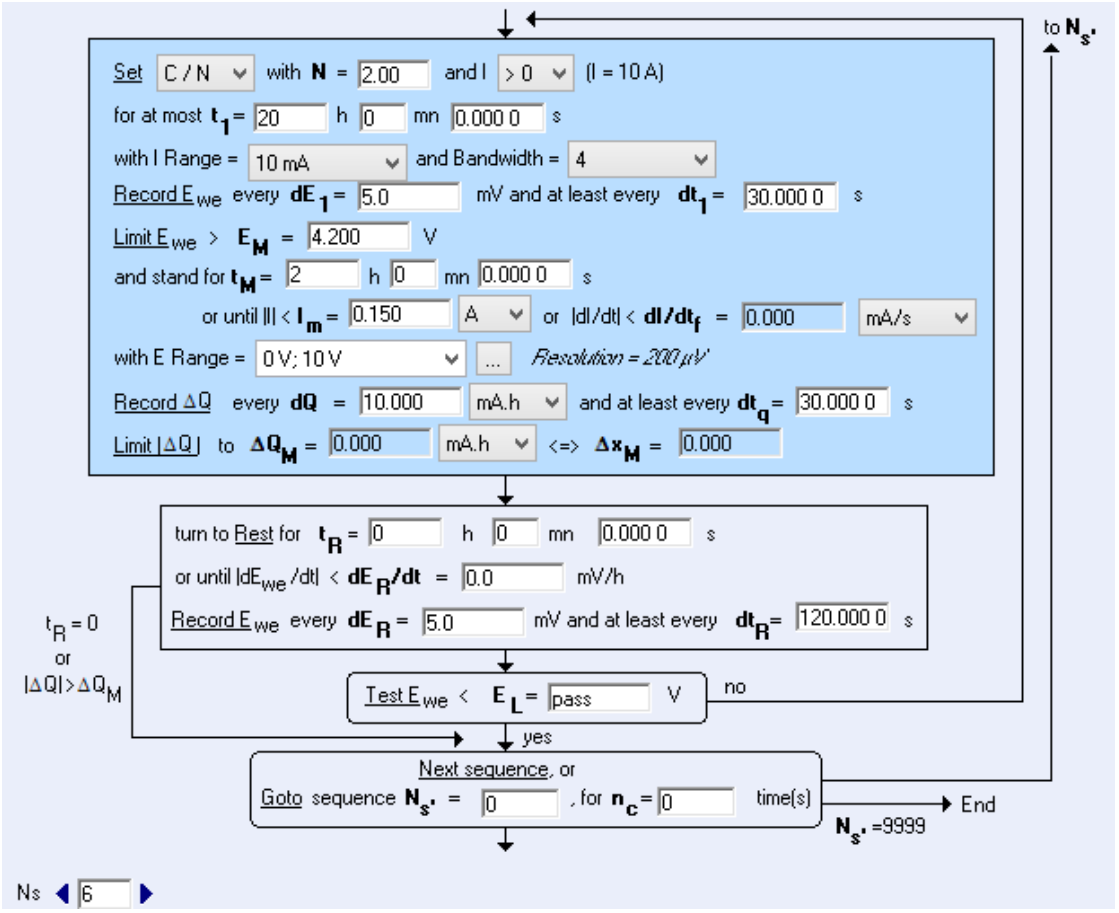
to Ns'
Set C / N with N = 2.00 and I > 0 (I = 10 A)
for at most t1 = 20 h 0 mn 0.000 0 s
with I Range = 10 mA and Bandwidth = 4
Record Ewe every dE1 = 5.0 mV and at least every dt1 = 30.000 0 s
Limit Ewe > EM = 4.200 V
and stand for tM = 2 h 0 mn 0.000 0 s
or until |I| < Im = 0.150 A or |dI/dt| < dI/dtf = 0.000 mA/s
with E Range = 0 V; 10 V ... Resolution = 200 µV
Record ΔQ every dQ = 10.000 mA.h and at least every dtq = 30.000 0 s
Limit |ΔQ| to ΔQM = 0.000 mA.h <=> ΔxM = 0.000
turn to Rest for tR = 0 h 0 mn 0.000 0 s
or until |dEwe /dt| < dER/dt = 0.0 mV/h
Record Ewe every dER = 5.0 mV and at least every dtR = 120.000 0 s
tR = 0 or |ΔQ|>ΔQM
Test Ewe < EL = pass V
no
yes
Next sequence, or
Goto sequence Ns' = 0 , for nc = 0 time(s)
End
Ns' =9999
Ns 6

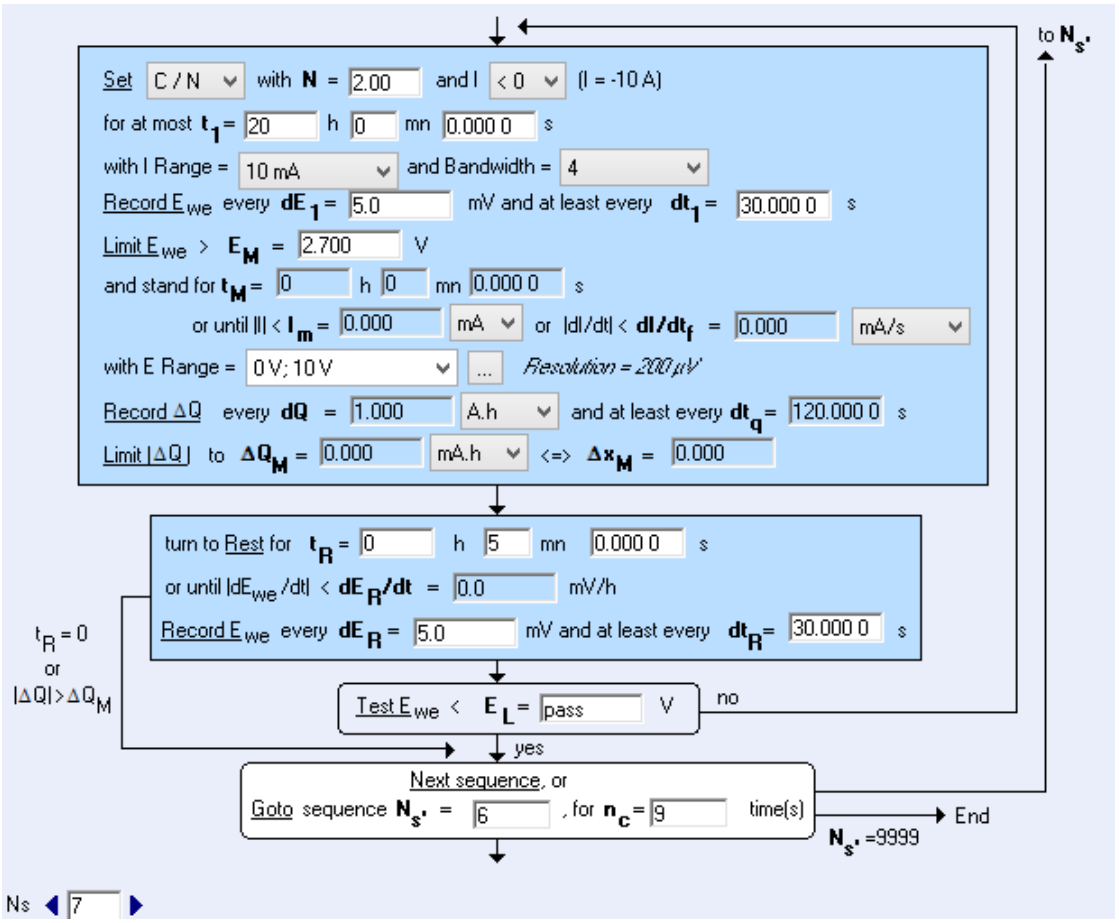
to Ns'
Set C / N with N = 2.00 and I < 0 (I = -10 A)
for at most t1 = 20 h 0 mn 0.000 0 s
with I Range = 10 mA and Bandwidth = 4
Record Ewe every dE1 = 5.0 mV and at least every dt1 = 30.000 0 s
Limit Ewe > EM = 2.700 V
and stand for tM = 0 h 0 mn 0.000 0 s
or until |I| < Im = 0.000 mA or |dI/dt| < dI/dtf = 0.000 mA/s
with E Range = 0 V; 10 V ... Resolution = 200 µV
Record ΔQ every dQ = 1.000 A.h and at least every dtq = 120.000 0 s
Limit |ΔQ| to ΔQM = 0.000 mA.h <=> ΔxM = 0.000
turn to Rest for tR = 0 h 5 mn 0.000 0 s
or until |dEwe /dt| < dER/dt = 0.0 mV/h
Record Ewe every dER = 5.0 mV and at least every dtR = 30.000 0 s
tR = 0 or |ΔQ|>ΔQM
Test Ewe < EL = pass V
no
yes
Next sequence, or
Goto sequence Ns' = 6 , for nc = 9 time(s)
End
Ns' =9999
Ns 7

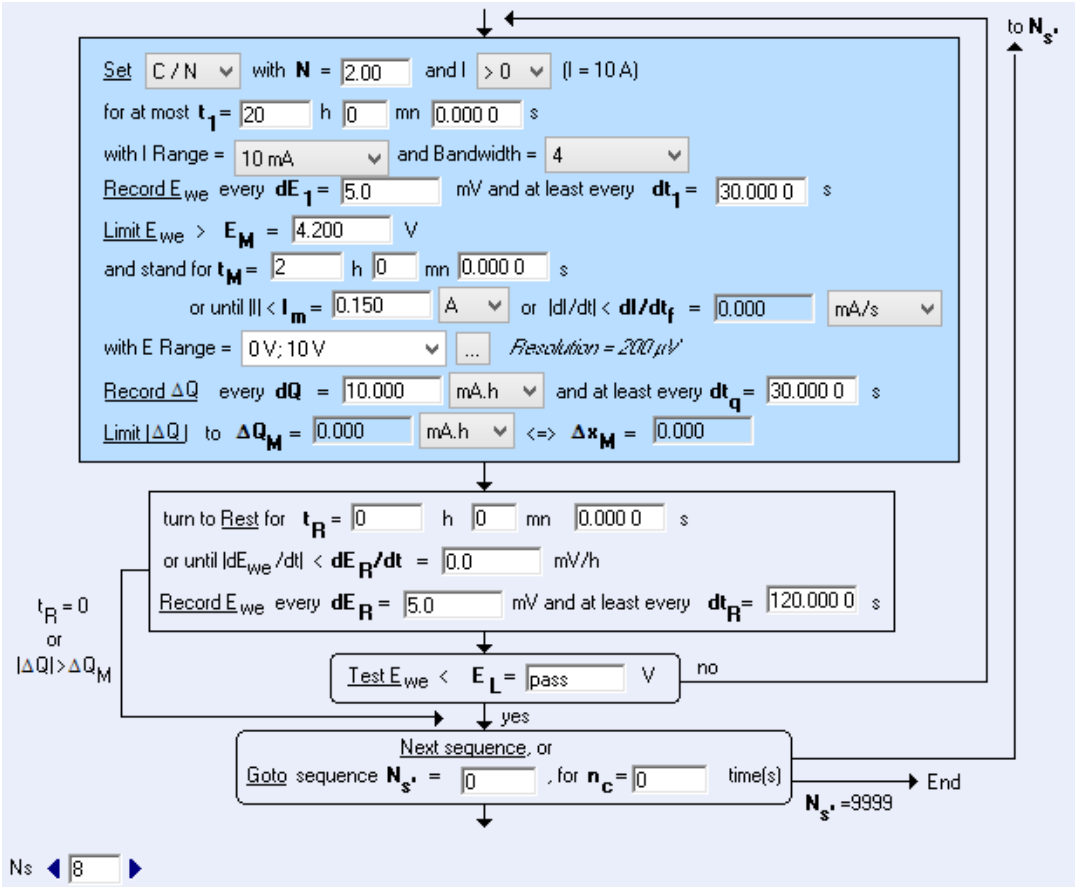
to Ns'
Set C / N with N = 2.00 and I > 0 (I = 10 A)
for at most t1 = 20 h 0 mn 0.000 0 s
with I Range = 10 mA and Bandwidth = 4
Record Ewe every dE1 = 5.0 mV and at least every dt1 = 30.000 0 s
Limit Ewe > EM = 4.200 V
and stand for tM = 2 h 0 mn 0.000 0 s
or until |I| < Im = 0.150 A or |dI/dt| < dI/dtf = 0.000 mA/s
with E Range = 0 V; 10 V ... Resolution = 200 µV
Record ΔQ every dQ = 10.000 mA.h and at least every dtq = 30.000 0 s
Limit |ΔQ| to ΔQM = 0.000 mA.h <=> ΔxM = 0.000
turn to Rest for tR = 0 h 0 mn 0.000 0 s
or until |dEwe /dt| < dER/dt = 0.0 mV/h
Record Ewe every dER = 5.0 mV and at least every dtR = 120.000 0 s
tR = 0 or |ΔQ|>ΔQM
Test Ewe < EL = pass V
no
yes
Next sequence, or
Goto sequence Ns' = 0 , for nc = 0 time(s)
End
Ns' =9999
Ns 8

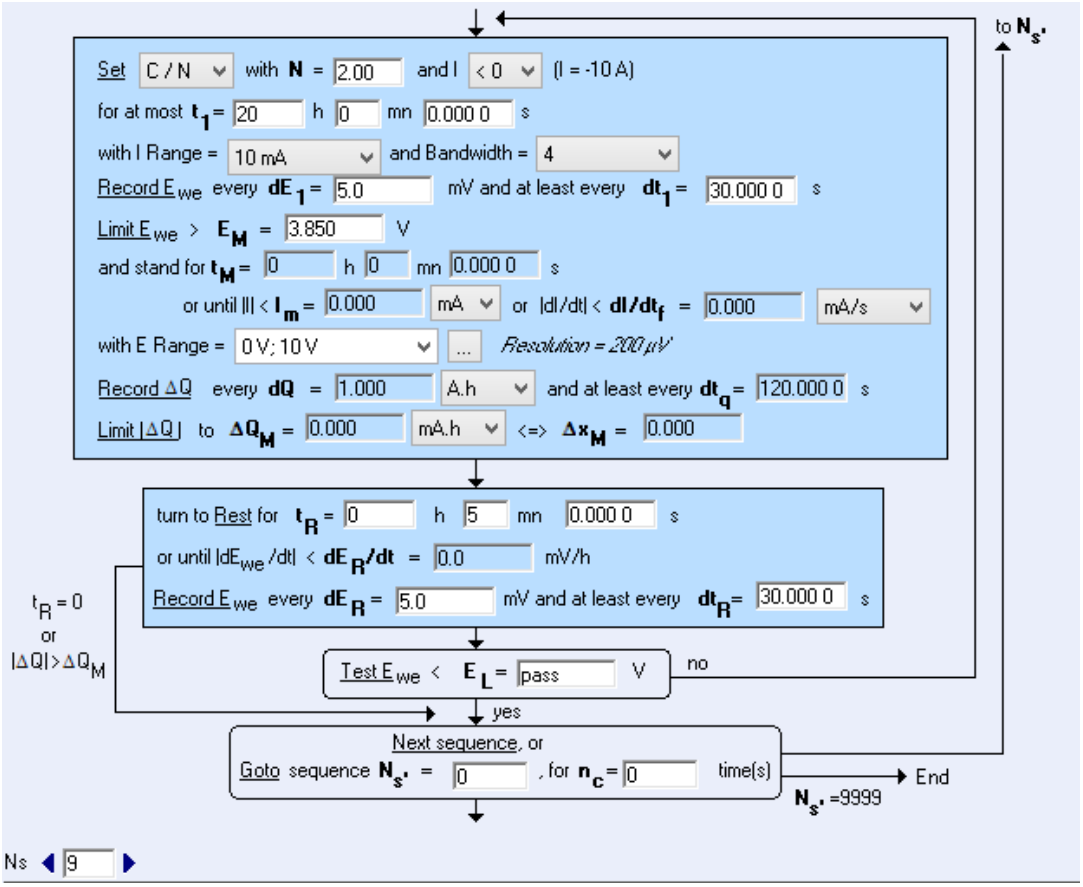
to Ns'
Set C / N with N = 2.00 and I < 0 (I = -10 A)
for at most t1 = 20 h 0 mn 0.000 0 s
with I Range = 10 mA and Bandwidth = 4
Record Ewe every dE1 = 5.0 mV and at least every dt1 = 30.000 0 s
Limit Ewe > EM = 3.850 V
and stand for tM = 0 h 0 mn 0.000 0 s
or until |I| < Im = 0.000 mA or |dI/dt| < dI/dtf = 0.000 mA/s
with E Range = 0 V; 10 V ... Resolution = 200 µV
Record ΔQ every dQ = 1.000 A.h and at least every dtq = 120.000 0 s
Limit |ΔQ| to ΔQM = 0.000 mA.h <=> ΔxM = 0.000
turn to Rest for tR = 0 h 5 mn 0.000 0 s
or until |dEwe /dt| < dER/dt = 0.0 mV/h
Record Ewe every dER = 5.0 mV and at least every dtR = 30.000 0 s
tR = 0 or |ΔQ|>ΔQM
Test Ewe < EL = pass V
no
yes
Next sequence, or
Goto sequence Ns' = 0 , for nc = 0 time(s)
End
Ns' =9999
Ns 9

F) Simulation Results of the Equivalent Circuit Model

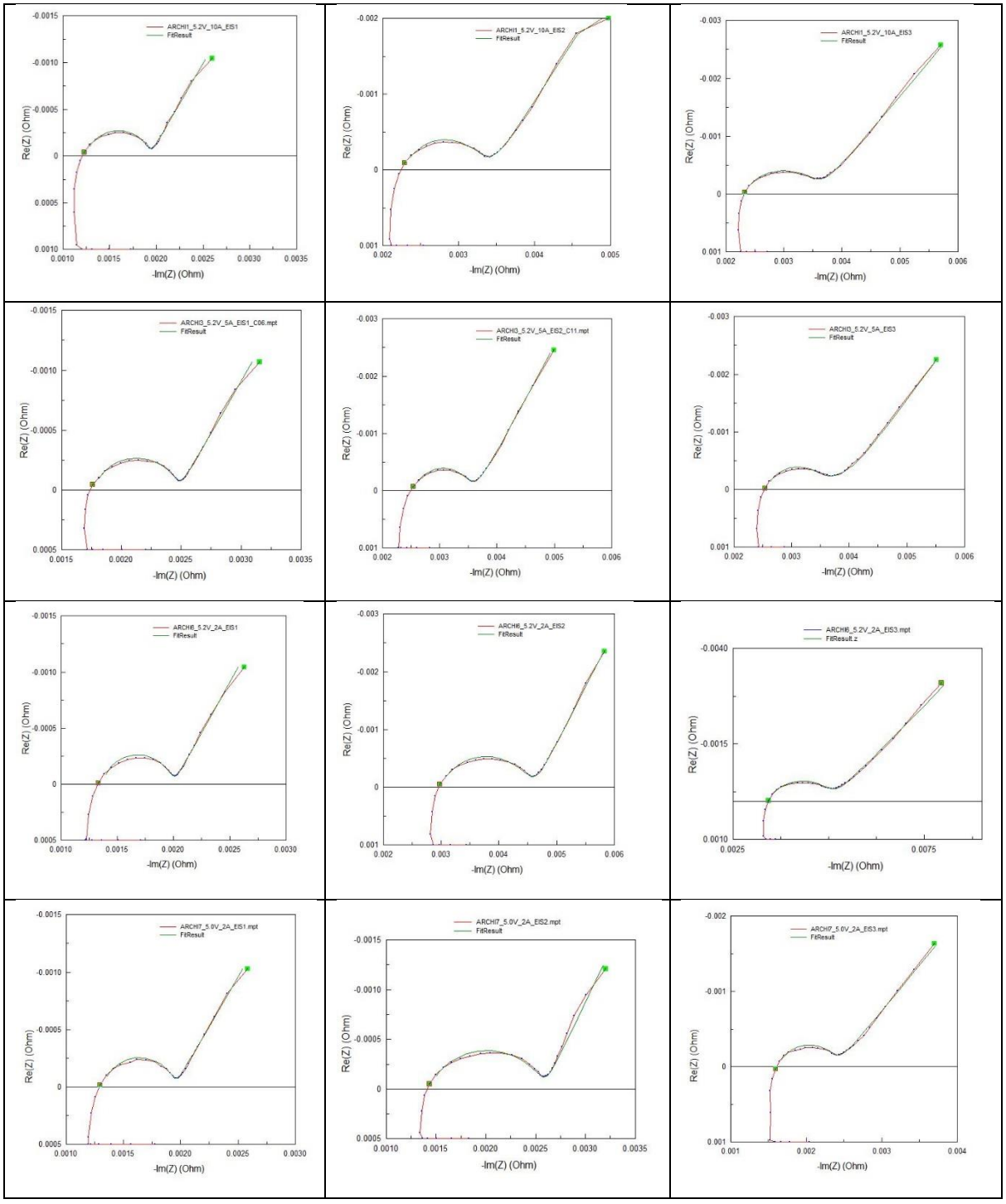

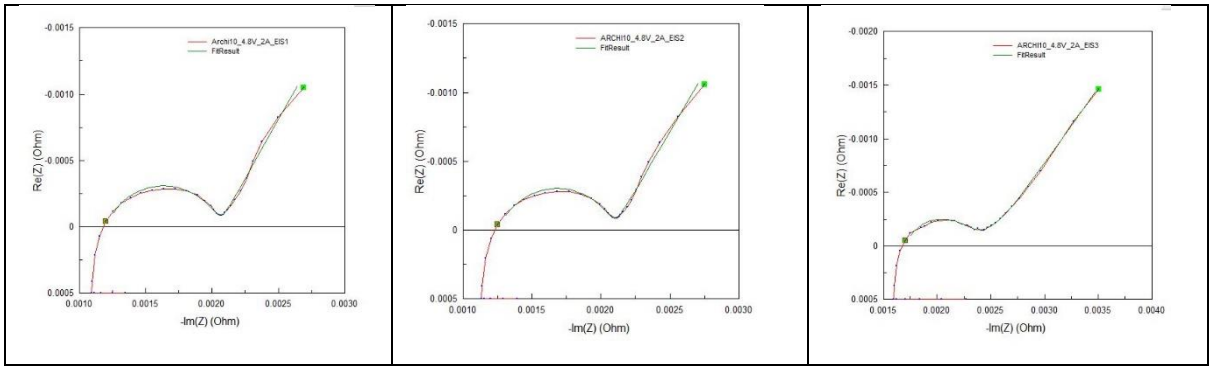

G) MACCOR Overcharge Regime Software Settings

Step	Type	Mode	Value	Limit	Value	End Type	Op	Value	Goto	Report Type	Value	Options
1	Rest					Step Time	=	00:30:00	002	Step Time	00:00:05	ANNN
2	Charge	Current	2.0			Voltage	>=	7.9	003	Voltage	0.01	ANNN
										Step Time	00:00:10	
										Thermocouple	1 / 1.0	
										Thermocouple	2 / 1.0	
3	Rest					Step Time	=	00:20:00	004	Step Time	00:00:01	ANYN
										Voltage	0.01	
										Thermocouple	1 / 1.0	
										Thermocouple	2 / 1.0	
4	Rest					Step Time	=	01:00:00	005	Step Time	00:01:00	ANYN
										Voltage	0.02	
										Thermocouple	1 / 2.0	
										Thermocouple	2 / 2.0	
5	Rest					Step Time	=	24:00:00	006	Step Time	00:05:00	ANYN
										Voltage	0.02	
										Thermocouple	1 / 5.0	
										Thermocouple	2 / 5.0	
6	End											